Philipp Ott

Measurement of $Z\gamma\gamma$ production in pp collisions at $\sqrt{s} = 13\,\text{TeV}$ with the ATLAS detector

Dissertation

HD-KIP-23-47

Dissertation

submitted to the

Combined Faculty of Mathematics, Engineering and

Natural Sciences

of Heidelberg University, Germany

for the degree of

Doctor of Natural Sciences

Put forward by

Philipp Sebastian Ott

born in: Offenburg

Oral examination: June 7th, 2023

Measurement of $Z\gamma\gamma$ production in pp collisions at $\sqrt{s} = 13\,\mathrm{TeV}$ with the ATLAS detector

Referees: Prof. Dr. Hans-Christian Schultz-Coulon
              Prof. Dr. Klaus Reygers

Zusammenfassung

Ereignisse, die multiple elektroschwache Eichbosonen im Endzustand enthalten, sind wichtige Signaturen, um die nicht-abelsche Struktur der $\mathrm{SU}(2)_\mathrm{L} \times \mathrm{U}(1)_\mathrm{Y}$ Symmetrie des Standard Modells zu untersuchen. Die $Z\gamma\gamma$ Produktion wird im Run 2 Datensatz analysiert, der vom ATLAS Detektor am LHC aufgenommen wurde. Der Datensatz enthält p–p Kollisionen bei einer Schwerpunktsenergie von $13\,\mathrm{TeV}$ und entspricht einer integrierten Luminosität von $139\,\mathrm{fb}^{-1}$. Der leptonische Zerfallskanal des Z-Bosons wird analysiert. Endzustände, in denen Photonen von Leptonen des Z-Boson Zerfalls abgestrahlt werden, werden unterdrückt, um ausschließlich die prompte Photon-Produktion zu messen. Der integrierte sowie differentielle Wirkungsquerschnitte in Abhängigkeit von sechs kinematischen Observablen werden in einem Phasenraum auf Teilchenebene gemessen. Hierbei wird der Einfluss des Detektors auf alle Wirkungsquerschnitte korrigiert. Die gemessenen Ergebnisse werden mit der Vorhersage von MC Ereignisgeneratoren mit NLO Präzision in QCD verglichen, wobei eine gute Übereinstimmung gesehen wird. Der differentielle Wirkungsquerschnitt, der die höchste Sensitivität für Neue Physik aufweist, wird verwendet, um innerhalb einer effektiven Feldtheorie Ausschlussgrenzen auf die Kopplung von Dimension-8 Operatoren zu setzen. Existierende Ausschlussgrenzen können um bis zu zwei Größenordnung verbessert werden.

Abstract

Final states with multiple electroweak gauge bosons are important signatures for probing the non-Abelian character of the Standard Model $\mathrm{SU}(2)_\mathrm{L} \times \mathrm{U}(1)_\mathrm{Y}$ symmetry. The triple gauge boson production of $Z\gamma\gamma$ is measured in Run 2 of the LHC at a centre-of-mass energy of $13\,\mathrm{TeV}$. The dataset contains p–p collisions recorded with the ATLAS detector and corresponds to an integrated luminosity of $139\,\mathrm{fb}^{-1}$. The fully leptonic decay channel of the Z boson is analysed. Final state radiation is suppressed to obtain a pure sample of $Z\gamma\gamma$ events with prompt photons. The integrated cross section and differential cross sections of six kinematic observables are measured in a fiducial volume at particle-level, where the cross sections are corrected for detector effects. The results are compared to predictions of MC event generators at NLO QCD precision showing good agreement. The measurement with the highest sensitivity for new physics effects is used to constrain dimension-8 operators in an effective field theory approach. Existing constraints are improved by up to two orders of magnitude.

Contents

1. Introduction

The Large Hadron Collider (LHC) at CERN produces particle collisions at the high-energy frontier of accelerator-based experiments. The amount of the centre-of-mass energy which enters the particle interactions is large enough to create all constituents of the Standard Model of Particle Physics (SM). This includes low-mass fermions like electrons and muons, the gauge bosons mediating the fundamental forces, and the heaviest SM particle, the top quark. A verification of the SM predictions is possible for energy scales stretching at least five orders of magnitude. The SM is remarkably successful in describing particle physics at high-energy collider experiments. There are, however, limitations such as the vanishing neutrino mass in the SM formalism[1]. Compelling evidence is found in the universe for the distribution of non-luminous matter accounting for approximately 27% of the total energy density [2]. Attempts to describe this matter density using the particles embedded in the SM theory have so far failed. Therefore, a broad physics program is initiated at the LHC to search for new physics signatures [3–5]. One of the many approaches for studying such effects at the LHC is to search for deviations in the distribution of observables sensitive to, for instance, the SM predictions in the electroweak sector.

The electroweak (EW) sector of the SM describes electromagnetic and weak interactions mediated by the massless photon and the massive W and Z bosons. Final states with multiple gauge bosons are important probes for the predictions of the EW sector but are challenging to measure due to small production cross sections [6, 7]. The $\gamma\gamma\gamma$ production has the largest cross section of triple gauge boson processes and was therefore the first of such processes to be observed at the LHC [8]. Exchanging one of the massless photons with a massive W or Z boson leads to a reduction of the cross section by approximately one order of magnitude. The first cross-section measurement of the $Z\gamma\gamma$ production was published at a centre-of-mass energy of $\sqrt{s} = 8\,\mathrm{TeV}$ in 2016. Datasets containing p–p collisions with an integrated luminosity of $19.4\,\mathrm{fb}^{-1}$ to $20.3\,\mathrm{fb}^{-1}$ were analysed [9, 10]. The integrated cross section was determined but the limited size of the recorded dataset did not allow to measure differential quantities. The vast amount of data recorded in Run 2 of the LHC makes the measurement of many triple gauge boson production channels feasible for the first time [7]. For the $Z\gamma\gamma$ process, a differential verification of the SM predictions and searching for new physics effects becomes possible.

---

[1] Oscillations of one neutrino flavour eigenstate into another are observed and require non-zero neutrino masses [1].

The non-Abelian structure of the $\mathrm{SU}(2)_\mathrm{L} \times \mathrm{U}(1)_\mathrm{Y}$ symmetry gives rise to triple and quartic gauge boson couplings. Quartic couplings of photons and Z bosons are prohibited in the SM but could contribute to the $Z\gamma\gamma$ phase-space via physics beyond the SM. The analysis presented in [11] measured the integrated cross section of $Z\gamma\gamma$ at a centre-of-mass energy of $13\,\mathrm{TeV}$ with the CMS detector. The analysed p–p collisions correspond to an integrated luminosity of $137\,\mathrm{fb}^{-1}$. Constraints for interactions of higher-dimensional operators giving rise to quartic couplings of neutral EW gauge bosons were derived.

The analysis presented in this thesis measures the $Z\gamma\gamma$ production at a centre-of-mass energy of $13\,\mathrm{TeV}$ with the ATLAS detector. The analysed dataset contains p–p collisions recorded in Run 2 of the LHC and corresponds to an integrated luminosity of $139\,\mathrm{fb}^{-1}$. The phase-space in this analysis is optimised to have a highly-efficient rejection of photons from final state radiation. This allows to measure the simultaneous triple gauge boson production at tree-level. The integrated cross section and, for the first time, differential cross sections as functions of six kinematic observables are measured. The contributions of the two most dominant background processes are determined using data-driven techniques – MC simulation is used for the remaining background processes. The cross-section measurements are corrected for detector effects. Inclusively, a correction factor derived from MC simulation is used, while differentially an iterative Bayesian unfolding is performed. The unfolded differential cross section with the highest sensitivity for new physics is used in the formalism of effective field theory to constrain the coupling strength of higher-dimensional operators.

This thesis is structured in the following way: Chapter 2 introduces the theoretical principles of the SM and effective field theory. It concludes with an overview of ATLAS triple gauge boson production measurements. The functionality of the LHC and the ATLAS sub-detectors is explained in Chapter 3. Chapter 4 describes the ATLAS particle reconstruction emphasising the $Z\gamma\gamma$ final state particles. The basic principles of MC event generators are outlined in the following. Chapter 5 summarises the event selection and presents the $Z\gamma\gamma$ analysis strategy. The determination of the background contributions and the associated uncertainty treatments are described in Chapter 6. The cross-section measurements are discussed in Chapter 7. This includes the treatment of systematic uncertainties, the correction of detector effects, and the final cross-section results. Chapter 8 describes the effective field theory approach which is used to constrain new physics effects. This thesis is concluded with a summary of the $Z\gamma\gamma$ analysis in Chapter 9.

Author's Contribution

The work presented in this thesis benefits heavily from the successful operation of the LHC as well as the abundance and high quality of the data recorded with the ATLAS detector. The frequent exchange with the ATLAS community and the excellent support of experts was helpful to converge on the details of certain aspects of this analysis. Official recommendations and frameworks provided by the ATLAS community are explicitly referenced where followed and used.

Before working on the $Z\gamma\gamma$ analysis, I performed trigger studies for the *Phase-II Upgrade* of the ATLAS Tile calorimeter [12–14]. The Phase-II Upgrade will prepare the ATLAS detector for data taking at unprecedented luminosity. New techniques for Level-1 trigger algorithms which enable to decrease the trigger rate are especially interesting in this context. I investigated if the electron trigger efficiency can be improved when using additional layer information from the central part of the ATLAS hadronic calorimeter (Tile calorimeter). The results of this study show that it is beneficial to use additional information from the first two layers of the Tile Calorimeter. The selection efficiency for genuine electrons remains roughly stable but the rejection of hadrons passing the electron trigger requirements can be improved by up to 19%.

I contributed to numerous aspects of the $Z\gamma\gamma$ analysis: I defined parts of the event selection and performed the trigger optimisation studies, which resulted in using more stringent lepton identification and isolation requirements. I also investigated the energy dependence of fake leptons, which allowed to lower the lepton momentum threshold. I tested the purity and efficiency of the FSR rejection requirement and compared it to alternative definitions. Furthermore, I developed the 2D template fit which serves as an alternative method for deriving the most dominant source of background contamination (previous analyses established this method; it was re-implemented and further developed in this thesis). The isolation energy profile of prompt and fake photons was studied in detail and compared to data. The fitting procedure was validated using MC simulation and one-fourth of the full Run 2 dataset. I determined the statistical uncertainty and derived all sources of systematic uncertainty in the 2D template fit and measured their impact on the fitted normalisation. Additionally, I determined other background sources, like the fake lepton contribution using a $W\gamma\gamma$ MC simulation at LO and NLO QCD precision. I was involved in the determination of the systematic uncertainties for the cross-section measurements, specifically the impact of theory uncertainties. I implemented and validated the effective field theory approach which is used to constrain the contributions of higher-dimensional operators. The MC samples were generated and a Rivet routine was

implemented to apply the fiducial selection. Feasibility studies were performed to find the observable most sensitive to new physics effects. The fitting framework was validated and both non-unitarised and unitarised confidence intervals were determined for the higher-dimensional operators. I converted all results of the $Z\gamma\gamma$ analysis into a format (*yaml*) readable by a central particle physics database (*HEPData*), in which they are now published. I was heavily involved in the publication process of the $Z\gamma\gamma$ analysis. I was one of the two contact physicists and editors for the ATLAS internal note and the paper. I also discussed and addressed the comments put forward by the ATLAS community and the journal referee during the review process. The $Z\gamma\gamma$ analysis is expected to be published soon in the *European Physical Journal C*.

2. Theoretical Background

The mathematical formulation of fundamental interactions between elementary particles is defined in the *Standard Model of Particle Physics* (SM) [15–17]. The quantum field theory (QFT) of the SM offers a description for three of the four fundamental interactions: The *electromagnetic force* is mediated by photons, which are exchanged in the interaction of electrically charged particles. Quarks experience the *strong force*, which is transmitted by gluons and leads to the formation of bound quark states, the nucleons. The massive $W^{\pm}$ and Z bosons are the mediators of the *weak force* responsible for radioactive processes like the $\beta^{\pm}$ decay or quark-flavour transitions. The fourth fundamental force is gravitation and attempts to merge it into the QFT of the SM, called *grand unification*, have yet failed because a quantisation of the gravitational force leads to a non-renormalizable theory [18]. The non-description of gravitational effects does not have a physical impact at subatomic scales due to the weakness of the gravitational force. On cosmological scales, observations from rotation curves of spiral galaxies or gravitational lensing effects [2] indicate large amounts of non-luminous matter distributed throughout the universe. This so-called *dark matter* (DM) makes up approximately 27% of the energy density in the universe, in comparison to the 5% of visible matter. Theories often assign a particle nature to DM, in which case the particle can only interact gravitationally and through a weak interaction. The SM does not deliver such a DM candidate, prompting decades of direct, indirect, and collider-based DM searches [19, 20]. The SM is thus not complete and theories beyond the SM are needed. It is, however, immensely successful in describing interactions between fundamental particles of ordinary matter that can be experienced in current high-energy collider experiments.

The following section gives a description of the SM QFT and the fundamental particles embedded in its theory. A model-independent extension of the SM is presented afterwards allowing to probe the effects of new physics on SM observables measurable with modern particle colliders. Lastly, triple gauge boson production is introduced, which describes a set of processes similar to the one studied in this thesis.

2.1. The Standard Model of Particle Physics

The Standard Model of Particle Physics is a quantum field theory which describes comprehensively particle interactions at subatomic scales. The elementary particles of its theory can be sorted according to their spin into *fermions* and *bosons*.

Particles with half-integer spin s, such as leptons and quarks with $s = \frac{1}{2}$, are called fermions. They come in three generations with increasing mass scale[2]:

$$\underbrace{\begin{pmatrix} e \\ \nu_e \end{pmatrix}, \begin{pmatrix} \mu \\ \nu_\mu \end{pmatrix}, \begin{pmatrix} \tau \\ \nu_\tau \end{pmatrix}}_{\text{3 lepton generations}} \qquad \underbrace{\begin{pmatrix} u \\ d \end{pmatrix}, \begin{pmatrix} c \\ s \end{pmatrix}, \begin{pmatrix} t \\ b \end{pmatrix}}_{\text{3 quark generations}}.$$

For quarks, the scale stretches five orders of magnitude from the lightest mass of up-quarks $m_u = 2.16^{+0.49}_{-0.26}\,\text{MeV}$ to the top-quark mass $m_t = 172.69 \pm 0.30\,\text{GeV}$ [22]. Charged leptons and neutrinos carry $Q = \pm 1e$ and $Q = 0$, respectively[3]. The electric charge of the six quark flavours differs between *up-type* quarks (u, c, t) with $Q = +\frac{2}{3}e$ and *down-type* quarks (d, s, b) with $Q = -\frac{1}{3}e$.

Gauge bosons mediate the fundamental forces between elementary particles. They have integer spin $s = 1$ and can be grouped as follows:

$$\underbrace{\text{QED} \Leftrightarrow \gamma \qquad \text{weak force} \Leftrightarrow W^\pm, Z}_{\text{EW theory}} \qquad \text{QCD} \Leftrightarrow g.$$

The QFT of electromagnetism and the strong force is called *quantum electrodynamics* (QED) and *quantum chromodynamics* (QCD), respectively. The *electroweak theory* (EW theory) unifies the effects of QED and the weak force in a single theory (see Section 2.1.4). The mediator of QED is the neutrally charged and massless photon (γ). The coupling of photons to fermions is proportional to the electric charge. This proportionality prohibits photon self-couplings in the SM. The charged $W^\pm$ bosons and the neutral Z boson are the mediators of the weak force. Contrary to the photon, the W and Z boson are massive having $m_W = 80.377 \pm 0.012\,\text{GeV}$ and $m_Z = 91.1876 \pm 0.0021\,\text{GeV}$ [22]. Interactions involving $W^\pm$ bosons enable the transition between quark flavours. Transitions between flavours of the same quark generation are maximal, whereas transitions between different generations are suppressed. The transition probability can be extracted from the elements of the *Cabibbo-Kobayashi-Maskawa* (CKM) matrix, which describes quark mixing (see [16] and [22] for the $|V_{ij}|$-associated uncertainties):

$$V_{ij} = \begin{pmatrix} V_{ud} & V_{us} & V_{ub} \\ V_{cd} & V_{cs} & V_{cb} \\ V_{td} & V_{ts} & V_{tb} \end{pmatrix} \xrightarrow{|V_{ij}|} \begin{pmatrix} 0.97373 & 0.2243 & 0.00382 \\ 0.221 & 0.975 & 0.00408 \\ 0.0086 & 0.00415 & 1.014 \end{pmatrix}.$$

---

[2]The mass hierarchy is true for charged leptons and quarks. For neutrinos, normal and inverted hierarchy scenarios are possible, with the former currently experimentally favoured [21].

[3]The unit $e = 1.602 \times 10^{-19}\,\text{C}$ refers to the elementary charge.

The squared magnitudes of the diagonal elements are close to unity and describe the aforementioned flavour transitions within the same generation. When the Z boson mediates the weak interactions, only same-flavour quarks can participate. Contrary to weak interactions involving quarks, *lepton universality* is observed for leptons. This means that the decay of a W and Z boson in the three lepton flavours occurs with approximately equal probability. Another special and unique characteristic of weak interactions is the maximal violation of parity and charge conservation [23] and the violation of the combined charge-parity symmetry [24]. The strong interaction between quarks is mediated by massless gluons (g). They are electrically neutral but instead carry a *colour charge*, which can take three values (red, green, blue) and to which the gluons couple. As the force carrier holds the quantum number which enables the coupling, gluon-gluon interactions are observed. Quarks are the only other SM particles that have a colour charge leading to quark-gluon couplings. A fundamental observation of QCD is that single quarks or gluons with non-zero colour states are not resolvable. This phenomenon is called *colour confinement* and leads to the formation of quark pairs, called *mesons*, e.g $\pi^{\pm}$ or ρ^0, or to a quark triplet, denoted as *baryons*, e.g. p and n. Recently, states with four quarks (*tetraquark*) and five quarks (*pentaquark*) have been discovered at CERN [25, 26]. The second type of boson in the SM is a scalar boson with $s = 0$, the Higgs boson (H). It is a crucial part of the SM as it is responsible for the generation of mass of both the fermions and gauge bosons. The underlying mechanism is further illustrated in Section 2.1.5. Measurements of the Higgs boson mass yield $m_H = 125.25 \pm 0.17\,\mathrm{GeV}$ [22].

2.1.1. Structure of the SM QFT

QFT combines the principles of relativistic quantum mechanics and classical field theory. The basis for the construction of the SM Lagrangian $\mathcal{L}$ is the verification of the *gauge principle* for symmetry operations, requiring invariance of $\mathcal{L}$ under *local transformations* (see Section 2.1.2). The symmetry group of the SM is

$$\mathrm{SU(3)_C} \otimes \mathrm{SU(2)_L} \otimes \mathrm{U(1)_Y}, \tag{2.1}$$

where S denotes special matrices with determinant 1 and U denotes unitary matrices fulfilling $\mathrm{UU}^{-1} = \mathrm{UU}^{\dagger} = \mathbb{1}$. Equation 2.1 is constructed from three building blocks:

- $\mathrm{U(1)_Y} \rightarrow$ symmetry group of QED with generator Y

- $\mathrm{SU(2)_L} \otimes \mathrm{U(1)_Y} \rightarrow$ symmetry group of EW theory with generators L and Y

- $\text{SU(3)}_\text{C} \rightarrow$ symmetry group of QCD with generators C

The generators of the symmetry groups above are all associated with a gauge boson vector field. A description of the individual parts of the SM QFT and symmetry group is given in the following.

2.1.2. Quantum Electrodynamics

The Lagrangian $\mathcal{L}_f$ of a free fermion field ψ with mass m, which satisfies the Dirac equation, and the Lagrangian $\mathcal{L}_A$ of a free photon vector field $A_\mu = \left(\phi, \vec{A}\right)$ are the pillars for the formulation of the QED theory:

$$\mathcal{L}_f = \bar{\psi}\left(i\gamma^\mu \partial_\mu - m\right)\psi. \tag{2.2}$$

$$\mathcal{L}_A = -\frac{1}{4}F_{\mu\nu}F^{\mu\nu}, \qquad F_{\mu\nu} = \partial_\mu A_\nu - \partial_\nu A_\mu. \tag{2.3}$$

Here, $\bar{\psi} = \psi^\dagger \gamma^0$ is the Dirac adjoint and $F_{\mu\nu}$ represents the field strength tensor. $\mathcal{L}_f$ and $\mathcal{L}_A$ are invariant under a *global* U(1)_Y transformation. For the free fermion field, the transformation can be written as $\psi(x) \rightarrow e^{i\alpha}\psi(x)$. The gauge principle requires the invariance of the Lagrangian under a local transformation, i.e. those affecting all space-time points x: $\psi(x) \rightarrow e^{i\alpha(x)}\psi(x)$. In this transformation, non-vanishing terms arising through $\partial_\mu e^{i\alpha(x)}\psi(x)$ require the presence of the gauge boson vector field in order to fulfil the QED U(1)_Y gauge invariance:

$$\mathcal{L}_{\text{QED}} = \bar{\psi}\left(i\gamma^\mu D_\mu - m\right)\psi - \frac{1}{4}F_{\mu\nu}F^{\mu\nu}. \tag{2.4}$$

The *covariante derivative* is defined by $D_\mu = \partial_\mu - ieA_\mu$. It is interesting to note that a photon mass term $\frac{m_A^2}{2}A_\mu A^\mu$ violates the gauge invariance.

2.1.3. Quantum Chromodynamics

The formulation of the QCD theory follows the same principles as those applied to QED but with a higher-dimensional symmetry group: SU(3)_C. The elements of an N-dimensional SU(N) group take the form

$$\text{U} = e^{i\theta^a \frac{\lambda^a}{2}}, \tag{2.5}$$

with generators λ^a and space-time dependent parameters θ^a. For SU(3)_C, the $N^2 - 1 = 8$ traceless and Hermitian Gell-Mann matrices are the generators, resulting in 8 massless

gluons as QCD mediators. Contrary to QED, QCD is a non-Abelian field theory, meaning that non-vanishing terms arise in the commutation relation of λ^a. This is reflected in the total QCD Lagrangian:

$$\mathcal{L}_{\text{QCD}} = \sum_{j=1}^{6} \bar{q}_j \left(i\gamma^\mu D_\mu - m_j \right) q_j - \frac{1}{4} \sum_{a=1}^{8} G^a_{\mu\nu} G_a^{\mu\nu}. \tag{2.6}$$

The first sum runs over all quark flavours. The covariant derivative is defined by $D_\mu = \partial_\mu + ig_s \frac{\lambda^a}{2} g^a_\mu$ with the eight gluon fields g^a_μ, analogous to the photon field A_μ, and the strong coupling constant g_s. The gluon fields also appear in the field strength tensor $G^a_{\mu\nu} = \partial_\mu g^a_\nu - \partial_\nu g^a_\mu + g_s f^{abc} g^b_\mu g^c_\nu$. The term $g_s f^{abc} g^b_\mu g^c_\nu$ is not present in the Abelian QED theory and introduces 3-gluon and 4-gluon vertices in QCD. f^{abc} is the $\text{SU}(3)_\text{C}$ structure constant. Multi-gluon interactions are experimentally confirmed [27, 28].

2.1.4. Weak Force and Electroweak Unification

The violation of parity and charge symmetry in weak interactions is visible as an exclusive coupling of the $W^\pm$ boson to left-handed fermions[4], i.e. with negative helicity[5], and to right-handed anti-fermions. Taking the first lepton and quark generation as an example, a typical notation is

$$\begin{pmatrix} \nu_e \\ e^- \end{pmatrix}_\text{L} , \begin{pmatrix} u \\ d \end{pmatrix}_\text{L} \quad \text{and} \quad e^-_\text{R}, u_\text{R}, d_\text{R}.$$

Left-handed fermions are grouped as doublets and their right-handed counterparts are grouped as singlets – neutrinos only occur as left-handed fermions and right-handed antifermions in the SM. The symmetry group which initiates flavour-transformations of the doublets but leaves the singlets unchanged, is $\text{SU}(2)_\text{L}$. The Pauli matrices σ_i are its generators. A new quantum number, the *weak isospin T*, with $T = \frac{1}{2}$ and $T_3 = \pm\frac{1}{2}$ ($T = T_3 = 0$) is assigned to the left-handed doublets (right-handed singlets). The combined $\text{SU}(2)_\text{L} \otimes \text{U}(1)_\text{Y}$ symmetry group fulfils the desired gauge invariance, hence the name *electroweak unification*. An additional quantum number is introduced, the *hypercharge* $Y = 2(Q - T_3)$. The total electroweak Lagrangian is constructed with covariant derivatives built of three $\text{SU}(2)_\text{L}$ fields W^i_μ with coupling g and one $\text{U}(1)_\text{Y}$ field B_μ with

---

[4]For massive right-handed fermions, there is also a β-dependant left-handed component, with $\beta = \frac{v}{c}$.
[5]The helicity corresponds to the projection of the spin on the direction of the particle momentum.

coupling g':

$$\mathcal{L}_{\text{EW}} = \sum_{\psi} \left[\bar{\psi}^{\text{L}} i\gamma^{\mu} D_{\mu} \psi^{\text{L}} + \bar{\psi}^{\text{R}} i\gamma^{\mu} D_{\mu} \psi^{\text{R}} \right] - \frac{1}{4} B_{\mu\nu} B^{\mu\nu} - \frac{1}{4} \sum_{i=1}^{3} W_{\mu\nu}^{i} W_{i}^{\mu\nu}. \qquad (2.7)$$

The first sum runs over all SM fermions. The covariant derivative for the doublets and singlets is

$$D_{\mu} \psi^{\text{L}} = \left(\partial_{\mu} - ig\frac{\sigma_i}{2} W_{\mu}^i - ig'\frac{Y}{2} B_{\mu} \right) \psi^{\text{L}},$$
$$D_{\mu} \psi^{\text{R}} = \left(\partial_{\mu} - ig'\frac{Y}{2} B_{\mu} \right) \psi^{\text{R}}. \qquad (2.8)$$

The tensor structure takes the form

$$W_{\mu\nu}^{i} = \partial_{\mu} W_{\nu}^{i} - \partial_{\nu} W_{\mu}^{i} + g\epsilon^{ijk} W_{\mu}^{j} W_{\nu}^{k},$$
$$B_{\mu\nu} = \partial_{\mu} B_{\nu} - \partial_{\nu} B_{\mu}, \qquad (2.9)$$

with the epsilon tensor ϵ^{ijk} as the $\text{SU}(2)_{\text{L}}$ structure constant. Similar as in QCD, triple and quartic gauge field vertices arise from the non-Abelian $\text{SU}(2)_{\text{L}}$ gauge group. Such multi-boson vertices have been probed experimentally, see for instance [6]. The physical $W_{\mu}^{\pm}$ gauge bosons can be derived from

$$W_{\mu}^{\pm} = \frac{W_{\mu}^1 \mp iW_{\mu}^2}{\sqrt{2}}. \qquad (2.10)$$

The photon A_{μ} and the Z_{μ} boson emerge from mixtures of W_{μ}^3 and B_{μ} with the *Weinberg angle* θ_W:

$$A_{\mu} = \cos\left(\theta_W\right) B_{\mu} + \sin\left(\theta_W\right) W_{\mu}^3,$$
$$Z_{\mu} = -\sin\left(\theta_W\right) B_{\mu} + \cos\left(\theta_W\right) W_{\mu}^3. \qquad (2.11)$$

2.1.5. Higgs Mechanism

The gauge bosons in the definition from Equation 2.10 and 2.11 are massless – including mass terms in the EW Lagrangian from Equation 2.7 violates the gauge invariance. This is in great contrast to the observation of heavy $W^{\pm}$ and Z boson mediators in nature. The *Higgs mechanism* [29, 30] offers a solution for the missing gauge boson masses by

10

introducing a complex, scalar $SU(2)_L$ field ϕ with $T = \frac{1}{2}$ and $Y = 1$ and Lagrangian

$$\mathcal{L} = (\partial_\mu \phi)^\dagger (\partial^\mu \phi) - V(\phi), \tag{2.12}$$

with potential $V(\phi) = \mu^2 \phi^\dagger \phi + \lambda \left(\phi^\dagger \phi \right)^2$. For $\mu^2 < 0$ and $\lambda > 0$, its form takes that of a *Mexican hat* with local maximum at $|\phi| = 0$ and global minimum at $|\phi| = v$ forming a non-zero vacuum expectation value (VEV) v. This minimum holds an infinite number of degenerate states at energy v. Explicitly choosing one of the states *spontaneously breaks* the symmetry. Evaluating the Lagrangian from Equation 2.12 around the ground state of the potential delivers a massless field (*Goldstone boson*, see [31]) which corresponds to fluctuations in the direction of the degenerate states. In addition, a massive field, the Higgs boson, emerges corresponding to perpendicular fluctuations which afford potential energy. For local transformations of $SU(2)_L \times U(1)_Y$, the Lagrangian in Equation 2.12 becomes

$$\mathcal{L}_{\text{Higgs}} = (D_\mu \phi)^\dagger (D^\mu \phi) - \mu^2 \phi^\dagger \phi - \lambda (\phi^\dagger \phi)^2,$$
$$D_\mu \phi = \left(\partial_\mu - ig \frac{\sigma_i}{2} W_\mu^i - ig' \frac{Y}{2} B_\mu \right) \phi. \tag{2.13}$$

Evaluating $\mathcal{L}_{\text{Higgs}}$ again around the minimum of the potential shows that the formerly massless EW $W^\pm$ and Z gauge bosons become massive by mixing with the three[6] degrees of freedom of ϕ (Goldstone bosons) that arise due to spontaneous symmetry breaking:

$$m_W = \frac{vg}{2}, \quad \text{and} \quad m_Z = \frac{v\sqrt{g^2 + g'^2}}{2} = \frac{m_W}{\cos(\theta_W)}. \tag{2.14}$$

The VEV is related to the Fermi coupling G_F: $v = \left(\sqrt{2} G_F \right)^{-1/2} \approx 246.22\,\text{GeV}$ [22].

The EW Lagrangian from Equation 2.7 does not allow to include fermion mass terms $-m_f \bar{\psi} \psi$ as they lead to a mixture between left- and right-handed fields, whereas the EW theory has a distinct treatment for both. Fermion masses can be generated, however, via interactions of the Higgs and fermion fields through the gauge-invariant *Yukawa Lagrangian*. For the first quark generation, the Yukawa Lagrangian takes the form

$$\mathcal{L}_{\text{Yukawa}} = -y_d \left(\bar{u}_L, \bar{d}_L \right) \phi\, d_R - y_u \left(\bar{u}_L, \bar{d}_L \right) \tilde{\phi}\, u_R + \text{h.c.}, \tag{2.15}$$

---

[6]The fourth degree of freedom corresponds to the massive Higgs boson.

with $\tilde{\phi} = i\sigma_2\phi^*$ and additional terms from the Hermitian conjugate. The fermion mass terms are

$$m_f = \frac{y_f v}{\sqrt{2}}, \tag{2.16}$$

in which y_f is called the *Yukawa coupling*.

2.2. Effective Field Theory

A multitude of searches for new physics (NP) is conducted at the LHC[7] experiments [4]. One often followed procedure is to search for NP mediator resonances in the falling spectrum of an observable, for instance the dijet mass spectrum. The sensitivity in these searches is naturally limited by the available centre-of-mass energy $\sqrt{s}$ at the LHC and the portion of the proton momentum x_i that the interacting partons carry. This limits the mediator mass to $m_{\mathrm{NP}} < \sqrt{sx_ix_j}$. An alternative, model-independent approach is realised in so-called *Effective Field Theories* (EFT) [5]. Instead of searching for the mediators themselves, low-energy NP contributions could manifest in a way that the expected shape of SM observables is varied in an experimentally accessible energy regime (see Figure 2.1). The NP energy scale Λ is assumed to be larger than the maximum achievable energy at the LHC and novel interactions need to fulfil the SM $\mathrm{SU}(3)_\mathrm{C} \otimes \mathrm{SU}(2)_\mathrm{L} \otimes \mathrm{U}(1)_\mathrm{Y}$ symmetry. The fields of the SM have mass-dimension $d \leq 4$. The EFT approach adds additional operators with $d > 4$:

$$\mathcal{L}_{\mathrm{EFT}} = \mathcal{L}_{\mathrm{SM}} + \sum_{d>4}\sum_k \frac{x_k^d}{\Lambda^{d-4}}\mathcal{O}_k^d = \mathcal{L}_{\mathrm{SM}} + \sum_i \frac{c_i^6}{\Lambda^2}\mathcal{O}_i^6 + \sum_j \frac{f_j^8}{\Lambda^4}\mathcal{O}_j^8 + \dots. \tag{2.17}$$

The higher-order operators $\mathcal{O}_k^d$ are built of the SM fields and introduce new contributions to SM interactions but also interactions that are not part of the SM QFT. The sums over (k, i, j) run over all possible operators at dimension d. The dimensionless Wilson coefficients (x_k, c_i, f_j) represent the coupling strengths of the respective operators. It is important to note that operators of odd dimension, i.e. $d \in \{5, 7, \dots\}$, do not appear in Equation 2.17 as they would violate baryon and lepton conservation [5]. The dimension-6 operators give the largest contribution of the expansion, as they are suppressed by Λ^2 instead of Λ^4 (dimension-8 operators) or higher powers of the scale.

In total, 59 operators form a unique basis for one generation of lepton and quarks[8]

---

[7]More information on the LHC is given in Section 3.
[8]For simplicity, only one generation is discussed here. For three generations, there are 2499 operators conserving baryon and lepton number.
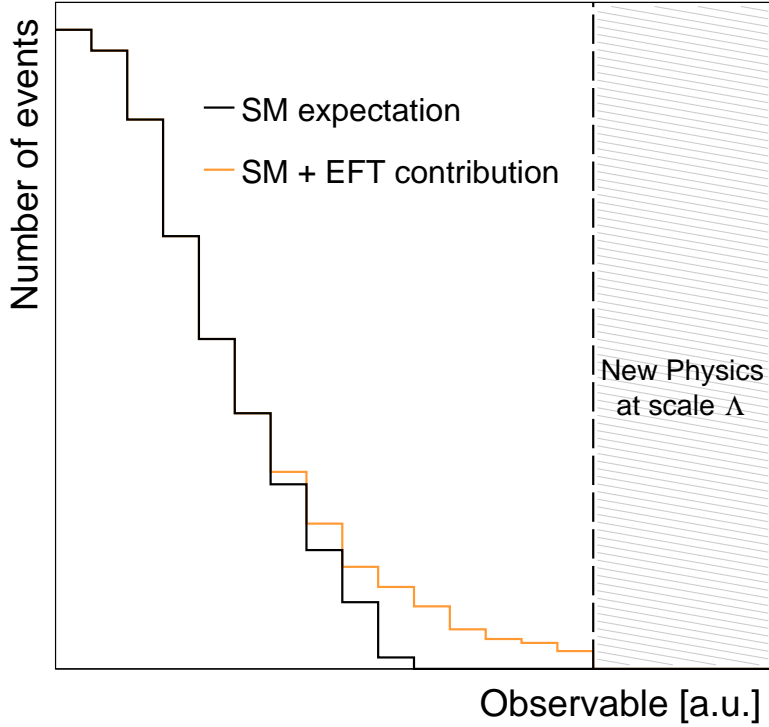
Figure 2.1.: Effective Field Theory approach: the low-energy effects of new physics occurring at energy scale Λ lead to shape variations of SM observables.

at dimension six [32]. They introduce 4-fermion interactions but also 3-gauge-boson[9] and 4-gauge-boson interactions, which are important in the context of this thesis. Table 2.1 displays all operators giving rise to interactions with ≥ 3 gauge bosons. The CP-conserving operator $\mathcal{O}_{\phi B} = \left(\phi^\dagger \phi\right) B^{\mu\nu} B_{\mu\nu}$, for instance, leads to the vertices $H \to \gamma\gamma$ and $H \to Z\gamma$, which only occur through an additional quark or gauge boson loop in the SM. Other operators, like $\mathcal{O}_W = (D_\mu \phi)^\dagger W^{\mu\nu} (D_\nu \phi)$, give rise to quartic gauge couplings (QGCs) between neutral and charged EW gauge bosons. Purely neutral EW gauge boson couplings, including QGCs, do not originate from dimension-6 operator interactions.

The number of operators increases further by going to dimension eight. There are 993 operators for one flavour generation and $O\!\left(10^4\right)$ operators for three generations [34]. In the following, only operators giving rise to QGCs are discussed. These 18 dimension-8 operators are shown in Table 2.2. Operators $\mathcal{O}_S$ contain only Higgs derivatives. They require the presence of four heavy gauge bosons; a further description is omitted as these

---

[9]In this context, gauge boson typically refers to EW gauge bosons and the Higgs boson.

Table 2.1.: Dimension-6 operators that introduce 3-gauge-boson and 4-gauge-boson interactions. The marker indicates whether the operators give rise to the vertices displayed in the columns. Photons are indicated by the letter 'A'. The table is taken from [33].

	ZWW	AWW	HWW	HZZ	HZA	HAA	WWWW	ZZWW	ZAWW	AAWW
$\mathcal{O}_{WWW}$	X	X					X	X	X	X
$\mathcal{O}_W$	X	X	X	X	X		X	X	X	
$\mathcal{O}_B$	X	X		X	X					
$\mathcal{O}_{\Phi d}$			X	X						
$\mathcal{O}_{\Phi W}$			X	X	X	X				
$\mathcal{O}_{\Phi B}$				X	X	X				
$\mathcal{O}_{\tilde{W}WW}$	X	X					X	X	X	X
$\mathcal{O}_{\tilde{W}}$	X	X	X	X	X					
$\mathcal{O}_{\tilde{W}W}$			X	X	X	X				
$\mathcal{O}_{\tilde{B}B}$				X	X	X				

Table 2.2.: Dimension-8 operators sensitive to QGCs. The marker indicates whether the operators give rise to the vertices displayed in the columns. Photons are indicated by the letter 'A'. It is shown in [35] that an additional operator $\mathcal{O}_{S,2}$ has to be added to the first row of operators. Furthermore, it is shown that $\mathcal{O}_{M,6}$ is not linearly independent. The table is taken from [33].

	WWWW	WWZZ	ZZZZ	WWAZ	WWAA	ZZZA	ZZAA	ZAAA	AAAA
$\mathcal{O}_{S,0}$, $\mathcal{O}_{S,1}$	X	X	X						
$\mathcal{O}_{M,0}$, $\mathcal{O}_{M,1}$,$\mathcal{O}_{M,6}$,$\mathcal{O}_{M,7}$	X	X	X	X	X	X	X		
$\mathcal{O}_{M,2}$,$\mathcal{O}_{M,3}$, $\mathcal{O}_{M,4}$,$\mathcal{O}_{M,5}$		X	X	X	X	X	X		
$\mathcal{O}_{T,0}$,$\mathcal{O}_{T,1}$,$\mathcal{O}_{T,2}$	X	X	X	X	X	X	X	X	X
$\mathcal{O}_{T,5}$,$\mathcal{O}_{T,6}$,$\mathcal{O}_{T,7}$		X	X	X	X	X	X	X	X
$\mathcal{O}_{T,8}$,$\mathcal{O}_{T,9}$			X			X	X	X	X

are generally not of interest for this thesis. Operators of the second type, seven so-called *mixed operators* $\mathcal{O}_M$, contain both Higgs derivatives and $\mathrm{SU(2)_L} \otimes \mathrm{U(1)_Y}$ field strength tensors:

$$\mathcal{O}_{M,0} = \mathrm{Tr}\left[\widehat{W}_{\mu\nu}\widehat{W}^{\mu\nu}\right] \times \left[(D_\beta\phi)^\dagger D^\beta\phi\right], \tag{2.18}$$

$$\mathcal{O}_{M,1} = \mathrm{Tr}\left[\widehat{W}_{\mu\nu}\widehat{W}^{\nu\beta}\right] \times \left[(D_\beta\phi)^\dagger D^\mu\phi\right], \tag{2.19}$$

$$\mathcal{O}_{M,2} = [B_{\mu\nu}B^{\mu\nu}] \times \left[(D_\beta\phi)^\dagger D^\beta\phi\right], \tag{2.20}$$

$$\mathcal{O}_{M,3} = \left[B_{\mu\nu}B^{\nu\beta}\right] \times \left[(D_\beta\phi)^\dagger D^\mu\phi\right], \tag{2.21}$$

$$\mathcal{O}_{M,4} = \left[(D_\mu\phi)^\dagger \widehat{W}_{\beta\nu}D^\mu\phi\right] \times B^{\beta\nu}, \tag{2.22}$$

$$\mathcal{O}_{M,5} = \left[(D_\mu\phi)^\dagger \widehat{W}_{\beta\nu}D^\nu\phi\right] \times B^{\beta\mu} + \mathrm{h.c.}, \tag{2.23}$$

$$\mathcal{O}_{M,7} = \left[(D_\mu\phi)^\dagger \widehat{W}_{\beta\nu}\widehat{W}^{\beta\mu}D^\nu\phi\right]. \tag{2.24}$$

In Equations 2.18 to 2.24, the abbreviation $\widehat{W}_{\mu\nu} = \sum_i \frac{\sigma^i W^i_{\mu\nu}}{2}$ is used. Mixed operators introduce QGCs between neutral EW gauge bosons, i.e. vertices $ZZZZ$, $ZZZ\gamma$, and $ZZ\gamma\gamma$, which are forbidden in the SM: the photon couples to the electric charge and the Z boson to the weak isospin ($T_3^\gamma = T_3^Z = 0$) and the electric charge. The last type of operators, eight so-called *transverse operators* $\mathcal{O}_T$, can be formed using solely field strength tensors of $\mathrm{SU}(2)_\mathrm{L} \otimes \mathrm{U}(1)_\mathrm{Y}$. Additionally to the neutral QGC vertices mentioned above, they add $Z\gamma\gamma\gamma$ and $\gamma\gamma\gamma\gamma$ couplings, thus yielding the largest contribution to any phase-space consisting of only neutral EW gauge bosons. The transverse operators are defined as:

$$\mathcal{O}_{T,0} = \mathrm{Tr}\left[\widehat{W}_{\mu\nu}\widehat{W}^{\mu\nu}\right] \times \mathrm{Tr}\left[\widehat{W}_{\alpha\beta}\widehat{W}^{\alpha\beta}\right], \tag{2.25}$$

$$\mathcal{O}_{T,1} = \mathrm{Tr}\left[\widehat{W}_{\alpha\nu}\widehat{W}^{\mu\beta}\right] \times \mathrm{Tr}\left[\widehat{W}_{\mu\beta}\widehat{W}^{\alpha\nu}\right], \tag{2.26}$$

$$\mathcal{O}_{T,2} = \mathrm{Tr}\left[\widehat{W}_{\alpha\mu}\widehat{W}^{\mu\beta}\right] \times \mathrm{Tr}\left[\widehat{W}_{\beta\nu}\widehat{W}^{\nu\alpha}\right], \tag{2.27}$$

$$\mathcal{O}_{T,5} = \mathrm{Tr}\left[\widehat{W}_{\mu\nu}\widehat{W}^{\mu\nu}\right] \times B_{\alpha\beta}B^{\alpha\beta}, \tag{2.28}$$

$$\mathcal{O}_{T,6} = \mathrm{Tr}\left[\widehat{W}_{\alpha\nu}\widehat{W}^{\mu\beta}\right] \times B_{\mu\beta}B^{\alpha\nu}, \tag{2.29}$$

$$\mathcal{O}_{T,7} = \mathrm{Tr}\left[\widehat{W}_{\alpha\mu}\widehat{W}^{\mu\beta}\right] \times B_{\beta\nu}B^{\nu\alpha}, \tag{2.30}$$

$$\mathcal{O}_{T,8} = B_{\mu\nu}B^{\mu\nu}B_{\alpha\beta}B^{\alpha\beta}, \tag{2.31}$$

$$\mathcal{O}_{T,9} = B_{\alpha\mu}B^{\mu\beta}B_{\beta\nu}B^{\nu\alpha}. \tag{2.32}$$

2.3. Triple Gauge Boson Production

The total inelastic cross section of proton–proton (p–p) collisions recorded with the ATLAS detector[10] at a centre-of-mass energy of $\sqrt{s} = 13\,\mathrm{TeV}$ is measured as $\sigma_\mathrm{inel} = 78.1 \pm 2.9\,\mathrm{mb}$ [36]. This is shown in Figure 2.2 (top left corner), along with the production cross section of various SM processes measured at $\sqrt{s} = 5$–$13\,\mathrm{TeV}$. The largest contribution to σ_inel stems from the production of jets through QCD interactions. This is driven by the size of the strong coupling constant, in the following abbreviated by α_s. It is scale-dependant, which is true for all SM coupling constants (*running coupling*) – a typical reference value is $\alpha_s\left(m_Z^2\right) = 0.118$ [22]. The QED coupling is less energy-dependent and commonly evaluated to be $\alpha_\mathrm{em} \approx 1/137$ [22] at small scales, which is one order of magnitude smaller than α_s. The strength of weak interactions is limited by the

---

[10]More information on the ATLAS detector is given in Section 3.

mediator mass appearing in propagator terms, which are proportional to $\left(q^2 - m_{W,Z}^2\right)^{-1}$ with the momentum transfer q^2. The cross section of the production of a single heavy EW gauge boson thus reduces by at least five orders of magnitude with respect to the inelastic case. Increasing the multiplicity of EW gauge bosons in the final state leads to a further reduction of the cross section and hence limits the number of expected events for a given process. The triple gauge boson production (TGP) in the electroweak sector is studied in this thesis (bottom right corner). The cross sections for such processes are typically below $100\,\mathrm{fb}$. This results in the smallest number of expected events for any of the SM processes presented in Figure 2.2. Despite this challenge, discoveries of the $\gamma\gamma\gamma$, $Z\gamma\gamma$, and $W\gamma\gamma$ processes were achieved with sufficient significance. All ATLAS TGP measurements are summarised in Table 2.3. It can be seen that nearly all states with combinations of massless and heavy EW gauge boson have been studied, either through a cross section measurement or an upper limit on it. Most of the TGP measurements show good agreement between the measured cross section and theoretical prediction. For the WWW analysis, a tension of 2.6σ to the SM prediction is observed, which requires more data to verify if the difference is a potential new physics sign.

Table 2.3.: Summary of triple gauge boson production measurements at the ATLAS detector for centre-of-mass energies of 8 and $13\,\mathrm{TeV}$. Note that some of the presented cross section measurements are corrected for detector effects. For the $WZ\gamma$ process, an upper limit on the cross section at 95% confidence level (CL) is derived.
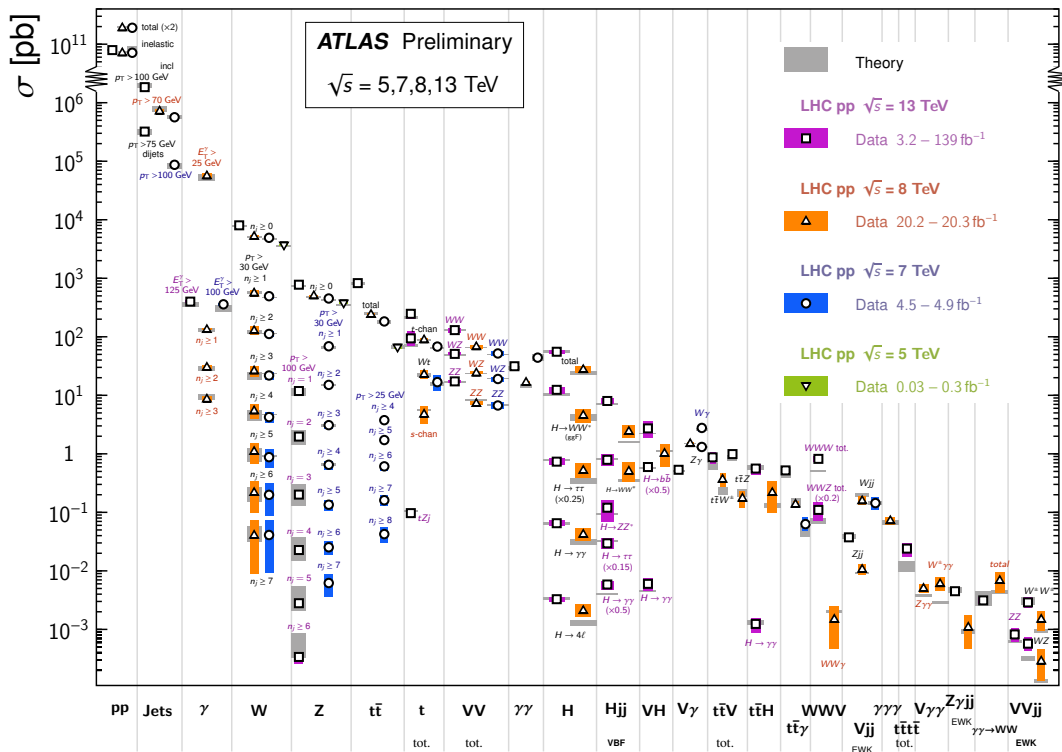
Process	$\sqrt{s}$ [TeV]	Cross section [fb]	Significance [σ]
$\gamma\gamma\gamma$ [8]	8	$72.6 \pm 6.5\,\mathrm{(stat.)} \pm 9.2\,\mathrm{(sys.)}$	observed
$W\gamma\gamma$ [37]	8	$6.1^{+1.1}_{-1.0}\,\mathrm{(stat.)} \pm 1.2\,\mathrm{(sys.)}$	> 3
$WW\gamma$ [38]	8	$1.5 \pm 0.9\,\mathrm{(stat.)} \pm 0.5\,\mathrm{(sys.)}$	1.4
$WZ\gamma$ [38]	8	$< 6\,(95\%\,\mathrm{CL})$	–
WWW [39]	13	$820 \pm 100\,\mathrm{(stat.)} \pm 80\,\mathrm{(sys.)}$	observed
WWZ [40]	13	$550 \pm 140\,\mathrm{(stat.)}^{+150}_{-130}\,\mathrm{(sys.)}^{a}$	3.5^{b}
$Z\gamma\gamma$ [41]	13	$2.45 \pm 0.20\,\mathrm{(stat.)} \pm 0.22\,\mathrm{(sys.)}$	observed

[a] WWZ cross section calculated from $\ell\nu\ell\nu\ell\ell$ and $qq\ell\ell\ell\ell$ final states and by setting the WZZ normalisation to the SM expectation; the ZZZ contribution is negligible.

[b] The significance corresponds to the combined WWZ and WZZ significance. It is reported that the sensitivity is insufficient to provide a separate cross section for WZZ.

Figure 2.2.: Summary of Standard Model production cross section measurements at the ATLAS detector for p–p collisions at centre-of-mass energies between 5 and $13\,\mathrm{TeV}$. The triple gauge boson production is situated at the right bottom corner with cross sections typically below $100\,\mathrm{fb}$. The image is taken from [42].

3. Experimental Environment: LHC and ATLAS Detector

The Large Hadron Collider (LHC) [43] is the world's most powerful particle accelerator and as such plays an important role in the understanding of the fundamental properties of nature and the forces and interactions between elementary particles. It is designed to provide particle collisions at unprecedented energies and holds the record for the highest hadron collider luminosity. The LHC was built and is maintained in a combined, international effort with many states across the world participating in its physics program [44]. It is located at CERN[11] right at the border between Switzerland and France. Various experiments along the circular shape of the LHC reconstruct the particle collisions, two of which are general-purpose detectors: the ATLAS[12] and CMS[13] experiment. The former represents the detector with which the data that is analysed in this thesis is collected.

The basic properties of the LHC and its major runs recording particle collisions at large energies are presented in the following section. Afterwards, the ATLAS detector is described with a focus on the working-principles of its sub-detectors and their role in the chain of particle detection.

3.1. The Large Hadron Collider

The LHC is a circular particle collider which uses radiofrequency cavities to accelerate charged particles to high energies. Dipole, quadrupole, and higher-order multipole electromagnets guide the particles along the ring structure and serve as focusing magnets to maximise the particle beam intensity. Depending on the physics program, the beams contain either protons or lead ions – in this thesis, p–p collisions are considered. The particles of a beam are arranged in so-called bunches, each containing more than 10^{11} protons. The bunches are guided in opposite directions along the two spatially separated beam pipes and each traverse the $26.7\,\mathrm{km}$ of the LHC tunnel with a revolution frequency of more than $10\,000\,\mathrm{Hz}$ until they are forced to collide. They are time-wise separated by $25\,\mathrm{ns}$ resulting in a collision frequency of $40\,\mathrm{MHz}$.

The full accelerator complex at CERN is displayed in Figure 3.1. The protons are pre-accelerated in four stages before being injected into the LHC at which point they have

---

[11]*Conseil Européen pour la Recherche Nucléaire.*
[12]*A Toroidal LHC ApparatuS.*
[13]*Compact Muon Solenoid.*
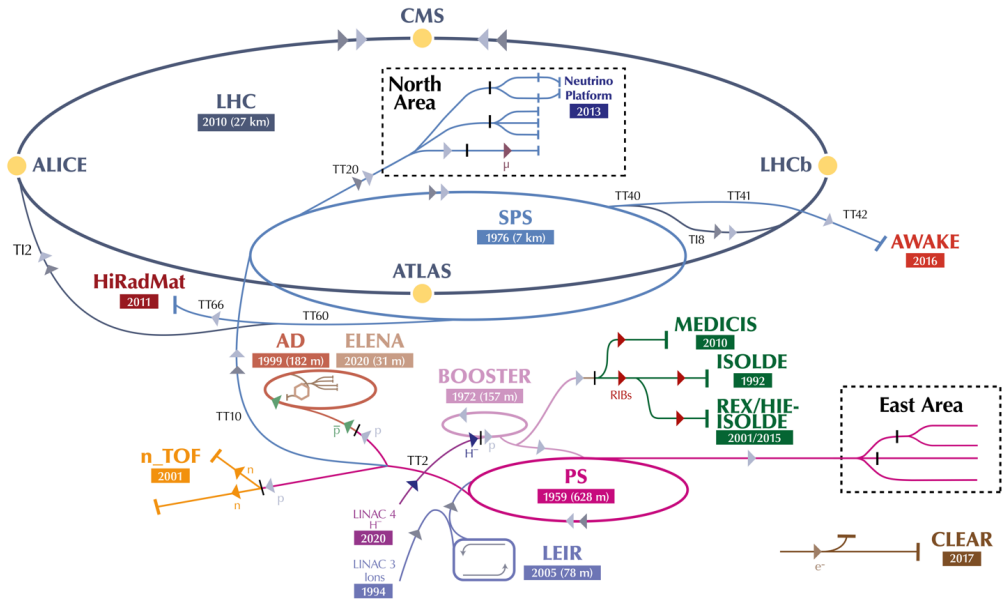
Figure 3.1.: The CERN accelerator complex. Before entering the LHC, the protons are pre-accelerated in a linear accelerator (LINAC2 in Run 2 and LINAC4 in Run 3; at this stage negatively charged hydrogen ions are used), followed by a series of circular accelerators, namely the Proton Synchrotron Booster (PSB), the Proton Synchrotron (PS), and finally the Super Proton Synchrotron (SPS). The image is taken and modified from [45].

energies of $450\,\mathrm{GeV}$. Two major data-taking periods at the LHC delivered p–p collisions at centre-of-mass energies $\sqrt{s}$ of $7\,\mathrm{TeV}$ and $8\,\mathrm{TeV}$ (*Run 1*) and centre-of-mass energies of $13\,\mathrm{TeV}$ (*Run 2*). The latter took place between 2015 and 2018 and represents the dataset that is analysed in this thesis. At the time of writing this dissertation, a third data-taking period (*Run 3*) at the LHC started to record collisions at even larger energies of $\sqrt{s} = 13.6\,\mathrm{TeV}$. Along with the centre-of-mass energy, the instantaneous luminosity is one of the key properties of a particle collider and describes the ability of the accelerator to provide collisions at high rates. For beams with Gaussian profiles, it is defined as

$$\mathcal{L} \sim \frac{f N_1 N_2 N_b}{\sigma_x \sigma_y}, \tag{3.1}$$

with the revolution frequency f, the number of particles N_1 and N_2 in each beam, the number of bunches N_b, and the beam spread σ_x and σ_y [46]. The LHC was able to surpass its design instantaneous luminosity reaching values of $\mathcal{L} = 2.1 \times 10^{34}\,\mathrm{cm}^{-2}\mathrm{s}^{-1}$ in 2017 during Run 2 [47]. A multitude of processes is produced in such an accelerator environment – from top quark and Higgs to single and multi boson production. The number of events in a given period of time $\mathrm{d}t$ for a process with cross section σ can be

expressed through

$$\frac{\mathrm{d}N}{\mathrm{d}t} = \mathcal{L} \times \sigma. \tag{3.2}$$

The integrated luminosity $L_{\text{int}} = \int \mathcal{L} \, \mathrm{d}t$ provides a measure for the size of a recorded dataset. The full Run 2 dataset amounts to $L_{\text{int}} = 139 \, \text{fb}^{-1}$, where the unit barn (b) corresponds to $10^{-28} \, \text{m}^2$.

3.2. The ATLAS Experiment

The ATLAS experiment [48] is a compound of sub-detectors, each uniquely designed to add one step in the full chain of particle detection. It is situated approximately $100 \, \text{m}$ below ground and has a total weight of $7000 \, \text{t}$ distributed over a length and diameter of $46 \, \text{m} \times 25 \, \text{m}$. The detector has an onion-shaped structure centred around the approximate point of interaction of the colliding proton beams; a sketch of the full system is shown in Figure 3.2. As a general purpose detector, the ATLAS experiment covers a wide physics program including precision measurements of SM processes and searches for new physics. One of the key achievements of the ATLAS experiment was the discovery of the SM Higgs boson [49].

The coordinate system that is used in the ATLAS experiment is defined in the following way: the z-axis is pointing along the direction of the beam pipe, while the x-axis and y-axis are pointing to the centre of the LHC and perpendicular upwards, respectively. The component of the particle momentum in the x–y plane is referred to as *transverse momentum* p_{T}. It is a convenient quantity as the total energy in the transverse plane is conserved in the ATLAS detector. The azimuthal angle ϕ is oriented around the beam pipe and is complemented by the so-called pseudorapidity η. It is defined using the polar angle θ as

$$\eta = -\ln\left(\tan\left(\frac{\theta}{2}\right)\right). \tag{3.3}$$

The values of the pseudorapidity can range from 0 to $\pm\infty$, where the former refers to a particle flying orthogonal to the z-axis at $\theta = 90°$ and the latter to an asymptotic alignment of the particle momentum and the beam pipe. The particle detection in the ATLAS experiment is enabled up to $|\eta| < 4.9$[14]. Distances in η–ϕ space are expressed through $\Delta R = \sqrt{(\Delta\eta)^2 + (\Delta\phi)^2}$.

The characteristics of the sub-detectors are explained in the following, starting from the innermost system close to the point of interaction and then moving outwards. Subse-

---

[14]Dependent on the particle type and typically largest for jets.
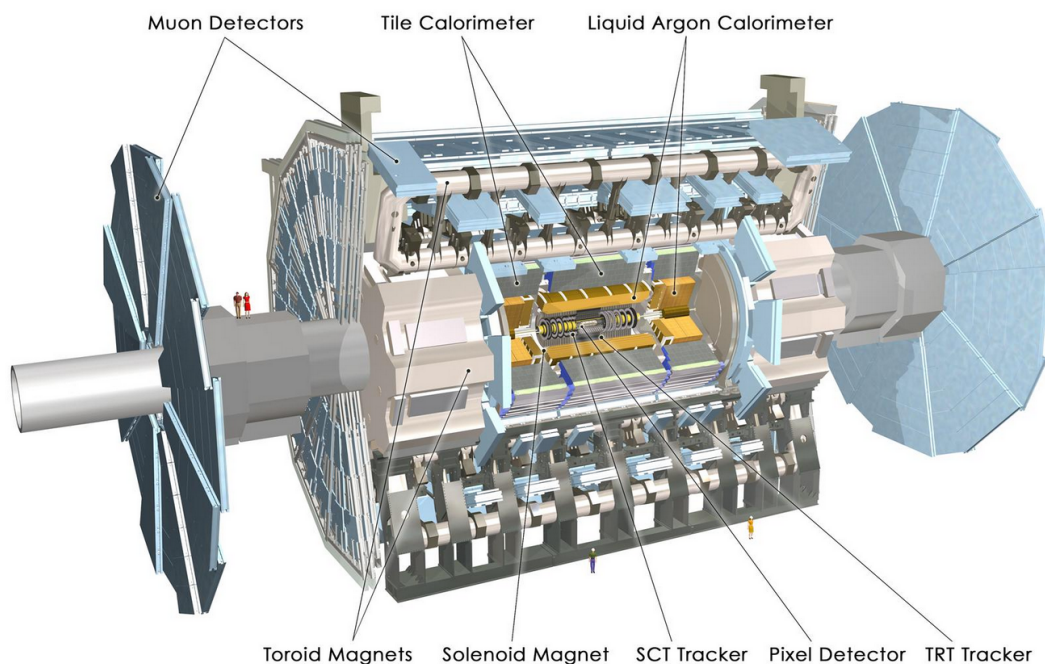
Figure 3.2.: The ATLAS experiment and its sub-detectors. Going from the innermost to the outermost layer, the inner detector, immersed in the field of the solenoid magnet, is followed by the calorimeter system and the muon detector. The latter is integrated into the magnetic field of the toroid magnet system. The image is taken from [50].

quently, the two-level trigger system of the ATLAS detector is outlined.

3.2.1. Inner Detector

Charged particles traversing the material of the Inner Detector (ID) [51] deposit a small amount of their energy, which is used to reconstruct the particle trajectory within a pseudorapidity range of $|\eta| < 2.5$. The ID is immersed in the $2\,\mathrm{T}$ field of a superconducting solenoid magnet system [52], allowing to determine the transverse momentum p_T in the plane orthogonal to the beam direction and the sign of the particle charge.

The ID is a compound of three sub-detectors called *Pixel Detector*, *Semiconductor Tracker* (SCT), and *Transition Radiation Tracker* (TRT). The Pixel Detector and SCT are silicon semiconductors. Charged particles penetrating the depletion zone of diode structures create electron-hole pairs that drift to electrodes of opposite charge where they induce a measurable pulse. The TRT uses a gas mixture filled into thin drift tubes, which is ionised by primary charged particles and the signal of the resulting cascade of secondary particles is measured at corresponding electrodes.

The Pixel Detector [53, 54] is the sub-detector of the ATLAS experiment closest to the point of interaction of the crossing proton beams. Its goal is a high-precision reconstruction of interaction vertices and tracks. This is realised using small silicon pixels offering a high granularity at a radial distance of only $3.3\,cm$ from the interaction point (IP). The nominal pixel size is $50\,\mu m \times 400\,\mu m$, reducing to $50\,\mu m \times 250\,\mu m$ for the innermost layer benefiting the resolution of the track reconstruction in z-direction. Four Pixel Detector layers are installed in the central part of the detector (*barrel region*), and three layers each in the outer parts of the detector (*endcap region*). Overall, the system consists of 92 million individual pixels.

The SCT [55] has a slightly worse spatial resolution than the Pixel Detector but improved lever arm for momentum reconstruction. It covers the radial distance of approximately $30\,cm$–$51\,cm$ (barrel region). The SCT has four layers of silicon strips in the barrel region and 9 layers of strips in the endcap region. Two-sided modules with silicon strips on each side are glued together at a relative angle of $40\,mrad$ to obtain two-dimensional spatial coordinates. The SCT contains over six million channels in total.

In the outermost volume of the ID the TRT [56] detects charged particles using nearly $300\,000$ drift tubes. Each tube of $4\,mm$ diameter contains a Xe-CO_2-O_2 or Ar-based gas mixture and a thin gold-plated tungsten wire. Particle interactions can be determined within a pseudorapidity $|\eta| < 2.0$ and radius $56\,cm < r < 108\,cm$ (barrel region). Typically, signals in 30 tubes are measured for charged particles, which is significantly more than for the Pixel Detector and SCT and compensates for the poorer spatial resolution of the TRT. In addition to the track measurement, the TRT enables a first particle identification, where electrons and pions can be differentiated through transition radiation [57]. The transition radiation occurs in a polypropylene radiator in which the drift tubes are embedded.

3.2.2. Electromagnetic and Hadronic Calorimeter

The ATLAS calorimeter system measures the energy of leptons, photons, and hadrons emerging from the interaction point. The characteristic form of the particle shower in the calorimeter also plays a crucial part in the particle identification (see Section 4.1). The *Electromagnetic Calorimeter* embraces the ID and is designed to fully absorb electrons, positrons, and photons. It also measures a substantial portion of the total energy that hadrons deposit in the detector. The *Hadronic Calorimeter* surrounds the electromagnetic calorimeter and measures the energy of charged and neutral hadrons such as protons or pions. Both calorimeter types are sampling calorimeters, where alternating layers of

dense absorber material and active medium are used. The purpose of the absorber is to create a shower of secondary particles, either through electromagnetic interactions (mainly electron-positron pair production and bremsstrahlung) or strong interactions (inelastic hadronic interactions such as nuclear spallation, evaporation, or fission) [58]. The cascade of secondary particles subsequently creates signals in the active material through ionisation or scintillation.

The electromagnetic calorimeter covers two main areas in pseudorapidity: the *Electromagnetic Barrel* (EMB) ranging up to $|\eta| < 1.475$ and two symmetrical *Electromagnetic Endcaps* (EMEC) spanning over $1.375 < |\eta| < 3.2$. Liquid Argon (LAr) is utilised as active material in all regions of the electromagnetic calorimeter [59]. It is filled into the gaps between the accordion structure of the absorber and electrodes – the accordion shape ensures a full-ϕ coverage. The electrodes read out the ionisation signals from LAr, induced by the particle shower emerging from the absorber. The longitudinal depth of the electromagnetic calorimeter is η-dependent and mostly larger than 22 radiation lengths X_0. The EMB uses a high-density lead absorber and is formed of three layers of varying η and ϕ granularity. The finest η segmentation is found in the first layer and allows to differentiate between electromagnetic showers induced by single photons and those created by the decay of a neutral meson into two close-by photons. Most of the particle energy is deposited in the second layer; the respective energy fraction is thus widely used in particle reconstruction algorithms. The third layer is sensitive to energy leaking beyond the electromagnetic calorimeter. Within $|\eta| < 1.8$ there is an additional thin layer of LAr and electrodes, the *presampler*, measuring the energy loss due to dead material in front of the electromagnetic calorimeter. The EMEC consists of two identical sides, each built of two co-axial wheels. The same arrangement of presampler and the three layers, albeit different η-ϕ granularity, is installed in the endcap region. An energy resolution of

$$\frac{\sigma_E}{E} = \frac{10\%}{\sqrt{E\,[\mathrm{GeV}]}} \oplus 0.17\% \tag{3.4}$$

is achieved in the EMB and EMEC [48].

The barrel region of the hadronic calorimeter is formed by the *Tile Calorimeter* covering $|\eta| < 1.7$. Contrary to the electromagnetic calorimeter, it uses steel as absorber and scintillating tiles as active medium. Particles traversing the tiles create scintillation light in the polystyrene material, which is converted from the ultraviolet spectrum to visible light and read out by photomultipliers. The longitudinal depth is segmented into three layers, with $\Delta\eta \times \Delta\phi$ of 0.1×0.1 for the first two layers and 0.2×0.1 for the last layer. The *Hadronic Endcap Calorimeter* (HEC) is situated behind the EMEC and extends the

hadronic energy measurement to $1.5 < |\eta| < 3.2$. It makes use of LAr as active medium and employs copper-plate absorbers, chosen due to its radiation hardness. Two successive wheels are located in each endcap region which are longitudinally segmented into two layers each. The granularity in the transverse plane is given by $\Delta\eta \times \Delta\phi = 0.1 \times 0.1$ for $|\eta| < 2.5$ and coarser ($\Delta\eta \times \Delta\phi = 0.2 \times 0.2$) for the remainder of the calorimeter. The energy resolutions of the Tile Calorimeter and the HEC were measured for pions as

$$\left(\frac{\sigma_E}{E}\right)_{\mathrm{Tile}} = \frac{52.7\%}{\sqrt{E\,[\mathrm{GeV}]}} \oplus 5.7\% \quad \text{and} \quad \left(\frac{\sigma_E}{E}\right)_{\mathrm{HEC}} = \frac{70.6\%}{\sqrt{E\,[\mathrm{GeV}]}} \oplus 5.8\%, \qquad (3.5)$$

see [60] and [48], respectively.

The *Forward Calorimeter* (FCal) is situated at the most extreme pseudorapidity values of $3.1 < |\eta| < 4.9$ and forms the outermost part of the calorimeter system in the endcap region. It consists of one wheel for the measurement of electromagnetic interactions and two wheels for hadronic interactions. Alternating layers of thin LAr regions and mostly copper or tungsten absorbers are employed.

3.2.3. Muon Spectrometer

Muons typically behave like minimum ionising particles in the energy regime of the LHC and have a suppressed probability to perform bremsstrahlung in the calorimeter due to the inverse quadratic mass dependence of the energy loss. This necessitates the installation of a dedicated detection system, the *Muon Spectrometer* (MS) [61, 62]. It forms the outermost part of the ATLAS detector and typically provides three sensitive detection layers for muons in the range $|\eta| < 2.7$. It is designed to achieve a muon transverse momentum resolution of 10% for $p_{\mathrm{T}} \approx 1\,\mathrm{TeV}$. Three large superconducting toroid magnet systems bend the muons in the MS. The magnetic field configuration is highly complex with field strengths of up to $3.5\,\mathrm{T}$ in the bore of the toroid magnets. The MS is constructed of four sub-detectors each utilising different detection technologies putting emphasis on either triggering, namely *Resistive Plate Chambers* (RPCs) and *Thin Gap Chambers* (TGCs), or precise track measurements, namely *Monitored Drift Tubes* (MDTs) and *Cathode Strip Chambers* (CSCs). While the former type measures the coordinates of the track in the bending (η) and non-bending (ϕ) plane, the latter delivers a precise measurement of the η-coordinate. The measuring procedure is similar in all MS sub-detectors and relies on charged-particle induced ionisation of a gas mixture and the subsequent readout of the ionisation avalanche.

The barrel region of the MS covers the pseudorapidity range $|\eta| < 1.05$ and is equipped

with MDTs and RPCs. The RPCs provide input for the ATLAS trigger system and consist of pairs of parallel resistive electrode plates with a thin $2\,mm$ gap filled with a gas mixture. A time resolution of $15\,ns$–$25\,ns$ is achieved, which hence also allows for the identification of the correct bunch crossing from which the muon emerges. The MDTs enable track reconstruction with $80\,\mu m$ precision using multiple layers of small cylindrical pressurised drift tubes with a diameter of approximately $3\,cm$.

The endcap region spans over $1.05 < |\eta| < 2.7$ and contains TGCs providing input for the trigger system and MDTs and CSCs for the track measurement. The TGCs have a slightly smaller pseudorapidity coverage up to $|\eta| = 2.4$, which thus represents the η-boundary of the first level of the ATLAS muon trigger system (see Section 3.2.4). The TGCs are multiwire proportional chambers, consisting of multiple wire anodes with $1.8\,mm$ pitch positioned within cathodes. A similar time resolution as for the RPCs in the barrel region is ensured. MDTs are mounted in all layers, with the exception of a portion of the inner layer at $|\eta| > 2.0$, where instead CSCs are placed which are optimised for higher particle rates. The CSCs are multiwire proportional chambers with segmented cathodes oriented parallel and orthogonal to the wires and achieve a resolution of $60\,\mu m$.

3.2.4. Trigger and Data Acquisition

The proton bunches at the LHC collide 40×10^6 times per second in the ATLAS experiment. The high proton intensity causes multiple p–p collisions in each bunch crossing (*pile-up*, see Section 4.3). With each event having a size of $1.6\,MB$ on average [63], it is impossible to store information of each collision. Significantly lower storage capacities are sufficient, as the typical p–p collision yields soft, low-energetic physics objects, whereas analyses usually aim to select higher-energetic objects probing rarer processes in nature. The ATLAS trigger system [64], which is divided into two levels, selects the interesting events. First, the hardware-based *Level-1* (L1) trigger system reduces the event rate by a factor of 400 to $100\,kHz$. The *High Level Trigger* (HLT) achieves an additional rejection factor of 100 resulting in a final rate of $1\,kHz$ using software-based, offline-like particle reconstruction algorithms.

The L1 trigger makes use of energy depositions in the calorimeter and muon spectrometer to form a fast trigger decision with a $2.5\,\mu s$ latency. The calorimeter information is coarsely read out and processed by the *L1 Calorimeter Trigger* (L1Calo). Local energy depositions are used to form electron, photon, tau, and jet candidates that have to pass a set of energy thresholds and, if requested, isolation requirements. Additionally, the total and missing transverse energy is determined. Coincidence hits in the RPCs and TGCs

are used to form muon candidates in the *L1 Muon Trigger* (L1Muon) [65]. Similarly to L1Calo, a set of trigger items with programmable energy thresholds are deployed, for which energy depositions are accessed with coarse granularity. The *Level-1 Topological Trigger* (L1Topo) combines information from L1Calo and L1Muon systems to estimate topological relations between physics objects, like invariant masses or angular distances. All three sub-components of the L1 trigger feed their output to the *Central Trigger Processor* where the final trigger decision is issued.

Upon receiving a L1 acceptance signal, events are transferred to the HLT. A two-step particle reconstruction is performed using input of all ATLAS sub-detectors, including track information from the ID, and the full detector granularity. The reconstruction takes place in either a confined η–ϕ space of the detector, called *Region of Interest*, or the full calorimeter when the missing transverse energy is calculated. In the first step, a simplified particle reconstruction is deployed allowing for fast rejection of a first portion of all propagated events. Afterwards, a sophisticated, offline-like particle reconstruction (see Sections 4.1 and 4.2) is performed. This takes significantly more time; the HLT latency can be at the order of seconds. For both steps, the computational power is provided by a central computing grid consisting of $40\,000$ CPU cores. The raw data of all events passing the HLT requirements are sent for permanent storage to the *Tier-0* data centre [66]. Here, the event information is further processed into data formats that can be used for offline analysis.

4. Particle Reconstruction and Monte Carlo Simulation

The particles that are produced in the high-energy p–p collisions at the LHC interact with the ATLAS detector – with the exception of neutrinos – leaving characteristic signatures in the detector sub-systems. Sophisticated algorithms combine energy depositions from these particles to form tracks and calorimeter clusters whose patterns are associated to specific particle types. The purity of this association can be enhanced by forming isolation and identification requirements that rely on combining the information of different sub-detectors. Comparing the properties of the detected particles and the full event information with theoretical predictions is challenging. Complex Monte Carlo (MC) simulation steps are necessary to emulate the full chain from the primary parton interaction to the particle reconstruction. The MC simulation allows to verify the SM by comparing its predictions to the cross sections and event kinematics measured in data, which also enables to search for new physics effects.

The ATLAS particle reconstruction is outlined in the following section emphasising the physics objects forming the final state that is studied in this thesis. An introduction to MC event generators is given subsequently and the steps are defined which are necessary to compare MC simulation to data.

4.1. Electron and Photon Reconstruction

Electrons and photons interact with the material of the ATLAS calorimeters creating a cascade of secondary particles in electromagnetic showers. As a charged particle, the electron deposits energy in the ID producing a particle track that is matched to the electromagnetic shower. Interactions with the material of the ATLAS detector can prompt photons to convert into an electron-positron pair and electrons to emit bremsstrahlung. Both the electron-positron pair from the photon conversion and the bremsstrahlung photons are usually emitted in a cone close to the momentum of the primary particle and are thus considered in its reconstruction. The electron and photon reconstruction takes place within the acceptance range of the ID: $|\eta| < 2.5$. A detailed description of the reconstruction is given in [67].

Electromagnetic showers are represented by so-called *topological clusters* in the electromagnetic and hadronic calorimeter. The size and form of a cluster develops dynamically,

which is optimised to account for the emission of bremsstrahlung and photon conversions. A *4-2-0 clustering algorithm* steers the formation of the calorimeter cluster. It relies on the significance $|\zeta_{\text{cell}}|$, which is defined by dividing the energy[15] of a calorimeter cell by its level of noise. The latter term accounts for electronics noise and energy from additional p–p interactions (*pile-up*). A cluster seed is formed by requiring $|\zeta_{\text{cell}}| \geq 4$. All neighbours with $|\zeta_{\text{cell}}| \geq 2$ are added and automatically become seed cells themselves, iteratively selecting neighbours passing $|\zeta_{\text{cell}}| \geq 2$ until this requirement is not satisfied anymore. Lastly, all cells surrounding the current cluster are added ($|\zeta_{\text{cell}}| \geq 0$).

The final step in the reconstruction of electromagnetic showers is the formation of so-called *superclusters*. A supercluster can consist of a single or merged topological clusters. Energy depositions of close-by clusters can be associated to secondary electromagnetic showers initiated by the same primary electron or photon – for instance when bremsstrahlung is emitted. A geometrical matching is performed to combine such clusters. The supercluster energy is calibrated to mitigate residual differences between MC simulation and data [68].

Track Reconstruction

The track reconstruction for electrons uses hits in the Pixel detector and SCT. Clusters of hits are fitted while considering energy loss from interactions with the detector material, which includes the radiation of bremsstrahlung photons. The fitted track candidates are extended to hits in the TRT. Up to 65% of photons at large $|\eta|$ values convert within the volume of the ID into an electron-positron pair [67]. This results in a *conversion vertex*, which is separated from the primary p–p interaction. The calorimeter cluster of *converted photons* points to the tracks of the electron-positron pair in the ID and the conversion vertex. The tracks must pass a particle-identification requirement based on TRT information increasing the probability that they belong to electron candidates. *Unconverted photons* are not associated to conversion vertices and ID tracks.

Identification and Isolation

The particle candidates fulfilling the selection of the reconstruction algorithms are not necessarily promptly-produced or genuine electrons and photons. Instead of emerging directly from the primary p–p interaction or from W and Z decays, they can be produced at a later stage of the particle formation in the ATLAS detector. The prompt production

---

[15]The energy is calibrated to the *EM scale*, an energy scale gauged for electromagnetic showers.

of electrons and photons has to be separated from photons emerging within the fragmentation of a jet and electrons stemming from the decay of heavy-flavour hadrons. Promptly-produced particles are typically isolated in η–ϕ space, which means that the hadronic activity in their surrounding is minimal. A significant amount of hadronic activity is found for non-prompt photons and electrons as they are in proximity to the jet remnant. A jet can also fake the signature of an electron or photon by depositing a significant amount of energy in the electromagnetic calorimeter. The identification and isolation requirements are designed to increase the purity of the particle reconstruction.

The electromagnetic shower induced by electrons and photons is typically laterally confined and most of the energy is expected to be deposited in the second layer of the electromagnetic calorimeter with little to no energy leaking into the hadronic calorimeter. These features are used in the definition of the particle identification; all of the requirements are summarised in Table 4.1. The identification is based on the quality of ID tracks, the lateral and longitudinal shower development in the calorimeter, and the compatibility of the track and cluster position. The fine granularity of the first electromagnetic layer allows to suppress the contribution of the aforementioned non-prompt photon production within jets. A neutral meson carrying a significant portion of the total jet momentum typically decays into a collimated pair of photons (mainly through $\pi^0 \to \gamma\gamma$ decays). Observables allowing to distinguish such close-by clusters from those initiated by a single photon are especially interesting in this thesis as non-prompt photons contribute dominantly to the total background contamination. Such observables measure, for instance, the lateral energy spread by comparing the energy deposited in proximity of the highest-energetic cell to that measured in a larger window ($w_{s\,\mathrm{tot}}$). The energy ratio E_{ratio} relates the difference between the maximum energy deposit (E_1) in an electromagnetic cluster and the largest energy deposit in a secondary maximum (E_2) to their sum: $E_{\mathrm{ratio}} = (E_1 - E_2)/(E_1 + E_2)$. It thus assesses how evenly the energy is shared between both maxima and is used in this analysis, among other observables, to define a phase-space enriched in non-prompt photons (see Section 6.1). Up to three identification working points (WPs) - *loose, medium,* and *tight* - are defined, with an increase in purity at the cost of losing efficiency[16]. The loose photon identification uses information based on the second calorimeter layer and the hadronic leakage. The tight photon identification adds all criteria related to the high-granular first calorimeter layer.

Non-prompt electrons and photons are typically surrounded by the remnants of the jet

---

[16]All three identification WPs are defined for electrons, whereas the photon identification contains the loose and tight WP. The efficiency decreases for electrons from on average 93% to 80% when requiring a tight instead of a loose identification, while offering a 3.5 times better background rejection [67].

Table 4.1.: Summary of the identification requirements for electrons and photons. The 'Usage' column indicates if the observable is used in either the electron or photon identification, or both. The observables are related to the longitudinal and lateral shower development in the calorimeters, to cluster-associated tracks, and the track-cluster compatibility. The table is taken from [67].

Category	Description	Name	Usage
Hadronic leakage	Ratio of E_T in the first layer of the hadronic calorimeter to E_T of the EM cluster (used over the ranges $|\eta| < 0.8$ and $|\eta| > 1.37$)	R_{had_1}	e/γ
	Ratio of E_T in the hadronic calorimeter to E_T of the EM cluster (used over the range $0.8 < |\eta| < 1.37$)	R_had	e/γ
EM third layer	Ratio of the energy in the third layer to the total energy in the EM calorimeter	f_3	e
EM second layer	Ratio of the sum of the energies of the cells contained in a 3×7 $\eta \times \phi$ rectangle (measured in cell units) to the sum of the cell energies in a 7×7 rectangle, both centred around the most energetic cell	R_η	e/γ
	Lateral shower width, $\sqrt{(\Sigma E_i \eta_i^2)/(\Sigma E_i) - ((\Sigma E_i \eta_i)/(\Sigma E_i))^2}$, where E_i is the energy and η_i is the pseudorapidity of cell i and the sum is calculated within a window of 3×5 cells	w_{η_2}	e/γ
	Ratio of the sum of the energies of the cells contained in a 3×3 $\eta \times \phi$ rectangle (measured in cell units) to the sum of the cell energies in a 3×7 rectangle, both centred around the most energetic cell	R_ϕ	e/γ
EM first layer	Total lateral shower width, $\sqrt{(\Sigma E_i (i - i_\mathrm{max})^2)/(\Sigma E_i)}$, where i runs over all cells in a window of $\Delta\eta \approx 0.0625$ and i_max is the index of the highest-energy cell	$w_{s\,\mathrm{tot}}$	e/γ
	Lateral shower width, $\sqrt{(\Sigma E_i (i - i_\mathrm{max})^2)/(\Sigma E_i)}$, where i runs over all cells in a window of 3 cells around the highest-energy cell	$w_{s\,3}$	γ
	Energy fraction outside core of three central cells, within seven cells	f_side	γ
	Difference between the energy of the cell associated with the second maximum, and the energy reconstructed in the cell with the smallest value found between the first and second maxima	ΔE_s	γ
	Ratio of the energy difference between the maximum energy deposit and the energy deposit in a secondary maximum in the cluster to the sum of these energies	E_ratio	e/γ
	Ratio of the energy measured in the first layer of the electromagnetic calorimeter to the total energy of the EM cluster	f_1	e/γ
Track conditions	Number of hits in the innermost pixel layer	$n_\mathrm{innermost}$	e
	Number of hits in the pixel detector	n_Pixel	e
	Total number of hits in the pixel and SCT detectors	n_Si	e
	Transverse impact parameter relative to the beam-line	d_0	e
	Significance of transverse impact parameter defined as the ratio of d_0 to its uncertainty	$|d_0/\sigma(d_0)|$	e
	Momentum lost by the track between the perigee and the last measurement point divided by the momentum at perigee	$\Delta p/p$	e
	Likelihood probability based on transition radiation in the TRT	eProbabilityHT	e
Track-cluster matching	$\Delta\eta$ between the cluster position in the first layer of the EM calorimeter and the extrapolated track	$\Delta\eta_1$	e
	$\Delta\phi$ between the cluster position in the second layer of the EM calorimeter and the momentum-rescaled track, extrapolated from the perigee, times the charge q	$\Delta\phi_\mathrm{res}$	e
	Ratio of the cluster energy to the measured track momentum	E/p	e

and thus by a large amount of hadronic activity. This activity is measured using energy deposits from clusters in the calorimeters (*calorimeter isolation*) or momenta from tracks

in the ID (*track isolation*) that are in proximity to the electron or photon under consideration. The *loose* and *tight* isolation are defined by requiring that the hadronic activity is significantly smaller than the particle momentum.

The hadronic activity in the calorimeter isolation is determined by summing the energy of all topological clusters that are found within a cone of radius $\Delta R = 0.2$ around the barycentre of the electron or photon cluster (see Figure 4.1). This yields the 'raw' calorimeter isolation $E_{\mathrm{T,raw}}$. It not only contains the desired jet-remnant energy but also the cluster energy $E_{\mathrm{T,core}}$ for the electron or photon candidate for which the isolation is determined and energy depositions from pile-up $E_{\mathrm{T,pile\text{-}up}}$. The energy in the calorimeter associated to hadronic activity $E_{\mathrm{T}}^{\mathrm{cone20}}$ is thus given by:

$$E_{\mathrm{T}}^{\mathrm{cone20}} = E_{\mathrm{T,raw}} - E_{\mathrm{T,core}} - E_{\mathrm{T,leakage}} - E_{\mathrm{T,pile\text{-}up}}. \tag{4.1}$$

The core energy $E_{\mathrm{T,core}}$ is determined by measuring the central energy in a $\Delta\eta \times \Delta\phi = 0.125 \times 0.175$ window. The larger size in ϕ-direction accounts for the magnetic field configuration, which is oriented parallel to the beam line and forces charged particles to be bend in the ϕ-plane. The fixed window size does not necessarily reflect a dynamically evolving electromagnetic shower for arbitrary energy densities. Energy- and $|\eta|$-dependent leakage corrections $E_{\mathrm{T,leakage}}$ are therefore applied. The energy correction due to pile-up is estimated $|\eta|$-dependent per event using the median energy density expected in the core-subtracted $\pi\Delta R^2$ area. The loose calorimeter isolation for electrons and photons requires $E_{\mathrm{T}}^{\mathrm{cone20}} < 0.2 \times p_{\mathrm{T}}^e$ and $E_{\mathrm{T}}^{\mathrm{cone20}} < 0.065 \times p_{\mathrm{T}}^\gamma$, respectively[17]. The thresholds are chosen by studying the isolation distributions of prompt and non-prompt electrons or photons.

The hadronic activity can also be measured in the ID by summing the momenta of tracks found within a cone of radius $\Delta R = 0.2$ centred around the track (cluster) of the tested electron (photon). The size of the cone can shrink dynamically for electrons, which accounts for collimated tracks from high-energetic heavy-flavour jet fragmentation. The hadronic activity $p_{\mathrm{T}}^{\mathrm{cone20}}$ is required to be significantly smaller than the momentum of the particle under consideration: $p_{\mathrm{T}}^{\mathrm{cone20}} < 0.15 \times p_{\mathrm{T}}^e$ and $p_{\mathrm{T}}^{\mathrm{cone20}} < 0.05 \times p_{\mathrm{T}}^\gamma$, for the loose electron and photon track isolation.

---

[17]The description of the tight isolation is omitted. The loose isolation WP is used nominally in the $Z\gamma\gamma$ analysis (see Section 5.1).
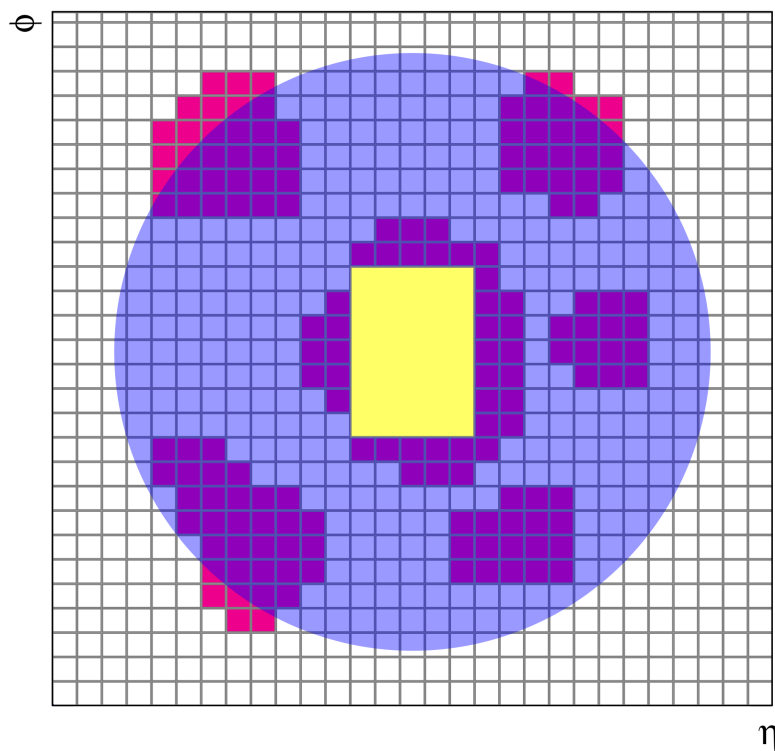
Figure 4.1.: Sketch of the derivation of hadronic activity in the second layer of the electromagnetic calorimeter. All cluster energies (cells marked in red), whose barycentre fall within a cone of size $\Delta R = 0.2$ (purple circle) around the barycentre of the photon or electron under consideration, are summed. From this sum, the central cluster energy in a $\Delta \eta \times \Delta \phi = 0.125 \times 0.175$ window (yellow rectangle), along with an associated leakage correction (red cells around yellow rectangle) and energy attributed to pile-up, are subtracted. The image is taken from [69].

4.2. Muon Reconstruction

Muons deposit energy in the ID and MS due to their electric charge but traverse the calorimeters with only little interaction. They are thus reconstructed from ID and MS tracks, and energy measured in the calorimeter systems consistent with that of a minimum ionising particle. The muon reconstruction can also purely rely on information provided by the MS extending the reconstruction to the full muon spectrometer coverage of $|\eta| < 2.7$ [70].

Track Reconstruction

Hits in the ID and MS are either used in a combined track fit or extrapolated from one system to the other, taking into account the magnetic field configuration and energy loss through traversal of the calorimeters. Additionally, stand-alone muons are reconstructed

34

from hits in the different muon chambers. The complementary reconstruction approaches maximise the reconstruction efficiency, for instance in regions of limited MS coverage. The muon four-momentum is then corrected to account for differences in the momentum scale and resolution between simulated events and data [71].

Identification and Isolation

Identification and isolation requirements allow to distinguish promptly produced muons from those emerging within the decay of heavy- and light-flavoured hadrons. The energy density in the detector around non-prompt muons is typically large and allows the differentiation to promptly-produced, isolated muons.

Muons that are produced from hadrons decaying within the volume of the ID can show a distinctive kink in the reconstructed track resulting in a poor quality of the combined track fit [71]. The muon identification requirements thus probe the general quality of reconstructed tracks, as well as the compatibility of the measured charge-momentum ratio q/p and of p_T between the ID and MS. The full MS coverage up to $|\eta| < 2.7$ is exploited by removing ID requirements, instead selecting muon tracks with a minimum number of quality hits in the MS. Three identification WPs are defined (*loose*, *medium*, and *tight*, see [70]).

The hadronic activity is determined by combining the measurement of momenta in the ID and energies of calorimeter clusters. The ID provides better momentum resolution and less pile-up dependence, while the calorimeter considers the deposited energy of neutral hadrons. The combination into a single isolation requirement with improved performance is done with a procedure called *particle-flow* [72]. Particle-flow algorithms assess the cluster energy in the calorimeter of exclusively neutral hadrons ensuring that no double-counting of the charged hadron energy, which is solely measured in the ID, takes place. The hadronic activity is determined via

$$E_{\mathrm{T,pflow}}^{\mathrm{had}} = p_{\mathrm{T,track}}^{\mathrm{ch\text{-}had}} + 0.4 \times E_{\mathrm{T}}^{\mathrm{neutral}}. \tag{4.2}$$

The momentum of charged hadrons $p_{\mathrm{T,track}}^{\mathrm{ch\text{-}had}}$ is measured by summing the momenta of all tracks in a cone of variable size around the muon. $E_{\mathrm{T}}^{\mathrm{neutral}}$ corresponds to the energy of neutral particle-flow objects within a cone of radius $\Delta R = 0.2$ around the tested muon. The weighting factor $w = 0.4$ is a result of efficiency studies optimised to give ideal rejection of non-prompt muons from heavy-flavour jets [73]. Two isolation WPs are

defined: *loose* and *tight*[18] with $E_{\mathrm{T,pflow}}^{\mathrm{had}} < 0.16 \times p_{\mathrm{T}}^{\mu}$ and $E_{\mathrm{T,pflow}}^{\mathrm{had}} < 0.045 \times p_{\mathrm{T}}^{\mu}$, respectively.

4.3. Monte Carlo Simulation

The MC simulation chain, which enables the comparison between the predictions of the SM and data, is comprised of four steps: the calculation of the cross section for a given particle interaction, the simulation of the interaction of the generated particles with the detector material, the digitisation of the analogue signals provided by the sub-detectors, and the particle reconstruction introduced in the previous sections.

The total cross section of $ab \rightarrow n$ processes describing the interaction of partons carrying a momentum fraction x_i of the total proton momentum can be factorised to [74]

$$\sigma_{pp \rightarrow n} = \sum_{a,b} \int \mathrm{d}x_a \mathrm{d}x_b f_a(x_a, \mu_{\mathrm{F}}^2) f_b(x_b, \mu_{\mathrm{F}}^2) \mathrm{d}\hat{\sigma}_{ab \rightarrow n}(\mu_{\mathrm{R}}^2, \mu_{\mathrm{F}}^2). \tag{4.3}$$

The hard interaction $\mathrm{d}\hat{\sigma}$ with large momentum transfer between the participating partons allows for a perturbative description in QCD. It is proportional to the product of the matrix element and the phase-space density: $\mathrm{d}\hat{\sigma}_{ab \rightarrow n}(\mu_{\mathrm{R}}^2, \mu_{\mathrm{F}}^2) \sim \left| M_{ab \rightarrow n}(\mu_{\mathrm{R}}^2, \mu_{\mathrm{F}}^2) \right|^2 \mathrm{d}\phi_n$. The perturbative calculation of the matrix element is done in orders of the strong coupling constant α_s. The least complex calculation is at *tree-level*, also called *leading order* (LO). *Next-to-leading order* (NLO) and *next-to-next-to-leading order* (NNLO) calculations, for instance, are increasingly more complex and add corrections of $O(\alpha_s)$ and $O(\alpha_s^2)$, respectively. The *renormalisation scale* μ_{R} and *factorisation scale* μ_{F} emerge as a necessity for preventing divergences in the integration when including corrections from loop diagrams (*ultraviolet divergence*) or from soft and collinear gluon emission (*infrared divergence*) [75]. The *parton distribution functions* (PDFs) $f_i(x_i, \mu_{\mathrm{F}}^2)$ give the probability of resolving a parton of flavour i with momentum fraction x_i within the proton. They are provided by various groups and are extracted from fits to data collected, for instance, through deep-inelastic scattering or from p–p collisions at the LHC [76, 77]. The analytic solution of a high-dimensional integral, such as the integration over $\mathrm{d}\phi_n$ in Equation 4.3, is often highly complex. Event generators use the *Monte Carlo* (MC) technique [74] to evaluate integrals numerically by sampling random numbers from probability density functions reflecting the interaction dynamics.

The partons that are generated in the previous step can radiate additional gluons and photons [74]. This emission occurs either in the initial state, before the hard interaction

---

[18]The isolation efficiencies for muons in the energy regime $20\,\mathrm{GeV} < p_{\mathrm{T}} < 100\,\mathrm{GeV}$ are 97% and 87% for the loose and tight WP, respectively. The purity increases from approximately 95% to 99% [73].

takes place, or in the final state; the interactions are denoted by *initial state radiation* (ISR) and *final state radiation* (FSR), respectively. The gluons that are emitted in this process can again radiate gluons, or create quark-antiquark pairs. Similarly, the photons can produce electron-positron pairs, all of which leads to a shower of new particles. This so-called *parton shower* (PS) is a dedicated step in the MC event generation.

The hard interaction takes place between two partons of the colliding protons. Additional hadronic activity not directly associated to the primary hard interaction is summarised under the term *underlying event* (UE) [22, 74]. It contains, for instance, secondary parton-parton interactions (predominantly through colour-exchange) from the remaining partons of the colliding protons. The parton shower is also considered for the UE.

Colour-charged particles from the hard interaction and partons from the parton shower and UE are governed by QCD, in particular by colour confinement. The formation of colour-neutral hadronic bound states is modelled in the so-called *hadronisation*. The hadronisation can not be treated perturbatively, as the PS ends at scales where QCD becomes strongly interacting. Empirical-driven methods, such as the *Lund string model* [78], are used instead. Non-stable hadrons emerging from the hadronisation process are subsequently decayed.

The MC event simulation described above generates events at so-called *particle-level*. The interaction of particles with the ATLAS detector is simulated using GEANT4 [79]. Incorporating the detector response leads to a shift of the generated kinematics and energy loss through passage of passive material has to be accounted for. The GEANT4 detector hits are digitised and a particle reconstruction takes place, analogous to that described in Sections 4.1 and 4.2. Events that went through the full MC simulation chain are available at *reconstruction-level*.

Before the events at reconstruction-level can be compared to data recorded with the ATLAS detector, additional p–p collisions (pile-up) have to be overlaid. The large luminosity at the LHC leads to multiple p–p collisions per bunch-crossing. The collision products overlay with the particles of the event of interest, drastically increasing the occupancy in the detector. The average number of simultaneous interactions per bunch-crossing $\langle \mu \rangle$ in Run 2 spans a wide range from a few to around 70 during 2017–2018 [80]. The total average for the full data taking period is $\langle \mu \rangle = 33.7$. The Run 2 pile-up profile is reflected in the MC simulation.

5. The $Z\gamma\gamma$ Analysis

The analysis presented in this thesis measures the triple gauge boson production of $Z\gamma\gamma$ [41], where the Z boson decays leptonically into a pair of electrons $Z \to e^+e^-$ or muons $Z \to \mu^+\mu^-$. The full Run 2 dataset recorded with the ATLAS experiment at a centre-of-mass energy of $13\,\mathrm{TeV}$ is analysed. It corresponds to an integrated luminosity of $L_{\mathrm{int}} = 139\,\mathrm{fb}^{-1}$. Events passing criteria ensuring good data taking quality are considered (*good run list*, see [81]). The $Z\gamma\gamma$ final state contains two high-p_{T} leptons and two isolated photons. The Feynman diagrams that give rise to such final states are depicted in Figure 5.1. One of the key aspects of this analysis is the suppression of FSR. The concept of FSR was introduced in Section 4.3 in the context of the parton shower and refers to radiative QED corrections here. Either one (Figure 5.1(b)) or both charged leptons (Figure 5.1(c)) can radiate off photons. This can be understood as higher-order QED corrections to the $Z\gamma$ or Drell-Yan production, while the focus of this analysis is the measurement of three promptly produced EW gauge bosons at tree-level. This represents the dominant difference between the measurement presented in this thesis and the $Z\gamma\gamma$ measurement performed with the ATLAS experiment at $8\,\mathrm{TeV}$ [10] and the CMS experiment at $13\,\mathrm{TeV}$ [11]. An ISR-enriched phase-space, i.e. Figure 5.1(a), is selected by imposing requirements on the invariant mass of the Z and $Z\gamma$ system and thus defining a *signal region* (SR) which predominantly contains photons which are radiated from initial quark lines. This phase-space is also sensitive to contributions from new physics arising through vertices coupling neutral EW gauge bosons, see Figure 5.1(d).

The following section gives a detailed description of the $Z\gamma\gamma$ SR event selection. Trigger optimisation studies are presented afterwards which are performed to enhance the number of signal events and to study trigger efficiency distributions. The signal contribution to the $\ell\ell\gamma\gamma$ phase-space is then compared amongst different MC event generators using the results of the trigger optimisation studies mentioned before. This chapter is concluded with a discussion of the analysis strategy which outlines the steps necessary for measuring integrated and differential cross sections at particle-level and for constraining effects of new physics.
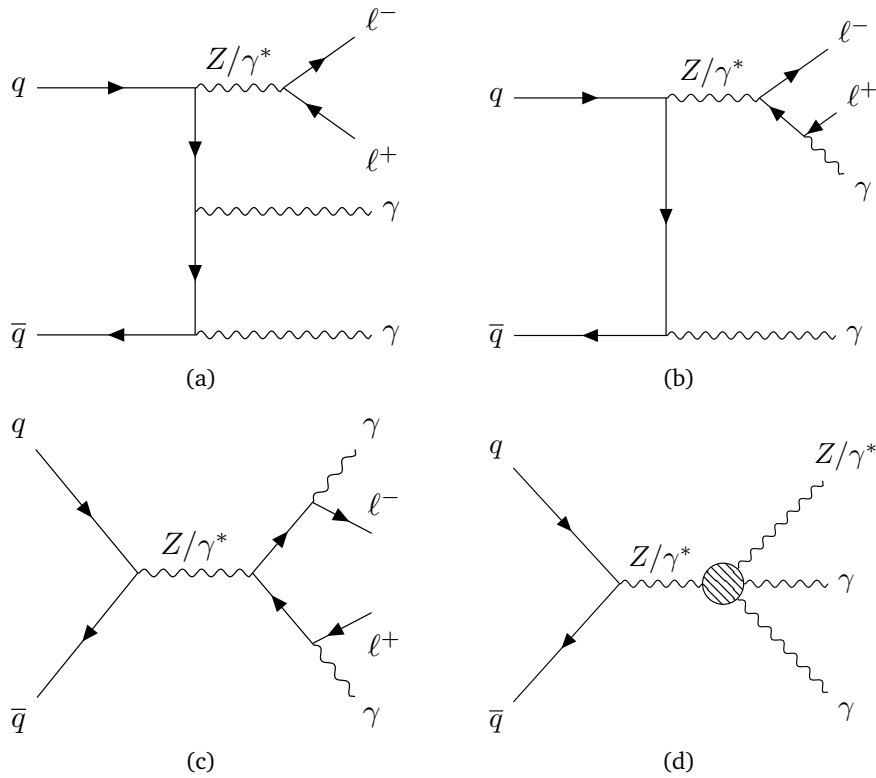
Figure 5.1.: Feynman diagrams of $Z\gamma\gamma$ production. The $\ell\ell\gamma\gamma$ final state can be produced through (a) ISR, (b)–(c) FSR, or (d) anomalous couplings between neutral EW gauge bosons. The Feynman diagram in (a) represents the SR of the analysis discussed in this thesis.

5.1. Object and Event Selection

A pre-selection is performed to select electron, muon, and photon candidates passing a set of baseline quality requirements. The transverse momentum of leptons from Z boson decays is $45\,\mathrm{GeV}$ on average when the Z boson is produced at rest, but the probability to find one of the leptons with significantly lower p_T is non-negligible. This can occur when the energy of electromagnetic clusters is mismeasured due to bremsstrahlung which is not associated to the cluster. The lepton baseline p_T threshold is thus set to $20\,\mathrm{GeV}$ to maximise the selection efficiency of the signal process. The minimal photon-p_T requirement is also set to $20\,\mathrm{GeV}$ which is a result of signal significance studies presented in Appendix A.

Electrons are required to be reconstructed within $|\eta| < 2.47$. The calorimeter transition region between the barrel and endcap of the electromagnetic calorimeter, which falls within $1.37 < |\eta| < 1.52$, is excluded. It typically features electrons with poor energy res-

olution due to an increase of passive material in front of the transition region and due to reduced instrumentation [67]. To suppress the misidentification of electrons, a medium identification is required for all electrons under consideration. The loose isolation WP is used to reject electrons emerging from flavour-transitions of heavy quarks.

Muons candidates are considered if they are reconstructed within $|\eta| < 2.5$. The rejection of muons from $|\eta| > 2.5$, where no ID information is available, increases the muon reconstruction quality. Similarly as for electrons, the medium identification WP is used. Isolation requirements help to suppress muons from heavy-flavour jet decays; all muons have to pass a loose isolation WP.

Cuts are also placed on the so-called *track-to-vertex association* (TTVA), which aims to increase the likelihood of leptons stemming from the hard interaction. In each event, it is possible to find more than one *primary vertex* (PV) due to additional inelastic collisions. PVs are formed from well-measured tracks that point to the same origin. The PV with the largest $\sum_i (p_{T,i})^2$ is used to define transverse (d_0) and longitudinal (z_0) impact parameters. They are a reference for the distance between the lepton track and the PV in the transverse plane and along the beam line, respectively. Electrons (muons) are required to fulfil a d_0 *significance* of $|d_0/\sigma_{d_0}| < 5$ (3) and both need to pass $|\Delta z_0 \sin(\theta)| < 0.5\,\mathrm{mm}$. The parameterisation of Δz_0 using the polar angle θ accounts for the degrading resolution in the forward region.

The reconstruction of photons is allowed in the range $|\eta| < 2.37$ ensuring that the fine η-segmentation of the first calorimeter layer is available for the suppression of photons from $\pi^0 \to \gamma\gamma$. The calorimeter transition region is excluded. As non-prompt photons from the fragmentation of jets contribute significantly to the background contamination, all photons are required to pass the loose isolation WP.

The reconstruction algorithms have a non-negligible probability of reconstructing multiple physics objects from a single cluster in the calorimeter or from the same ID hits in the ATLAS detector. It is hence necessary to perform a so-called *overlap removal* for the particles defined above, which removes physics objects that are located nearby in ΔR space. Photons are removed, if they are found within $\Delta R(\gamma, \ell) < 0.4$ of an electron or muon. Subsequently, electrons are removed if their distance to muons is $\Delta R(e, \mu) < 0.2$. The overlap removal does not include jets as the $Z\gamma\gamma$ analysis is performed in a phase-space of arbitrary jet multiplicity: $n_{\mathrm{jets}} \geq 0$.

The leptons and photons passing the overlap removal are used to define event-based selections. Each event is required to have at least one opposite-sign same-flavour (OSSF) lepton pair. The leading p_T of the pair is expected to be larger than $30\,\mathrm{GeV}$. This choice is

driven by the efficiency of single lepton triggers, which select events in data with at least one high-p_T lepton. Trigger optimisation studies are discussed in Section 5.2. At least one of the selected leptons has to be matched in ΔR space to the region identified by the HLT during data taking. The invariant mass of the lepton pair $m_{\ell\ell}$ needs to exceed $40\,\text{GeV}$, which allows to reject low-mass resonances (like ϕ, J/Ψ, and Y mesons [22]) and contributions from virtual photons. If the leading lepton is an electron (muon), it has to fulfil a tight identification (isolation). This is a result of the *offline-to-online harmonisation* that is discussed in the next section. The $Z\gamma\gamma$ phase-space also needs to contain two photons passing $\Delta R\,(\gamma,\gamma)\,>\,0.4$ and the most stringent (tight) identification requirement. If more than two photons pass the requirements, the two highest-p_T ones are chosen. In case both an electron and muon OSSF pair are found, the muon pair is preferred as the associated uncertainties from the reconstruction, isolation, and identification tend to be smaller.

Finally, the ISR-enriched SR is defined using $m_{\ell\ell}$ and the three-body invariant mass $m_{\ell\ell\gamma}$. Leptons radiating FSR photons have a softer p_T spectrum and the two-body invariant mass is not centred around m_Z but is instead smaller due the loss of the photon energy in the formation of the Z boson four-momentum (see Figure 5.2(a)). This feature is exploited in the FSR rejection requirement:

$$m_{\ell\ell} + \min(m_{\ell\ell\gamma1}, m_{\ell\ell\gamma2}) > 2 \times m_Z. \tag{5.1}$$

For events containing FSR, adding the photon four-momentum to the dilepton system results in three-body invariant masses close to the Z boson mass $m_{\ell\ell\gamma} \approx m_Z$ and therefore $m_{\ell\ell} < m_Z$. The sum $m_{\ell\ell} + \min(m_{\ell\ell\gamma1}, m_{\ell\ell\gamma2})$ will most likely not exceed twice the Z boson mass. The minimum of the two three-body-masses is used to satisfy the rejection of FSR from either or both leptons. The requirement in Equation 5.1 is presented as the red dotted line in Figure 5.2(b). The full event selection is summarised in Table 5.1.
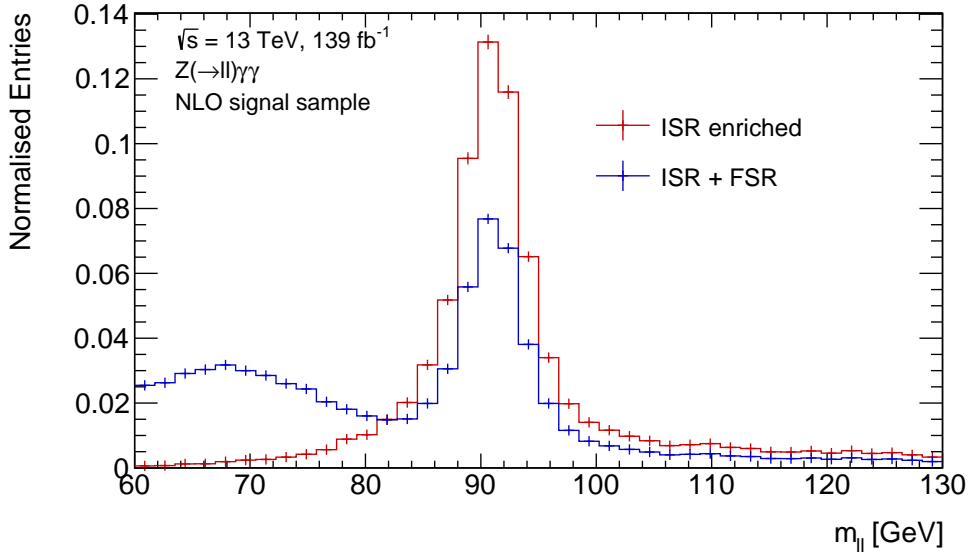
(a)
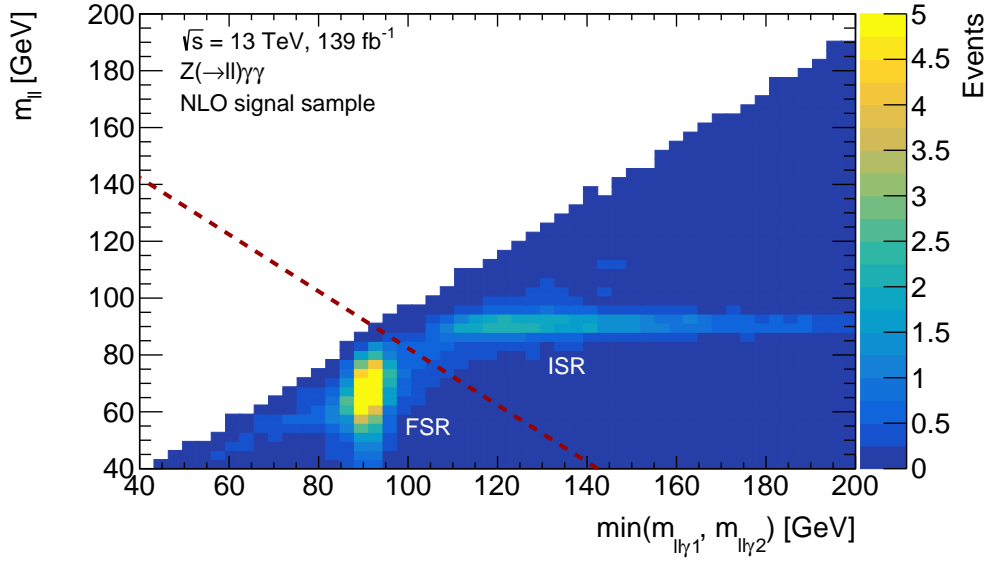
(b)

Figure 5.2.: Impact of FSR on $Z\gamma\gamma$ events. The invariant mass of the dilepton system $m_{\ell\ell}$ is shown in (a) for an ISR-enriched phase-space (red) using Equation 5.1 and for no distinction between ISR and FSR (blue). The peak around $70\,\text{GeV}$ is driven by the $Z\gamma\gamma$ photon p_T selection of $20\,\text{GeV}$. The correlation between $m_{\ell\ell}$ and $\min(m_{\ell\ell\gamma1}, m_{\ell\ell\gamma2})$ is displayed in (b). The first area of dense correlation below the red dotted line corresponds to FSR, for which $\min(m_{\ell\ell\gamma1}, m_{\ell\ell\gamma2}) \approx m_Z$ and $m_{\ell\ell} < m_Z$. A second correlation band corresponding to ISR events is visible for $m_{\ell\ell} \approx m_Z$ and $\min(m_{\ell\ell\gamma1}, m_{\ell\ell\gamma2}) > m_Z$.

Table 5.1.: SR event selection of the $Z\gamma\gamma$ analysis. The index for the leptons in brackets, i.e. (ℓ_1) or (ℓ_2), indicates whether the selection is performed for the leading or subleading lepton.

	Requirement
Electrons	$p_T(\ell_1) > 30\,\text{GeV}$, $p_T(\ell_2) > 20\,\text{GeV}$
	$|\eta| < 2.47$, excluding $1.37 < |\eta| < 1.52$
	$|d_0/\sigma_{d_0}| < 5$, $|z_0 \sin\theta| < 0.5\,\text{mm}$
	Tight identification (ℓ_1), Medium identification (ℓ_2)
	Loose isolation for both
Muons	$p_T(\ell_1) > 30\,\text{GeV}$, $p_T(\ell_2) > 20\,\text{GeV}$
	$|\eta| < 2.5$
	$|d_0/\sigma_{d_0}| < 3$ and $|z_0 \sin\theta| < 0.5\,\text{mm}$
	Medium identification for both
	Tight isolation (ℓ_1), Loose isolation (ℓ_2)
Photons	$p_T > 20\,\text{GeV}$
	$|\eta| < 2.37$, excluding $1.37 < |\eta| < 1.52$
	Tight identification
	Loose isolation
Multiplicity	≥ 1 OSSF lepton pair, ≥ 2 photons
Overlap	$\Delta R(\gamma, \ell) > 0.4$, $\Delta R(e, \mu) > 0.2$, $\Delta R(\gamma, \gamma) > 0.4$
Invariant mass	$m_{\ell\ell} > 40\,\text{GeV}$, $m_{\ell\ell} + \min(m_{\ell\ell\gamma 1}, m_{\ell\ell\gamma 2}) > 2 \times m_Z$

5.2. Trigger Studies

The trigger optimisation studies are conducted to verify the performance of triggers searching for lepton or photon signatures in the context of the $\ell\ell\gamma\gamma$ final state. Additionally, it is tested how the signal sensitivity depends on trigger requirements placed on the per-event multiplicity of physics objects. Increasing the multiplicity of electrons and photons for a given trigger item of fixed rate enables the reduction of the corresponding trigger p_T threshold, making multi-lepton triggers especially interesting. Trigger items can also come with a prescale value n to further reduce the p_T threshold. Events fired by such an item are only saved every n-th time, effectively reducing the trigger rate. The downside of the prescale is that trigger-related uncertainties are scaled up by n and p_T spectra of events recorded with different prescaled triggers can show non-smooth transi-

tion edges. It was thus decided to only use the lowest-energy unprescaled triggers in this thesis. The lowest p_{T} threshold of single photon triggers is $120\,\mathrm{GeV}$ in Run 2, which is in strong contradiction to the desired photon p_{T} cut of $20\,\mathrm{GeV}$. Diphoton triggers either require one higher-p_{T} photon and one lower-p_{T} photon with medium or loose identification, like $p_{\mathrm{T}}^{\gamma 1} > 35\,\mathrm{GeV}$ and $p_{\mathrm{T}}^{\gamma 2} > 25\,\mathrm{GeV}$, or two photons with smaller momenta (e.g. $p_{\mathrm{T}}^{\gamma} > 20\,\mathrm{GeV}$) and tight identification. The former trigger type again leads to the same contradiction mentioned above resulting in a loss of signal sensitivity. The second diphoton-trigger definition with tight identification would induce a strong bias in the measurement of the dominant non-prompt photon background using dedicated control regions where identification requirements are inverted. For this reason, solely single and dilepton triggers are further discussed.

The optimisation of the predicted number of events is performed using a $Z\gamma\gamma$ LO MC simulation. All results are shown after the signal selection presented in Section 5.1 is applied – cuts on the lepton p_{T} threshold, identification, and isolation are not required as they depend on the trigger choice. All trigger items considered are summarised in Table 5.2.

Single and Dielectron Triggers

Single electron triggers with isolation requirements are typically paired with high-p_{T} triggers that do not require isolation cuts to recover selection inefficiencies in the high-energy regime, e.g. `e26_lhtight_nod0_ivarloose`[19] paired with `e60_lhmedium_nod0`. Dielectron triggers, like `2e17_lhvloose_nod0` usually require less-stringent identification cuts. For both types, it is first verified whether the offline selection needs to be adjusted to account for online trigger criteria. The HLT identification and isolation requirements imposed during data taking closely follow what is required offline. It is thus recommended to perform an online-to-offline harmonisation in which the offline selections are tightened to match at least those defined online. The lepton requirements prior to the harmonisation are listed in Appendix B. For single electron triggers, it is investigated which trigger items are fired as a function of the offline leading electron p_{T} for all simulated events passing the event selection (see Figure 5.3). In the energy regime 30–$60\,\mathrm{GeV}$, events are nearly exclusively selected via `e26_lhtight_nod0_ivarloose`; for $p_{\mathrm{T}} > 60\,\mathrm{GeV}$ `e26_lhtight_nod0_ivarloose` is as efficient as the remaining trigger items. The probability for offline electrons to pass the tight identification and loose

---

[19]The numerical number indicates the p_{T} threshold of the trigger item. The online identification (isolation) WP is written after the prefix 'lh' ('i'). More information is given in [82].

Table 5.2.: List of single and dilepton triggers used in the trigger optimisation studies. The numerical numbers indicate the p_T threshold of the trigger item. The year marks the period in which the listed items were the lowest-energy unprescaled triggers. The online identification (isolation) WP is written after the prefix 'lh' ('i'). More information is given in [82, 83].

Trigger	Electron channel	Muon channel

Single lepton	(2015)
	`e24_lhmedium`
	`e60_lhmedium`
	`e120_lhloose`
	(2016–2018)
	`e26_lhtight_nod0_ivarloose`
	`e60_lhmedium_nod0`
	`e140_lhloose_nod0`
		(2015)
		`mu20_iloose_L1MU15`
		`mu50`
		–
		(2016–2018)
		`mu26_ivarmedium`
		`mu50`
		–

Dilepton symmetric	(2015)
	`2e12_lhloose`
	(2016)
	`2e17_lhvloose_nod0`
	(2017–2018)
	`2e17_lhvloose_nod0`[a]
	`2e24_lhvloose_nod0`
		(2015)
		`2mu10`
		(2016–2018)
		`2mu14`
		–
		–
		–

Dilepton asymmetric	–
	–
	–
	–
		(2015)
		`mu18_mu8noL1`
		(2016–2018)
		`mu22_mu8noL1`

[a] `2e17_lhvloose_nod0` is listed for 2016 and 2017–2018 but differs in the L1 seed, which contained additional isolation requirements during 2017–2018.

isolation is hence large. This can lead to a bias when, for instance, identification-related properties are inverted offline. The offline electron identification is therefore increased from medium to tight for events selected with single lepton triggers; the isolation WP is already set to loose. Dielectron triggers do not impose a bias because the offline requirements are stringent enough.

It is also investigated how the efficiency of single and dilepton triggers is distributed and if the p_T of the offline leptons is chosen reasonably. The p_T threshold should ideally be placed close to the plateau of the trigger efficiency to reduce uncertainties from data to MC efficiency corrections that are typically larger in the turn-on area. Representative electron efficiency distributions are shown in Figure 5.4. A sharp turn-on behaviour is observed and the trigger efficiency saturates just below 100%. The cut $p_\mathrm{T} > 30\,\mathrm{GeV}$ is
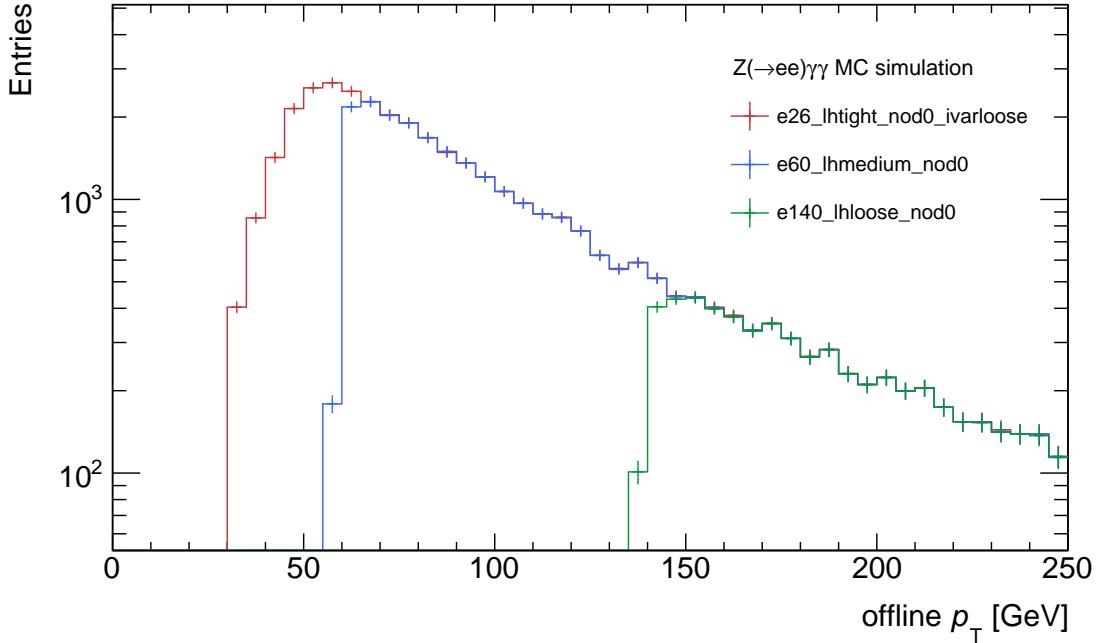
Figure 5.3.: In all simulated $Z(\to ee)\,\gamma\gamma$ events surviving the event selection, it is tested which of the single electron trigger items listed in Table 5.2 have been fired as a function of the p_T of the leading offline electron. Trigger items that were only active in 2015 are omitted.

close to the plateau of the single electron trigger and the threshold can not be further loosened to avoid the aforementioned larger uncertainties. For the dielectron trigger, the requirement $p_\mathrm{T} > 20\,\mathrm{GeV}$ corresponds to efficiencies that fall within the turn-on area – an additional optimisation of the p_T threshold is omitted due to the results presented in Table 5.3. The results show the expected $Z\gamma\gamma$ event yield after applying all SR selections. Single electron triggers show a slightly better performance and are hence preferred in the analysis.

Table 5.3.: Expected $Z\gamma\gamma$ event yield for the set of lowest-energy unprescaled single electron and dielectron triggers. The first (second) entry in brackets represents the identification and isolation requirement for the leading (subleading) lepton.

Trigger	Expected $Z\gamma\gamma$ event yield
Single electron ID (tight, medium) Iso (loose, loose)	83.1
Dielectron ID (medium, medium) Iso (loose, loose)	82.0
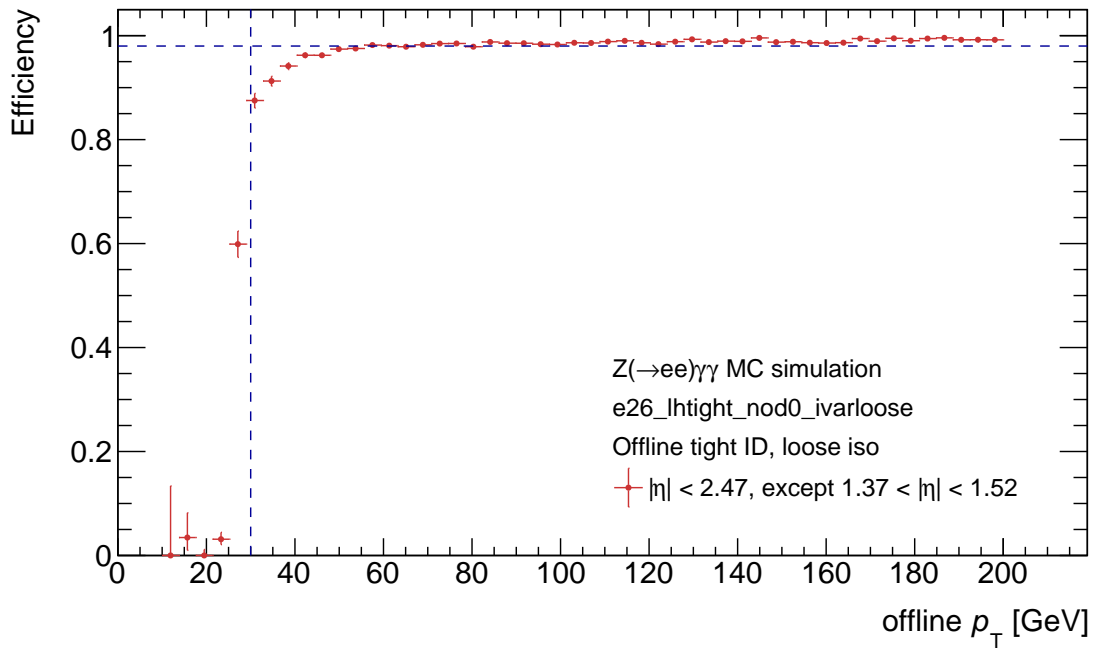
(a)
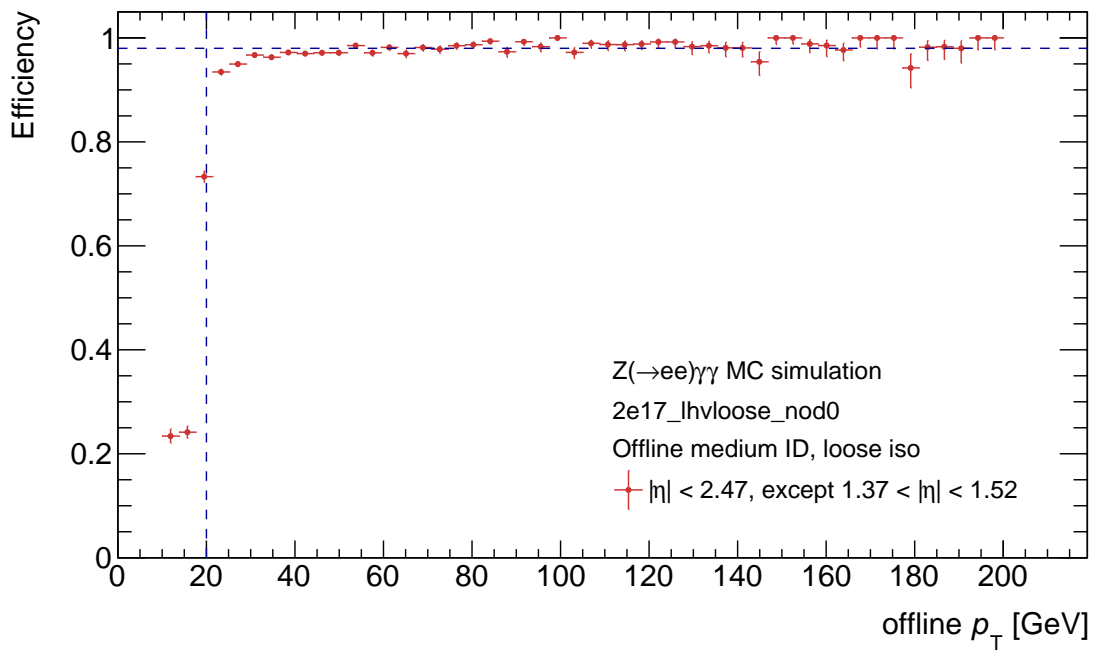
(b)

Figure 5.4.: Efficiency for (a) `e26_lhtight_nod0_ivarloose` measured for the offline leading electron and (b) `2e17_lhvloose_nod0` measured for the offline subleading electron. The efficiency is steeply rising in vicinity of the threshold of the trigger item and saturates at values close to unity. The horizontal dashed line shows the 98% efficiency limit, whereas the vertical dashed line represents the offline transverse momentum requirement.

Single and Dimuon Triggers

Similarly as in the electron channel, single muon triggers with isolation requirements are paired with items requiring no isolation but a larger p_T threshold: `mu26_ivarmedium` paired with `mu50`. Dimuon triggers either select muon candidates with symmetric p_T thresholds, like `2mu14`, or one muon triggered with the HLT (`mu22`) plus at least two muons using the full detector granularity not requiring any of the previous steps of the trigger chain (`mu8noL1`, i.e. at least two muons with $p_T > 22\,\text{GeV}$ and $p_T > 8\,\text{GeV}$) [83]. Neglecting the seed on L1 allows to recover lost efficiency as the L1 algorithms have to operate with small latency and therefore coarse granularity. The selection requirements prior to the offline-to-online harmonisation are summarised in Appendix B. For single muon triggers, it is again investigated which trigger items are fired in all simulated events passing the event selection (see Figure 5.5). Over the full energy range, `mu26_ivarmedium` (selecting medium-isolated muons) is fired and as efficient as `mu50`. The offline isolation is therefore set to tight as no offline medium isolation WP exists. No harmonisation is necessary for symmetric or asymmetric dimuon triggers.

The muon trigger efficiency is studied in the following. The efficiency distribution for single muon triggers, see Figure 5.6, is split into three η-ranges to highlight the η-dependence of the muon trigger system and reconstruction. This dependence is due to different amounts of passive material in the ATLAS detector in front of the muon spectrometer (mostly from support structures), especially in the barrel region ($|\eta|$ ¡ 1.05). Here, the geometric acceptance of the L1 muon trigger is 80% and increases to 99% for $|\eta| > 1.05$ [83]. The efficiency for `mu26_ivarmedium` saturates between 90%–95% and the offline p_T threshold of $30\,\text{GeV}$ is close to the trigger plateau. The distributions of dimuon trigger efficiencies are shown in Figure 5.7. Symmetric dimuon triggers are clearly outperformed by the asymmetric ones, with the former saturating at 70% and the latter at 90%–95% efficiency – a direct result of the circumvention of the L1 trigger inefficiencies mentioned above. The `mu22_mu8noL1` efficiency is already large ($\approx 80\%$) below the HLT trigger threshold of $22\,\text{GeV}$, as it is measured for the subleading muon which only needs to pass $8\,\text{GeV}$. The predicted $Z\gamma\gamma$ event yields for Run 2 luminosity are given in Table 5.4. As expected, the event number for symmetric dimuon triggers is well below that of single or asymmetric dimuon triggers. Asymmetric dimuon triggers offer a slightly larger signal sensitivity with an improvement below 3.0%. Single muon triggers are nevertheless preferred in this analysis. In contrast to dilepton triggers, single lepton triggers do not impose online requirements on the subleading lepton. This means that subleading lepton quantities, like p_T and the identification, can be varied without
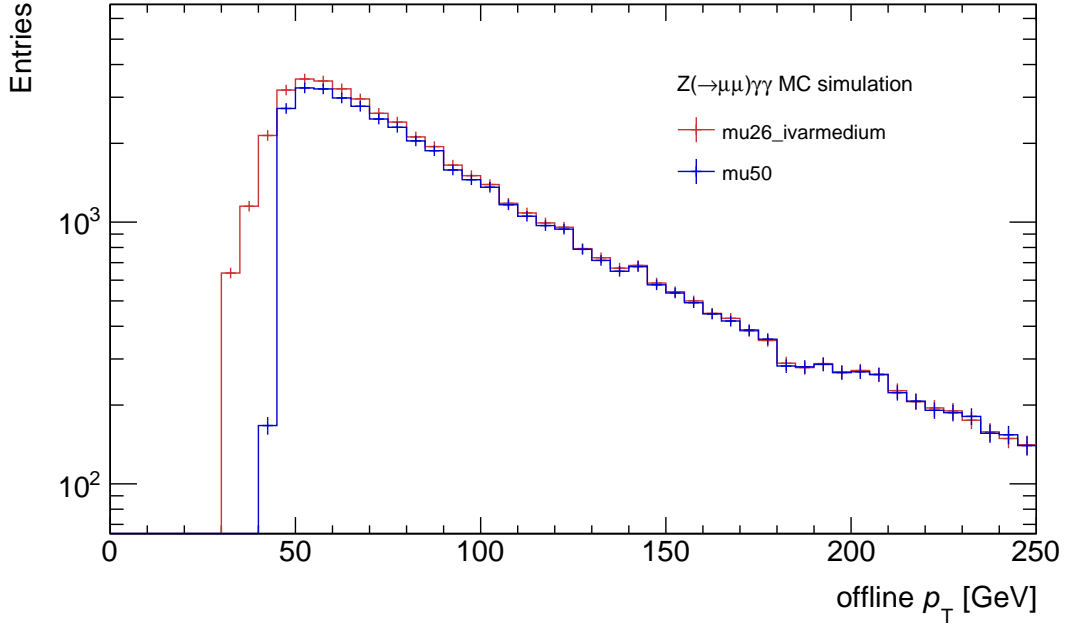
Figure 5.5.: In all simulated $Z(\to \mu\mu)\,\gamma\gamma$ events surviving the event selection, it is tested which of the single muon trigger items listed in Table 5.2 have been fired as a function of the p_T of the leading offline muon. Trigger items that were only active in 2015 are omitted.

introducing any trigger bias.

Table 5.4.: Expected $Z\gamma\gamma$ event yield for the set of lowest-energy unprescaled single muon and dimuon triggers. The first (second) entry in brackets is the identification and isolation requirement for the leading (subleading) muon.

Trigger	Expected $Z\gamma\gamma$ event yield
Single muon ID (medium, medium) Iso (tight, loose)	112.5
Dimuon symmetric ID (medium, medium) Iso (loose, loose)	84.1
Dimuon asymmetric ID (medium, medium) Iso (loose, loose)	115.7
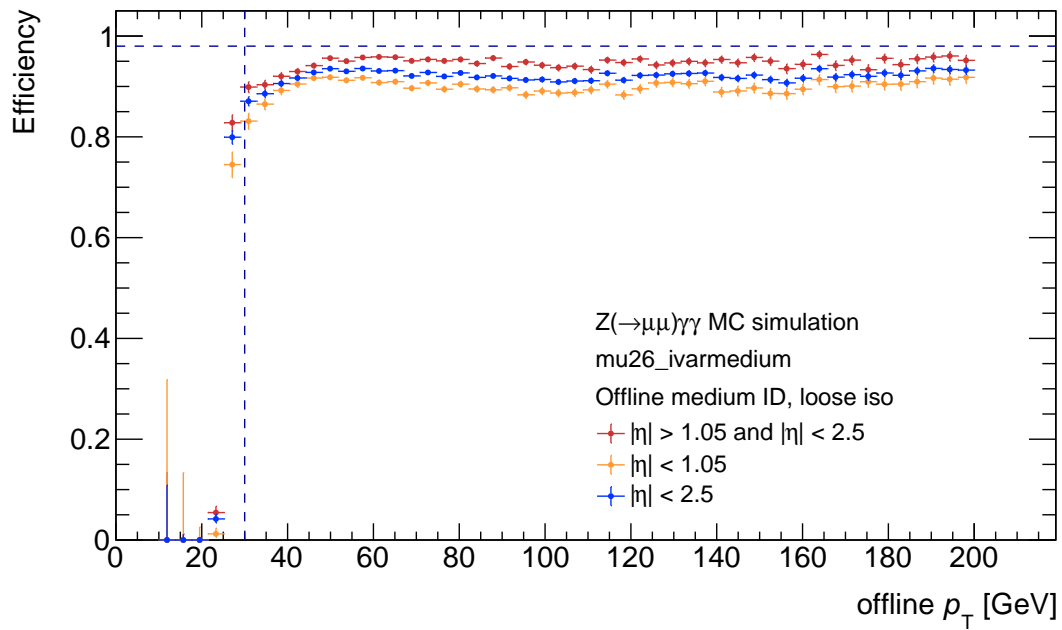
Figure 5.6.: Efficiency for `mu26_ivarmedium` measured for the offline leading muon and three η ranges: $|\eta| > 1.05$ (endcap), $|\eta| < 1.05$ (barrel), and $|\eta| < 2.5$ (full range). The efficiency is steeply rising in vicinity of the threshold of the trigger item and saturates around $\approx 90\%$. The horizontal dashed line shows the 98% efficiency limit, whereas the vertical dashed line represents the offline transverse momentum requirement.
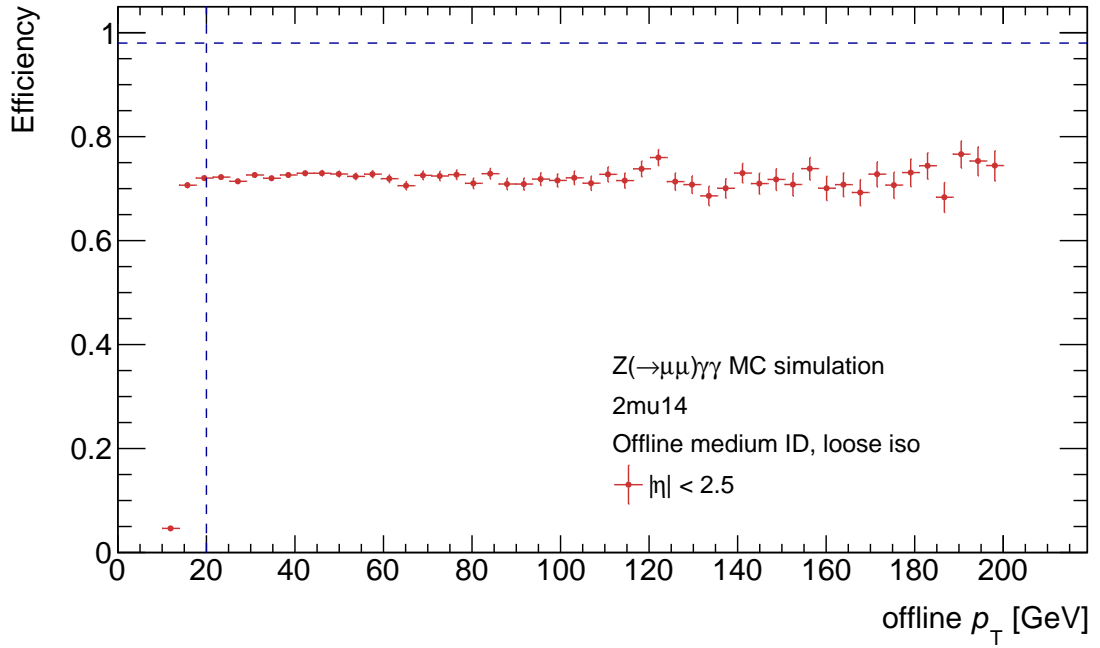
(a)
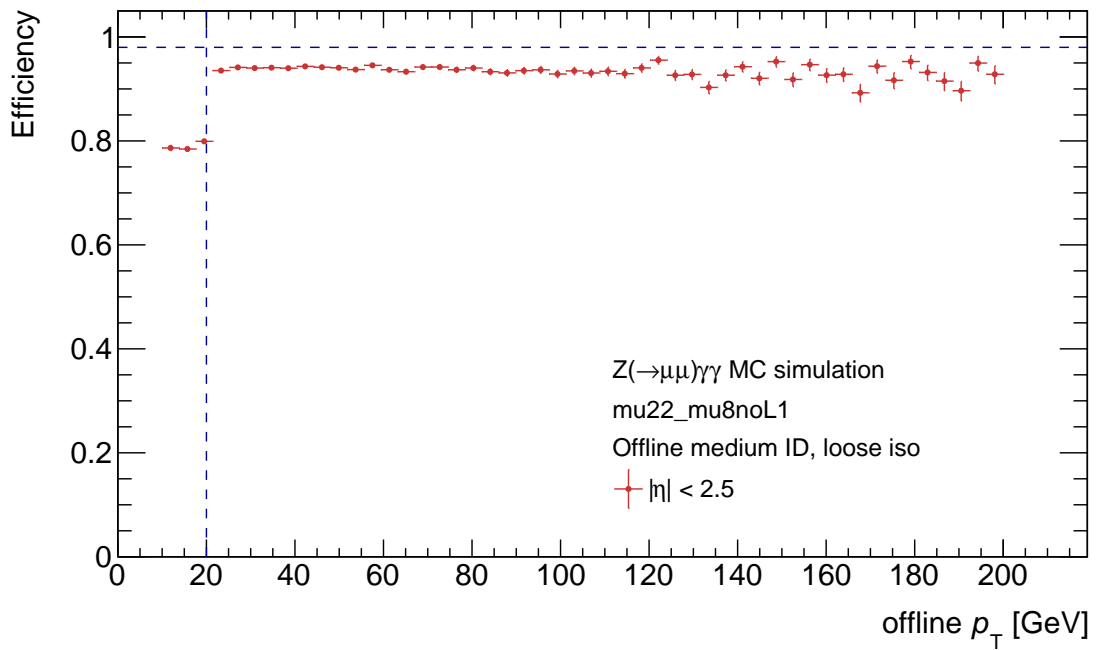
(b)

Figure 5.7.: Efficiency for (a) `2mu14` and (b) `mu22_mu8noL1` measured for the offline subleading muon. The efficiency is steeply rising in vicinity of the threshold of the trigger item and saturates at 70% (a) and 90%–95% (b). The horizontal dashed line shows the 98% efficiency limit, whereas the vertical dashed line represents the offline transverse momentum requirement.

5.3. Event Expectation and MC Samples

The $Z\gamma\gamma$ modelling in the SR phase-space and the Run 2 event expectation are predicted using three MC event generators accurate up to NLO QCD precision:

- SHERPA 2.2.4 (0,1j@LO) with up to two additional jets at LO in the matrix element; used mainly in the trigger studies

- SHERPA 2.2.10 (0j@NLO + 1,2j@LO) with zero additional jets at NLO and up to two jets at LO in the matrix element. This is the nominal signal sample used in the full analysis. It has by far the largest statistical precision

- MADGRAPH5_AMC@NLO 2.7.3 (0,1j@NLO) with up to one additional jet at NLO in the matrix element; used to verify the SHERPA 2.2.10 predictions and uncertainties

All simulated events undergo a p_{T}- and η-dependent reweighting. It accounts for differences in the measured and predicted efficiency of the lepton and photon reconstruction, identification, and isolation. A similar correction is applied for single-lepton trigger efficiencies. The simulated pile-up profile is compared to three representative runs in data covering the periods 2015–2016, 2017, and 2018, from which correction factors are derived and applied to the MC simulation. The reweighting is discussed in more detail in Section 7.2. The $Z\gamma\gamma$ event expectation in the SR with the full set of corrections defined above is shown in Table 5.5. SHERPA and MADGRAPH5_AMC@NLO predict a similar yield of roughly 210 $Z\gamma\gamma$ events at NLO for the combined electron and muon channel. The expected $Z(\to \mu\mu)\,\gamma\gamma$ event yield is approximately 30% larger than that in the electron channel – a consequence of the more-efficient muon reconstruction and identification. The predicted yield at NLO is roughly 8% larger than at tree-level highlighting the impact of one-loop corrections on the predicted cross section.

Table 5.6 lists all MC samples used in the thesis and gives information about the generator, QCD accuracy, PDF set, and the parton shower – Chapter 6 introduces background processes contributing to the SR.

Table 5.5.: Prediction of the $Z\gamma\gamma$ event yield in Run 2 after the requirements in Table 5.1 have been applied. The uncertainty comprises the statistical uncertainty only.

$Z\gamma\gamma$ MC simulation	QCD order	e-channel	μ-channel
SHERPA 2.2.4	LO	83.0 ± 1.9	112.2 ± 2.3
SHERPA 2.2.10	NLO	91.5 ± 0.9	119.5 ± 1.0
MADGRAPH5_AMC@NLO 2.7.3	NLO	91.0 ± 1.0	118.1 ± 1.2

Table 5.6.: List of MC simulations used in the $Z\gamma\gamma$ analysis. The first three rows summarise the $Z\gamma\gamma$ signal MC samples. The subsequent rows list the samples used in the background estimation. The two simulations for $Z\gamma$ + jets are used to determine fake-photon related systematic uncertainties (see Section 6.1).

Process	Generator	QCD order	PDF set	PS	Ref.
$Z\gamma\gamma$	SHERPA 2.2.4	LO	NNPDF3.0NNLO	SHERPA 2.2.4	[84][85]
$Z\gamma\gamma$	SHERPA 2.2.10	NLO	NNPDF3.0NNLO	SHERPA 2.2.10	[84][85]
$Z\gamma\gamma$	MADGRAPH5_AMC@NLO 2.7.3	NLO	NNPDF3.0NLO	PYTHIA 8.244	[86][85][87]
$Z\gamma$ + jets	SHERPA 2.2.4	LO	NNPDF3.0NNLO	SHERPA 2.2.4	[84][85]
$Z\gamma$ + jets	MADGRAPH5_AMC@NLO2.3.3	NLO	NNPDF3.0NLO	PYTHIA 8.212	[86][85][87]
Z + jets	POWHEG BOX v1	NLO	CT10NLO	PYTHIA 8.186	[88–91][92][87]
$t\bar{t}\gamma\gamma$	MADGRAPH5_AMC@NLO 2.3.3	LO	NNPDF2.3LO	PYTHIA 8.212	[86][85][87]
$ZZ\,(\to \ell\ell\ell\ell)$	SHERPA 2.2.2	NLO	NNPDF3.0NNLO	SHERPA 2.2.2	[84][85]
$WZ\gamma\,(\to \ell\nu\ell\ell\gamma)$	SHERPA 2.2.5	NLO	NNPDF3.0NNLO	SHERPA 2.2.5	[84][85]
$Z\,(\to \ell\ell)\,H\,(\to \gamma\gamma)$	POWHEG BOX v2	NLO	NNPDF3.0NLO	PYTHIA 8.212	[88–91][85][87]
γ + jets	SHERPA 2.2.2	NLO	NNPDF3.0NNLO	SHERPA 2.2.2	[84][85]
$\gamma\gamma$ + jets	SHERPA 2.2.2	NLO	NNPDF3.0NNLO	SHERPA 2.2.2	[84][85]

5.4. Analysis Strategy

The full event selection defined in Table 5.1 is required for the $139\,\mathrm{fb}^{-1}$ of Run 2 data. This enriches a phase-space of $\ell\ell\gamma\gamma$ events which predominantly contains ISR photons. Background processes can enter this phase-space and pass the requirements of the event selection due to the finite purity of the reconstruction, identification, and isolation algorithms. By far the largest background contribution stems from non-prompt photons – abbreviated as *fake photons* in the following – emerging within the fragmentation of a jet containing neutral mesons (e.g. $\pi^0 \to \gamma\gamma$, see Section 4.1). The abundance of jet production at the LHC (see Section 2.3) inflates such topologies. MC simulation typically underestimates the rate at which these fake photon processes occur; the fake photon background is instead measured with two data-driven methods. The photon-associated top quark production $t\bar{t}\gamma\gamma$ is the second most dominant source of background contamination and its normalisation is measured in a data-driven CR selecting events with two opposite-flavour and opposite-sign leptons ($e^{\pm}\mu^{\mp}\gamma\gamma$). Other background processes containing prompt photons, like the the triple gauge boson production of $WZ\gamma\,(\to \ell\nu\ell\ell\gamma)$ or

two Z bosons decaying leptonically $ZZ\,(\to \ell\ell\ell\ell)^{20}$, contribute less significant and their normalisation is calculated with MC simulation. All background events are subtracted from data yielding the number of measured $Z\gamma\gamma$ events $N_{Z\gamma\gamma}^{\mathrm{meas}}$, which is used to obtain the integrated $Z\gamma\gamma$ cross section at reconstruction-level:

$$\sigma_{Z\gamma\gamma}^{\mathrm{reco}} = \frac{N_{\mathrm{data}} - N_{\mathrm{bkg}}}{L_{\mathrm{int}}} = \frac{N_{Z\gamma\gamma}^{\mathrm{meas}}}{L_{\mathrm{int}}}. \tag{5.2}$$

Additionally, differential cross sections as functions of six observables describing the $\ell\ell\gamma\gamma$ system are measured at reconstruction-level. The first three observables represent the transverse momentum of the participating EW gauge bosons: $E_{\mathrm{T}}^{\gamma 1}$, $E_{\mathrm{T}}^{\gamma 2}$, and $p_{\mathrm{T}}^{\ell\ell}$. The transverse momentum of the four-body-system $p_{\mathrm{T}}^{\ell\ell\gamma\gamma}$ reflects the hadronic recoil in the event and is non-zero for additional jet production allowing to probe the QCD modelling. The invariant mass of both photons $m_{\gamma\gamma}$ is sensitive to background processes producing diphoton resonances, for instance $H \to \gamma\gamma$. Lastly, the total energy scale of $\ell\ell\gamma\gamma$ events is measured in terms of the invariant mass of the four-body-system $m_{\ell\ell\gamma\gamma}$. To improve the durability and accessibility of the results of this analysis, the cross sections are corrected for detector effects, which simplifies the comparison to theoretical models. For the integrated cross section, this is done with a single correction factor $C_{Z\gamma\gamma}$:

$$C_{Z\gamma\gamma} = \frac{N_{Z\gamma\gamma}^{\mathrm{reco}}}{N_{Z\gamma\gamma}^{\mathrm{truth}}}, \qquad \sigma_{Z\gamma\gamma}^{\mathrm{fid}} = \frac{N_{Z\gamma\gamma}^{\mathrm{meas}}}{C_{Z\gamma\gamma} \times L_{\mathrm{int}}}. \tag{5.3}$$

$C_{Z\gamma\gamma}$ is obtained from the nominal SHERPA 2.2.10 NLO signal sample by dividing the predicted event yield at reconstruction-level by the yield at particle-level (also called *truth-level*). $N_{Z\gamma\gamma}^{\mathrm{truth}}$ reflects the $Z\gamma\gamma$ SHERPA 2.2.10 NLO prediction at particle-level after applying the parton shower but before the detector response, digitisation and the particle reconstruction is performed. The phase-space, in which $N_{Z\gamma\gamma}^{\mathrm{truth}}$ is measured, is called *fiducial phase-space* and follows the offline reconstruction from Table 5.1 as close as possible to minimise model-dependencies in the extrapolation from reconstruction-level to truth-level[21]. The six differential cross sections are also measured in the fiducial volume at particle-level. An unfolding procedure (see Section 7.4) is performed incorporating possible bin migrations when correcting for detector effects. The cross sections are determined separately in the electron and muon channel and are combined using an averaging

---

[20]For both $ZZ\,(\to \ell\ell\ell\ell)$ and $WZ\gamma\,(\to \ell\nu\ell\ell\gamma)$ it is ensured that the selected photons are prompt photons, probing the misidentification of electrons as photons: $e \to \gamma$.

[21]The definition of the fiducial volume allows to minimise purely theory-based extrapolation into particle-level regions where the detector has low efficiency and acceptance.

procedure. The combined integrated and differential cross sections at particle-level are then compared to the NLO predictions from SHERPA and MADGRAPH5_AMC@NLO. The differential cross section of the observable with the highest sensitivity to new physics occurring via neutral EW gauge boson couplings (see Figure 5.1(d)) is taken to set limits on dimension-8 operators in the framework of an effective field theory.

6. Background Determination

The event selection in the signal region defines a phase-space enriched in $\ell\ell\gamma\gamma$ events originating from the prompt triple gauge boson production. Although stringent identification and isolation requirements are used, there is a non-negligible contribution of background processes fulfilling the phase-space requirements. This can occur if particles are falsely identified or non-promptly produced, or when particles from different decay chains are combined to form the $\ell\ell\gamma\gamma$ final state (combinatorial background). The contamination of these processes is determined from MC simulation or using data-driven methods in case the rate of a process is difficult to model. A reliable measurement of the $Z\gamma\gamma$ cross section is only possible when all sources of background processes are considered. The systematic uncertainties arising from the background determination have to be understood and controlled.

The data-driven methods which are used to determine the contribution of events with fake photons are described and compared in the following. A procedure correcting the normalisation of the $t\bar{t}\gamma\gamma$ process using a $e^{\pm}\mu^{\mp}\gamma\gamma$ CR in data is presented afterwards. The contribution of PU events containing Z bosons and photons from different p–p collisions is measured in the subsequent section. Smaller background processes are introduced, for instance those containing electrons misidentified as photons: $e \rightarrow \gamma$. Lastly, the contribution of all sources of backgrounds to the $\ell\ell\gamma\gamma$ phase-space is summarised and the distributions of the reconstruction-level observables are presented.

6.1. Fake Photons

The contamination of the $Z\gamma\gamma$ SR by fake photon events is measured using two data-driven methods: the matrix method and the 2D template fit. For both approaches, a loosened SR is defined. A photon identification called *LoosePrime4* is required as a new baseline, which is identical to the tight identification except for four criteria that are removed [67]. These criteria are sensitive to the shower shape – for instance E_{ratio} as introduced in Section 4.1 – and only loosely correlated to the photon isolation. Fake-enriched CRs are defined by requiring photon candidates to pass the LoosePrime4 identification but fail the tight identification. This corresponds to a failure of at least one of the four requirements mentioned above. The electromagnetic component of the jet fragmentation from $\pi^0 \rightarrow \gamma\gamma$ decays is selected via the LoosePrime4 identification and the hadronic component of the jet remnant via the failure of the tight identification. The largest fake

photon contribution is expected to originate from events with a subleading fake photon ($Z\gamma j$). It is not likely for a fake photon emerging from the decay chain within a jet to be higher energetic than a promptly produced photon. Events with a leading fake photon ($Zj\gamma$) are expected to contribute more than events where both photons stem from jet fragmentation (Zjj). Both data-driven methods are based on probing the photon isolation: in the matrix method through a numerical procedure counting events in data regions and in the 2D template fit by assessing shape differences of the isolation distribution between prompt and fake photons. The loose isolation WP[22] is defined photon-p_T dependent to have a stronger rejection at lower photon p_T^γ for which the fake rate is larger [93]:

$$
\begin{aligned}
E^\text{iso} &= E_\text{T}^\text{cone20} - 0.065 \times p_\text{T}^\gamma, \\
p^\text{iso} &= p_\text{T}^\text{cone20} - 0.05 \times p_\text{T}^\gamma.
\end{aligned}
\tag{6.1}
$$

The calorimeter isolation energy E_T^cone20 corresponds to the cluster energy in the calorimeter associated to hadronic activity for cone radii of $\Delta R = 0.2$. The hadronic activity measured in the ID in a cone of radius $\Delta R = 0.2$ around the photon is denoted by p_T^cone20. Photons fulfilling the loose isolation need to pass the conditions $E^\text{iso} < 0\,\text{GeV}$ and $p^\text{iso} < 0\,\text{GeV}$.

6.1.1. Matrix Method

The matrix method is a numerical method translating the total number of events measured in the signal and control regions to the fraction of prompt and fake photon events in the signal region via a four-dimensional matrix mapping. It has been used in previous ATLAS diphoton analyses [94, 95]. Photon identification and isolation requirements are combined to define data regions with the following photon composition:

- A $\rightarrow$ Pass tight identification, pass loose isolation

- B $\rightarrow$ Pass tight identification, fail loose isolation

- C $\rightarrow$ Fail tight identification, pass loose isolation

- D $\rightarrow$ Fail tight identification, fail loose isolation

For two photon candidates, the $Z\gamma\gamma$ SR with photons fulfilling the (AA) requirement and 15 fake-enriched data CRs (AB)-(DD) can be defined. The first (second) letter corresponds to the leading (subleading) photon selection. The isolation energy E^iso in

---

[22]A detailed description of the photon isolation is given in Section 4.1 and [67]

Equation 6.1 is adjusted by adding an isolation gap of $E_{\mathrm{G}} = 2\,\mathrm{GeV}$ for photons failing the isolation requirements, i.e. selections (B) and (D): $E_{\mathrm{T}}^{\mathrm{cone20}} - 0.065 \times p_{\mathrm{T}}^{\gamma} > 2\,\mathrm{GeV}$. This reduces the leakage of signal events into the fake-photon enriched regions increasing their purity.

6.1.1.1. Matrix Mapping

The four-dimensional mapping is performed using real (ϵ) and fake photon efficiencies (f) constructing four independent linear equations:

$$
\begin{pmatrix} N_{\mathrm{AA}} \\ N_{\mathrm{AB}} \\ N_{\mathrm{BA}} \\ N_{\mathrm{BB}} \end{pmatrix} = \begin{pmatrix} \epsilon_1\epsilon_2 & \epsilon_1 f_2 & f_1\epsilon_2 & f_1 f_2 \\ \epsilon_1(1-\epsilon_2) & \epsilon1(1-f_2) & f_1(1-\epsilon_2) & f_1(1-f_2) \\ (1-\epsilon_1)\epsilon_2 & (1-\epsilon1)f_2 & (1-f_1)\epsilon_2 & (1-f_1)f_2 \\ (1-\epsilon_1)(1-\epsilon_2) & (1-\epsilon1)(1-f_2) & (1-f_1)(1-\epsilon_2) & (1-f_1)(1-f_2) \end{pmatrix} \begin{pmatrix} N'_{\gamma\gamma} \\ N'_{\gamma j} \\ N'_{j\gamma} \\ N'_{jj} \end{pmatrix} \quad (6.2)
$$

The left side of the linear equations corresponds to the total number of events in data measured in the SR N_{AA} and the CRs N_{AB} to N_{BB}, where photons pass the tight identification but fail the loose isolation. The real photon efficiencies correspond to the probability of prompt photons to pass the loose isolation and are determined using the $Z\gamma\gamma$ signal MC simulation as

$$
\epsilon_1 = \frac{N_{\mathrm{AA}}^{\mathrm{sim}}}{N_{\mathrm{AA}}^{\mathrm{sim}} + N_{\mathrm{BA}}^{\mathrm{sim}}} \quad \text{and} \quad \epsilon_2 = \frac{N_{\mathrm{AA}}^{\mathrm{sim}}}{N_{\mathrm{AA}}^{\mathrm{sim}} + N_{\mathrm{AB}}^{\mathrm{sim}}}, \quad (6.3)
$$

with indices $(1,2)$ indicating the efficiencies for the leading or subleading photon candidate.

Similarly, the fake photon efficiencies correspond to the probability of a fake photon to pass the loose isolation:

$$
f_1 = \frac{N_{\mathrm{CA}}}{N_{\mathrm{CA}} + N_{\mathrm{DA}}} \quad \text{and} \quad f_2 = \frac{N_{\mathrm{AC}}}{N_{\mathrm{AC}} + N_{\mathrm{AD}}}. \quad (6.4)
$$

The data CRs (C) and (D) are used to determine f_1 and f_2, as MC simulation typically underpredicts fake-photon associated probabilities, i.e. rates and efficiencies. The other photon candidate in events with one fake photon, for instance the subleading photon in f_1, needs to fulfil the selection of a prompt photon (A). This is done to replicate the photon composition of $Z\gamma j$ and $Zj\gamma$ events, which are expected to contribute dominantly. Background contributions from prompt photons are subtracted from the observed number of events in all data CRs – this concerns N_{AA} to N_{BB} and the yields for measuring f_1 and f_2. The prompt photon background comprises the processes $t\bar{t}\gamma\gamma$, $Z\,(\to \ell\ell)\,H\,(\to \gamma\gamma)$, $ZZ\,(\to \ell\ell\ell\ell)$, and $WZ\gamma\,(\to \ell\nu\ell\ell\gamma)$; the contributions are listed in Table 6.9. The unknown

event yields $N'_{\gamma\gamma}$ to N'_{jj} are measured by inverting the matrix in Equation 6.2. The first linear equation then yields the desired normalisation of the signal process and events with fake photons in the $Z\gamma\gamma$ SR:

$$N_{\mathrm{AA}} = N_{\gamma\gamma} + N_{\gamma j} + N_{j\gamma} + N_{jj} = \epsilon_1\epsilon_2 N'_{\gamma\gamma} + \epsilon_1 f_2 N'_{\gamma j} + f_1\epsilon_2 N'_{j\gamma} + f_1 f_2 N'_{jj}. \qquad (6.5)$$

The calculated pile-up contribution is subtracted from $N_{\gamma\gamma}$ to obtain the event yield purely attributed to the triple gauge boson production of $Z\gamma\gamma$. The fake photon efficiencies in Equation 6.5 need to be corrected to account for signal leakage and a possible correlation between the isolation and identification requirements.

6.1.1.2. Correction of Photon Efficiencies

Prompt photons have a non-negligible probability to pass the requirements of the fake-enriched CRs. This signal leakage is taken into account via correction factors $c_{\mathrm{XY}}^{\mathrm{sig}}$ determined from the $Z\gamma\gamma$ MC simulation yielding the efficiency of the signal process leaking into data CR XY:

$$c_{\mathrm{XY}}^{\mathrm{sim}} = \frac{N_{\mathrm{XY}}^{\mathrm{sim}}}{N_{\mathrm{AA}}^{\mathrm{sim}}}. \qquad (6.6)$$

Two additional corrections are introduced to include a potential correlation between the isolation and the choice of the photon identification. As mentioned before, the failure of the tight identification while passing the LoosePrime4 WP assesses photon shower shape observables which are chosen due to their small correlation with respect to the photon isolation. This is verified for fake photons through the relations

$$R_1 = \frac{N_{\mathrm{AX}} N_{\mathrm{DX}}}{N_{\mathrm{BX}} N_{\mathrm{CX}}} \quad \text{and} \quad R_2 = \frac{N_{\mathrm{XA}} N_{\mathrm{XD}}}{N_{\mathrm{XB}} N_{\mathrm{XC}}}. \qquad (6.7)$$

The values of R_1 and R_2 are unity without any correlation and deviate from unity if a correlation is observed. The letter 'X' indicates that no requirements are placed on the identification and isolation of the respective photon in order to avoid biasing the correlation determination. The event yields are taken from MC simulation, which was shown to give reliable results in [94–96]. Incorporating the signal leakage and the correlation

Table 6.1.: Determination of correlation parameters in $Zj\gamma$, $Z\gamma j$, and Zjj events. MAD-GRAPH5_AMC@NLO is abbreviated by MG5. The last row contains the combined correlation parameter. The uncertainty corresponds to the statistical uncertainty.

Correlation	$Z\gamma$ + jets (SHERPA)	$Z\gamma$ + jets (MG5)	Z + jets
R_1	0.74 ± 0.23	1.23 ± 0.21	1.62 ± 0.40
R_2	1.22 ± 0.33	1.15 ± 0.16	1.30 ± 0.13
R	0.92 ± 0.19	1.18 ± 0.13	1.44 ± 0.25

parameters leads to the following expression for the fake photon efficiencies:

$$f_1 = \frac{\left(N_{\mathrm{CA}} - c_{\mathrm{CA}}^{\mathrm{sim}} N_{\mathrm{AA}}^{\mathrm{sim}}\right) R_1}{\left(N_{\mathrm{CA}} - c_{\mathrm{CA}}^{\mathrm{sim}} N_{\mathrm{AA}}^{\mathrm{sim}}\right) R_1 + N_{\mathrm{DA}} - c_{\mathrm{DA}}^{\mathrm{sim}} N_{\mathrm{AA}}^{\mathrm{sim}}},$$
$$f_2 = \frac{\left(N_{\mathrm{AC}} - c_{\mathrm{AC}}^{\mathrm{sim}} N_{\mathrm{AA}}^{\mathrm{sim}}\right) R_2}{\left(N_{\mathrm{AC}} - c_{\mathrm{AC}}^{\mathrm{sim}} N_{\mathrm{AA}}^{\mathrm{sim}}\right) R_2 + N_{\mathrm{AD}} - c_{\mathrm{AD}}^{\mathrm{sim}} N_{\mathrm{AA}}^{\mathrm{sim}}}. \tag{6.8}$$

6.1.1.3. Results

The calculation of the real photon efficiencies results in $\epsilon_1 = (94.4 \pm 0.2)\,\%$ and $\epsilon_2 = (90.9 \pm 0.2)\,\%$, where the uncertainty is the statistical uncertainty. The higher-energetic photon has a larger probability to pass the loose isolation, which is an artefact of the photon momentum subtraction in the definition of the isolation requirement.

The correlation parameters are determined in events covering the fake photon compositions $Zj\gamma$, $Z\gamma j$, and Zjj. Three MC event generators are used for this purpose: SHERPA and MADGRAPH5_AMC@NLO $Z\gamma$ + jets samples ($Zj\gamma$ and $Z\gamma j$) and a POWHEG Z + jets sample (Zjj). The usage of the SHERPA and MADGRAPH5_AMC@NLO generators for the $Z\gamma$ + jets process allows to test the impact of the different hadronisation models on the photon isolation applied on generator-level (*Frixione isolation*, see [97]). The photons are fake-matched using truth-information stored in the MC simulation. The results of the correlation determination are summarised in Table 6.1. The correlations R_1 and R_2 agree within statistical uncertainty except for the estimation using the SHERPA simulation where a deviation smaller than 1.5σ is seen. The correlation parameters are then combined for each simulation to increase the statistical precision adding the respective predicted event yields in the numerator and denominator. The average of the three correlations is $R = 1.18 \pm 0.11$ indicating a small dependence of the isolation on the identification requirement.

The fake photon efficiencies are determined using the above mentioned value of R and are $f_1 = (37 \pm 5)\,\%$ and $f_2 = (30 \pm 5)\,\%$. As expected, the efficiency for fake photons to

pass the loose isolation is much smaller than for prompt photons.

The final results for the extraction of prompt and fake photons in full Run 2 data is summarised and compared to the 2D template fit in Section 6.1.3.

6.1.1.4. Statistical Uncertainties

Toy data is generated to calculate the statistical uncertainty on the event yields $N_{\gamma\gamma}$, $N_{\gamma j}$, $N_{j\gamma}$, and N_{jj}. Statistical fluctuations are modelled by Poisson distributions. The number of events in all data regions used in the matrix method are sampled from a Poisson distribution whose mean is equivalent to the nominal observed yield in the respective region. This is done 1000 times and for each replica dataset the matrix method is repeated. The statistical uncertainty is finally extracted from the root-mean-square of the normalisation distributions.

6.1.1.5. Systematic Uncertainties

The following sources of systematic uncertainty are studied:

- Definition of the isolation gap

- Real photon efficiencies

- Correlation parameters

- Dependence on shower shape observables

- Limited MC simulation statistics

The effect of each uncertainty is stated with respect to the variation of the total fake photon background N_{fakes}. This is chosen as the quantity N_{fakes} is used in the subtraction of data to obtain the cross sections.

Definition of the Isolation Gap

A systematic uncertainty is assigned for the choice of the isolation gap. The width of the isolation gap is reduced in two steps to $1\,\text{GeV}$ and $0\,\text{GeV}$, the latter corresponding to the nominal isolation definition. The largest variation to the nominally measured prompt and fake photon event yield is chosen. This results in a shift of 11% for the total fake photon background normalisation.

Table 6.2.: Comparison of the inclusive prompt photon efficiency with the efficiency evolution over three p_T^γ bins for the NLO SHERPA and MADGRAPH5_AMC@NLO (MG5) simulation. The bin range is given in GeV. The uncertainties corresponds to the statistical uncertainty.

Efficiency	Inclusive	$20 < p_T^{\gamma 1} < 50$	$50 < p_T^{\gamma 1} < 80$	$p_T^{\gamma 1} > 80$
ϵ_1 [%] (SHERPA NLO)	94.4 ± 0.2	92.3 ± 0.3	95.2 ± 0.3	96.4 ± 0.1
ϵ_1 [%] (MG5 NLO)	94.6 ± 0.2	92.0 ± 0.3	95.4 ± 0.3	97.0 ± 0.2
Efficiency	Inclusive	$20 < p_T^{\gamma 2} < 40$	$40 < p_T^{\gamma 2} < 60$	$p_T^{\gamma 2} > 60$
ϵ_2 [%] (SHERPA NLO)	90.9 ± 0.2	89.6 ± 0.2	93.9 ± 0.3	95.1 ± 0.2
ϵ_2 [%] (MG5 NLO)	90.9 ± 0.2	89.2 ± 0.3	93.9 ± 0.4	96.3 ± 0.4

Real Photon Efficiencies

The real photon efficiencies ϵ_1 and ϵ_2 are calculated inclusively and applied to photons of any transverse momentum. The p_T dependence of the efficiency is investigated and summarised in Table 6.2. The inclusive efficiencies are in excellent agreement across both MC simulations. A 3% p_T dependence is seen for ϵ_1 and 4% for ϵ_2. The nominal (inclusive) efficiencies are shifted by these uncertainties and the average of the $\pm 1\sigma$ variations is calculated for ϵ_1 and ϵ_2 and subsequently added in quadrature. The systematic uncertainty accounts for a 8% variation of the total fake photon background normalisation. This uncertainty also covers the slightly different p_T dependence between both MC event generators.

Correlation Parameters

The combined correlation parameter is $R = 1.18 \pm 0.11$. The uncertainty is increased to cover the case where no correlation is observed: $R = 1.18 \pm 0.18$. The correlation parameter is varied by $\pm 1\sigma$ of its uncertainty for each fake efficiency and the matrix method is repeated. The average normalisation variation of each process is determined and the shifts for f_1 and f_2 are added in quadrature. A 10% variation is observed for the normalisation of the total fake photon background.

Dependence on Shower Shape Observables

The baseline identification selection for fake photons is the LoosePrime4 WP. It is investigated how strongly the fake photon efficiencies depend on the photon shower shape observables. The *LoosePrime3* WP adds an additional condition to the shower shape enhancing the similarity to the tight identification. This results in a strong reduction of statistics in the fake-enriched CRs and increases statistical fluctuations influencing the

63

estimation of the systematic uncertainty. The *LoosePrime5* WP is tested instead, which additionally allows fake photons to fail a condition related to the total lateral shower width $w_{s\,\mathrm{tot}}$. The total fake photon background varies by 3%.

Limited MC Simulation Statistics

The predicted event yield by MC simulation is known within a certain statistical uncertainty due to the finite number of generated events. This uncertainty is propagated to the real and fake photon efficiencies as well as to the signal leakage corrections. The overall effect is small; the fake photon background shifts by 1%.

Summary of Systematic Uncertainties

The systematic uncertainties which affect the normalisation of the total fake photon background in the matrix method are summarised in Table 6.3. The dominant systematic uncertainty of 11% is connected to the choice of the isolation gap. The isolation gap has a large impact as it affects the data events yields measured in regions (AB) to (BB) as well as the real and fake photon efficiencies.

Table 6.3.: Summary of systematic uncertainties in the determination of fake photons in the matrix method.

Source of uncertainty	Variation of N_{fakes} [%]
Isolation gap	11
Real photon efficiencies	8
Correlation parameter	10
Shower shape observables	3
MC statistics	1

6.1.2. 2D Template Fit

The 2D template fit provides a complementary approach for the determination of events with fake photons in data. It is inspired by previous ATLAS analyses [98, 99] and is implemented from scratch within *RooFit* [100] and further developed in this thesis. The 2D template fit exploits differences in the shape of the isolation energy distribution of prompt and fake photons. The isolation energy E^{iso} is introduced in Equation 6.1 and is the observable which allows to distinguish prompt from fake photons in the 2D template fit. Prompt photons are surrounded by only minimal hadronic activity, whereas fake photons are expected to have large quantities of isolation energy from the jet remnant.

Similarly to the matrix method, the full event selection is applied except for the photon identification and isolation. The photon identification is used to define a signal-like region[23] containing prompt photons and control regions enriched in fake photons:

- γ_1 and γ_2 pass the tight identification (TT)

- γ_1 passes the tight identification, γ_2 fails the tight identification (TF)

- γ_1 fails the tight identification, γ_2 passes the tight identification (FT)

- γ_1 and γ_2 fail the tight identification (FF)

The signal-like region is selected by requiring TT photons and is the region the 2D template fit is performed in. Control regions enriched in fake photons are obtained by imposing the TF, FT, and FF criteria and are used for the validation and extraction of E^{iso} fake photon templates. As shown in Equation 6.1, the loose isolation requirement imposes a selection on the track isolation: $p^{\text{iso}} < 0\,\text{GeV}$. The isolation energy E^{iso} provides sufficient separation power between prompt and fake photons. For this reason, all events considered in the 2D template fit must contain photons fulfilling the track isolation condition, which reduces the complexity of the method.

6.1.2.1. Definition of the 2D Isolation Energy

The 2D template fit is as a binned maximum likelihood fit of E^{iso} templates to the observed two-dimensional isolation energy I in data:

$$I = N_{\gamma\gamma}T_{\gamma\gamma} + N_{\gamma j}T_{\gamma j} + N_{j\gamma}T_{j\gamma} + N_{jj}T_{jj}. \tag{6.9}$$

The templates T_{xy} are probability density functions (PDFs) of the isolation energy which are fitted to I in the signal region. In this fit, the number of events with two real photons $N_{\gamma\gamma}$, i.e. the signal process, and fake photons $N_{\gamma j}$, $N_{j\gamma}$, and N_{jj} are extracted. A simplified example for such a fit is depicted in Figure 6.1. The shape of the isolation energy for prompt and fake photons is clearly distinguishable, particularly in the transition area between the peak and the tails of the isolation energy.

The two-dimensional isolation energy presented in Equation 6.9 can be simplified by splitting the two-dimensional PDFs T_{xy} into two 1D templates. This is a valid operation if the correlation between the leading and subleading isolation energy can be neglected. For events with at most one fake photon candidate, i.e. requirements TT, TF, and FT,

---

[23]No isolation requirement is imposed at this stage.
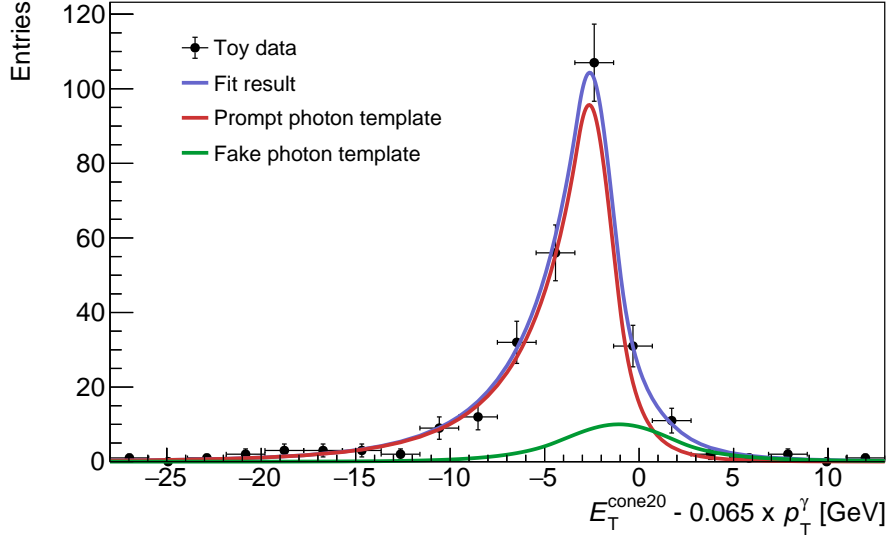
Figure 6.1.: Illustration of the 2D template fit. Isolation energy templates of prompt and fake photons are fitted to toy data in a binned maximum likelihood estimation. The normalisation of the prompt (red) and fake (green) photon E^{iso} template is allowed to float in the fit; the shape of each template is fixed. The number of generated events corresponds to the Run 2 expectation of $Z\gamma\gamma$ events plus the total predicted number of events containing fake photons.

it is validated that this correlation is at most 4% (using the *Pearson correlation coefficient* [101]). For events with two fake photons (FF), the colour connection between the jets from which the non-prompt photon candidate arises leads to a non-negligible correlation; a correlated two-dimensional template is extracted instead. This results in the following expression for the total isolation energy measured in data:

$$I = N_{\gamma\gamma}T_{\gamma_1}T_{\gamma_2} + N_{\gamma j}T_{\gamma_1}T_{j_2} + N_{j\gamma}T_{j_1}T_{\gamma_2} + N_{jj}T_{jj}. \tag{6.10}$$

6.1.2.2. Extraction of Isolation Energy Templates

Dedicated fitting functions are used to extract the probability density of the isolation energy. The core of the isolation energy is modelled with Gaussian distributions, to which two independent tails can be multiplied to account for E^{iso} asymmetries:

- The isolation energy of prompt photons (γ_1 and γ_2 in TT, γ_1 in TF, γ_2 in FT) is fitted with a *Double Sided Crystal-Ball* [102] (DSCB) PDF where two power-laws in the tails of the probability density are stitched together via a Gaussian core

- The isolation energy of events with exactly one fake photon (γ_2 in TF, γ_1 in FT) is fitted with a *Bukin* [103] PDF. It combines the features of a Gaussian core and two

asymmetric tails modelled via exponential functions. These exponential functions give more flexibility to describe the E^{iso} probability density for significant amounts of hadronic activity but are more susceptible to statistical fluctuations

- The 2D isolation energy of events containing two fake photons (γ_1 and γ_2 in FF) is extracted using an *adaptive kernel estimation* [104]. This is done due to the limited number of Zjj events, for which reason a smoothing procedure is chosen. The isolation energy is modelled by a superposition of Gaussian kernels whose width is dynamically adapted according to the distribution of events: narrow Gaussian width for E^{iso} regions of large event density and vice versa. A smooth PDF emerges for which the correlation between the leading and subleading photon isolation energy is considered

The PDFs of the isolation energy for events containing at most one fake photon are extracted from fake-enriched control regions in MC simulation. This brings the advantage of much higher statistics in MC simulation with respect to data; the $Z\gamma + \mathrm{jets}$ simulation has ten times more events than observed in data. This is beneficial for the reduction of systematic uncertainties associated to the extraction of the isolation energy templates (see Section 6.1.2.5). The E^{iso} templates are validated in Appendix C.1. It is shown that the templates extracted from MC simulation adequately describe the isolation energy distribution observed in data control regions.

Two exemplary fit results yielding the PDFs of a prompt and fake photon are shown in Figure 6.2. The E^{iso} distribution of prompt photons is shifted towards negative values as the photon energy is much larger than the energy in the cone surrounding the photon. The contrary case is observed for fake photons, where the hadronic activity is substantial leading to a tail at positive E^{iso} values. Both functional forms (DSCB and Bukin) describe the modelled isolation energy well. The kernel estimation for events with two fake photons is carried out in a data control region where the photon candidates need to pass the FF identification requirement. The estimation is performed in data as the $Z + \mathrm{jets}$ MC simulation lacks statistics. The resulting, smooth 2D PDF is shown in Figure 6.3.

6.1.2.3. Fit Procedure

The observed 2D isolation energy in data has contributions from events containing the signal process, fake photons, the prompt photon background and pile-up. The isolation energy profile of pile-up events resembles that of the signal process within the shape uncertainty introduced in Section 6.1.2.5. Once the 2D template fit is performed and
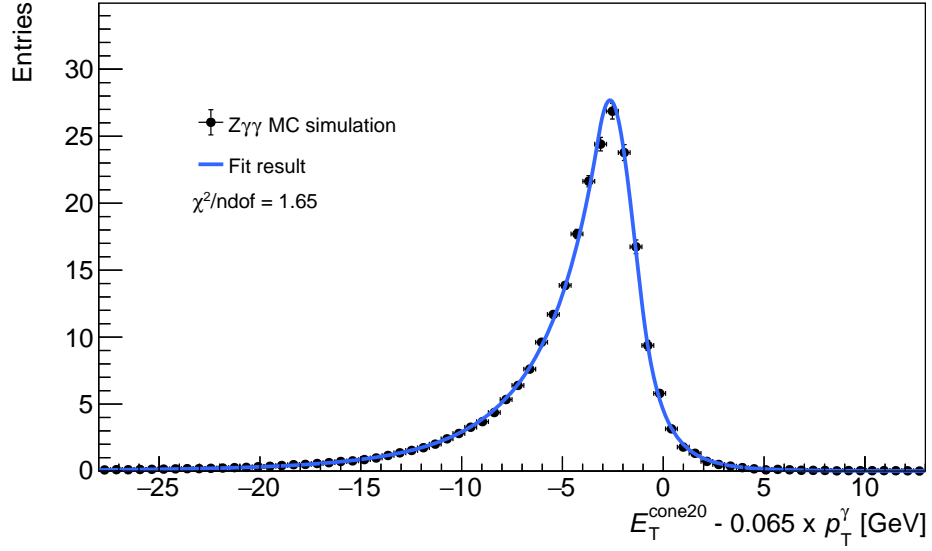
(a)
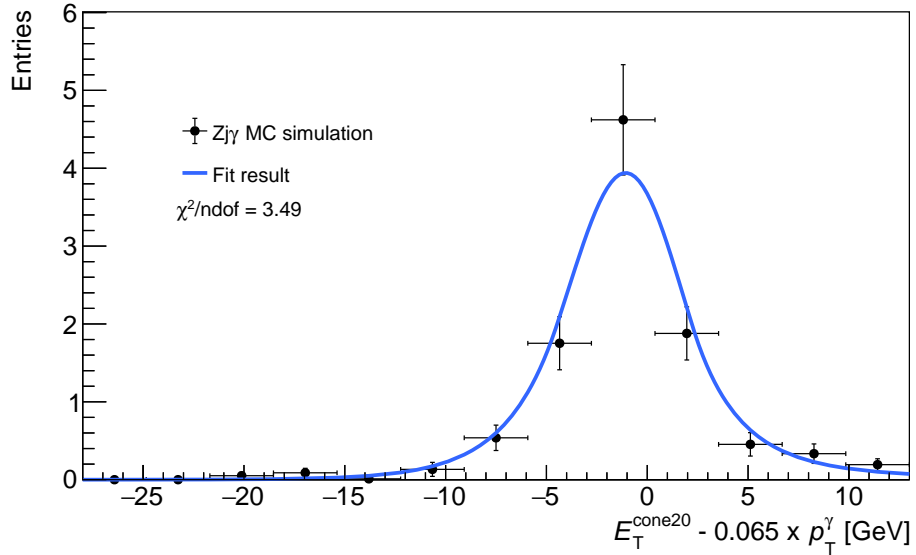
(b)

Figure 6.2.: E^{iso} template extraction for (a) a prompt photon of the $Z\gamma\gamma$ MC simulation and (b) a fake photon of the $Z\gamma$ + jets MC simulation. Significant differences in the E^{iso} shapes are observed, which is the feature exploited in the 2D template fit. The normalisation of the distributions is scaled to match the amount of expected $Z\gamma\gamma$ and $Z\gamma$ + jets events in Run 2. The reduced χ^2 value, i.e. normalised to the degrees of freedom ndof, is depicted as well and is reasonably close to unity in (a). A single bin with large MC event generator weights causes a worse reduced χ^2 value in (b).

the signal yield is extracted, the expected pile-up contribution is subtracted from the $Z\gamma\gamma$ normalisation. The prompt photon background consisting of $t\bar{t}\gamma\gamma$, $ZZ\,(\to \ell\ell\ell\ell)$,
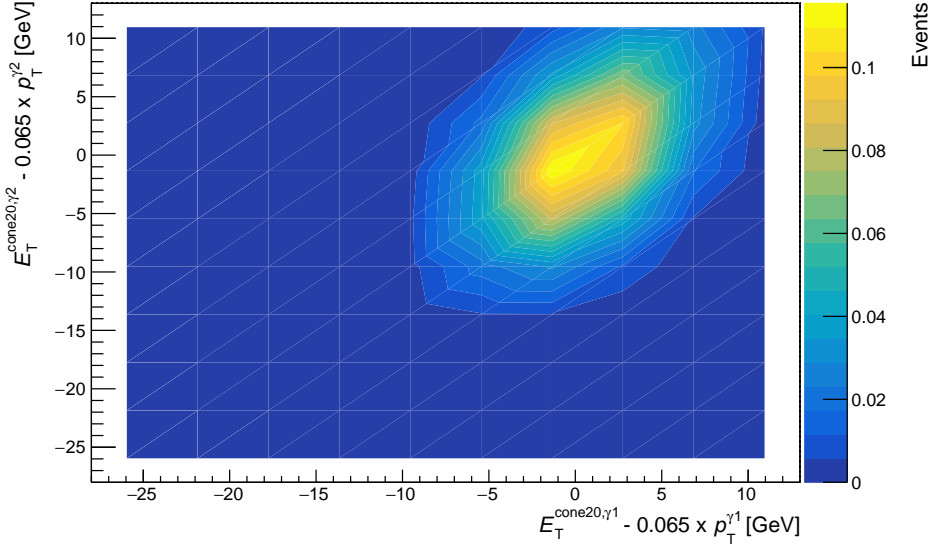
Figure 6.3.: Result of the adaptive kernel estimation performed in a FF data control region, depicted as a correlation of the E^{iso} distribution of both fake photons. Despite a limited amount of events, the adaptive kernel estimation is able to provide a smooth E^{iso} distribution which accounts for the correlation of the photon isolation energy.

$Z(\to \ell\ell)\,H(\to \gamma\gamma)$, and $WZ\gamma(\to \ell\nu\ell\ell\gamma)$ processes (see Section 6.6 for a list of their contributions) is bin-wise subtracted from the observed 2D isolation energy in data before the 2D template fit is performed.

The PDFs derived through the procedure described in Section 6.1.2.2 are used to fit the corrected (prompt-photon background subtracted) isolation energy in data following Equation 6.10. The floating parameters in the fit are the number of events containing prompt and fake photons: $N_{\gamma\gamma}$, $N_{\gamma j}$, $N_{j\gamma}$, and N_{jj}. They are constrained to be non-negative. The shape of the PDFs is fixed. The likelihood estimation is performed in the range from -28 to $13\,\mathrm{GeV}$ to incorporate the isolation energy profile of all events seen in data. The fit result is presented in Figure 6.4 and the numeric results are listed in Table 6.6 in the next section. The sum of all E^{iso} templates describes the observed isolation energy distribution well; the reduced χ^2 value is close to unity.

In a final step, a correction is applied to the extracted yields. This allows to obtain the number of events with signal and fake photons passing all requirements of the $Z\gamma\gamma$ SR. It is also necessary to compare the results of the 2D template fit with the matrix method. The loose isolation working point requires $E_{\mathrm{T}}^{\mathrm{cone20}} - 0.065 \times p_{\mathrm{T}}^{\gamma} < 0\,\mathrm{GeV}$. Integrating over all two-dimensional PDFs T_{xy} from $-\infty$ to zero yields correction factors $f_{xy} < 1$,

which are multiplied to the fitted event yields:

$$N_{xy}^{\text{corr}} = N_{xy} \times f_{xy} = N_{xy} \times \int\limits_{-\infty}^{0} T_{xy} \, \mathrm{d}E^{\text{iso}}. \tag{6.11}$$
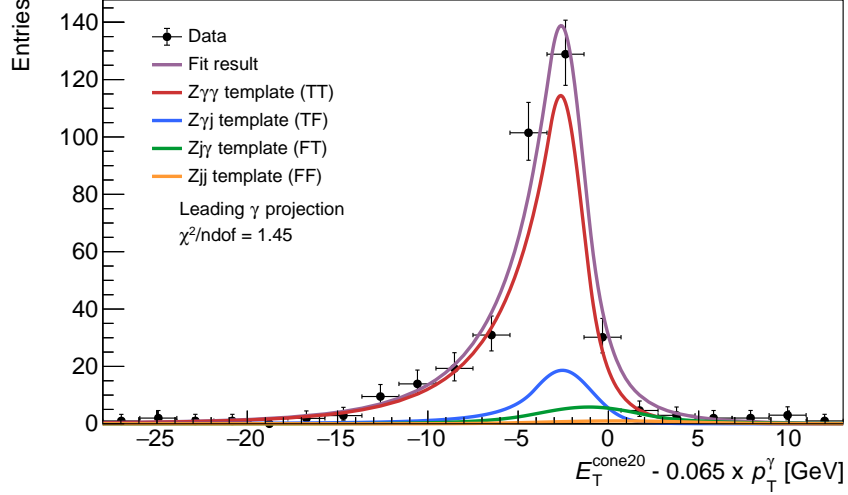
(a)
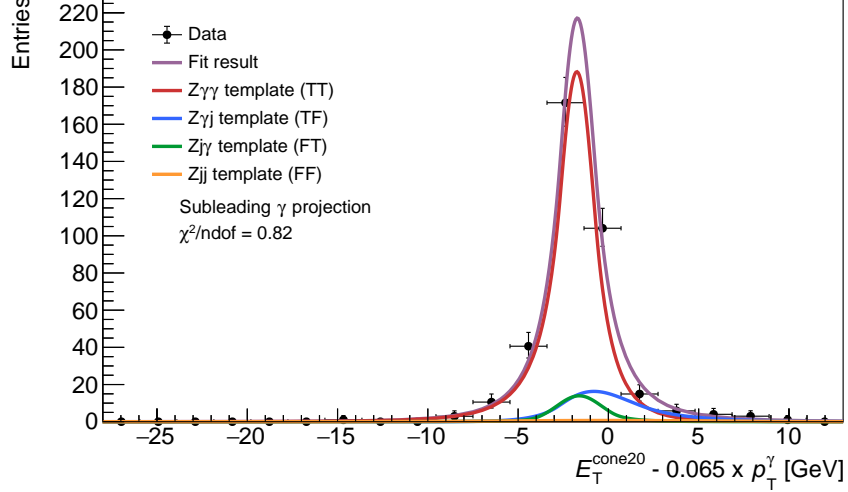
(b)

Figure 6.4.: Fit of the E^{iso} templates to the full Run 2 dataset as a projection on (a) the leading photon and (b) the subleading photon. The shapes of all PDFs are fixed and the floating parameters are the event yields for each process: $N_{\gamma\gamma}$, $N_{\gamma j}$, $N_{j\gamma}$, and N_{jj}. The coloured templates (red to orange) give the breakdown of the fit result (magenta). The reduced χ^2 value, i.e. normalised to the degrees of freedom ndof, is depicted as well and is reasonably close to unity.

6.1.2.4. Statistical Uncertainties

The statistical uncertainty on the extracted event yields is estimated by generating toy data. A Poisson distribution is sampled taking into account the probability density of the post-fit isolation energy (magenta distribution in Figure 6.4). For each bin in data, the probability density is assessed and multiplied by the total number of fitted events. The mean of the Poisson distribution is set to this number and toy data is generated in all bins. In total, 1000 replica datasets are generated and the maximum likelihood estimation is repeated for each set individually. The statistical uncertainty is taken as the root-mean-square of the resulting normalisation distributions of $N_{\gamma\gamma}$, $N_{\gamma j}$, $N_{j\gamma}$, and N_{jj} from all fits.

6.1.2.5. Systematic Uncertainties

Systematic uncertainties are all related to variations of the isolation energy shape. The following sources of uncertainty are investigated:

- Signal leakage into FF data CR

- Dependence on shower shape observables

- Effect of statistical precision on PDF extraction

- Isolation energy correlation for $Z\gamma\gamma$ and $Z\gamma + \text{jets}$

For each of the sources, 1000 sets of toy data are sampled from a Poisson distribution. This increases the statistical significance of the impact of systematic uncertainties. The toy data is generated similar to the procedure introduced for the statistical uncertainty and the shifted templates for each systematic uncertainty are fitted to it (with the exception of the signal leakage uncertainty, for which a numerical corrections is performed). The mean of the resulting normalisation distributions of $N_{\gamma\gamma}$, $N_{\gamma j}$, $N_{j\gamma}$, and N_{jj} is compared to the nominal fit result to Run 2 data to derive the magnitude of the uncertainty. The variation of the total fake photon background N_{fakes} is stated for each source, as this quantity is used in the subtraction of data to obtain the cross sections.

Signal Leakage into FF Data CR

The data control region with two fake photons in which the two-dimensional E^{iso} PDF is extracted contains a small contamination of prompt, real photons passing the FF selection. This can alter the extracted isolation energy shape, which affects the fitted

event yields in the SR: N_{jj} becomes larger, whereas $N_{\gamma\gamma}$, $N_{\gamma j}$, $N_{j\gamma}$ are artificially reduced. A numeric correction of the fitted event yields is performed; its derivation is presented in Appendix C.3. The signal leakage shifts the normalisation of the total fake photon background by 3.8%.

Dependence on Shower Shape Observables

The dependence of the isolation energy PDFs on photon shower shape observables is tested. The LoosePrime3 identification reduces the statistics of the $Z\gamma + $ jets MC simulation and especially that of the data control region FF making it impossible to obtain E^{iso} templates. New E^{iso} PDFs are instead extracted for photons passing the LoosePrime5 WP. A systematic uncertainty of 9.4% is assigned to the normalisation of the fake photon background. The magnitude of this uncertainty is roughly three times larger than the corresponding uncertainty in the matrix method. The 2D template fit is performed differentially and therefore sensitive to small variations of the isolation energy distribution. It is also more susceptible to statistical fluctuations. This results in a larger uncertainty compared to the matrix method, which is performed inclusively.

Effect of Statistical Precision on PDF Extraction

The phase-space regions in which the E^{iso} templates are extracted contain a finite number of events. The statistical precision is assessed by considering the uncertainty on the fit parameters of the DSCB and Bukin PDFs. For each PDF, the value of one fit parameter at a time is shifted by $\pm 1\sigma$ of its nominal value. This creates an alternative set of PDFs which are re-fitted to the Run 2 dataset. For each PDF, the variation with the largest deviation to the nominal event yield is taken as a systematic uncertainty. This means that the signal normalisation $N_{\gamma\gamma}$ and the normalisation of all other processes containing fake photons are susceptible to six additional sources of uncertainty – four shifted DSCB templates and two shifted Bukin templates.

An alternative approach is chosen for the $Z + $ jets process. A parameter called *bandwidth* is used to smooth the shape of the Gaussian kernels [104]. The bandwidth can be scaled to make the kernel more robust against individual statistical fluctuations of the input dataset. To assess the statistical precision of the data CR where the kernel estimation is performed, a conservative shift of the scale by $\pm 25\%$ of its nominal value is applied. The variation with the stronger magnitude is chosen to define a symmetric uncertainty band.

The magnitude of the PDF variations on the total fake photon normalisation is pre-

Table 6.4.: Shift of the total fake photon normalisation N_{fakes} by varying the floating parameters of the DSCB and Bukin PDFs by $\pm 1\sigma$ in the extraction of the E^{iso} templates of $Z\gamma\gamma$, $Z\gamma j$, and $Zj\gamma$. Only one parameter at a time is shifted, the remaining parameters are fixed to their nominal value. The scale variation in the kernel estimation is shown as well.

Process	N_{fakes} variation	N_{fakes} variation
$Z\gamma\gamma$	$\gamma_1\,(\text{real}) \to 8.4\%$	$\gamma_2\,(\text{real}) \to 6.0\%$
$Z\gamma j$	$\gamma_1\,(\text{real}) \to 6.6\%$	$\gamma_2\,(\text{fake}) \to 20.1\%$
$Zj\gamma$	$\gamma_1\,(\text{fake}) \to 13.3\%$	$\gamma_2\,(\text{real}) \to 5.4\%$
Zjj	$\gamma_1\,(\text{fake})\,\gamma_2\,(\text{fake}) \to 5.5\%$	

sented in Table 6.4. N_{fakes} varies most when the parameters of the Bukin function are shifted in the extraction of fake photon E^{iso} templates. The effect of the scale variation in the kernel estimation is shown as well. A total systematic uncertainty of 28.1% is assigned to the fake background yield – the dominant contribution of 27.6% stems from the $\pm 1\sigma$ variations of the fit parameters.

Isolation Energy Correlation for $Z\gamma\gamma$, $Z\gamma j$, and $Zj\gamma$

The isolation energy templates for processes with at most one fake photon are derived independently for the leading and subleading photon. This is valid if the correlation of the calorimeter isolation energy $E_{\text{T}}^{\text{cone20}}$ is small (a correlation is expected for event topologies with two fake photons, where the jet remnants are colour-connected). For events passing the TT and TF requirements, the correlation is at most 0.2%. For the FT CR a small correlation of 4% is observed. It is validated whether this correlation influences the extracted normalisation in the 2D template fit. Instead of propagating two one-dimensional E^{iso} templates through the fit, a two-dimensional template is extracted. Similarly to what is done for events with two fake photons (FF CR), an adaptive kernel is estimated that takes the isolation energy correlation into account. The normalisation of $N_{\gamma\gamma}$, $N_{\gamma j}$, $N_{j\gamma}$, and N_{jj} shifts by at most 0.1%. This source of uncertainty is therefore neglected.

Summary of Systematic Uncertainties

All systematic uncertainties affecting the normalisation of the total fake photon background in the 2D template fit are summarised in Table 6.5. The by far largest variation stems from the uncertainty in the functional form of the fit functions which are used to extract the E^{iso} templates. Varying the isolation energy PDFs, especially in the regions of

the isolation energy distribution with large separation power between prompt and fake photons, leads to a strong shift of the total fake photon background normalisation.

Table 6.5.: Summary of systematic uncertainties in the determination of fake photons in the 2D template fit. The uncertainty due to the correlation of the isolation energy in TT, TF, and FT events is negligible.

Source of uncertainty	Variation of N_{fakes} [%]
Signal leakage	4
Shower shape observables	9
Statistical precision in PDF extraction	28
Isolation energy correlation	–

6.1.3. Comparison of Fake Photon Methods

The results of the matrix method and the 2D template fit are displayed in Table 6.6. The 2D template fit predicts a slightly larger number of signal events $N_{\gamma\gamma}$ and therefore a smaller total background yield N_{fakes}. The number of measured $Z\gamma\gamma$ events, which is used to calculate the cross sections, is determined by subtracting N_{fakes} from data. The fake photon method providing the total number of fake photons with the smallest relative uncertainty is therefore preferred. The combined uncertainty on N_{fakes} is 26.5% (40.2%) for the matrix method (2D template fit). The matrix method is thus used nominally to predict the number of fake photons in the $Z\gamma\gamma$ analysis and the 2D template fit serves as a validation of the results of the primary method. The compatibility of N_{fakes} between both methods is within 1.2σ under the assumption that the statistical and systematic uncertainties between both methods are largely uncorrelated. The by far most dominant source of systematic uncertainty in the 2D template fit stems from the statistical precision in the determination of the fake photon templates. For the $Z\gamma$ + jets process, the templates are derived from the MADGRAPH5_AMC@NLO MC simulation. The same sample is used in the matrix method to obtain one of the three correlation parameters that serve as input to calculate the combined correlation (see Table 6.1). The uncertainty on the combined correlation parameter is dominated by uncertainties in the prediction of the SHERPA and POWHEG generators. Additionally, the variation of the correlation accounts for only one of five systematic uncertainties considered in the matrix method; its contribution to the total uncertainty is below 20%. In the matrix method and 2D template fit, the dependence on photon shower shape observables is tested by requiring the LoosePrime5 identification. The associated systematic uncertainty is very small in both methods compared to the total uncertainty. To test the correlation of the statistical uncertainty, a *bootstrap* technique [105] is deployed. This method provides replica datasets,

Table 6.6.: Comparison of the determination of prompt and fake photons in Run 2 data between the matrix method and the 2D template fit. N_{fakes} is formed from the normalisation of $N_{\gamma j}$, $N_{j\gamma}$, and N_{jj}, and thus contains information on the correlation between the three processes when measuring systematic uncertainties.

	Matrix method	2D template fit
$Z\gamma\gamma$ event yield	$225.9 \pm 21.9 \, (\text{stat.}) \pm 11.8 \, (\text{sys.})$	$239.3 \pm 20.4 \, (\text{stat.}) \pm 19.9 \, (\text{sys.})$
$Z\gamma j$ event yield	$26.2 \pm 8.5 \, (\text{stat.}) \pm 8.3 \, (\text{sys.})$	$22.9 \pm 8.0 \, (\text{stat.}) \pm 8.4 \, (\text{sys.})$
$Zj\gamma$ event yield	$29.0 \pm 9.8 \, (\text{stat.}) \pm 7.4 \, (\text{sys.})$	$12.5 \pm 6.8 \, (\text{stat.}) \pm 5.5 \, (\text{sys.})$
Zjj event yield	$9.0 \pm 3.6 \, (\text{stat.}) \pm 2.9 \, (\text{sys.})$	$1.4 \pm 1.3 \, (\text{stat.}) \pm 0.4 \, (\text{sys.})$
Total fakes N_{fakes}	$64.2 \pm 12.3 \, (\text{stat.}) \pm 11.8 \, (\text{sys.})$	$36.8 \pm 9.9 \, (\text{stat.}) \pm 11.0 \, (\text{sys.})$

where each nominal event is reweighted by a weight sampled from a Poisson distribution with a mean of unity[24]. 1000 replica datasets are propagated through both fake photon methods allowing to determine the correlation of N_{fakes}, which is 15%. This is due to the fact that both methods explore only partially overlapping regions. The regions (AB) to (BB) in the matrix method, for instance, require at least one photon to fail the isolation condition. The 2D template fit is performed in the TT data region, which contains photons passing at least one of two requirements of the loose isolation ($p^{\text{iso}} < 0 \, \text{GeV}$). Treating the uncertainties largely uncorrelated between both methods should thus give a good approximation.

The number of fake photons events is determined for the combined electron and muon channel. To obtain the per-channel contribution, the number of $Z\gamma\gamma$ signal events and of each fake photon process including N_{fakes} is scaled by the fraction of events in data containing $Z(\to ee)$ (46.4%) and $Z(\to \mu\mu)$ (53.6%) decays.

6.1.4. Fake Photon Modelling

The matrix method and the 2D template fit both measure the fake photon contamination inclusively. The statistical precision is insufficient to measure the number of fake photon events for the observables of interest differentially in each bin. The fake photon shape is therefore estimated using MC simulation and the total normalisation is taken from the matrix method. Ideally, the shape would be extracted directly in the $Z\gamma\gamma$ SR. The statistical precision in this region is, however, very limited; for the $Z + \text{jets}$ simulation only two events pass the requirements of the SR. A slightly looser selection is therefore implemented, where up to one of the photon identification and isolation cuts are allowed

---

[24]This means that the probability of assigning, for instance, a weight of zero occurs with a probability of 36.8% [105].
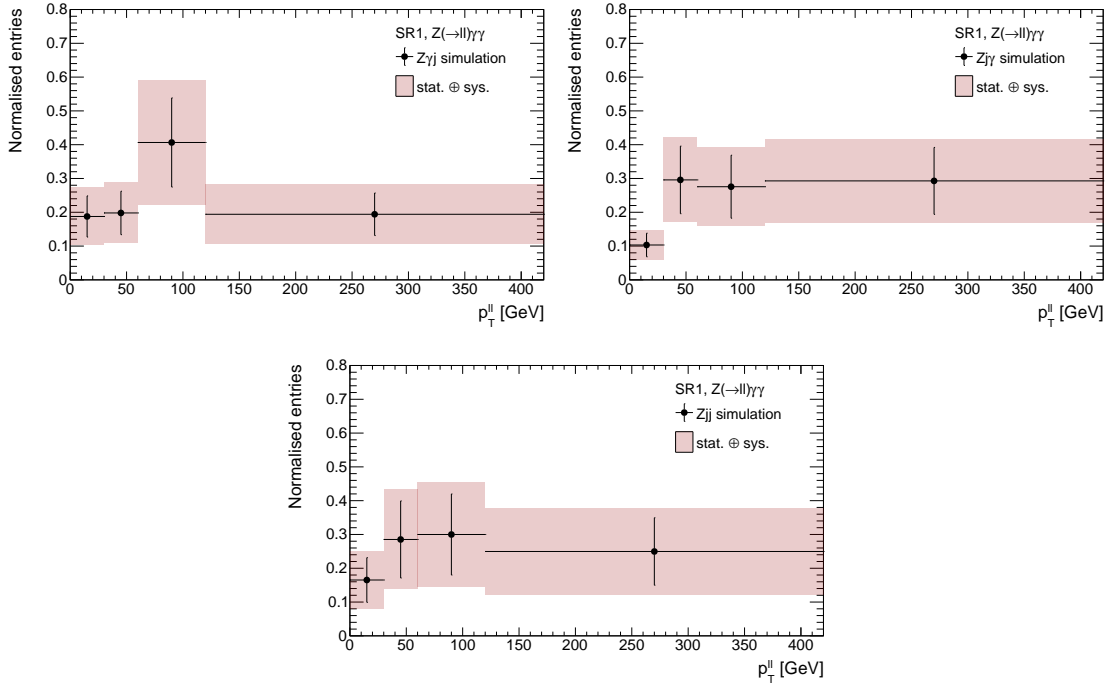
Figure 6.5.: Modelling of $p_T^{\ell\ell}$ from MC simulation in SR1 for (a) $Z\gamma j$, (b) $Zj\gamma$, and (c) Zjj events. The vertical error bars correspond to the statistical uncertainty, while the red bands correspond to the quadratic sum of the statistical and systematic uncertainty. The magnitude of both sources of uncertainty is taken from the matrix method results in Table 6.6.

to be failed. While this region, abbreviated as *SR1* in the following, is still close to the $Z\gamma\gamma$ SR in terms of the requirements, the statistics are improved to enable the extraction of the fake photon modelling[25]. Examples for the fake photon modelling in SR1 are shown in Figure 6.5 for $p_T^{\ell\ell}$ and Figure 6.6 for $m_{\ell\ell\gamma\gamma}$.

6.1.4.1. Systematic Uncertainties

The ability of the $Z\gamma$ + jets and Z + jets MC simulation to describe the kinematics of events containing fake photons is tested in a fake-enriched CR in data denoted by *CR1*. A systematic uncertainty is assigned to account for shape differences between the predicted distributions and those measured in data. The region CR1 is defined by requiring that at least two of the photon identification and isolation requirements that are nominally applied in the $Z\gamma\gamma$ SR are failed. $Z\gamma j$, $Zj\gamma$, and especially Zjj events contribute to CR1; a potential leakage of signal events is estimated with the $Z\gamma\gamma$ simulation and subtracted

---

[25] 22 events pass the SR1 requirements for the Z + jets simulation.
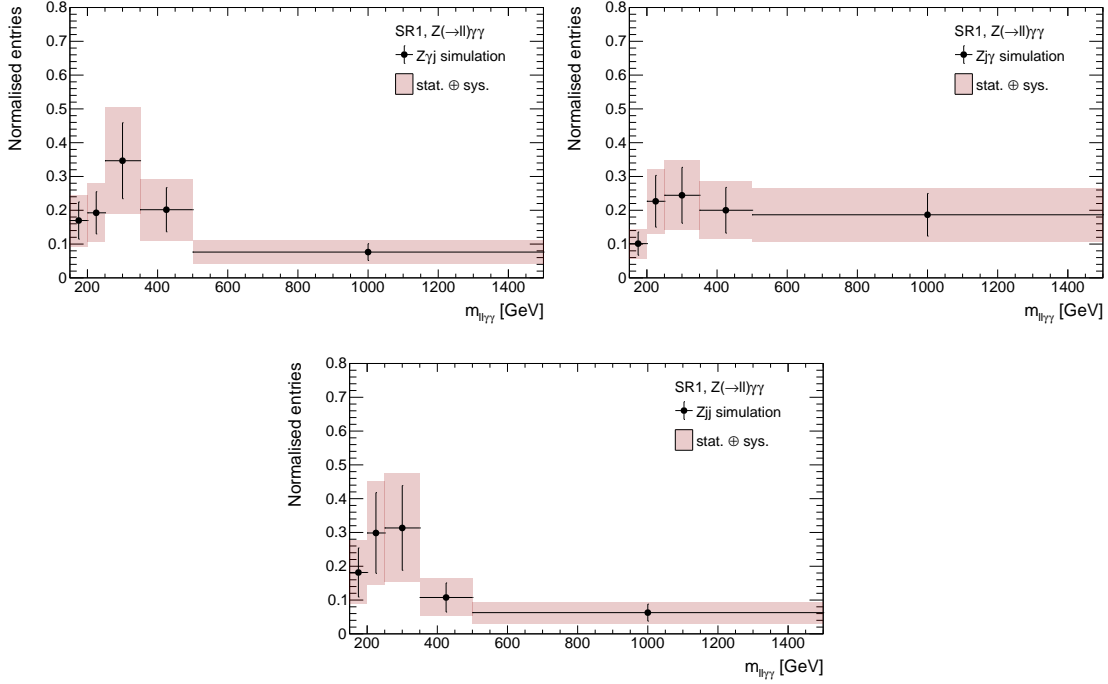
Figure 6.6.: Modelling of $m_{\ell\ell\gamma\gamma}$ from MC simulation in SR1 for (a) $Z\gamma j$, (b) $Zj\gamma$, and (c) Zjj events. The vertical error bars correspond to the statistical uncertainty, while the red bands correspond to the quadratic sum of the statistical and systematic uncertainty. The magnitude of both sources of uncertainty is taken from the matrix method results in Table 6.6.

from the observed data event yield. The MC simulation is not able to accurately predict the relative fraction of fake photon events. Adding the predicted distributions and event yields of the $Z\gamma + \text{jets}$ and $Z + \text{jets}$ simulations thus results in distortions of the shape and the fraction of events stemming from a specific fake photon source. A data-driven correction is applied using CRs enriched in one fake photon component. The regions are formed by imposing the set of requirements (AD) (see Section 6.1.1) enriching $Z\gamma j$ events, (DA) enriching $Zj\gamma$ events, and (DD) which enriches events with two fake photons, Zjj. The largest normalisation shift is expected to be seen for the latter case of events where both photons are fakes. Corrections to the relative fractions of fake photon events are calculated via the following linear equations:

$$N_{\text{AD}} - N_{\text{AD}}^{Z\gamma\gamma} = f_{\gamma j} N_{\text{AD}}^{Z\gamma j} + f_{jj} N_{\text{AD}}^{Zjj}, \tag{6.12}$$

$$N_{\text{DA}} - N_{\text{DA}}^{Z\gamma\gamma} = f_{j\gamma} N_{\text{DA}}^{Zj\gamma} + f_{jj} N_{\text{DA}}^{Zjj}, \tag{6.13}$$

$$N_{\text{DD}} - N_{\text{DD}}^{Z\gamma\gamma} = f_{\gamma j} N_{\text{DD}}^{Z\gamma j} + f_{j\gamma} N_{\text{DD}}^{Zj\gamma} + f_{jj} N_{jj}^{Zjj}, \tag{6.14}$$

with the signal leakage $N_{XY}^{Z\gamma\gamma}$ into region XY. Equations 6.12 and 6.13 assume that the predicted number of $Zj\gamma$ events in region (AD) and the predicted number of $Z\gamma j$ events in region (DA) are negligible as the prompt photons need to fail the identification and isolation requirements, whereas the fake photons need to fulfil both of these requirements. The correction factors for the predicted fake photon contributions are $f_{\gamma j} = 2.0$, $f_{j\gamma} = 1.4$, and $f_{jj} = 9.4$. The contributions of $Z\gamma j$, $Zj\gamma$, and Zjj events in CR1 are scaled by the correction factors and the total fake photon modelling is compared to data. This comparison is presented in Figure 6.7 for the observables $p_{\mathrm{T}}^{\ell\ell\gamma\gamma}$ and $m_{\ell\ell\gamma\gamma}$. The remaining observables are presented in Appendix D, which also contains a description of the reweighting performed for $p_{\mathrm{T}}^{\ell\ell}$ to account for missing higher order QCD contributions. Generally, the modelling of fake photons in simulation provides a good description of the kinematic distributions observed in data with deviations below 20% in most bins. The hard scale of the interaction ($m_{\ell\ell\gamma\gamma}$) shows larger discrepancies, but no systematic shift is seen.
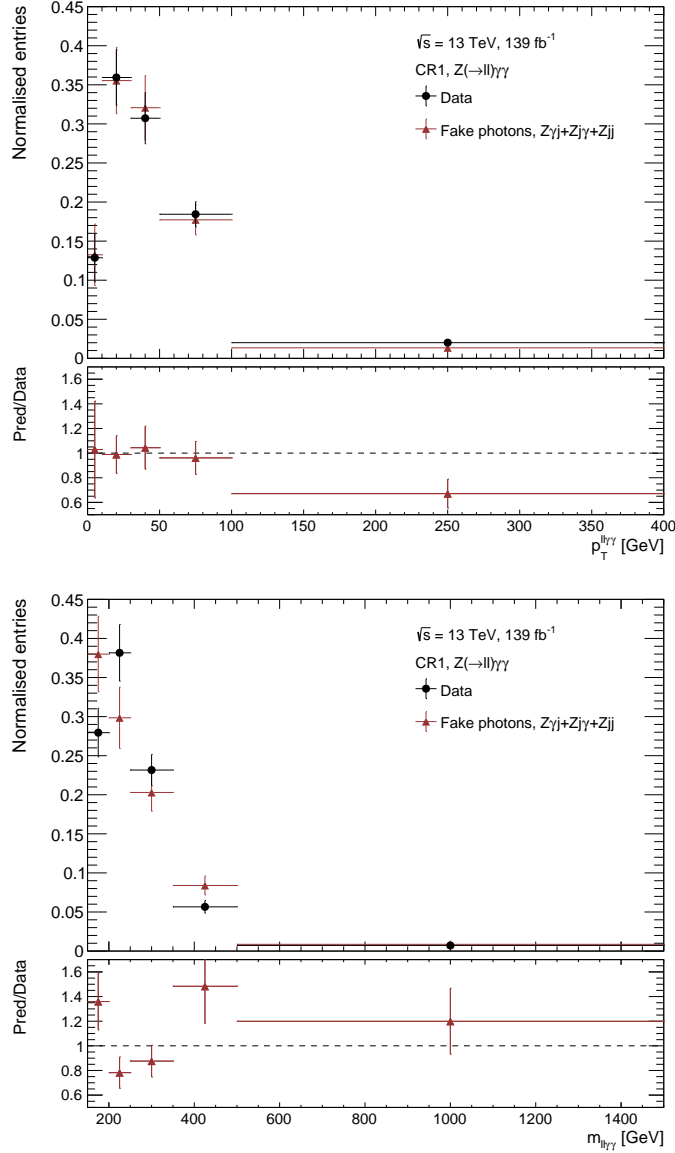
Figure 6.7.: Extraction of fake photon shape uncertainties in CR1. The observed distributions of (a) $p_{\mathrm{T}}^{\ell\ell\gamma\gamma}$ and (b) $m_{\ell\ell\gamma\gamma}$ are compared to the predicted fake photon distributions in $Z\gamma j$, $Zj\gamma$, and Zjj events. The ratio between the prediction and data (lower panel) is taken as systematic uncertainty on the shape of the fake photon background.

6.2. Contribution of Top-Quark Pair Production

The contribution of a pair of top quarks produced in association with two photons ($t\bar{t}\gamma\gamma$) is the second most dominant source of background contamination in the $Z\gamma\gamma$ analysis. In order to produce the $\ell\ell\gamma\gamma$ final state, the W bosons from $t \to Wb$ decay chain need

to decay into a same-flavour lepton pair. The photons can emerge from ISR (for quark-initiated top-quark pair production) or from the emission of one of the charged leptons. It is also possible to produce a non-prompt photon in the fragmentation of the b quarks. The modelling of the $t\bar{t}\gamma\gamma$ background process is taken from MC simulation. Instead of relying on the predicted normalisation from simulation, a data-driven approach is chosen. An orthogonal CR in data is defined by selecting opposite-flavour lepton pairs: $e^{\pm}\mu^{\mp}\gamma\gamma$. The predicted $t\bar{t}\gamma\gamma$ event yield is then scaled to match the observed number of events in the data CR defining a normalisation correction. Although the data CR is enriched in top-quark plus prompt photon pairs, fake photon events contribute to the observed event yield. The fake photon contamination in the $e^{\pm}\mu^{\mp}\gamma\gamma$ CR is measured with the matrix method and the breakdown of the 20 events is the following: 2.0 events for $e^{\pm}\mu^{\mp}\gamma j$, 0.6 events for $e^{\pm}\mu^{\mp}j\gamma$, and 0.1 events for $e^{\pm}\mu^{\mp}jj$. This results in a normalisation correction factor of $f_{\mathrm{corr}}^{t\bar{t}\gamma\gamma} = 0.70 \pm 0.15$ with respect to the 17.3 $e^{\pm}\mu^{\mp}\gamma\gamma$ events. All systematic uncertainties of the matrix method are considered. The statistical uncertainty dominates the total uncertainty on $f_{\mathrm{corr}}^{t\bar{t}\gamma\gamma}$. The corrected event expectation in the electron and muon channel is given in Table 6.7.

A validation of the normalisation correction procedure is shown in Figure 6.8. The measured $E_{\mathrm{T}}^{\gamma 1}$ and $m_{\gamma\gamma}$ distributions in the $e^{\pm}\mu^{\mp}\gamma\gamma$ data CR are compared to those predicted by the $t\bar{t}\gamma\gamma$ simulation. Additionally, the contributions of fake photons are added, which are properly normalised to the results of the matrix method. The shapes of fake photon events are taken from data enriched in events with one specific fake photon composition: $e^{\pm}\mu^{\mp}\gamma j$ with photons fulfilling requirements (AD) (see Section 6.1.1), $e^{\pm}\mu^{\mp}j\gamma$ with photons fulfilling requirements (DA), and $e^{\pm}\mu^{\mp}jj$ where both photons pass the (DD) criteria. A reasonable description of the data distributions is observed validating the modelling of $t\bar{t}\gamma\gamma$ events in simulation and, to the extent possible with the limited statistics, the matrix method results.

Table 6.7.: Contribution of $t\bar{t}\gamma\gamma$ events to the electron and muon channel of the $Z\gamma\gamma$ SR. The predicted normalisation from MC simulation is corrected using $f_{\mathrm{corr}}^{t\bar{t}\gamma\gamma} = 0.70 \pm 0.15$ derived in the $e^{\pm}\mu^{\mp}\gamma\gamma$ data CR.

Process	e-channel	μ-channel
$t\bar{t}\gamma\gamma$	$6.4 \pm 0.4\,(\mathrm{stat.}) \pm 1.4\,(\mathrm{sys.})$	$8.4 \pm 0.5\,(\mathrm{stat.}) \pm 1.8\,(\mathrm{sys.})$
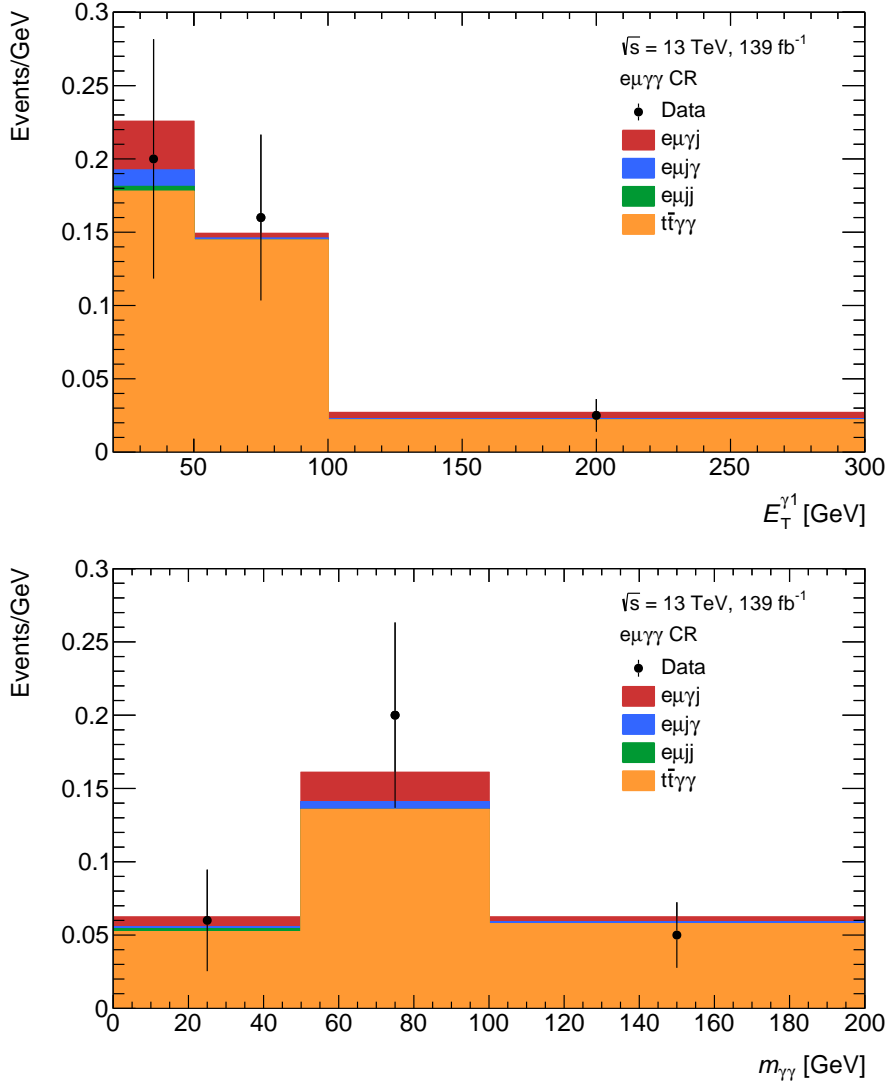
Figure 6.8.: Comparison of the measured distributions of (a) $E_T^{\gamma 1}$ and (b) $m_{\gamma\gamma}$ in the $e^\pm \mu^\mp \gamma\gamma$ CR to those predicted by $t\bar{t}\gamma\gamma$ events (scaled by $f_{corr}^{t\bar{t}\gamma\gamma}$) and those predicted by fake photon events (normalised to the results of the matrix method).

6.3. Contribution of Pile-Up

The high instantaneous luminosity of the LHC results in multiple p–p collisions per bunch crossing in the interaction point of the ATLAS detector. The $\ell\ell\gamma\gamma$ final state can be formed by accidentally combining particles from different p–p collision, for instance combining single Z boson events with events containing two photons. In such cases, the photons point to a different primary vertex than the leptons. It is not feasible to require photon-

related impact parameter cuts, which would reduce the PU background to a minimum. Such requirements would result in a significant sensitivity loss for unconverted photons, which typically have a poor vertex reconstruction due to the missing tracks in the ID. Two categories of PU events contribute to the SR: $Z + \gamma\gamma$ and $Z\gamma + \gamma$ events. The expected PU event yield is predicted with MC simulation using the following expressions:

$$N_{Z+\gamma\gamma}^{\mathrm{PU}} = \epsilon_{Z+\gamma\gamma} \frac{\sigma_Z \sigma_{\gamma\gamma}}{\sigma_{\mathrm{inel}}} L_{\mathrm{int}} \langle \mu \rangle \,, \tag{6.15}$$

$$N_{Z\gamma+\gamma}^{\mathrm{PU}} = \epsilon_{Z\gamma+\gamma} \frac{\sigma_{Z\gamma} \sigma_{\gamma}}{\sigma_{\mathrm{inel}}} L_{\mathrm{int}} \langle \mu \rangle \,. \tag{6.16}$$

These equations are based on the combined probability of observing two independent processes A and B, which is proportional to the product of the individual cross sections: $\sigma_A \sigma_B$. The product is normalised to the total inelastic cross section measured in Run 2: $\sigma_{\mathrm{inel}} = 78.1 \pm 2.9\,\mathrm{mb}$ (see Section 2.3). It is then scaled by the average number of simultaneous interactions per bunch-crossing $\langle \mu \rangle = 33.7$ and corrected using efficiency parameters $\epsilon_{Z+\gamma\gamma}$ and $\epsilon_{Z\gamma+\gamma}$. These parameters denote the efficiency to select $\ell\ell\gamma\gamma$ final states in $Z + \gamma\gamma$ and $Z\gamma + \gamma$ events. The efficiency is calculated by overlaying random events at particle-level (for instance from $Z\gamma$ and $\gamma + \mathrm{jets}$ simulations) and by requiring the leptons and photons to pass the SR event selection. Additionally, this procedure delivers particle-level distributions for the six observables of interest: $E_{\mathrm{T}}^{\gamma 1}$, $E_{\mathrm{T}}^{\gamma 2}$, $p_{\mathrm{T}}^{\ell\ell}$, $p_{\mathrm{T}}^{\ell\ell\gamma\gamma}$, $m_{\gamma\gamma}$, $m_{\ell\ell\gamma\gamma}$. The observables are normalised to $N_{Z+\gamma\gamma}^{\mathrm{PU}}$ or $N_{Z\gamma+\gamma}^{\mathrm{PU}}$. The particle-level $E_{\mathrm{T}}^{\gamma 1}$ distribution is shown in Figure 6.9 for the $Z+\gamma\gamma$ overlay. It is compared to the predictions of the $Z\gamma\gamma$ simulation highlighting the softer energy spectrum of PU events. This is explained by the recoil of the $\gamma\gamma$ system. In the $Z + \gamma\gamma$ overlay, the diphoton system recoils against potential hadronic activity, whereas the diphoton systems recoils against the heavy Z boson in the $Z\gamma\gamma$ signal process.

6.3.1. Folding Procedure

It is required to also obtain the PU contribution on reconstruction-level, both in terms of the integrated event yield and the differential distributions. This then enables to compare the observed event yield in data to the sum of the predicted signal contribution and the total background contamination. For this purpose, correction factors $C_{Z\gamma\gamma} = \frac{N_{Z\gamma\gamma}^{\mathrm{reco}}}{N_{Z\gamma\gamma}^{\mathrm{truth}}}$ are derived from the signal MC simulation (see Section 5.4) which correct for the detector acceptance[26] and the finite efficiencies of the reconstruction, identification, and isolation

---

[26]The different types of particles can only be detected within the sensitive volume of the ATLAS detector.
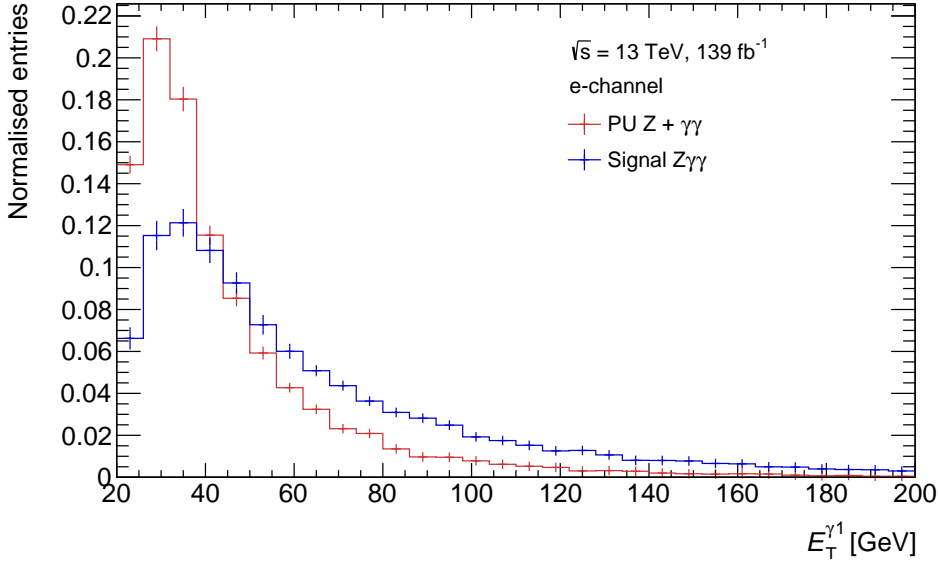
Figure 6.9.: Comparison of $E_T^{\gamma 1}$ at particle-level between $Z + \gamma\gamma$ PU events and the $Z\gamma\gamma$ signal process. The comparison is shown for the electron channel.

algorithms as well as of the trigger selection. This folding procedure is done with the $Z\gamma\gamma$ MC simulation, since it is not feasible to propagate all information through the particle-level overlay that would be necessary for the simulation of the particle interaction with the ATLAS detector. A systematic uncertainty is assigned to account for kinematic differences between the $Z\gamma\gamma$ signal process and $Z + \gamma\gamma$ or $Z\gamma + \gamma$ PU events. The correction factors are $C_{Z\gamma\gamma}^{e\text{-ch}} = 0.286 \pm 0.003$ in the electron channel and $C_{Z\gamma\gamma}^{\mu\text{-ch}} = 0.379 \pm 0.004$ in the muon channel, where the uncertainties are statistical uncertainties. As expected, a smaller correction is needed for muons due to the higher efficiency of the muon reconstruction. The correction factors are not only derived inclusively but also as functions of the six observables for which the differential cross section is measured. This is demonstrated in Figure 6.10 for $E_T^{\gamma 1}$ in $Z + \gamma\gamma$ PU events. The energy dependence of the photon reconstruction and especially the identification and isolation below $100\,\mathrm{GeV}$ [67] is directly reflected in the evolution of the correction factor. The total expectation of PU events at reconstruction-level is calculated with the inclusive correction factors and the results are given in Table 6.8. The largest contamination of PU in the SR stems from $Z\gamma + \gamma$ events, where the driving factor is the large cross section of single photon production.
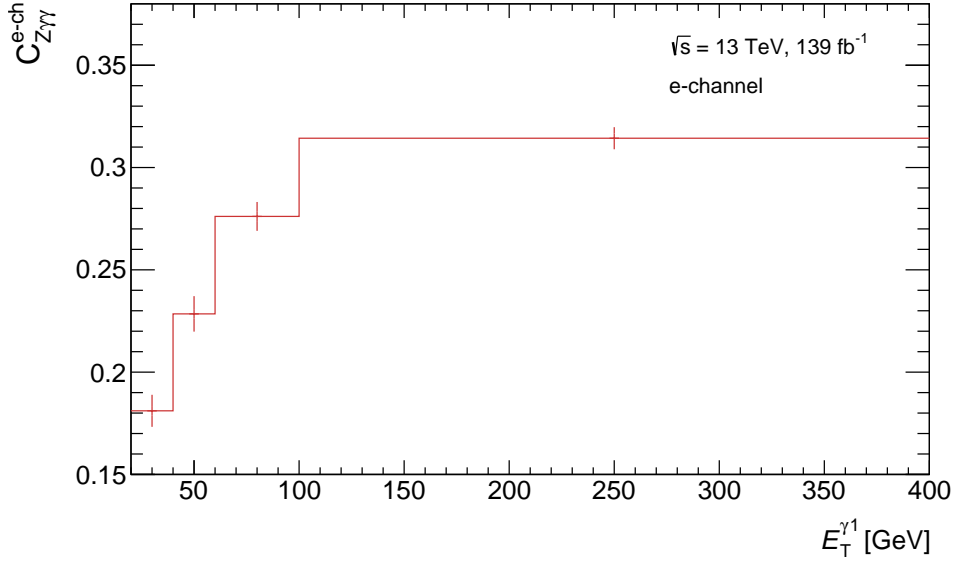
Figure 6.10.: Correction factor as a function of $E_{\mathrm{T}}^{\gamma 1}$ in the electron channel. The binning is identical to the one optimised for the unfolding procedure, see Section 7.4.

Table 6.8.: Contribution of $Z + \gamma\gamma$ and $Z\gamma + \gamma$ PU events to the electron and muon channel of the $Z\gamma\gamma$ SR.

PU process	e-channel	μ-channel
$Z + \gamma\gamma$	$1.44 \pm 0.04\,\text{(stat.)} \pm 0.39\,\text{(sys.)}$	$1.90 \pm 0.05\,\text{(stat.)} \pm 0.51\,\text{(sys.)}$
$Z\gamma + \gamma$	$2.07 \pm 0.16\,\text{(stat.)} \pm 0.72\,\text{(sys.)}$	$2.74 \pm 0.21\,\text{(stat.)} \pm 0.96\,\text{(sys.)}$

6.3.2. Systematic Uncertainties

The first source of systematic uncertainty is related to the correction factor. It is calculated using the particle- and reconstruction-level event expectation of the $Z\gamma\gamma$ signal process. The $Z\gamma\gamma$ events have photons with harder energy spectra compared to PU events (see Figure 6.9). The correction factor therefore leads to an overestimation of the PU contribution in the SR. The systematic uncertainty is estimated at particle-level by reweighting the photon energy of the signal process to match the energy of photons in PU events. The correction factors are then re-evaluated; a reduction of 23% and 16% is seen for $Z\gamma + \gamma$ and $Z + \gamma\gamma$ events, respectively. This variation is assigned as uncertainty. Additionally, so-called *combined performance* (CP) uncertainties which are centrally provided by the ATLAS experiment and which account, for instance, for the lepton and photon efficiencies, are propagated through the correction factors and amount to roughly 5%[27].

The remaining systematic uncertainties are connected to theory uncertainties on the

---

[27]Section 7.2 provides a description of CP uncertainties.

cross sections used in the calculation of $N_{Z+\gamma\gamma}^{\mathrm{PU}}$ and $N_{Z\gamma+\gamma}^{\mathrm{PU}}$. These comprise variations of the renormalisation and factorisation scales as well as uncertainties on the parton distribution functions and the strong coupling constant (a detailed description of the sources of theory uncertainty is given in Section 7.1). The by far most dominant theory uncertainties stem from single and diphoton production cross sections reaching values between 20%–30% [106] and 17%–23% [107], respectively.

6.4. Electron to Photon Fakes

Due to the shape similarities of electromagnetic clusters between electrons and photons, a non-negligible amount of electrons is falsely identified as photons. This is mostly connected to inefficiencies in the track reconstruction or in the track-cluster matching [108]. The contribution of such background processes to the $Z\gamma\gamma$ SR is measured using MC simulations of $ZZ\,(\to \ell\ell\ell\ell)$ and $WZ\gamma\,(\to \ell\nu\ell\ell\gamma)$ events. The larger contribution stems from the $ZZ\,(\to \ell\ell\ell\ell)$ process with 2.26 ± 0.15[28] events. This is driven by the larger multiplicity of charged leptons increasing the $e \to \gamma$ probability. The predicted number of events for the $WZ\gamma\,(\to \ell\nu\ell\ell\gamma)$ process is 1.21 ± 0.08. For both background sources, a conservative systematic uncertainty of 50% is assigned accounting for the mis-modelling of the $e \to \gamma$ probability in simulation [108].

6.5. Other Background Sources

The simultaneous production of a Z and Higgs boson can enter the phase-space of the $Z\gamma\gamma$ analysis through Higgs boson decays via quark or gauge boson loops into a photon pair: $Z\,(\to \ell\ell)\,H\,(\to \gamma\gamma)$. The predicted event yield for Run 2 is 2.45 ± 0.01 events. A 20% systematic uncertainty is assigned to this background source to account for theoretical uncertainties presented in a recent Run 2 ATLAS ZH analysis [109].

Physics objects faking the signature of a prompt photon are by far the largest source of background in this thesis. It is, however, also possible to falsely identify a particle as an electron. The contamination of the SR through such background processes is predicted with a $W\gamma\gamma\,(\to \ell\nu\gamma\gamma)$ MC simulation and amounts to 0.05 ± 0.01 events for the integrated luminosity of Run 2. This background process is therefore neglected.

The $\ell\ell\gamma\gamma$ final state can also be populated via $Z\gamma\gamma\,(\to \tau^+\tau^-\gamma\gamma)$ events, in which the Z boson decays to a pair of τ leptons. The taus are required to decay leptonically.

---

[28]All uncertainties in Section 6.4 and 6.5 are due to the limited number of simulated events. The presented event yields account for both lepton flavours.

The resulting electron or muon pairs are not likely to pass the invariant mass selection required in this analysis due to the loss of the tau-neutrino energy. This is reflected in the predicted Run 2 expectation of 0.37 ± 0.11 events, for which reason this background process is neglected.

6.6. Total Background Contribution

The contribution to the $Z\gamma\gamma$ SR of all background processes that were discussed in the previous sections is shown in Table 6.9. Approximately 20% of all events seen in data are due to the fake photon background, which is thus the largest source of background contamination in this thesis. The contribution of the $t\bar{t}\gamma\gamma$ process is 4.6%. The remaining background processes amount to 4.4% with respect to the total number of observed events and are hence of similar size as the $t\bar{t}\gamma\gamma$ process. The background-subtracted data event yield is compared to the predictions of SHERPA and MADGRAPH5_AMC@NLO. Good agreement is seen for both the electron and muon channel.

The differential distributions of $E_{\mathrm{T}}^{\gamma 1}$ and $E_{\mathrm{T}}^{\gamma 2}$ at reconstruction-level are displayed in Figure 6.11 and Figure 6.12, respectively. The measured per-bin yields typically agree well with the sum of the total background and $Z\gamma\gamma$ signal yields. The remaining reconstruction-level observables are presented in Appendix E.

Table 6.9.: Total number of observed events in the electron and muon channel and breakdown of background contributions to the $Z\gamma\gamma$ SR. The number of background subtracted events in data (indicated by '"Data $-$ background"') is compared to predictions from SHERPA and MADGRAPH5_AMC@NLO.

	$e^+e^-\gamma\gamma$	$\mu^+\mu^-\gamma\gamma$
Data	148	171
Fake photons: $Z\gamma j + Zj\gamma + Zjj$	$29.8 \pm 5.7\,\text{(stat.)} \pm 5.5\,\text{(sys.)}$	$34.4 \pm 6.6\,\text{(stat.)} \pm 6.3\,\text{(sys.)}$
$t\bar{t}\gamma\gamma$	$6.4 \pm 0.4\,\text{(stat.)} \pm 1.4\,\text{(sys.)}$	$8.4 \pm 0.5\,\text{(stat.)} \pm 1.8\,\text{(sys.)}$
$ZZ\,(\to \ell\ell\ell\ell)$	$1.03 \pm 0.10\,\text{(stat.)} \pm 0.51\,\text{(sys.)}$	$1.24 \pm 0.11\,\text{(stat.)} \pm 0.62\,\text{(sys.)}$
$WZ\gamma\,(\to \ell\nu\ell\ell\gamma)$	$0.69 \pm 0.06\,\text{(stat.)} \pm 0.35\,\text{(sys.)}$	$0.52 \pm 0.05\,\text{(stat.)} \pm 0.26\,\text{(sys.)}$
$Z\,(\to \ell\ell)\,H\,(\to \gamma\gamma)$	$1.08 \pm 0.01\,\text{(stat.)} \pm 0.22\,\text{(sys.)}$	$1.38 \pm 0.01\,\text{(stat.)} \pm 0.28\,\text{(sys.)}$
PU $Z\gamma + \gamma$	$2.07 \pm 0.16\,\text{(stat.)} \pm 0.72\,\text{(sys.)}$	$2.74 \pm 0.21\,\text{(stat.)} \pm 0.96\,\text{(sys.)}$
PU $Z + \gamma\gamma$	$1.44 \pm 0.04\,\text{(stat.)} \pm 0.39\,\text{(sys.)}$	$1.90 \pm 0.05\,\text{(stat.)} \pm 0.51\,\text{(sys.)}$
Data $-$ background	$105.5 \pm 12.2\,\text{(stat.)} \pm 8.1\,\text{(sys.)}$	$120.4 \pm 13.1\,\text{(stat.)} \pm 9.4\,\text{(sys.)}$
$Z\gamma\gamma$ SHERPA NLO	$91.5 \pm 0.9\,\text{(stat.)}$	$119.5 \pm 1.0\,\text{(stat.)}$
$Z\gamma\gamma$ MADGRAPH5_AMC@NLO	$91.0 \pm 1.0\,\text{(stat.)}$	$118.1 \pm 1.2\,\text{(stat.)}$
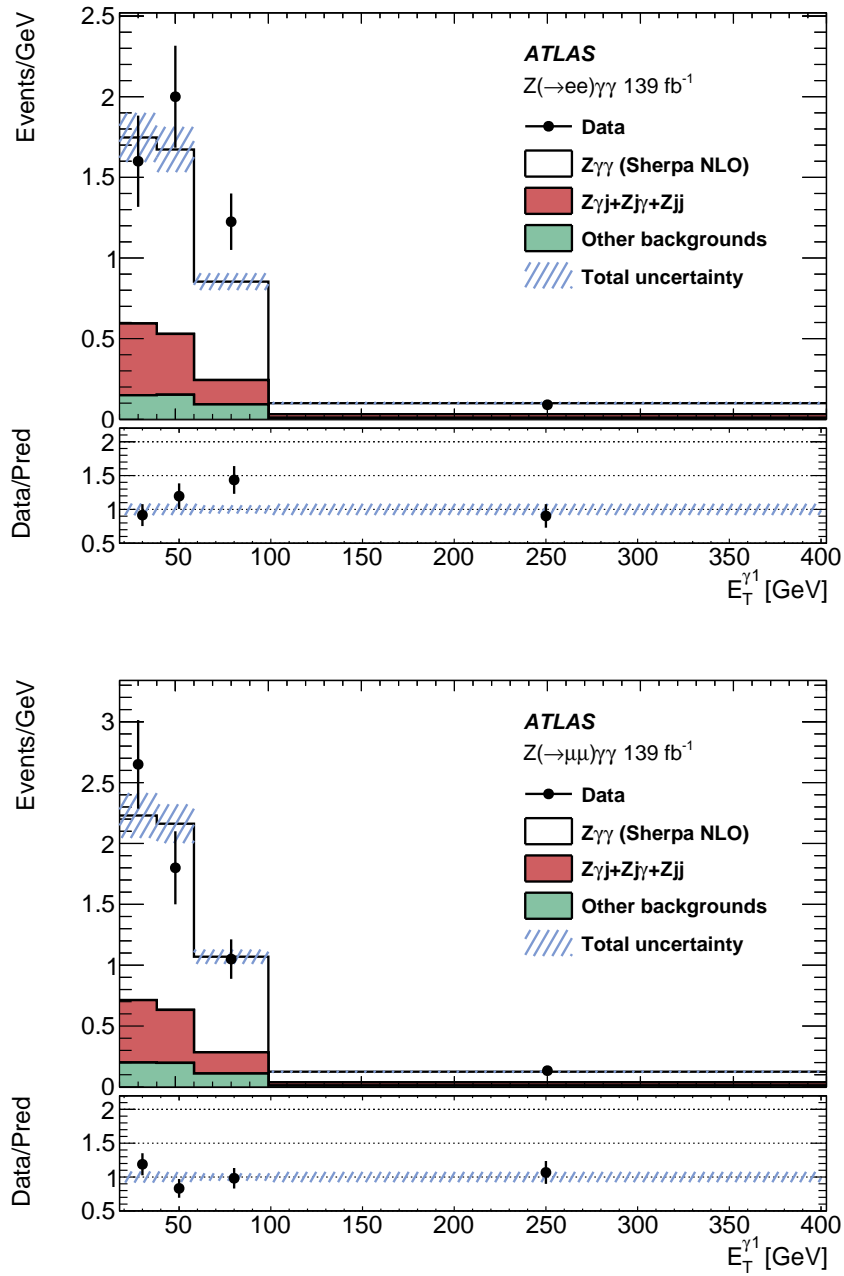
Figure 6.11.: The observed $E_T^{\gamma 1}$ distribution is shown in (a) the electron channel and (b) the muon channel. It is compared to the sum of the total background contribution and the $Z\gamma\gamma$ prediction. The uncertainty band accounts for the statistical and systematic uncertainties on the number of background events, and for the CP uncertainties of the signal process. The figures are taken from [41].
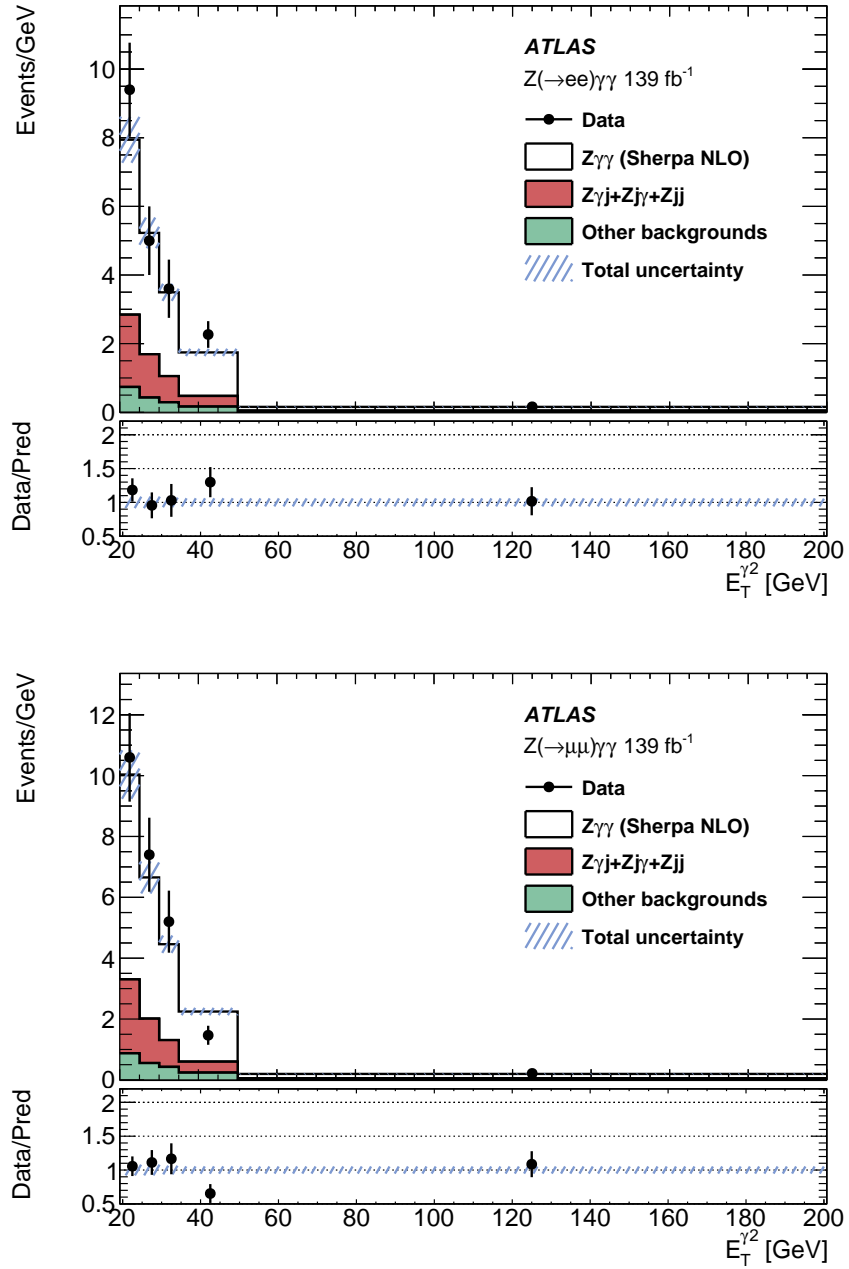
Figure 6.12.: The observed $E_T^{\gamma 2}$ distribution is shown in (a) the electron channel and (b) the muon channel. It is compared to the sum of the total background contribution and the $Z\gamma\gamma$ prediction. The uncertainty band accounts for the statistical and systematic uncertainties on the number of background events, and for the CP uncertainties of the signal process. The figures are taken from [41].

7. Cross-Section Measurements

The efficiency and purity of the lepton and photon reconstruction as well as the geometric acceptance and resolution of the detector impact the reconstruction-level measurements in this thesis. The tight muon isolation, for instance, is 87% efficient in the energy regime $20\,\mathrm{GeV} < p_\mathrm{T} < 100\,\mathrm{GeV}$, resulting in a 13% probability to reject a genuine muon (99% purity, see Section 4.2). Correcting for the detector effects allows to compare the cross section measurements directly to theoretical predictions. The integrated cross section is corrected with an inclusive correction factor $C_{Z\gamma\gamma}$, while the differential cross sections are corrected in an iterative unfolding procedure. To minimise the model dependence, a fiducial volume is defined at particle-level which closely follows the reconstruction-level requirements (see Table 7.1). To account for final-state QED radiation, photons are added to the four-momentum of electrons or muons if they are found within a cone of size $\Delta R (\ell, \gamma) = 0.1$. A common pseudorapidity cut for both lepton flavours is required. The calorimeter transition region ($1.37 < |\eta| < 1.52$) is not excluded in the fiducial volume. A theory-based extrapolation into this region at particle-level is therefore required but is preferred in order to simplify the definition of the fiducial volume. This extrapolation is expected to be small.

Isolation requirements are applied to photons at particle-level as follows. The transverse energy of stable particles that is found within $\Delta R = 0.2$ around each photon is summed. Particles are considered stable if they have a lifetime fulfilling $c\tau \geq 10\,\mathrm{mm}$. Contributions from neutrinos and muons are excluded in the formation of the photon isolation. The summed energy is compared to the photon energy and an upper requirement is placed on the ratio:

$$E_\mathrm{T}^{\mathrm{cone20}}/E_\mathrm{T}^{\gamma} < 0.07. \tag{7.1}$$

The value of the threshold is extracted similarly to the method performed in the $13\,\mathrm{TeV}$ ATLAS $Z\gamma$ analysis given in [96]. It corresponds to the value of $E_\mathrm{T}^{\mathrm{cone20}}/E_\mathrm{T}^{\gamma}$ at particle-level for which it is equally probable to pass and fail the loose isolation on reconstruction-level[29]. This ensures that the isolation requirement at particle-level has a similar performance to that on reconstruction-level, which minimises the model dependence.

The theoretical and experimental uncertainties affecting the predicted and measured cross sections of the $Z\gamma\gamma$ production are discussed in detail in the following two sections. The different approaches which are used to correct the measurements for detector

---

[29]Events with photons fulfilling (failing) $E_\mathrm{T}^{\mathrm{cone20}}/E_\mathrm{T}^{\gamma} < 0.07$ at particle-level have a larger probability to also contain a photon at reconstruction-level passing (failing) the isolation requirement.

effects are outlined afterwards. This chapter concludes with the discussion of the detector-corrected cross-section results.

Table 7.1.: Definition of the fiducial volume at particle-level. The index for the leptons in brackets, i.e. (ℓ_1) or (ℓ_2), indicates whether the selection is performed for the leading or subleading lepton.

	Requirement
Leptons	$p_T(\ell_1) > 30\,\text{GeV}, p_T(\ell_2) > 20\,\text{GeV}, |\eta| < 2.47$
Photons	$p_T > 20\,\text{GeV}, |\eta| < 2.37, E_T^{\text{cone20}}/E_T^\gamma < 0.07$
Multiplicity	≥ 1 OSSF lepton pair, ≥ 2 photons
Overlap	$\Delta R(\gamma, \ell) > 0.4, \Delta R(\gamma, \gamma) > 0.4$
Invariant mass	$m_{\ell\ell} > 40\,\text{GeV}, m_{\ell\ell} + \min(m_{\ell\ell\gamma1}, m_{\ell\ell\gamma2}) > 2 \times m_Z$

7.1. Theory Uncertainties

Uncertainties in the theoretical prediction of MC event generator cross sections are linked to the parameters entering the cross-section calculation:

$$\sigma_{pp\to n} = \sum_{a,b} \int \mathrm{d}x_a \mathrm{d}x_b f_a(x_a, \mu_F^2) f_b(x_b, \mu_F^2) \mathrm{d}\hat{\sigma}_{ab\to n}(\mu_R^2, \mu_F^2),$$

see Section 4.3. The uncertainties are encoded as weights in the $Z\gamma\gamma$ MC simulation, which are used to reweight the generated events altering the cross section and the differential shapes.

The first source of uncertainty is connected to the cross section of the hard interaction $\hat{\sigma}_{ab\to n}$. It is calculated at fixed order of the strong coupling constant α_s; the effect of missing higher orders of the expansion can be assessed by varying the renormalisation and factorisation scale. A seven-point variation of (μ_F, μ_R) is considered, in which the scales are multiplied by a factor of two or one-half: $(0.5, 0.5)$, $(1.0, 0.5)$, $(0.5, 1.0)$, $(1.0, 1.0)$, $(2.0, 1.0)$, $(1.0, 2.0)$, and $(2.0, 2.0)$. The nominal case corresponds to $(\mu_F, \mu_R) = (1.0, 1.0)$. The total scale uncertainty is taken as the envelope of the seven-point variation.

The uncertainty treatment for the parton distribution functions $f_a(x_a, \mu_F^2)$ and $f_b(x_b, \mu_F^2)$, and the choice of α_s follows the recommendations listed in [110]. The parton distribution functions are determined in fits to data and are therefore susceptible to experimental uncertainties. The NNPDF3.0NNLO set is used in the $Z\gamma\gamma$ NLO SHERPA MC simulation. Here, 100 replica PDF sets are constructed which encapsulate the uncer-

tainties and lead to a variation of the generator cross section and final state kinematics. The PDF uncertainty is taken as the root-mean-square of the predicted cross sections of all replica PDFs (both inclusively and per-bin). The nominal value of the strong coupling constant is set to $\alpha_s(m_Z^2) = 0.118$, which is also used in each replica PDF. A theory uncertainty on α_s is constructed by evaluating the PDF at slightly shifted values of the coupling constant: $\alpha_s = 0.117$ and $\alpha_s = 0.119$, which roughly reflects the uncertainty on the determination of the world-average of $\alpha_s(m_Z^2)$ [22]. The average of both fluctuations is assigned as uncertainty. The PDF and α_s uncertainties are combined by adding the uncertainties in quadrature.

The differential cross sections of $E_T^{\gamma 1}$ and $p_T^{\ell\ell\gamma\gamma}$ are shown in Figure 7.1 for the particle-level predictions of the $Z\gamma\gamma$ Sherpa NLO simulation. The three sources of theory uncertainty are displayed as well. The $E_T^{\gamma 1}$ uncertainties are representative for the remaining observables $E_T^{\gamma 2}$, $p_T^{\ell\ell}$, $m_{\gamma\gamma}$, and $m_{\ell\ell\gamma\gamma}$: the combined PDF and α_s uncertainty is smaller than 1% in all bins; the by far dominant source of theory uncertainty comes from the variation of the renormalisation and factorisation scale. The uncertainty rises in dependence of the transverse energy reaching a value of 20% in the last measurement bin. The theory uncertainties for $p_T^{\ell\ell\gamma\gamma}$ are generally larger: up to 2% for the combined PDF and α_s uncertainty and up to 30% for the scale variations. This is a consequence of the $p_T^{\ell\ell\gamma\gamma}$ recoil against hadronic activity and the limited QCD precision (0j@NLO) of the NLO SHERPA simulation. The $E_T^{\gamma 1}$ and $p_T^{\ell\ell\gamma\gamma}$ distributions are shown in Appendix F for the MADGRAPH5_AMC@NLO prediction, where the higher QCD precision (0,1j@NLO) leads to smaller scale uncertainties.
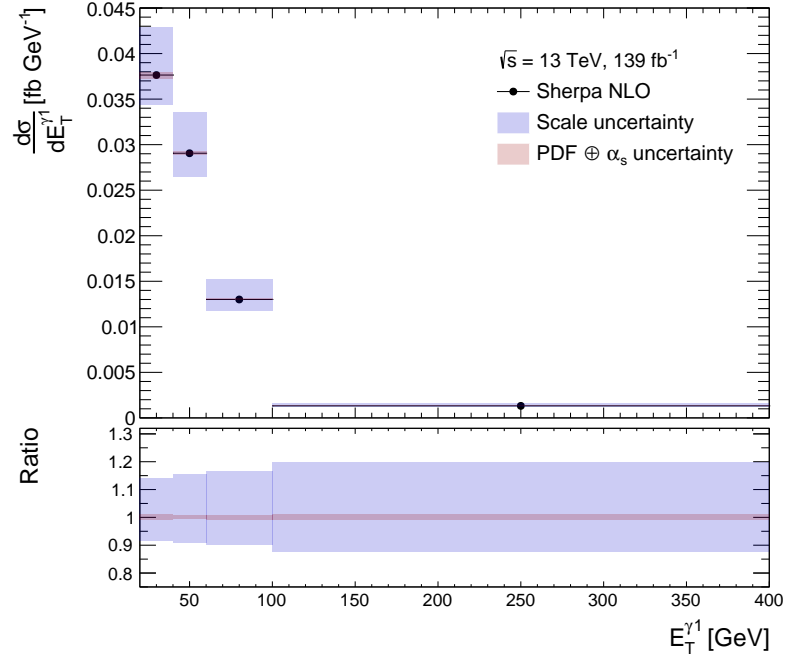
(a)
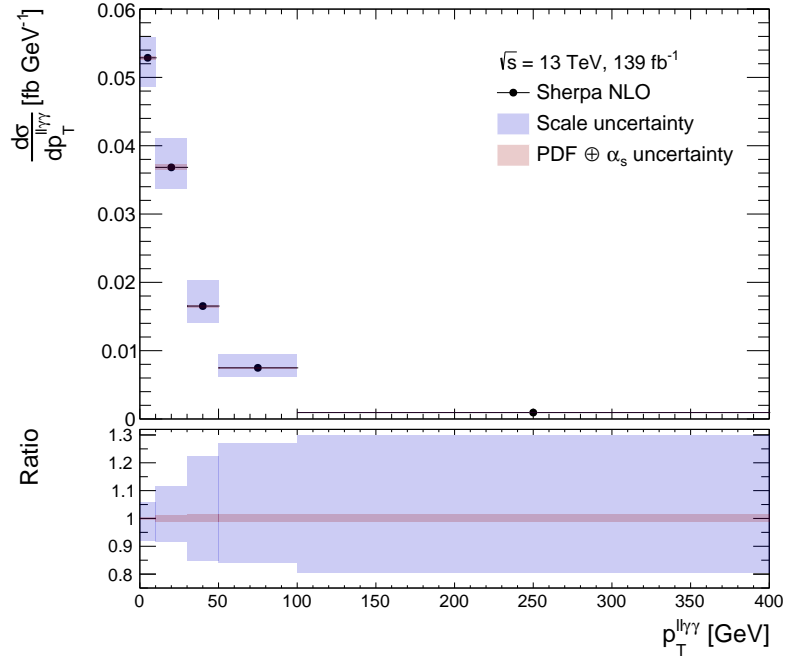
(b)

Figure 7.1.: Predicted differential cross section of $E_T^{\gamma 1}$ and $p_T^{\ell\ell\gamma\gamma}$ at particle-level for the $Z\gamma\gamma$ Sherpa NLO simulation. Theory uncertainties consisting of μ_F and μ_R scale variations (blue band), and of the combined PDF and α_s uncertainty (red band) are shown as well. The lower panel displays the per-bin variation of each theory uncertainty with respect to the nominal prediction.

7.2. Systematic Uncertainties

Ten sources of systematic uncertainty are considered in this thesis. The CP uncertainties are comprised of uncertainties related to the lepton and photon efficiencies, the energy (momentum) scale and resolution, and the pile-up reweighting. They are centrally provided by the ATLAS experiment and their $\pm 1\sigma$ variation is propagated through this analysis. Additional systematic uncertainties arise in the determination of background contributions, from theory uncertainties and the limited signal MC statistics as well as from the Run 2 luminosity measurement. The full set of systematic uncertainties is summarised in the following.

Electron efficiencies: The predicted efficiencies of the electron reconstruction, identification, and isolation, and the predicted efficiency of single electron triggers are compared to the efficiencies measured in data to detect residual performance differences. p_{T}- and η-dependent *scale factors* (SFs) are derived and used to reweight the MC simulation [67, 69]. The efficiencies are determined in data via tag-and-probe methods using, for instance, Z boson or J/ψ decays. A single systematic uncertainty per source[30] (reconstruction, identification, isolation, and trigger) is taken into account in this thesis because the $Z\gamma\gamma$ analysis is not expected to be sensitive to electron efficiency uncertainties. This is due to the fact that the statistical uncertainty and the systematic uncertainties related to the fake photon determination are much more dominant.

Photon efficiencies: p_{T}- and η-dependent SFs for the photon reconstruction, identification, and isolation are applied to the MC simulation [67, 108]. The efficiency in data is measured using FSR photons from $Z \to \ell\ell\gamma$ decays, which reduces the fake photon contamination. Additionally, photons from inclusive photon production in events collected by single photon triggers are used. One systematic uncertainty per source is taken into account.

Electron and photon energy scale and resolution: Corrections obtained from $Z \to ee$ decays are applied in bins of η to MC simulation and data to achieve a similar detector response [67, 111]. The energy-scale correction is applied to data, while the resolution correction is applied to MC simulation. One systematic uncertainty each (adding all effects in quadrature, assuming a full correlation across all η bins) is assigned for the energy scale and resolution.

Muon efficiencies: Muon efficiency corrections are taken into account for the recon-

---

[30]Alternatively, uncertainties for each bin in p_{T} and η can be included, which are separated into statistical and systematic effects. This is recommended for analyses which are sensitive to the electron efficiency uncertainties.

struction, identification, and the isolation as well as for single muon triggers. Additionally, the predicted efficiency of the track-to-vertex association is corrected. The efficiency in data is determined with a tag-and-probe method using $Z \to \mu\mu$ or $J/\psi \to \mu\mu$ decays [73]. All SFs are binned in muon p_T and η and the associated uncertainties are separated into statistical and systematic effects; two uncertainties per source are thus propagated to the cross section measurements in this thesis.

Muon momentum scale and resolution: The muon momentum corrections are treated slightly different than the energy-related corrections for electrons and photons. The muon momentum scale is corrected in data, while both the momentum scale and resolution are corrected in MC simulation. The corrections are derived from $Z \to \mu\mu$ or $J/\psi \to \mu\mu$ decays and applied as functions of η and ϕ [112, 113]. Five associated systematic uncertainties are considered[31].

Pile-up reweighting: The simulated vertex multiplicity (a measure for the pile-up profile) is compared to that recorded in representative runs for the data taking periods 2015–2016, 2017, and 2018 to derive SFs [114]. The uncertainty on the SFs is taken into account in the $Z\gamma\gamma$ analysis.

Background contribution: The systematic uncertainties arising in the determination of the background contributions are discussed in Section 6.1 (fake photon background) and Section 6.2 (remaining background sources). The by far largest systematic effect on the measurement of cross sections in this thesis stems from uncertainties in the fake photon determination.

Integrated luminosity: The integrated luminosity of the Run 2 dataset is $L_\mathrm{int} = 139\,\mathrm{fb}^{-1}$. This value is determined in p–p collisions using special luminosity-sensitive detectors, mainly the *LUCID* detector, with a 1.7% uncertainty [115]. The uncertainty affects the measurement of the integrated cross section in the fiducial volume and the determination of differential cross sections after the unfolding is performed.

MC statistics of $Z\gamma\gamma$ signal: The limited number of generated signal events causes uncertainties for the correction factor $C_{Z\gamma\gamma}$ (integrated cross section) and the unfolding procedure (C_fid, C_eff and migration matrices, see Section 7.4).

Theory uncertainties: The sources of theory uncertainty comprise the variations of the factorisation and renormalisation scale (μ_F and μ_R), and the combined PDF plus α_s variation.

---

[31]Two uncertainties are taken into account for the momentum resolution in the ID and MS and three uncertainties for the momentum scale.

7.3. Determination of the Integrated Cross Section

The integrated cross section in the fiducial volume of the $Z\gamma\gamma$ analysis is calculated via $\sigma_{Z\gamma\gamma}^{\mathrm{fid}} = \frac{N_{Z\gamma\gamma}^{\mathrm{meas}}}{C_{Z\gamma\gamma} \times L_{\mathrm{int}}}$, where the parameter $C_{Z\gamma\gamma} = N_{Z\gamma\gamma}^{\mathrm{reco}}/N_{Z\gamma\gamma}^{\mathrm{truth}}$ corrects for detector effects (see Section 5.4). The number of signal events $N_{Z\gamma\gamma}^{\mathrm{meas}}$ is obtained by subtracting all background contributions from the observed number of events in data. The systematic uncertainties entering the calculation of $\sigma_{Z\gamma\gamma}^{\mathrm{fid}}$ are summarised in Table 7.2. A total systematic uncertainty of 9.3% is determined in the electron and muon channel. It is slightly smaller than the statistical uncertainty of the analysed dataset, which amounts to 11.5% (e-channel) and 10.9% (μ-channel).

The value of $C_{Z\gamma\gamma}$ is determined independently for both lepton flavours: $C_{Z\gamma\gamma}^{e\text{-ch}} = 0.286 \pm 0.014$ in the electron channel and $C_{Z\gamma\gamma}^{\mu\text{-ch}} = 0.379 \pm 0.017$ in the muon channel. The uncertainties contain the statistical uncertainty (indicated as 'MC signal statistics' in Table 7.2) and the CP uncertainties. The latter is the dominant source of uncertainty with roughly 5%, which is driven by the pile-up reweighting, the photon identification and isolation, and the efficiency of the electron identification. The theory uncertainties are assessed by varying the scales and considering the PDF plus α_s uncertainties in the calculation of $N_{Z\gamma\gamma}^{\mathrm{reco}}$ and $N_{Z\gamma\gamma}^{\mathrm{truth}}$. The impact of theory uncertainties on the integrated cross section is small with a contribution of 1.1%.

The largest systematic uncertainty on $N_{Z\gamma\gamma}^{\mathrm{meas}}$ stems from the determination of the fake photon background amounting to roughly 7.5% across both channels. Uncertainties related to the determination of the remaining background contributions are smaller than 2%. This is driven by the fact that the number of fake photon events is more than twice as large as the sum of the remaining background yields.

Table 7.2.: Relative systematic uncertainties on the integrated cross section in the fiducial volume. Sources of uncertainty which contribute $\leq 0.1\%$ are not listed. The dagger symbol indicates which uncertainties are correlated between the electron and muon channel. The statistical uncertainty on the number of events observed in the analysed dataset is shown as well.

Uncertainty	$e^+e^-\gamma\gamma$	$\mu^+\mu^-\gamma\gamma$
Electron identification efficiency	2.0	-
Electron reconstruction efficiency	0.3	-
Electron–photon energy resolution†	0.2	0.1
Electron–photon energy scale†	0.8	0.6
Muon isolation efficiency	-	0.4
Muon reconstruction efficiency	-	0.4
Muon trigger efficiency	-	0.3
Muon momentum scale	-	0.2
Photon identification efficiency†	2.5	2.6
Photon isolation efficiency†	2.0	2.0
Pile-up reweighting†	2.8	2.9
MC signal statistics	1.1	1.0
Theory uncertainties†	1.1	1.1
Integrated luminosity†	1.7	1.7
Fake photon background†	7.5	7.6
Other backgrounds†	1.7	1.9
Total systematic uncertainty	9.3	9.3
Data statistical uncertainty	11.5	10.9
Total uncertainty	14.8	14.3

7.4. Determination of the Differential Cross Sections

Several event categories require a dedicated correction to determine the differential cross sections at particle-level:

- Events passing the reconstruction-level selection but failing the fiducial-volume selection. This so-called *fiducial correction* C_{fid} is small in this analysis due to the purity of the stringent identification and isolation requirements

- Events passing the fiducial-volume selection but not the one on reconstruction-level. The *efficiency correction* C_{eff} is significantly larger as a result of the finite efficiency of the lepton and photon identification and isolation

- Events passing both the fiducial-volume and reconstruction-level selections. A correction is required to account for bin migrations: a cross section measurement in a

given bin of an observable at particle-level does not necessarily correspond to the same bin at reconstruction-level due to the detector resolution

The three types of corrections are determined for the observables $E_\mathrm{T}^{\gamma 1}$, $E_\mathrm{T}^{\gamma 2}$, $p_\mathrm{T}^{\ell\ell}$, $p_\mathrm{T}^{\ell\ell\gamma\gamma}$, $m_{\gamma\gamma}$, and $m_{\ell\ell\gamma\gamma}$ using the SHERPA NLO signal simulation. The bin width of each observable is non-uniform and optimised to have enough statistics for the unfolding, i.e. at least 15 events. The bin edge of the last bin is chosen to limit the range of each observable to the phase-space the $Z\gamma\gamma$ analysis is sensitive to: the expected contribution of the SHERPA NLO signal sample above the right bin edge is required to be smaller than one event. The inclusive values of C_fid and C_eff are shown in Table 7.3. The magnitude of C_fid is approximately equal for the electron and muon channel indicating a similar purity of the identification and isolation. A larger efficiency correction is needed in the electron channel. Exemplary differential distributions of C_fid and C_eff are shown in Appendix G. The migration matrices are mostly diagonal and migrations are typically small ($< 6\%$). The largest effect is seen for the fine binning of $p_\mathrm{T}^{\ell\ell\gamma\gamma}$, where migrations up to 18% are observed. Representative migration matrices are shown in Figure 7.2 for the muon channel. The same trends are seen in the electron channel.

The detector effects are corrected in an *iterative Bayesian unfolding* [116, 117]. It is performed for each measured, background-subtracted observable at reconstruction-level. The *detector response* incorporates the detector-related corrections: the efficiency and fiducial correction, and the bin migrations. The desired probability to observe a cross section in a certain bin at particle-level, given the measured differential cross section, is determined from the detector response and the particle-level prior. The latter corresponds to the differential cross section predicted by the $Z\gamma\gamma$ signal MC simulation at particle-level. The prior is iteratively updated to reduce the bias from its initial choice. A larger number of iterations reduces the aforementioned bias but increases statistical uncertainties. The unfolding results are compared for one, two, and three iterations. There

Table 7.3.: Corrections accounting for events passing the reconstruction-level selection but failing the fiducial-volume requirements C_fid and for those passing the fiducial-volume selection but no the one on reconstruction-level C_eff. The corrections are determined from the SHERPA NLO $Z\gamma\gamma$ simulation in the electron and muon channel. The inclusive correction factor C, which is used in the determination of the integrated cross section in the fiducial volume, is shown for comparison and can be obtained via $C = C_\mathrm{eff}/C_\mathrm{fid}$.

Correction	e-channel	μ-channel
C_fid	0.939 ± 0.013	0.935 ± 0.011
C_eff	0.268 ± 0.003	0.354 ± 0.004
C	0.286 ± 0.003	0.379 ± 0.004
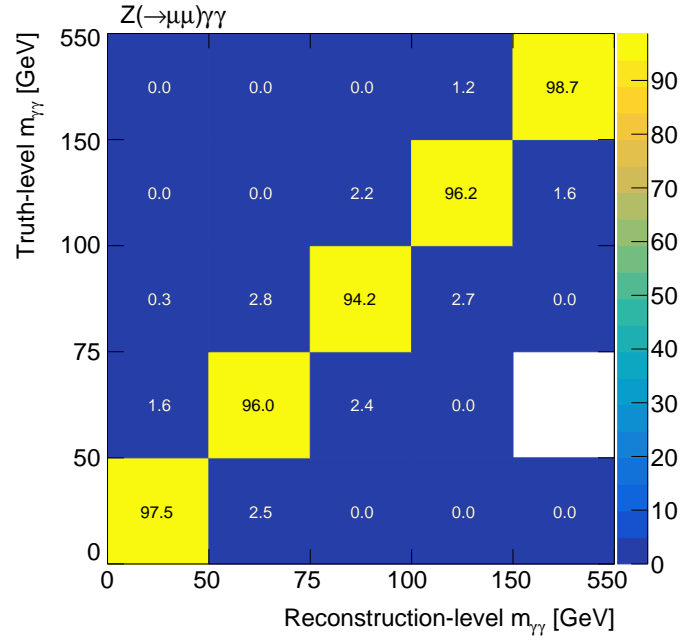
(a)
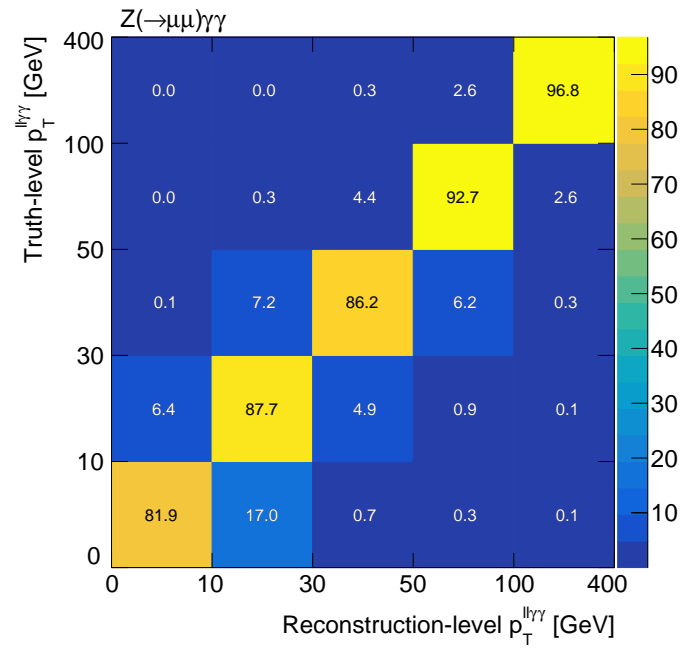
(b)

Figure 7.2.: Migration matrices for (a) $m_{\gamma\gamma}$ and (b) $p_T^{\ell\ell\gamma\gamma}$ determined with the SHERPA NLO signal simulation in the muon channel. The migrations ($1 - p$, where p is the z-axis value) are given in %.

are very few significant differences in the unfolded distributions between one and two iterations; the largest deviation of 20% is seen for one $p_\mathrm{T}^{\ell\ell\gamma\gamma}$ with large uncertainty. The differences between two and three iterations are typically small ($< 3\%$). The unfolding is therefore performed with two iterations.

The treatment of statistical and systematic uncertainties in the unfolding is discussed in the following:

- The effect of the statistical uncertainty in data is determined with a bootstrap method. The input events in data are reweighted according to a Poisson distribution with a mean of unity. 1000 replica datasets are propagated through the unfolding and the root-mean-square of the measured cross section in each bin is assigned as statistical uncertainty

- Several sources of uncertainty impact the migration matrices and the corrections C_eff and C_fid. The uncertainty in the number of generated events of the SHERPA NLO simulation is assessed similarly as the statistical uncertainty in data by propagating bootstrap replica datasets. The one sigma up and down variation of each CP uncertainty is taken into account by constructing new corrections and repeating the unfolding. The average uncertainty from the up and down variation is formed in each measurement bin and assigned as uncertainty. The theory uncertainties (scale, PDF, and α_s variations) have a negligible effect on the total uncertainty of the unfolded differential cross sections

- The number of fake photon events and the event yield for the remaining background processes are varied by one standard deviation before they are subtracted from the observed number of events. The shifted differential cross sections are unfolded and the per-bin average of the up and down variation is taken into account

- The uncertainty in the integrated luminosity affects each bin of the unfolded differential cross sections with a magnitude of 1.7%

- A data-driven test is performed to determine the bias caused by the choice of the prior. The differential cross sections predicted by the SHERPA NLO signal simulation at reconstruction-level are reweighted to achieve better agreement with the observed distributions in data. The reweighted observables are propagated through the unfolding utilising the nominal response matrix. The unfolded distributions are compared to the SHERPA $Z\gamma\gamma$ predictions at truth-level, which are reweighted following the same procedure. The variation is typically below 2%; the most signifi-

cant shift of 8% is seen for $p_T^{\ell\ell\gamma\gamma}$ in one bin. These uncertainties are assigned to the unfolded cross section measurements

The unfolded differential cross sections in the electron and muon channel are combined in an averaging procedure based on a χ^2 minimisation similar to that described in [118, 119]. It takes correlations of systematic uncertainties between both channels into account. The correlated uncertainties are indicated in Table 7.2; the largest sources of correlated uncertainty are related to the pile-up reweighting, the fake-photon background determination, and the photon identification and isolation efficiencies. The uncertainties on the combined cross-section measurement of $m_{\ell\ell\gamma\gamma}$ are presented in Figure 7.3. The statistical uncertainty dominates the total uncertainty in each bin. The most significant systematic uncertainty stems from the fake photon determination and ranges from approximately 8% to 17%. The remaining sources of uncertainty contribute less significantly ($\leq 4\%$).
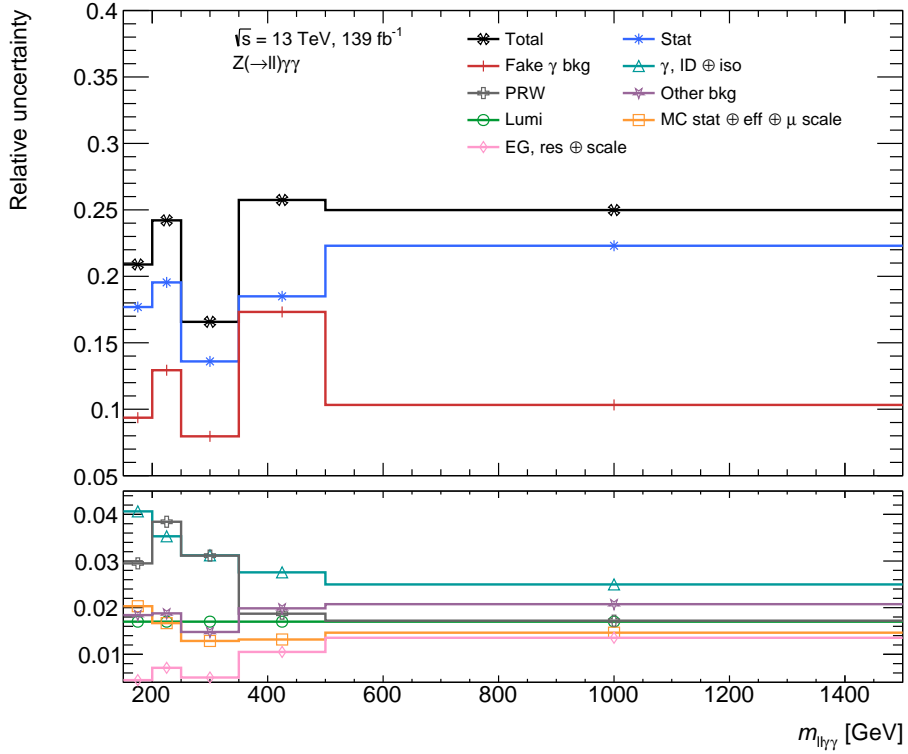
Figure 7.3.: Sources of experimental uncertainty on the unfolded cross-section measurement of $m_{\ell\ell\gamma\gamma}$. Certain uncertainties are added in quadrature, symbolised by $\oplus$, to improve the visibility. The largest contribution to the total uncertainty stems from the data statistics (blue line). The orange line corresponds to uncertainties that are not correlated between the electron and muon channel: statistics from the MC samples, the lepton efficiencies, and the muon momentum scale.

7.5. Cross-Section Results

The integrated cross section of the $Z\gamma\gamma$ triple gauge boson production at particle-level is measured in the electron channel as

$$\sigma_{ee\gamma\gamma}^{\text{fid}} = 2.65 \pm 0.31 \,(\text{stat.}) \pm 0.24 \,(\text{sys.}) \pm 0.05 \,(\text{lumi.})\,\text{fb}. \qquad (7.2)$$

The measurement in the muon channel results in

$$\sigma_{\mu\mu\gamma\gamma}^{\text{fid}} = 2.29 \pm 0.25 \,(\text{stat.}) \pm 0.21 \,(\text{sys.}) \pm 0.04 \,(\text{lumi.})\,\text{fb}. \qquad (7.3)$$

Both cross sections are well compatible within one standard deviation. The result of the combined cross section is

$$\sigma_{\ell\ell\gamma\gamma}^{\text{fid}} = 2.45 \pm 0.20 \,(\text{stat.}) \pm 0.22 \,(\text{sys.}) \pm 0.04 \,(\text{lumi.})\,\text{fb}. \qquad (7.4)$$

The total uncertainty has roughly equal contributions from statistical and systematic uncertainties. $\sigma_{\ell\ell\gamma\gamma}^{\text{fid}}$ is determined with a total precision of 12.2%. This represents the currently most accurate measurement of the cross section of the $\ell\ell\gamma\gamma$ final state compared to previous $Z\gamma\gamma$ analyses [10, 11]. The combined measurement is compared to theoretical predictions of SHERPA and MADGRAPH5_AMC@NLO at NLO precision in QCD in Figure 7.4. The predictions of both MC event generators agree within the uncertainty with the measured cross section. The theory uncertainties for the MADGRAPH5_AMC@NLO simulation are significantly smaller. As mentioned in Section 7.1, variations of μ_{F} and μ_{R} account for missing higher-order corrections in the finite-order calculation of the cross section. The MADGRAPH5_AMC@NLO samples are simulated with a larger QCD precision, i.e. with a $0,1\text{j@NLO}$ matrix element, compared to the 0j@NLO simulation of the SHERPA sample. This results in larger scale corrections for the SHERPA simulation. The unfolded differential cross sections for all observables are compared to theoretical predictions of both MC event generators in Figures 7.5 – 7.7. Good agreement is typically observed across all bins, which validates the predictions of the SM electroweak sector in the $\ell\ell\gamma\gamma$ phase-space. The most significant deviation is seen in the last $p_{\text{T}}^{\ell\ell\gamma\gamma}$ bin. The SHERPA and MADGRAPH5_AMC@NLO predictions are compatible with the measured cross section within 1.6 and 2.0 standard deviations, respectively. The measurements in the remaining $p_{\text{T}}^{\ell\ell\gamma\gamma}$ bins agree well with the SM predictions. The deviation is not expected to be statistically significant considering the number of cross sections determined in all bins of the six unfolded observables. The cross-section measurements are published
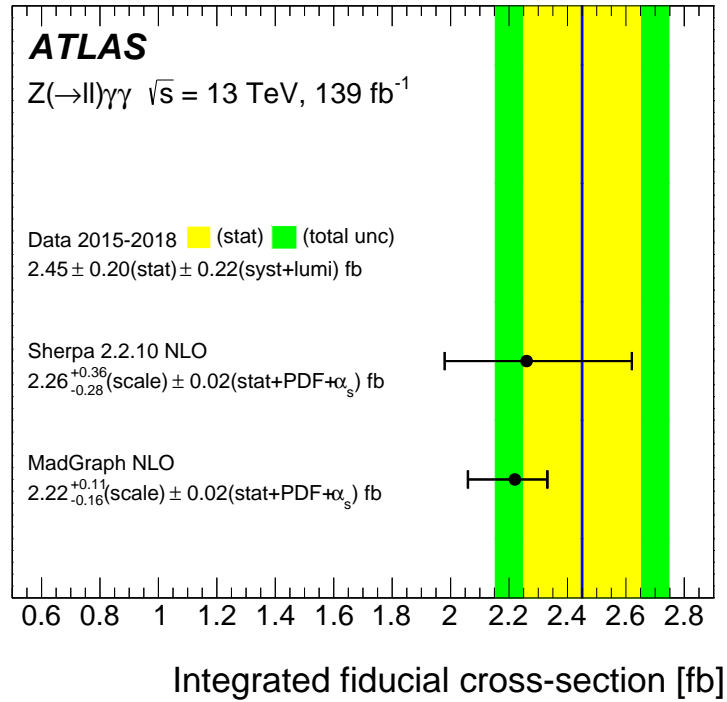
Figure 7.4.: Comparison of the combined integrated cross section in the fiducial volume to the NLO predictions of SHERPA and MADGRAPH5_AMC@NLO. The yellow uncertainty band corresponds to the statistical uncertainty on the measured cross section and the green uncertainty band reflects the total uncertainty. The uncertainty bars for the MC simulation correspond to the quadratic sum of theory uncertainties (μ_F and μ_R, and PDF plus α_s variations) and the statistical uncertainty. The figure is taken from [41].

in a central particle physics database (*HEPData*) [120].
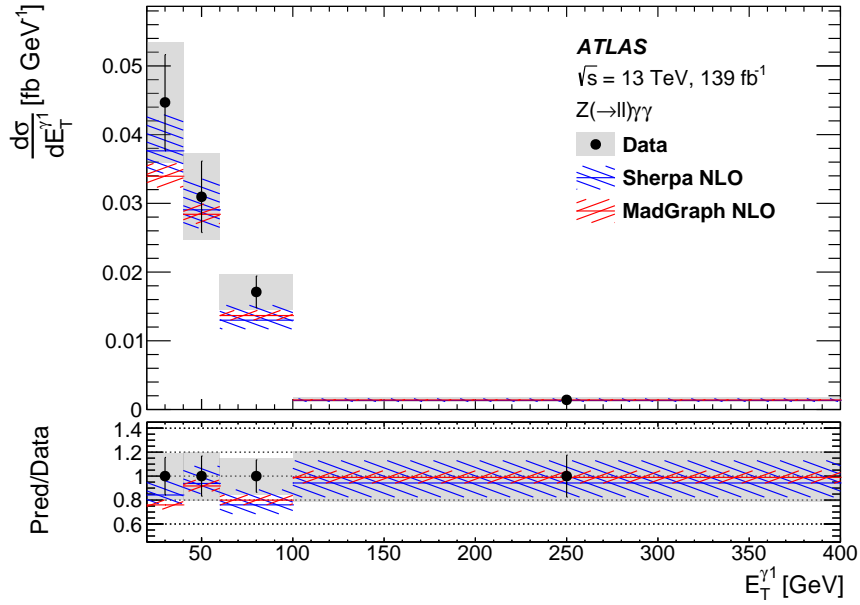
(a)
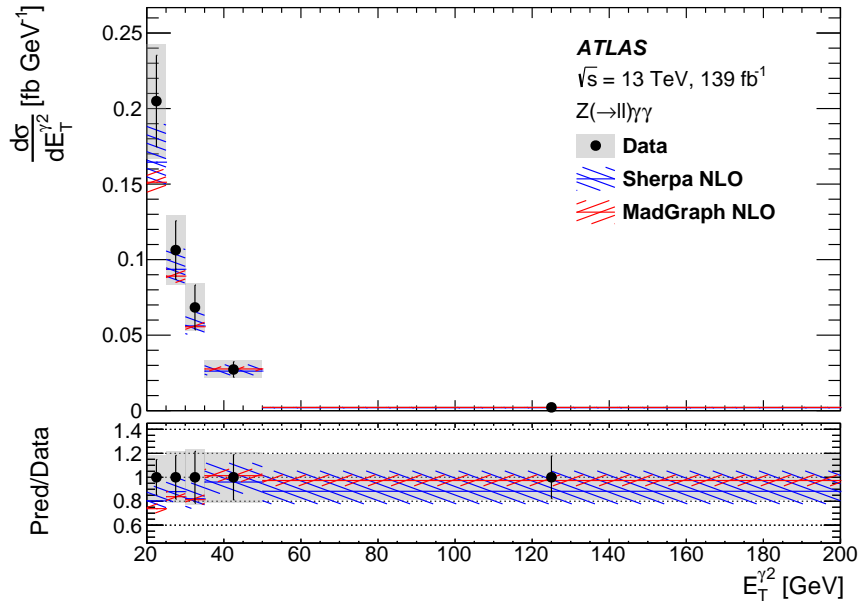
(b)

Figure 7.5.: Comparison of the unfolded differential cross section measurements to the predictions of the SHERPA and MADGRAPH5_AMC@NLO simulation for (a) $E_T^{\gamma 1}$ and (b) $E_T^{\gamma 2}$. The error bar on data corresponds to the statistical uncertainty and the grey error band reflects the total uncertainty. The coloured areas for the predictions of the MC simulation correspond to the quadratic sum of theory uncertainties (μ_F and μ_R, and PDF plus α_s variations) and the statistical uncertainty. The figures are taken from [41].
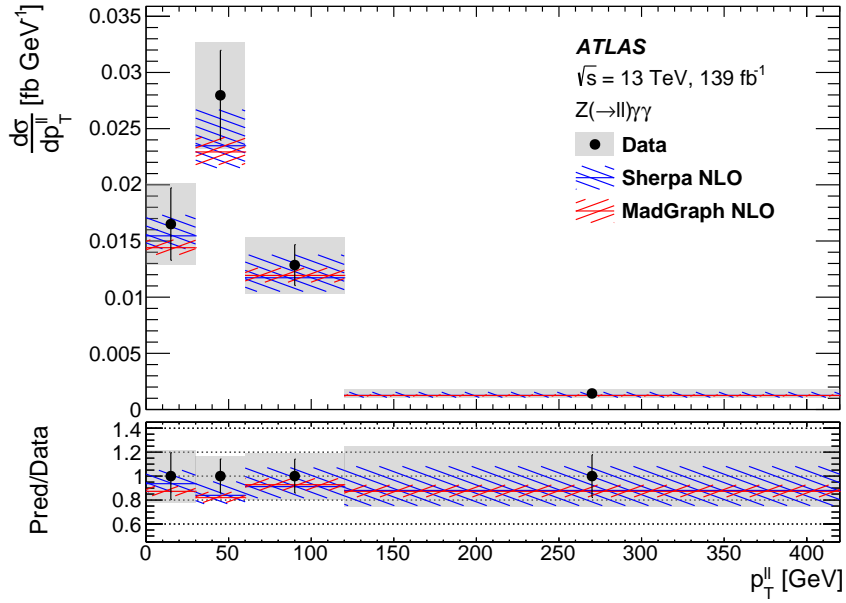
(a)
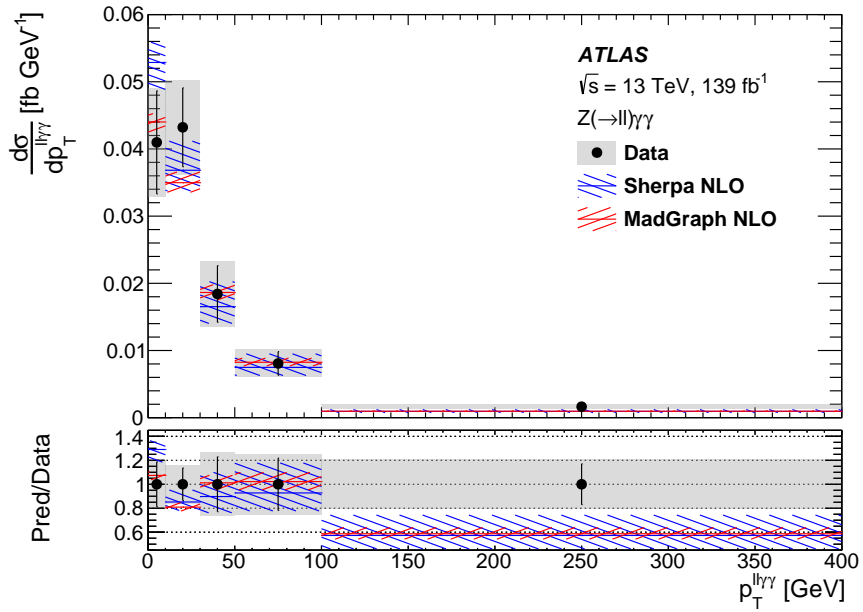
(b)

Figure 7.6.: Comparison of the unfolded differential cross section measurements to the predictions of the SHERPA and MADGRAPH5_AMC@NLO simulation for (a) $p_T^{\ell\ell}$ and (b) $p_T^{\ell\ell\gamma\gamma}$. The error bar on data corresponds to the statistical uncertainty and the grey error band reflects the total uncertainty. The coloured areas for the predictions of the MC simulation correspond to the quadratic sum of theory uncertainties (μ_F and μ_R, and PDF plus α_s variations) and the statistical uncertainty. The figures are taken from [41].
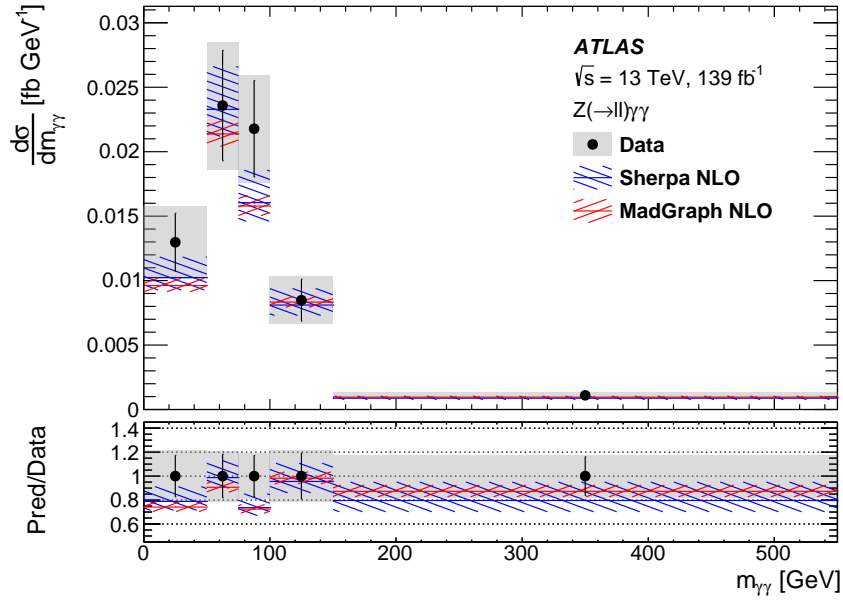
(a)
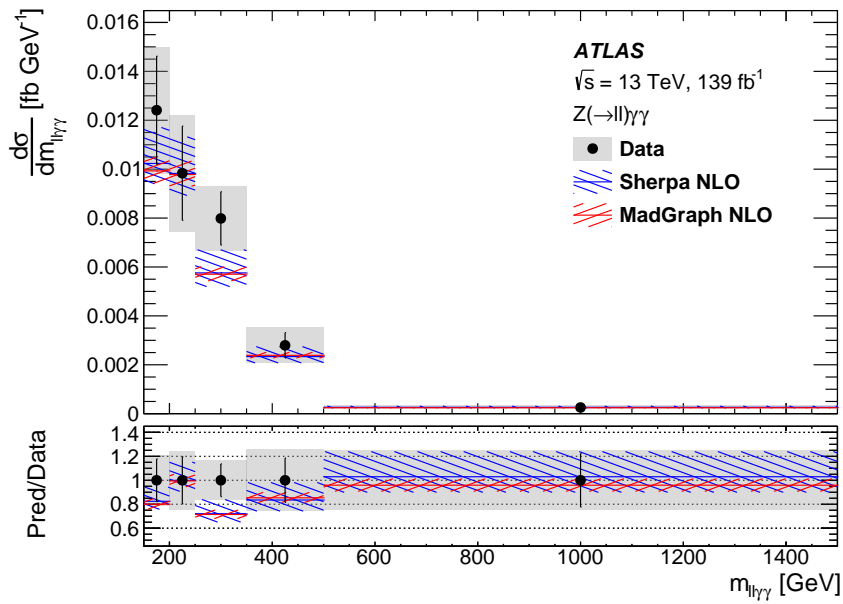
(b)

Figure 7.7.: Comparison of the unfolded differential cross section measurements to the predictions of the SHERPA and MADGRAPH5_AMC@NLO simulation for (a) $m_{\gamma\gamma}$ and (b) $m_{\ell\ell\gamma\gamma}$. The error bar on data corresponds to the statistical uncertainty and the grey error band reflects the total uncertainty. The coloured areas for the predictions of the MC simulation correspond to the quadratic sum of theory uncertainties (μ_F and μ_R, and PDF plus α_s variations) and the statistical uncertainty. The figures are taken from [41].

8. Effective Field Theory Interpretation

The non-Abelian nature of the $SU(2)_L \times U(1)_Y$ symmetry of the SM electroweak sector gives rise to triple and quartic gauge-boson self-interactions. The $\ell\ell\gamma\gamma$ final state is sensitive to modifications of these self-interactions arising through new physics (NP). An EFT approach is used in this thesis to investigate NP effects. The interactions of dimension-8 operators are incorporated with the Lagrangian

$$\mathcal{L}_{\mathrm{EFT}} = \mathcal{L}_{\mathrm{SM}} + \sum_i \frac{f_i^8}{\Lambda^4} \mathcal{O}_i^8. \tag{8.1}$$

All of the 18 operators giving rise to $\ell\ell\gamma\gamma$ final states can alter the differential cross section measured in this thesis. Recalling the quartic couplings of dimension-8 operators presented in Table 2.2, the seven mixed operators $\mathcal{O}_{M,i}^8$ with $i \in \{0, 1, 2, 3, 4, 5, 7\}$ and the eight transverse operators $\mathcal{O}_{T,j}^8$ with $j \in \{0, 1, 2, 5, 6, 7, 8, 9\}$ introduce $ZZ\gamma\gamma$ vertices. Additionally, $Z\gamma\gamma\gamma$ and $\gamma\gamma\gamma\gamma$[32] vertices appear in each $\mathcal{O}_{T,j}^8$ Lagrangian. The $Z\gamma\gamma$ analysis is thus expected to have the largest sensitivity for contributions of $\mathcal{O}_{T,j}^8$. Any combination of field strength tensors for the longitudinal operators $\mathcal{O}_{S,k}^8$ does not allow to introduce the final states mentioned above, for which reason they are disregarded in the EFT interpretation.

The treatment of NP effects in this thesis follows the ATLAS recommendations (partially summarised in [121]). The NP scale is chosen uniformly as $\Lambda = 1\,\mathrm{TeV}$ and all Wilson coefficients are set to unity. Limits are extracted for one Wilson coefficient at a time, while all other coefficients are set to zero.

8.1. Sensitivity Scan

The EFT samples for mixed $\mathcal{O}_{M,i}^8$ and transverse $\mathcal{O}_{T,j}^8$ operators are generated in MAD-GRAPH5_AMC@NLO 2.8.1 at LO in QCD with the NNPDF3.0NLO PDF set. The parton shower is performed with PYTHIA 8.244. NP effects are incorporated with the *Eboli model* [35, 122]. The process $pp \to \ell^+\ell^-\gamma\gamma$ is simulated, which includes contributions from FSR and virtual photons in the matrix element. This allows to reproduce the phase-space in the fiducial-volume to which the $Z\gamma\gamma$ analysis is unfolded. Throughout the EFT interpretation, a *decomposition approach* is chosen, which splits the matrix element into

---

[32] The $\gamma\gamma\gamma\gamma$ vertex must contain exactly one virtual photon $\gamma^* \to \ell\ell$ in the final state to contribute to the $\ell\ell\gamma\gamma$ phase-space.

SM and EFT contributions as well as interference terms:

$$|A|^2 = |A_{\mathrm{SM}} + f_i A_i|^2 = |A_{\mathrm{SM}}|^2 + \underbrace{f_i 2\mathrm{Re}\,(A_{\mathrm{SM}} A_i)}_{\text{linear term}} + \underbrace{f_i^2\,|A_i|^2}_{\text{quadratic term}} + \underbrace{f_i f_j 2\mathrm{Re}\,(A_i A_j)}_{\text{cross term}}. \quad (8.2)$$

A_{SM} and A_i describe the SM amplitude and the amplitude of all dimension-8 operators under consideration. The dimensionless Wilson coefficients are denoted by f_i. The *linear term* represents the SM-EFT interference and the *quadratic term* describes the pure EFT contribution. The *cross term* accounts for interference effects between different operators but is set to zero in the EFT interpretation as the contribution of one operator at a time is studied. A validation of the decomposition approach is presented in Appendix H.1. It demonstrates the agreement of the cross section and the modelling when generating one combined sample containing the full SM and EFT amplitude and when generating individual samples for each contribution in Equation 8.2. To verify the sensitivity of the $\ell\ell\gamma\gamma$ final state to contributions of $\mathcal{O}_{M,i}^8$ and $\mathcal{O}_{T,j}^8$, the generator cross sections for both types of operators are presented in Table 8.1. The interference term can be positive or negative and is larger (smaller) than the quadratic term for $\mathcal{O}_{M,i}^8$ ($\mathcal{O}_{T,j}^8$). Only one neutral vertex ($ZZ\gamma\gamma$) contributes to the $\ell\ell\gamma\gamma$ final state for $\mathcal{O}_{M,i}^8$ minimising the quartic contribution while the magnitude of the interference remains relatively large. The contribution of transverse operators is typically three orders of magnitude larger than that of mixed operators – all $\mathcal{O}_{M,i}^8$ operators are thus neglected due to the suppressed sensitivity.

In order to impose the fiducial selection summarised in Table 7.1, a $Z\gamma\gamma$ *Rivet* routine [123] is implemented. The fiducial phase-space requirements are applied to the generated $\mathcal{O}_{T,j}^8$ events and the differential cross sections are determined. Figure 8.1(a) shows a comparison between the SM expectation and the linear and quadratic term of $\mathcal{O}_{T,2}^8$ for $E_{\mathrm{T}}^{\gamma 1}$ after the selections of the Rivet routine are imposed. The linear and quadratic term predict harder $E_{\mathrm{T}}^{\gamma 1}$ spectra; for energies above approximately $800\,\mathrm{GeV}$ the quadratic term becomes the dominating contribution in the $Z\gamma\gamma$ phase-space. The predicted differential $p_{\mathrm{T}}^{\ell\ell}$ cross section is presented in Figure 8.1(b) for the SM and $\mathcal{O}_{T,8}^8$ – Appendix H.2 shows the same comparison for the remaining observables unfolded to particle-level. The transverse momentum of the dilepton system $p_{\mathrm{T}}^{\ell\ell}$ offers the largest sensitivity for EFT effects in the $Z\gamma\gamma$ analysis: the predicted integrated cross section of the $\mathcal{O}_{T,8}^8$ quadratic term amounts to 3.1% of the SM expectation[33]. Most sensitivity stems from the last bin where the SM contribution is expected to be small and the quadratic term has a sizeable impact.

---

[33]The second-largest contribution is 1.2% for $E_{\mathrm{T}}^{\gamma 2}$, see Appendix H.2.
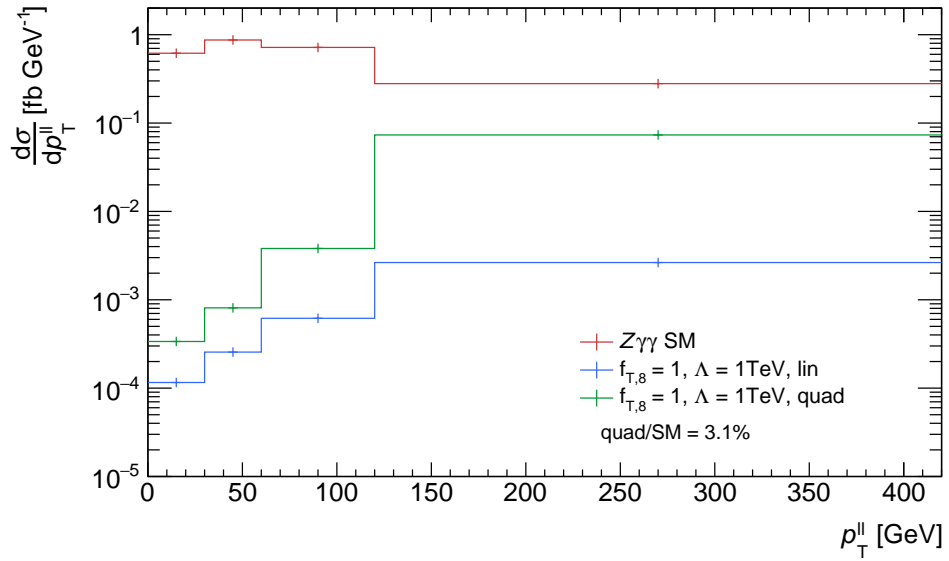
Table 8.1.: Generator cross sections for $\mathcal{O}^8_{M,i}$ and $\mathcal{O}^8_{T,j}$ with minimal kinematic requirements for p^ℓ_{T}, p^γ_{T}, and the invariant mass $m_{\ell\ell}$. The Wilson coefficients are set to unity and the NP scale is chosen as $\Lambda = 1\,\mathrm{TeV}$. The linear and quadratic terms are indicated by '*lin*' and '*quad*', respectively.

Operator	*lin* cross section [fb]	*quad* cross section [fb]
$\mathcal{O}^8_{M,0}$	$+2.7 \times 10^{-5}$	$+1.7 \times 10^{-7}$
$\mathcal{O}^8_{M,1}$	-7.3×10^{-6}	$+6.3 \times 10^{-8}$
$\mathcal{O}^8_{M,2}$	$+1.7 \times 10^{-4}$	$+7.3 \times 10^{-6}$
$\mathcal{O}^8_{M,3}$	-4.8×10^{-5}	$+2.7 \times 10^{-6}$
$\mathcal{O}^8_{M,4}$	-4.8×10^{-5}	$+5.6 \times 10^{-7}$
$\mathcal{O}^8_{M,5}$	-2.6×10^{-5}	$+8.2 \times 10^{-7}$
$\mathcal{O}^8_{M,7}$	$+3.6 \times 10^{-6}$	$+1.6 \times 10^{-8}$
$\mathcal{O}^8_{T,0}$	$+3.2 \times 10^{-3}$	$+1.7 \times 10^{-2}$
$\mathcal{O}^8_{T,1}$	$+3.2 \times 10^{-3}$	$+1.7 \times 10^{-2}$
$\mathcal{O}^8_{T,2}$	$+2.3 \times 10^{-3}$	$+4.4 \times 10^{-3}$
$\mathcal{O}^8_{T,5}$	$+3.0 \times 10^{-3}$	$+7.1 \times 10^{-2}$
$\mathcal{O}^8_{T,6}$	$+1.3 \times 10^{-3}$	$+3.9 \times 10^{-2}$
$\mathcal{O}^8_{T,7}$	$+1.5 \times 10^{-3}$	$+8.2 \times 10^{-3}$
$\mathcal{O}^8_{T,8}$	$+8.4 \times 10^{-3}$	$+7.2 \times 10^{-1}$
$\mathcal{O}^8_{T,9}$	$+6.0 \times 10^{-3}$	$+1.8 \times 10^{-1}$

(a)

(b)

Figure 8.1.: Comparison of the SM expectation and the EFT predictions of $\mathcal{O}_{T,2}^8$ and $\mathcal{O}_{T,8}^8$ in the $Z\gamma\gamma$ fiducial phase-space. The $E_T^{\gamma_1}$ modelling of $\mathcal{O}_{T,2}^8$ is presented in (a). The differential $p_T^{\ell\ell}$ cross section predicted by $\mathcal{O}_{T,8}^8$ is shown in (b). The integrated cross section of the quadratic term divided by the $Z\gamma\gamma$ SM expectation represents a measure for the sensitivity to EFT effects (indicated by 'quad/SM'). The MC simulations are performed with $f_{T,2}^8 = f_{T,8}^8 = 1$ and $\Lambda = 1\,\text{TeV}$.

8.2. Statistical Model

Constraints are placed on the *coupling parameters* of transverse operators $\mathcal{O}_{T,j}^8$ in a fitting framework centrally provided by the ATLAS experiment [124]. The coupling parameters are defined by dividing the Wilson coefficients by the NP energy scale: $f_{T,j}^8/\Lambda^4$. The constraints are constructed from a profile likelihood ratio scan using the measured and predicted differential cross sections of $p_T^{\ell\ell}$ and all sources of uncertainty. The predicted cross section μ^{pred} in a single bin is parametrised as the sum of the SM expectation and possible EFT contributions in the form of linear and quadratic terms:

$$
\begin{aligned}
\mu^{\mathrm{pred}}\left(\boldsymbol{f},\boldsymbol{\theta}\right) = \sigma^{\mathrm{SM}} &\times \prod_i \left(1 + \theta_i u_i\right) \\
&+ \sum_j \sigma_j^{\mathrm{lin}} f_j \times \prod_i \left(1 + \theta_{i,j}^{\mathrm{lin}} u_{i,j}^{\mathrm{lin}}\right) \\
&+ \sum_j \sigma_j^{\mathrm{quad}} f_j^2 \times \prod_i \left(1 + \theta_{i,j}^{\mathrm{quad}} u_{i,j}^{\mathrm{quad}}\right).
\end{aligned}
\tag{8.3}
$$

The vector $\boldsymbol{f}$ consists of the coupling parameters of all transverse operators. As mentioned before, constraints are placed on one parameter at a time, while all other parameters are set to zero. $\boldsymbol{\theta} = (\theta_1, \ldots, \theta_{n_{\mathrm{theo}}})$ contains the n_{theo} theoretical uncertainties (described in more detail below) that are separately derived for the SM expectation, and the linear and quadratic term of each operator. The relative shift of the theory uncertainties is given by u_i. The measured cross section $\boldsymbol{x}^{\mathbf{meas}}$ and $\boldsymbol{\mu}^{\mathbf{pred}}$ are used to construct the likelihood function represented by a multivariate Gaussian distribution:

$$
\begin{aligned}
L\left(\boldsymbol{x}^{\mathbf{meas}} \mid \boldsymbol{f},\boldsymbol{\theta}\right) = \frac{1}{\sqrt{(2\pi)^k \det\left(\boldsymbol{\Sigma}\right)}} &\times \exp\left(-\frac{1}{2}\boldsymbol{\Delta x}^{\mathrm{T}}\boldsymbol{\Sigma}^{-1}\boldsymbol{\Delta x}\right) \\
&\times \prod_l^{n_{\mathrm{theo}}} \prod_i \left[\mathcal{G}_i\left(\theta_i\right)\right]_l.
\end{aligned}
\tag{8.4}
$$

Theory uncertainties for the SM and EFT contributions, indicated by $l \in \{\mathrm{SM}, \mathrm{lin}, \mathrm{quad}\}$, are modelled by additional Gaussian constraints $\mathcal{G}_i\left(\theta_i\right)$. The difference between the measured and predicted cross section for all k bins is represented by $\boldsymbol{\Delta x} = \boldsymbol{x}^{\mathbf{meas}} - \boldsymbol{\mu}^{\mathbf{pred}}$. The covariance matrix $\boldsymbol{\Sigma}$ is constructed from the sources of experimental uncertainty and contains correlations between the k $p_T^{\ell\ell}$ bins. All systematic uncertainties are assumed to be fully correlated between bins. A given systematic uncertainty therefore shifts the cross section in all bins in the same direction. The correlation between different sources

of uncertainty is neglected. Bin migrations occurring in the unfolding procedure can also introduce a correlation of the statistical uncertainty. The $p_{\mathrm{T}}^{\ell\ell}$ bin migrations are typically small, resulting in at most 8% correlation of the statistical uncertainty. The variation of the limits when accounting for this correlation is smaller than 1% for which reason it was decided to neglect the inclusion of statistical correlations. The profile likelihood ratio is defined by

$$\lambda_{\mathrm{p}}\left(f_j\right) = -2\ln\left(\frac{L\left(f_j, \hat{\hat{\theta}}\right)}{L\left(\hat{f}_j, \hat{\theta}\right)}\right).\tag{8.5}$$

The term $L\left(f_j, \hat{\hat{\theta}}\right)$ determines the maximum of the likelihood for fixed values of f_j, while $L\left(\hat{f}_j, \hat{\theta}\right)$ measures the absolute maximum likelihood at $\hat{f}_j$. Limits at 95% confidence level (CL) on the coupling parameters are derived from λ_{p} by applying Wilks' theorem [125] and thus assuming that the test statistic follows a χ^2 distribution. The total experimental uncertainty, and the breakdown into the individual contributions, is shown in Figure 8.2. The contributions of certain uncertainties, e.g. the photon identification and isolation, are added for improved visibility but are kept separated in the fit to maintain the maximum constraining power. The total experimental uncertainty ranges from 17% to 25% in the last $p_{\mathrm{T}}^{\ell\ell}$ bin. The list of theoretical uncertainties is identical to the one discussed in Section 7.1: variations of μ_F and μ_R, of the PDF set, and of α_s are included. This is done for the SHERPA NLO signal sample and the linear and quadratic terms of $\mathcal{O}_{T,j}^8$. The scale uncertainty has the largest magnitude reaching up to 22.8%. A consistency test of the fitting procedure is performed in Appendix H.3, where it is demonstrated that the limits published by a previous $Z\gamma\gamma$ analysis can be recovered.
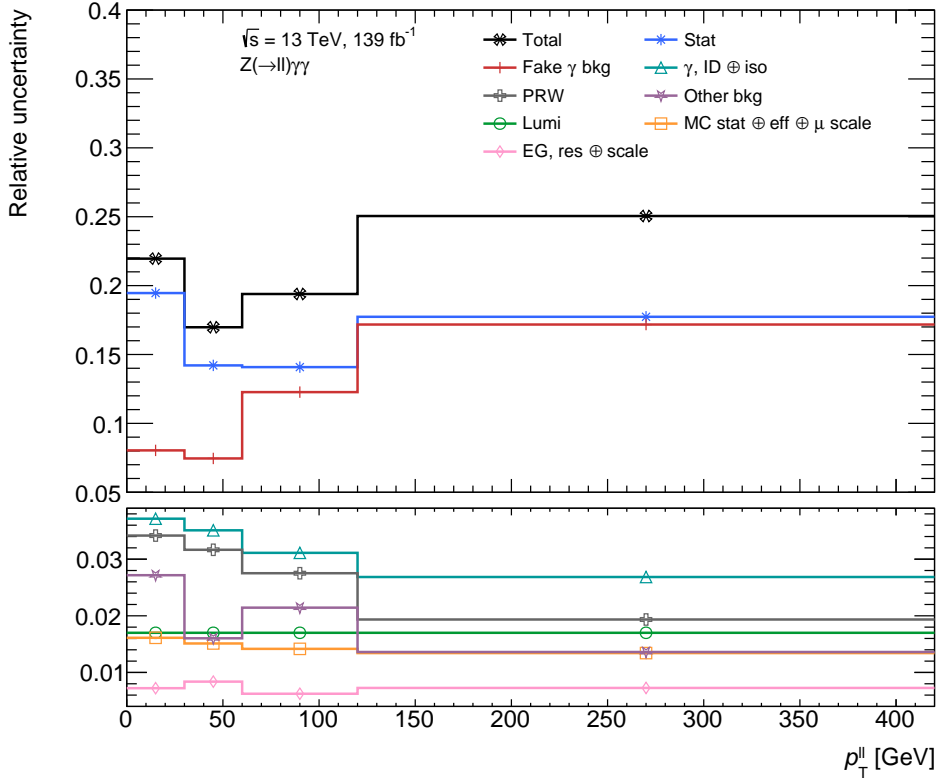
Figure 8.2.: Sources of experimental uncertainty on the unfolded cross-section measurement of $p_T^{\ell\ell}$. Certain uncertainties are added in quadrature, symbolised by $\oplus$, to improve the visibility. The largest contribution to the total uncertainty stems from the data statistics (blue line). The orange line corresponds to uncertainties that are not correlated between the electron and muon channel: statistics from the MC samples, the lepton efficiencies, and the muon momentum scale.

8.3. Non-unitarised Limits

Expected and observed limits are derived by using the profile likelihood ratio scan presented in Equation 8.5. The treatment of unitarisation constraints is discussed in Section 8.4. Limits are derived for the combined electron and muon channel. The nominal SHERPA NLO prediction is used as SM expectation in the fit. Its pre-fit contribution is shown in Figure 8.3(a), together with the measured differential cross section and the summed EFT prediction (lin + quad) of $\mathcal{O}_{T,8}^8$. The EFT prediction in the last bin with the highest NP sensitivity is sizeable and amounts to 17.8% of the measured cross section. A SM LO $Z\gamma\gamma$ prediction is depicted as well, which is used in the next paragraph to derive higher-order QCD correction factors; a slightly softer $p_T^{\ell\ell}$ spectrum is predicted at LO. Figure 8.3(b) shows the λ_p distribution, which is scanned in the determination of confidence intervals for the coupling parameter $f_{T,8}^8/\Lambda^4$. The observed intervals are

slightly anti-symmetric and amount to $[-1.64, 1.61] \times \Lambda^{-4}$. The results of the measured and expected confidence intervals for all transverse operators $\mathcal{O}_{T,j}^{8}$ are given in Figure 8.4. The expected confidence intervals are derived by constructing Asimov datasets, in which the measured cross section and experimental uncertainties are replaced by the expected ones. The observed limits are typically 11%–12% less stringent than those expected. This is driven by two effects. The larger contribution of fake photons in data increases the fake photon normalisation and shape uncertainty on the differential cross section. Additionally, the measured cross section in the last bin is approximately 13.6% larger than the predicted one, which decreases the EFT contribution in this bin.

The EFT predictions are determined at LO accuracy in QCD as higher-order corrections are not available in the EFT formalism. The effect of such corrections on the confidence intervals can be estimated by assuming that the EFT prediction scales similarly to the SM in terms of higher-order QCD corrections. The differential cross section predicted by the $Z\gamma\gamma$ MADGRAPH5_AMC@NLO NLO simulation (see Table 5.6) is divided by the $Z\gamma\gamma$ MADGRAPH5_AMC@NLO LO prediction shown in Figure 8.3(a). This procedure delivers bin-by-bin correction factors, which are multiplied to the differential cross sections predicted by $\mathcal{O}_{T,j}^{8}$. The scan of the profile likelihood ratio is repeated and new confidence intervals are extracted. The expected and observed constraints on the coupling parameters $f_{T,j}^{8}/\Lambda^{4}$ are 13%–15% more stringent. This demonstrates that higher-order QCD corrections have a sizeable impact on the extracted confidence intervals. The underlying assumption can not be validated in the EFT formalism, for which reason the nominal limits are determined without the correction factors.

This analysis provides the first constraints published the ATLAS experiment at a centre-of-mass energy of $13\,\text{TeV}$ for the four transverse operators $\mathcal{O}_{T,1}^{8}$, $\mathcal{O}_{T,2}^{8}$, $\mathcal{O}_{T,6}^{8}$, and $\mathcal{O}_{T,7}^{8}$. The confidence intervals are up to two orders of magnitude more stringent than those extracted at $8\,\text{TeV}$.
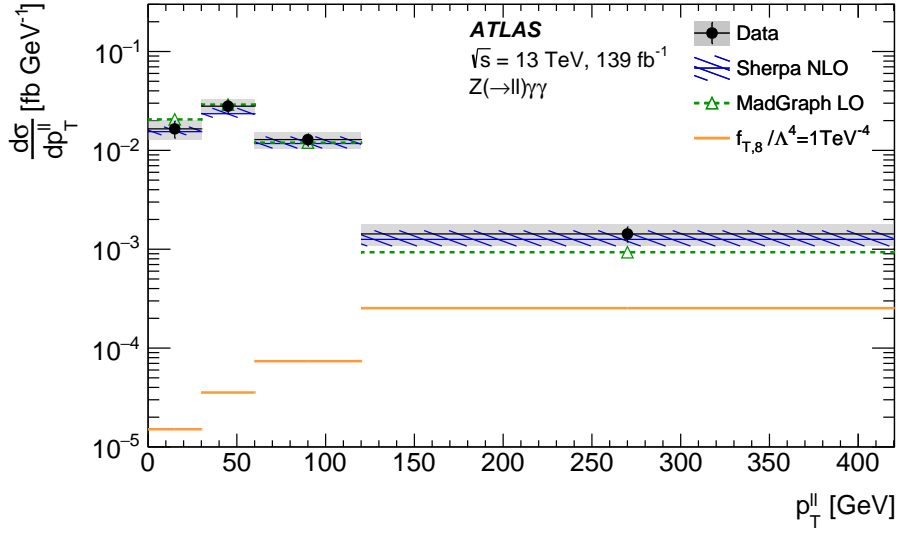
(a)
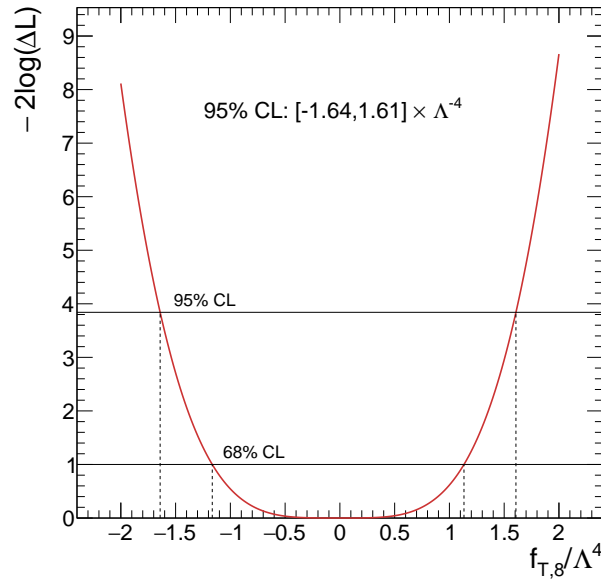
(b)

Figure 8.3.: Distribution of (a) the $p_T^{\ell\ell}$ cross section prior to the maximum likelihood estimation and (b) the profile likelihood ratio λ_p, both for NP contributions of $\mathcal{O}_{T,8}^8$. The black uncertainty bar on data in (a) represents the statistical uncertainty and the grey uncertainty band corresponds the total uncertainty. The uncertainty in the SHERPA prediction includes both the statistical and theoretical uncertainties. The NP contribution contains the sum of the linear and quadratic term. The vertical dashed lines in (b) indicate the confidence intervals at 95% and 68% CL. The horizontal solid lines represent the value of λ_p below which the area of a χ^2 distribution corresponds to the 95th and 68th percentile of the probability density. The figure in (a) is taken from [41].
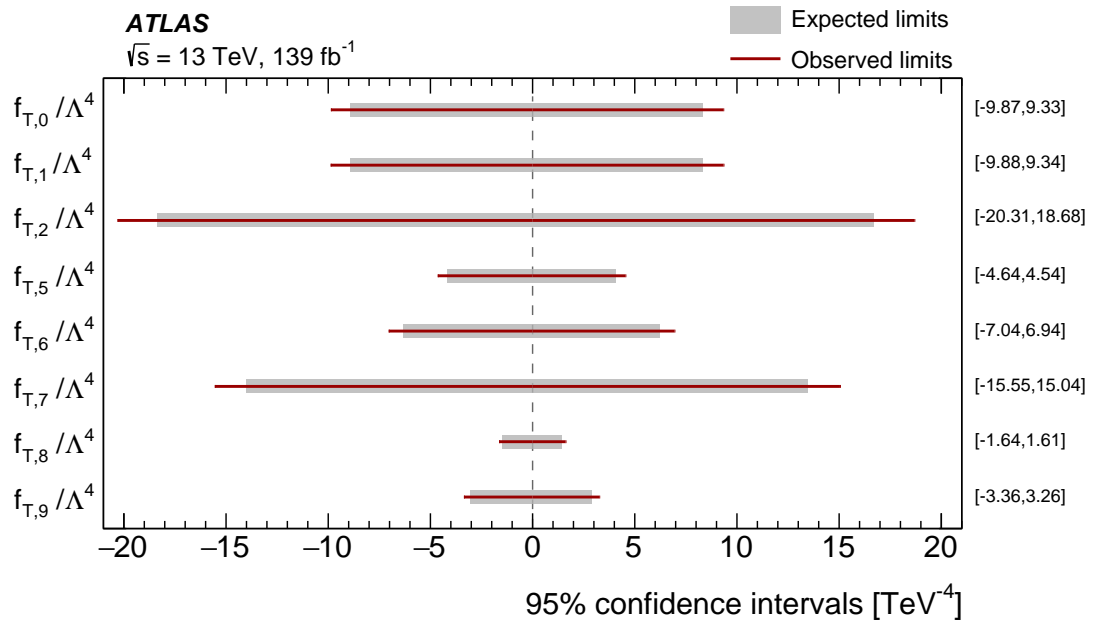
Figure 8.4.: Expected and observed limits on the coupling parameters $f^8_{T,j}/\Lambda^4$ of transverse operators $\mathcal{O}^8_{T,j}$. The values of the coupling parameters outside of the presented range are excluded at 95% confidence level. The right border of the figure contains the numeric values of the observed limits. Unitarisation constraints are not considered. The figure is taken from [41].

8.4. Unitarisation Treatment

Amplitudes predicted by EFT operators can grow proportional to s violating unitarity at sufficiently high energies; the theoretical model of EFT is therefore not complete. A cut-off scale is introduced to prevent the violation of unitarity at large energies. The confidence intervals for all transverse operators are determined as functions of this scale. A technique which is typically referred to as *clipping* [126] is used in this thesis. Various *clipping energies*[34] E_c are chosen, above which the contributions of the linear and quadratic terms are suppressed. This is realised by studying the generated EFT samples at parton-level, i.e. before the parton shower is performed. The EFT contributions are suppressed in events where the invariant mass of the four-body-system $m_{\ell\ell\gamma\gamma}$, which is a measure for the hard scale of the interaction, exceeds the clipping energy. The SM contribution is not truncated. The effect of this clipping procedure is demonstrated in Figure 8.5. The more stringent E_c becomes, the more truncated the EFT prediction gets for large energies. Figure 8.6 presents the evolution of the confidence intervals for transverse operator $\mathcal{O}_{T,8}^8$. The clipping energy is varied between $1.1\,\mathrm{TeV}$ and $5\,\mathrm{TeV}$. The confidence intervals become 4–5 more stringent in this range. A similar behaviour is observed for the remaining dimension-8 operators (see Appendix H.4). The non-unitarised and unitarised confidence intervals are published on HEPData [120].

---

[34]The thresholds are chosen to harmonise the clipping procedure along various ATLAS analyses placing limits on dimension-8 operators, such as [127].
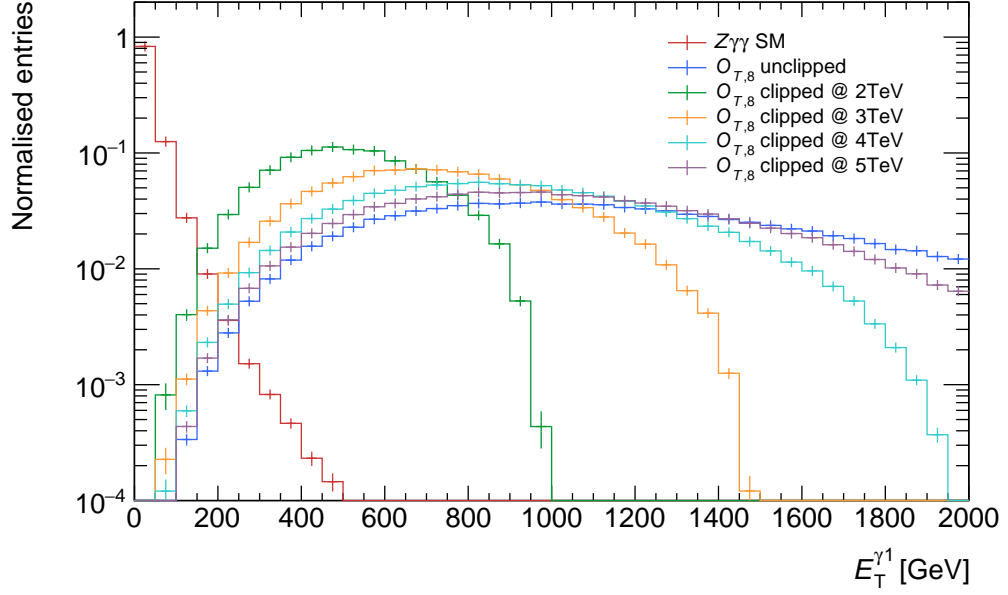
Figure 8.5.: Effect of clipping procedure on $E_T^{\gamma 1}$ predicted by $\mathcal{O}_{T,8}^8$ (quadratic term only) for E_c thresholds between 2 and $5\,\mathrm{TeV}$. The distribution of the SM expectation, which is not truncated, is shown as reference.
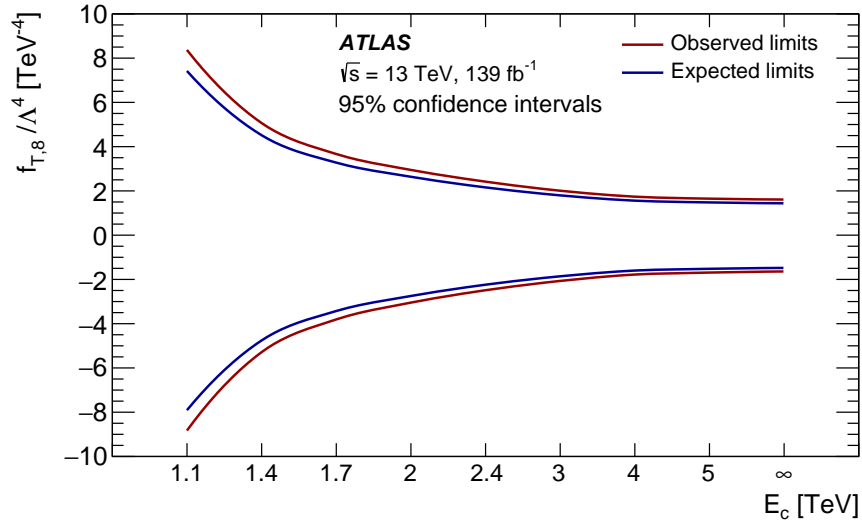
Figure 8.6.: Evolution of the expected and observed limits as functions of the clipping energy between $1.1\,\mathrm{TeV}$ and $5\,\mathrm{TeV}$ for the coupling parameter $f_{T,8}^8/\Lambda^4$. The non-unitarised limits correspond to $E_c = \infty$. The values of the coupling parameter above the upper or below the lower expected and observed limits are excluded at 95% confidence level. The figure is taken from [41].

9. Summary

Experimental measurements which probe the predictions of the SM electroweak sector are crucial to understand fundamental properties like gauge-boson self-interactions. Final states with multiple electroweak gauge bosons can test the non-Abelian character of the $\mathrm{SU(2)_L \times U(1)_Y}$ symmetry, which prohibits purely neutral triple or quartic gauge boson couplings. The simultaneous production of $Z\gamma\gamma$ is therefore sensitive to new physics contributions of higher-dimensional operators.

The Run 2 dataset is analysed containing $139\,\mathrm{fb}^{-1}$ of p–p collisions delivered by the LHC at $\sqrt{s} = 13\,\mathrm{TeV}$ and recorded with the ATLAS detector. The event selection is optimised to select $\ell\ell\gamma\gamma$ events while having a strong background suppression and contains a highly efficient rejection requirement for photons from final state radiation. Integrated and differential cross sections are measured for the $Z\gamma\gamma$ triple gauge boson production.

Events containing $\ell\ell\gamma\gamma$ final states are selected with 71% purity. The dominant background contribution originates from non-prompt photon production. The event yield of this background process is determined with two data-driven methods utilising the hadronic activity that is found in proximity of non-prompt photons. Both methods deliver compatible results and a 20% non-prompt photon contamination is measured. The remaining background contributions stem predominantly from the $t\bar{t}\gamma\gamma$ process and from pile-up, where two independent processes overlay to form the $\ell\ell\gamma\gamma$ final state.

The cross-section measurements are performed in a fiducial volume at particle-level. The detector effects are corrected inclusively by comparing the predicted number of events passing the reconstruction- and particle-level requirements and differentially by performing an iterative Bayesian unfolding. The measured integrated cross section is $\sigma_{\ell\ell\gamma\gamma}^{\mathrm{fid}} = 2.45 \pm 0.20\,(\mathrm{stat.}) \pm 0.22\,(\mathrm{sys.}) \pm 0.04\,(\mathrm{lumi.})\,\mathrm{fb}$, which is the most accurate $Z\gamma\gamma$ cross-section measurement up to date. Differential $Z\gamma\gamma$ cross sections are determined for the first time for six kinematic observables and are compared to predictions of MC event generators at NLO QCD precision showing good agreement across all bins.

The cross-section measurement as a function of $p_{\mathrm{T}}^{\ell\ell}$ is used to constrain new physics effects in an EFT approach. The contributions of dimension-8 operators are generated in the fiducial volume and a profile likelihood ratio scan is performed to obtain limits for the Wilson coefficients. Unitarisation constraints are taken into account by truncating EFT contributions above high energy scales. The non-unitarised limits for several dimension-8 operators are the first published by the ATLAS experiment at $13\,\mathrm{TeV}$ and improve the previous constraints by up to two orders of magnitude.

A. Signal Significance Optimisation

The photon p_T threshold significantly impacts the $Z\gamma\gamma$ analysis. Ideally, it would be chosen as small as possible to increase the signal sensitivity. However, the relative contributions of background processes, primarily non-prompt photons from the fragmentation of jets (abbreviated as fake photons), increase with smaller p_T as such processes typically contain low-energetic photons. A similar p_T dependence is seen for systematic uncertainties affecting the determination of the number of events with fake photons. A scan of the signal sensitivity as a function of the photon p_T is thus performed, which is based on the predictions of a LO $Z\gamma\gamma$ simulation and the two background processes which are expected to contribute the most: the aforementioned fake photon background and the photon-associated top-quark pair production $t\bar{t}\gamma\gamma$[35].

The optimisation of the signal significance was performed at a time when the $Z\gamma\gamma$ analysis was still blinded. The blinding procedure is done in order to avoid introducing a bias to the analysis when optimising the event selection while having access to the full available dataset. This means that the fake photon background could not yet be determined in the $Z\gamma\gamma$ SR in data. The number of events containing fake photons for each photon p_T threshold is instead calculated with MC simulation. The predicted event yield is corrected by comparing the number of predicted fake photon events in a fake-enriched data CR to the number of observed events[36].

The signal significance Z is calculated with the following equation [128]:

$$Z = \frac{N_S}{\sqrt{N_\mathrm{S} + N_\mathrm{B} + \sigma_\mathrm{B,sys}^2}}, \tag{A.1}$$

where N_S and N_B denote the number of signal and background events, respectively. Systematic uncertainties on the background contributions $\sigma_\mathrm{B,sys}$ are included in the estimation of Z. The systematic uncertainties on the number of fake photons is determined with a data-driven method using toydata constructed from the predicted SR contributions of signal and fake photon events. This method is based on a similar approach as the matrix method (nominal data-driven method to determine the number of fake photon events, see Section 6.1.1) but uses additional control regions in data. It was found to be unstable yielding fits with zero signal normalisation, for which reason it was not further considered in the $Z\gamma\gamma$ analysis. It gives, however, a reasonable approximation of the

---

[35]More information on the signal and the background processes is given in Sections 5.3 – 5.4.
[36]This procedure is introduced in Section 6.1.4.

Table A.1.: Determination of the signal significance in dependence of three photon p_{T} thresholds. The two values in the first column indicate the p_{T}^{γ} requirement applied to the leading and subleading photon. Note that the event yields for $Z\gamma\gamma$ and $t\bar{t}\gamma\gamma$ presented here and in Section 6.6 differ as the signal significance study was performed before the event selection was fully finalised.

p_{T}^{γ} cut [GeV]	$Z\gamma\gamma$ Events	Fake γ events	$t\bar{t}\gamma\gamma$ events	Significance Z
$15, 15$	297	53 ± 27	26 ± 8	8.8
$20, 20$	206	25 ± 6	20 ± 6	11.4
$25, 25$	149	18 ± 14	12 ± 4	7.7

size of the systematic uncertainty. The most dominant systematic uncertainty on the fake photon background is considered and related to a correlation parameter. It accounts for the correlation of the photon identification and isolation in fake-enriched control regions. The second source of systematic uncertainty stems from the $t\bar{t}\gamma\gamma$ process. A conservative uncertainty of 30% is assigned on its normalisation. This accounts for missing higher-order corrections in the cross-section calculation [129].

The results of the signal significance optimisation are summarised in Table A.1. The largest signal sensitivity is obtained when both photons need to pass the lowest p_{T} threshold ($p_{\mathrm{T}}^{\gamma} > 15\,\mathrm{GeV}$), but this phase-space also contains the largest contribution of fake photons and large associated systematic uncertainties. The most stringent requirement of $p_{\mathrm{T}}^{\gamma} > 25\,\mathrm{GeV}$ leads to a substantial loss of signal events. The largest signal significance is thus given for photons passing $p_{\mathrm{T}}^{\gamma} > 20\,\mathrm{GeV}$.

B. Trigger Studies

Table B.1 summarises the requirements placed on electrons before the offline-to-online harmonisation is performed.

Table B.1.: Offline electron requirements prior to the offline-to-online harmonisation for single and dielectron triggers.

Trigger	Lepton requirements
Single electron	$p_T(\ell_1) > 30\,\mathrm{GeV}$, $p_T(\ell_2) > 20\,\mathrm{GeV}$ medium ID loose iso
Dielectron	$p_T(\ell_1) > 20\,\mathrm{GeV}$, $p_T(\ell_2) > 20\,\mathrm{GeV}$ medium ID loose iso

The requirements that are placed on muons prior to the offline-to-online harmonisation are listed in Table B.2.

Table B.2.: Offline muon requirements prior to the offline-to-online harmonisation for single, symmetric, and asymmetric dimuon triggers.

Trigger	Lepton requirements
Single muon	$p_T(\ell_1) > 30\,\mathrm{GeV}$, $p_T(\ell_2) > 20\,\mathrm{GeV}$ medium ID loose iso
Dimuon symmetric	$p_T(\ell_1) > 20\,\mathrm{GeV}$, $p_T(\ell_2) > 20\,\mathrm{GeV}$ medium ID loose iso
Dimuon asymmetric	$p_T(\ell_1) > 25\,\mathrm{GeV}$, $p_T(\ell_2) > 20\,\mathrm{GeV}$ medium ID loose iso

C. 2D Template Fit

C.1. Validation of Prompt Photon Templates

The shape of the isolation energy of prompt photons is verified in a CR in data. The ISR selection is inverted to exclusively select photons being emitted in FSR:

$$m_{\ell\ell} + \min\left(m_{\ell\ell\gamma 1}, m_{\ell\ell\gamma 2}\right) < 2 \times m_Z - m_{\mathrm{g}}. \tag{C.1}$$

To distinguish the ISR and FSR phase-space further, an additional mass gap of $m_{\mathrm{g}} = 2\,\mathrm{GeV}$ is introduced.

The full Run 2 luminosity is analysed in the data CR. The same procedure is performed for events of the SHERPA 2.2.10 $Z\gamma\gamma$ simulation to compare the shape of the observables that are used in the definition of the isolation energy $E^{\mathrm{iso}} = E_{\mathrm{T}}^{\mathrm{cone20}} - 0.065 \times p_{\mathrm{T}}^{\gamma}$. Except for the ISR inversion, the nominal event selection of the 2D template fit in the signal region is required. This selects events in which both photons pass the TT identification. The validation of the shape of the calorimeter isolation energy $E_{\mathrm{T}}^{\mathrm{cone20}}$ and the full isolation energy E^{iso} is shown in Figure C.1 for the leading photon. The same behaviour is seen for the subleading photon. The predicted shape of the $Z\gamma\gamma$ simulation agrees with the dataset within the statistical uncertainty for most bins. No systematic shift is visible. It is concluded that the observables of interest are well modelled for the FSR-enriched phase-space, i.e. events containing typically lower-p_{T} photons.

To verify the modelling of the isolation energy of higher-p_{T} photons, the dataset for which the ISR selection is inverted is compared to the $Z\gamma\gamma$ simulation where the nominal ISR selection is required. This gives rise to photon p_{T} and E^{iso} spectra that deviate significantly between the simulation and data due to the difference in the photon energy scale. However, the bare calorimeter isolation energy is not expected to depend on the photon energy - this is verified in Figure C.2. Under the assumption that the p_{T} spectrum of higher energy photons is reasonably well modelled in MC simulation, it is concluded that the E^{iso} modelling of prompt photons in the $Z\gamma\gamma$ simulation reflects the behaviour observed in data.
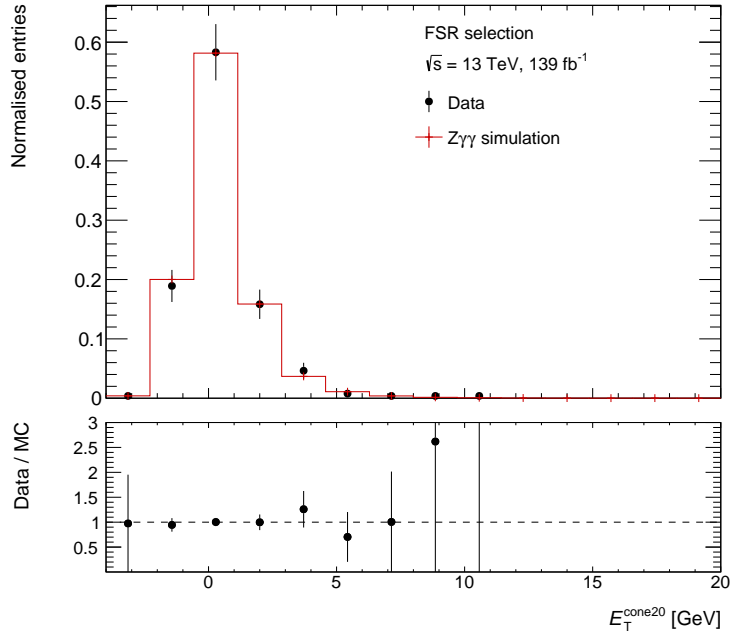
(a)
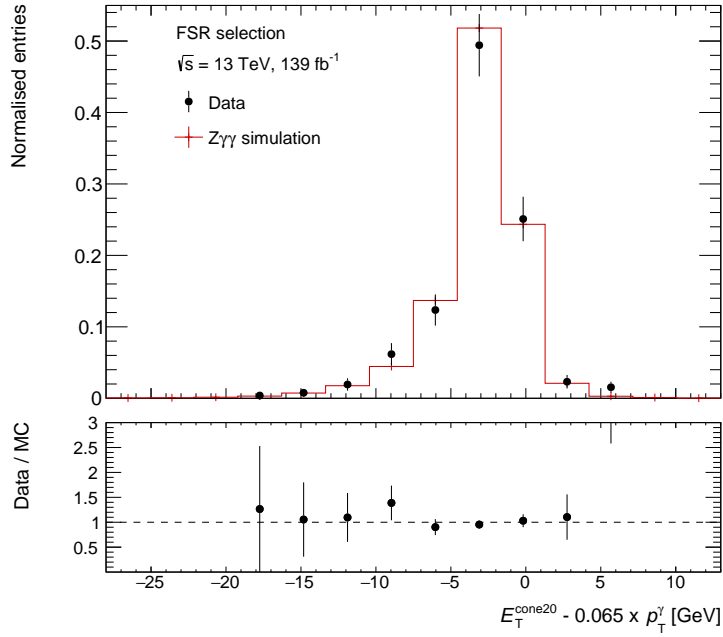
(b)

Figure C.1.: Validation of the modelling of (a) the calorimeter isolation energy E_T^{cone20} and (b) the full isolation energy E^{iso}. For both the SHERPA 2.2.10 $Z\gamma\gamma$ simulation and the full Run 2 dataset, the ISR selection is inverted to exclusively select FSR photons. Events are required to have two photons passing the TT identification.
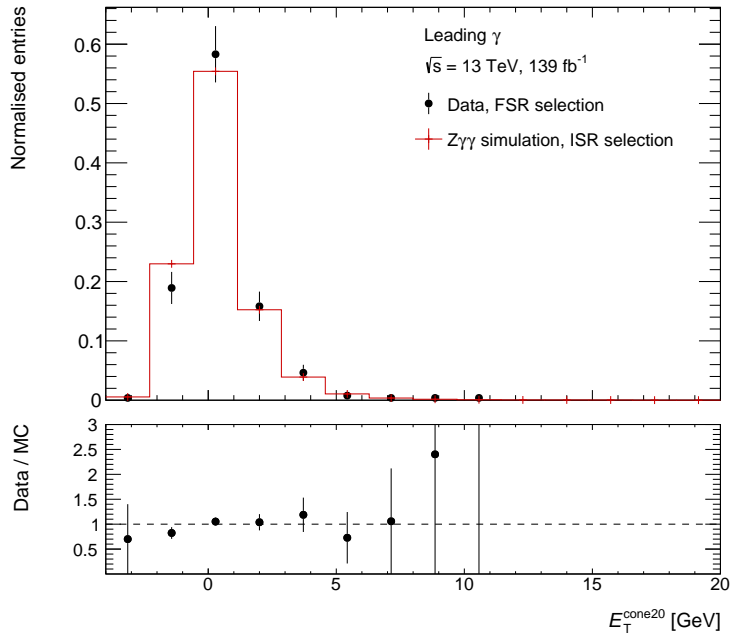
(a)
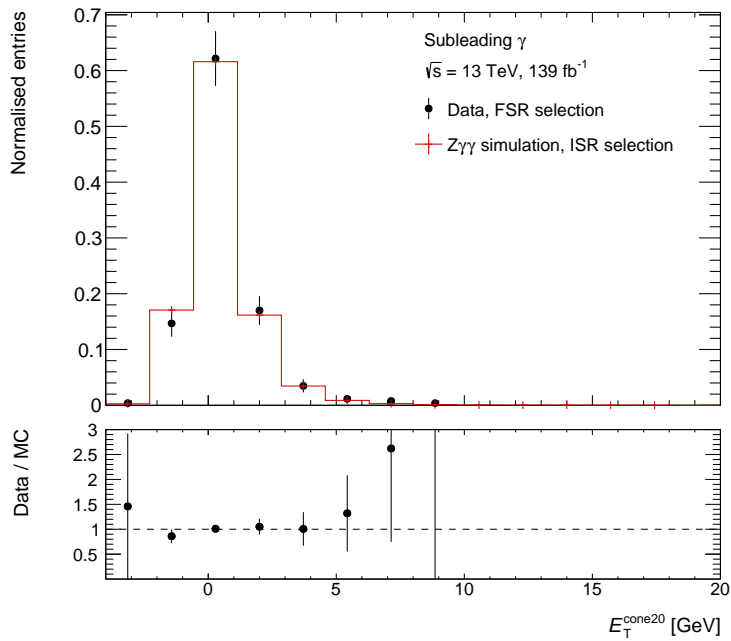
(b)

Figure C.2.: Validation of the modelling of the calorimeter isolation energy for (a) the leading photon and (b) the subleading photon. The nominal ISR selection is required for the SHERPA 2.2.10 $Z\gamma\gamma$ simulation, whereas the ISR selection is inverted for the full Run 2 dataset. Events are required to have two photons passing the TT identification.

C.2. Validation of Fake Photon Templates

The isolation energy shape for processes having exactly one fake photon is validated in a CR in data. The FT (TF) identification is required to select events containing a leading (subleading) fake photon. The nominal event selection of the 2D template fit is performed.

Fake photon PDFs are extracted from the $Z\gamma + $ jets MC simulation completely analogues to the procedure described in Section 6.1.2.2. The shape of the PDFs is fixed and they are subsequently fitted to the observed isolation energy in the data CR to verify the simulated E^{iso} distribution. The normalisation of $N_{\gamma j}$ or $N_{j\gamma}$ is allowed to float in the fit. A set of subsequent fits is performed where the nominal PDFs are replaced by shifted ones to consider the $\pm 1\sigma$ variations of the fit parameters of the Bukin function accounting for the statistical precision in the nominal template extraction[37]. The shifted PDFs are chosen to verify if the dominant source of systematic uncertainty covers deviations in the comparison of the E^{iso} shape in the FT and TF data CRs. The results are split into $+1\sigma$ up-variations, see Figure C.3, and -1σ down-variations, see Figure C.4. The reduced χ^2 value of the fit of the nominal PDFs to E^{iso} in the data CRs is shown as well and is close to unity, which highlights the decent modelling of the isolation energy in simulation. For both the comparison in the FT and TF data CR a fit can be found which brings the pull in nearly all bins below $\pm 1\sigma$. This is considered to cover potential shape mis-modelling of the $Z\gamma + $ jets MC simulation such that no additional systematic uncertainty is assigned.

---

[37]See the discussion of systematic uncertainties in Section 6.1.2.5 for a detailed description of the $\pm 1\sigma$ variations.
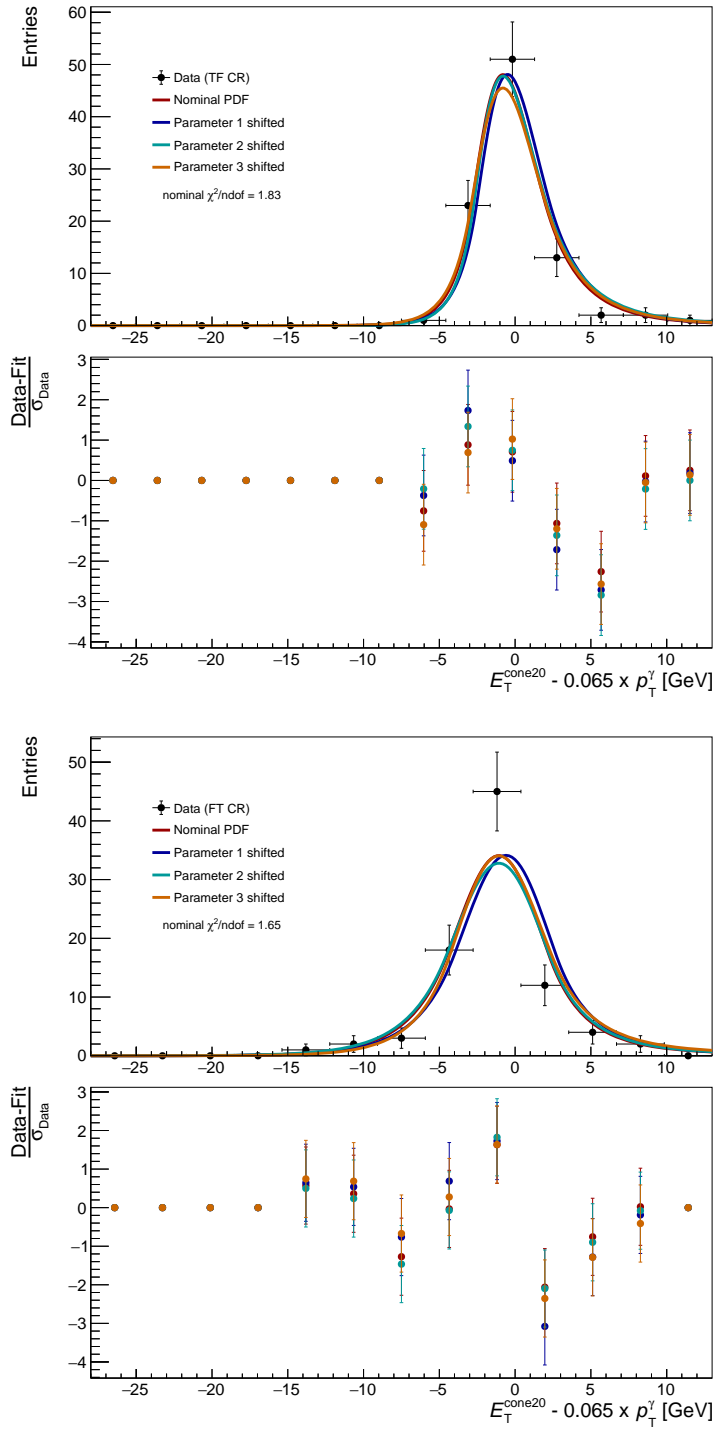
Figure C.3.: Validation of fake photon E^{iso} modelling. The nominal fake photon template (red) and shifted templates (blue to orange) are fitted to (a) the subleading photon in the TF data CR and (b) the leading photon in the FT data CR. The shifts correspond to $+1\sigma$ up-variations of the Bukin PDF parameters.
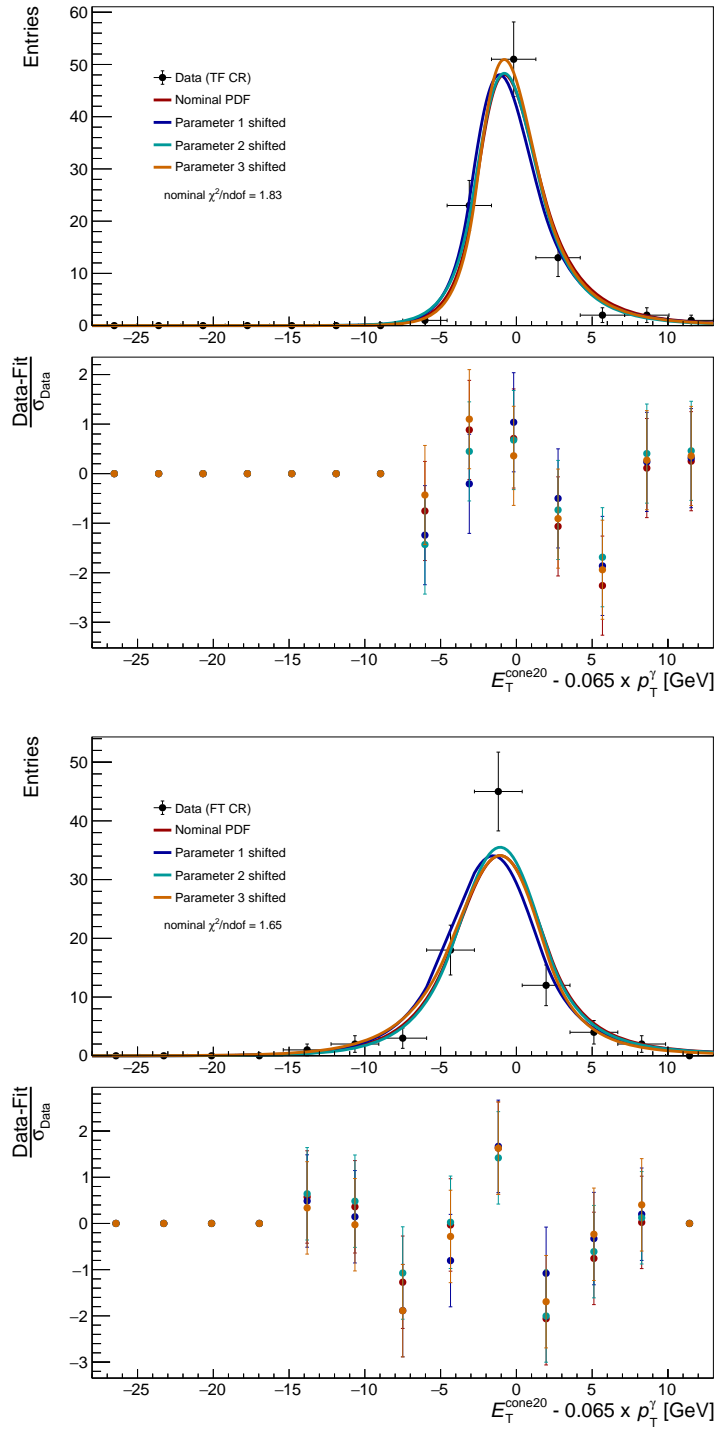
Figure C.4.: Validation of fake photon E^{iso} modelling. The nominal fake photon template (red) and shifted templates (blue to orange) are fitted to (a) the subleading photon in the TF data CR and (b) the leading photon in the FT data CR. The shifts correspond to -1σ down-variations of the Bukin PDF parameters.

C.3. Numeric Approach for Signal Leakage Correction

The measured isolation energy in the SR is given by

$$I = N_{\gamma\gamma}T_{\gamma_1}T_{\gamma_2} + N_{\gamma j}T_{\gamma_1}T_{j_2} + N_{j\gamma}T_{j_1}T_{\gamma_2} + N_{jj}T_{jj}. \tag{C.2}$$

It represents the ideal case, in which no signal leakage is present. This leakage affects the extracted E^{iso} templates in data CRs, i.e. the FF CR in the 2D template fit. Equation C.2 can be re-written in the following way to account for leakage of prompt photons into region FF:

$$I^{\mathrm{M}} = N_{\gamma\gamma}^{\mathrm{M}}T_{\gamma_1}T_{\gamma_2} + N_{\gamma j}^{\mathrm{M}}T_{\gamma_1}T_{j_2} + N_{j\gamma}^{\mathrm{M}}T_{j_1}T_{\gamma_2} + N_{jj}^{\mathrm{M}}T_{\mathrm{mm}}. \tag{C.3}$$

The measured isolation energy I^{M} is expressed by introducing a new mixed template T_{mm} consisting of real and fake photon contributions. T_{mm} is defined by:

$$T_{\mathrm{mm}} = \alpha_1 T_{j_1}T_{\gamma_2} + \alpha_2 T_{\gamma_1}T_{j_2} + \alpha_3 T_{\gamma_1}T_{\gamma_2} + (1 - \alpha_1 - \alpha_2 - \alpha_3)T_{jj}. \tag{C.4}$$

The parameters $\alpha_{1(2,3)}$ describe the ratio between the number of real photon events in CR FF, where either the leading, subleading, or both photons pass the fake identification, and the total number of events measured in this region. Equation C.4 delivers an expression for T_{jj} which is inserted in Equation C.2, after which a comparison to the coefficients defined in Equation C.3 is possible. This relates the measured event yields to those corrected for signal leakage:

$$\begin{aligned}
N_{\gamma\gamma}^{\mathrm{M}} &= N_{\gamma\gamma} - N_{jj}\frac{\alpha_3}{\beta}, \\
N_{\gamma j}^{\mathrm{M}} &= N_{\gamma j} - \frac{\alpha_2}{\beta}N_{jj}, \\
N_{j\gamma}^{\mathrm{M}} &= N_{j\gamma} - \frac{\alpha_1}{\beta}N_{jj}, \\
N_{jj}^{\mathrm{M}} &= \frac{1}{\beta}N_{jj},
\end{aligned} \tag{C.5}$$

with $\beta = 1 - \alpha_1 - \alpha_2 - \alpha_3$. The fraction of real photon events $\alpha_{1(2,3)}$ in the FF CR is calculated as the product of the leakage efficiency $\epsilon_{xy}^{\mathrm{TT}\to\mathrm{FF}}$ and the ratio of (signal-leakage corrected) N_{xy} events in the signal region over the total number of events seen in the FF control region N^{FF}. The leakage efficiency is derived from MC simulation – from the SHERPA 2.2.10 $Z\gamma\gamma$ sample for events with two real photons (α_3) and the $Z\gamma$ + jets sample for events with one real and one fake photon (α_1 and α_2). The parameters $\alpha_{1(2,3)}$

are thus defined by:

$$\alpha_1 = \epsilon_{j\gamma}^{\mathrm{TT}\to\mathrm{FF}} \frac{N_{j\gamma}}{N^{\mathrm{FF}}} = \left(\frac{N_{j\gamma}^{\mathrm{FF}}}{N_{j\gamma}^{\mathrm{TT}}}\right)_{\mathrm{MC}} \frac{N_{j\gamma}}{N^{\mathrm{FF}}},$$

$$\alpha_2 = \epsilon_{\gamma j}^{\mathrm{TT}\to\mathrm{FF}} \frac{N_{\gamma j}}{N^{\mathrm{FF}}} = \left(\frac{N_{\gamma j}^{\mathrm{FF}}}{N_{\gamma j}^{\mathrm{TT}}}\right)_{\mathrm{MC}} \frac{N_{\gamma j}}{N^{\mathrm{FF}}}, \qquad (\mathrm{C.6})$$

$$\alpha_3 = \epsilon_{\gamma\gamma}^{\mathrm{TT}\to\mathrm{FF}} \frac{N_{\gamma\gamma}}{N^{\mathrm{TT}}} = \left(\frac{N_{\gamma\gamma}^{\mathrm{FF}}}{N_{\gamma\gamma}^{\mathrm{TT}}}\right)_{\mathrm{MC}} \frac{N_{\gamma\gamma}}{N^{\mathrm{FF}}}.$$

In total, $N^{\mathrm{FF}} = 18$ events are observed in control region FF. The signal leakage efficiency is listed in Table C.1. It is most likely for a photon with smaller energy (subleading photon in $j\gamma$) to pass the fake photon requirements. The leakage efficiency for two prompt photons into the FF CR is less than 0.5%.

Table C.1.: Signal leakage efficiencies determined from the SHERPA 2.2.10 $Z\gamma\gamma$ MC sample (α_3) and the $Z\gamma$ + jets MC sample (α_1 and α_2). Only statistical uncertainties are presented.

Coefficient	Leakage efficiency
$\alpha_1 \Rightarrow \epsilon_{j\gamma}^{\mathrm{TT}\to\mathrm{FF}}$	0.1066 ± 0.0214
$\alpha_2 \Rightarrow \epsilon_{\gamma j}^{\mathrm{TT}\to\mathrm{FF}}$	0.0518 ± 0.0164
$\alpha_3 \Rightarrow \epsilon_{\gamma\gamma}^{\mathrm{TT}\to\mathrm{FF}}$	0.0043 ± 0.0005

D. Fake Photon Shape Uncertainties

The measured distributions of $E_T^{\gamma 1}$ and $E_T^{\gamma 2}$ in the fake-enriched region CR1 are compared to those predicted by the $Z\gamma$ + jets and Z+jets MC simulations (containing $Z\gamma j$, $Zj\gamma$, and Zjj events) in Figure D.1. The same comparison is shown in Figure D.2 for $p_T^{\ell\ell}$ and $m_{\gamma\gamma}$. The Z + jets simulation is generated with POWHEG BOX v1 using a matrix element with zero jets at NLO: 0j@NLO. As the dilepton system $\ell\ell$ recoils against hadronic activity in the event, an imprecise modelling of $p_T^{\ell\ell}$ is expected in presence of missing higher order expansions of α_s. This discrepancy is demonstrated in Reference [130], which is especially visible for $p_T^{\ell\ell} > 100\,\text{GeV}$. The contribution of Zjj events in CR1 is sizeable leading to an inflation of the discrepancy. A reweighting is introduced to correct for this effect by comparing the POWHEG BOX v1 simulation to a SHERPA 2.2.11 simulation with up to two additional jets at NLO in the matrix element. This comparison is performed at particle-level to circumvent detector effects; the ratio of $p_T^{\ell\ell}$ between both simulations is fitted with a straight line above $p_T^{\ell\ell} > 100\,\text{GeV}$. The result of this fit is

$$f_{p_T^{\ell\ell}} = 0.797\,(\pm 0.032) - 0.0001\,(\pm 0.0002) \times p_T^{\ell\ell}. \tag{D.1}$$

Simulated POWHEG BOX v1 events fulfilling $p_T^{\ell\ell} > 100\,\text{GeV}$ are weighted by $f_{p_T^{\ell\ell}}$, after which the extraction of the shape uncertainty for $p_T^{\ell\ell}$ is repeated. The uncertainty decreases from 60% to approximately 40% in the last bin. While this reweighting is important due to the large contribution of the Zjj process in CR1, no reweighting is performed in the $Z\gamma\gamma$ SR as Zjj events contribute less than 3% to the total event yield.
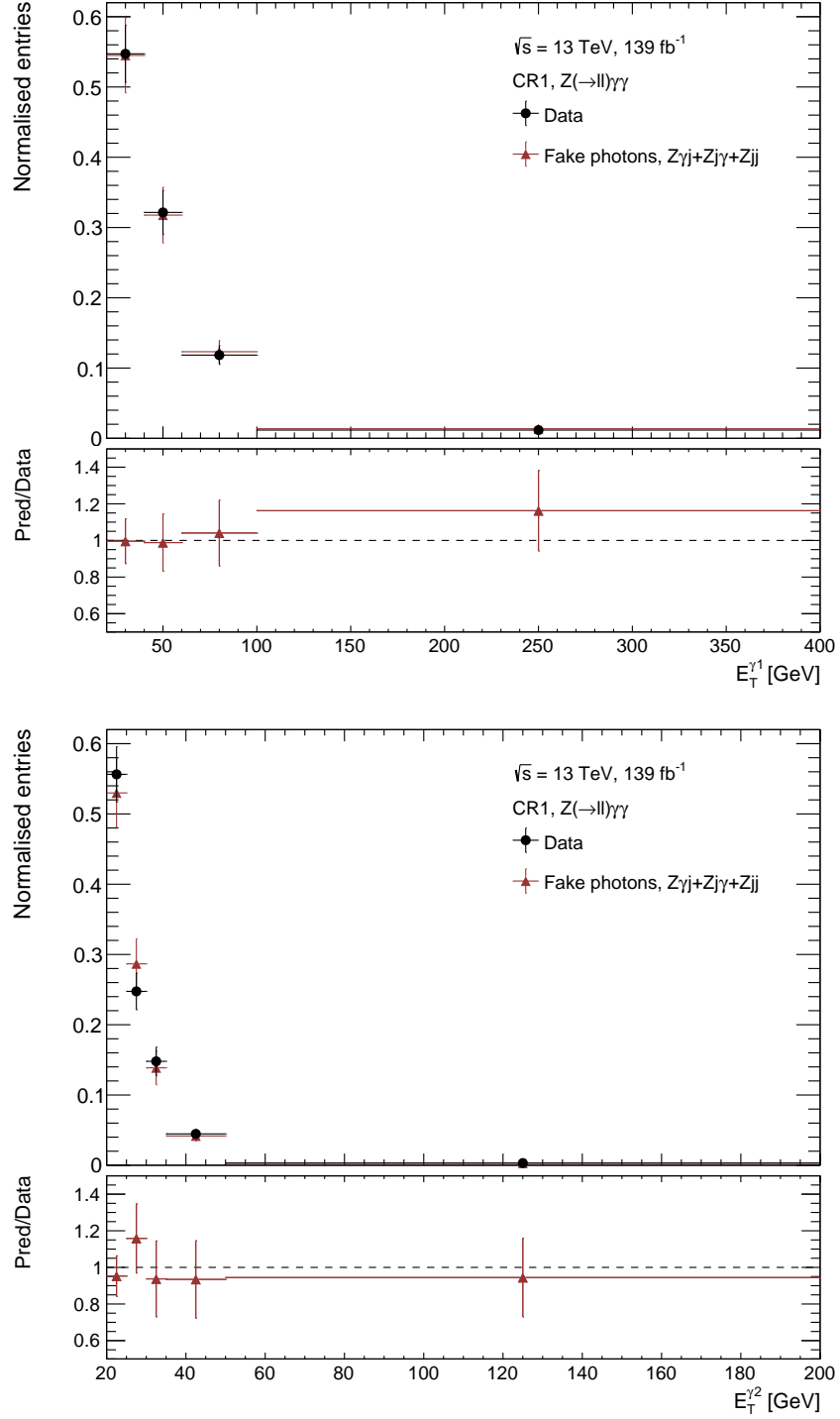
Figure D.1.: Extraction of fake photon shape uncertainties in CR1. The observed distributions of (a) $E_T^{\gamma 1}$ and (b) $E_T^{\gamma 2}$ are compared to the predicted fake photon distributions in $Z\gamma j$, $Zj\gamma$, and Zjj events. The ratio between the prediction and data (lower panel) is taken as systematic uncertainty on the shape of the fake photon background.
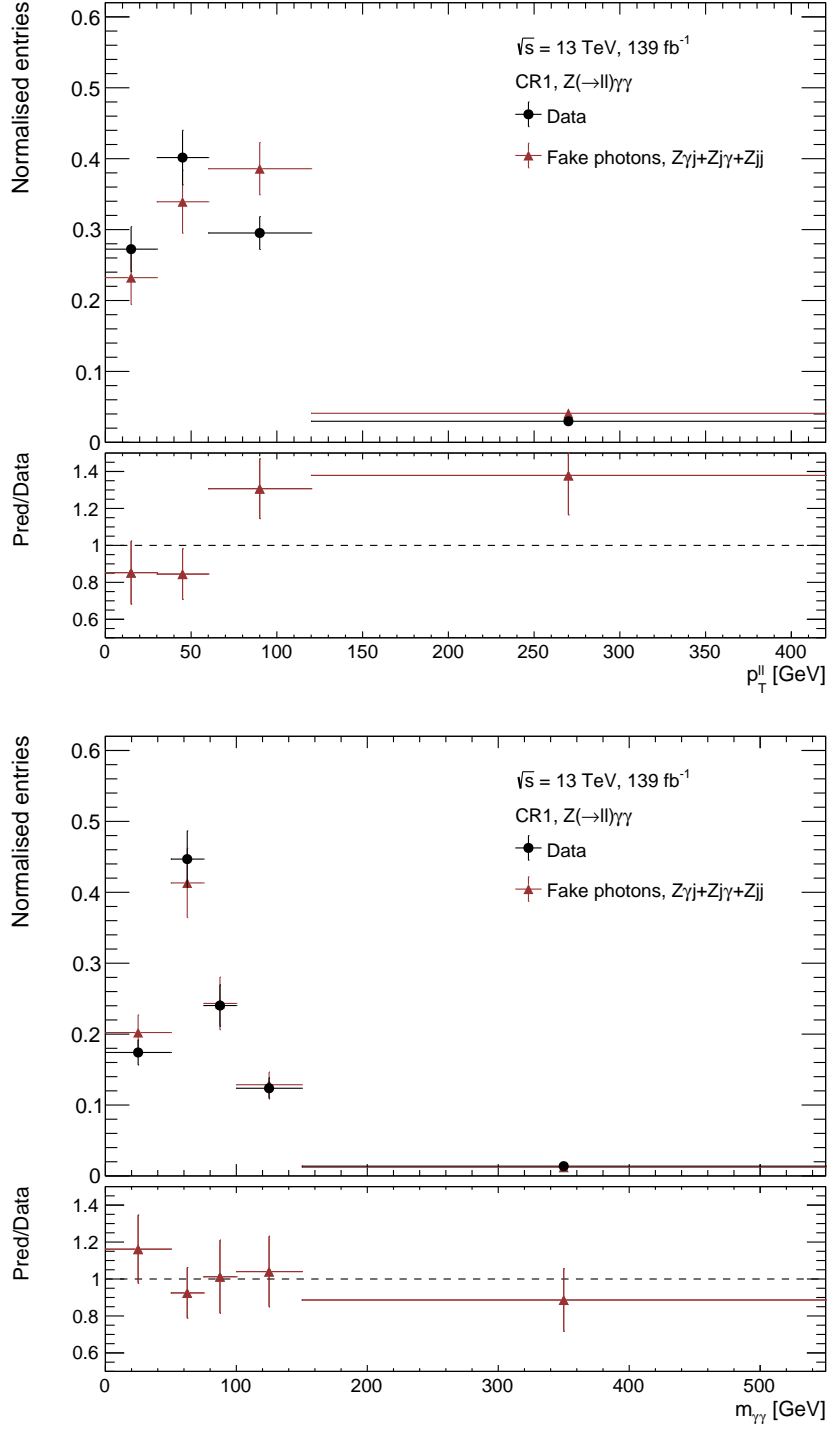
Figure D.2.: Extraction of fake photon shape uncertainties in CR1. The observed distributions of (a) $p_T^{\ell\ell}$ and (b) $m_{\gamma\gamma}$ are compared to the predicted fake photon distributions in $Z\gamma j$, $Zj\gamma$, and Zjj events. The ratio between the prediction and data (lower panel) is taken as systematic uncertainty on the shape of the fake photon background.

E. Reconstruction-level Observables

Figures E.1 – E.4 present the comparison between the measured $p_T^{\ell\ell}$, $p_T^{\ell\ell\gamma\gamma}$, $m_{\gamma\gamma}$, and $m_{\ell\ell\gamma\gamma}$ distributions and the sum of the total background and $Z\gamma\gamma$ signal distributions. Good agreement is typically seen across most measurement bins.
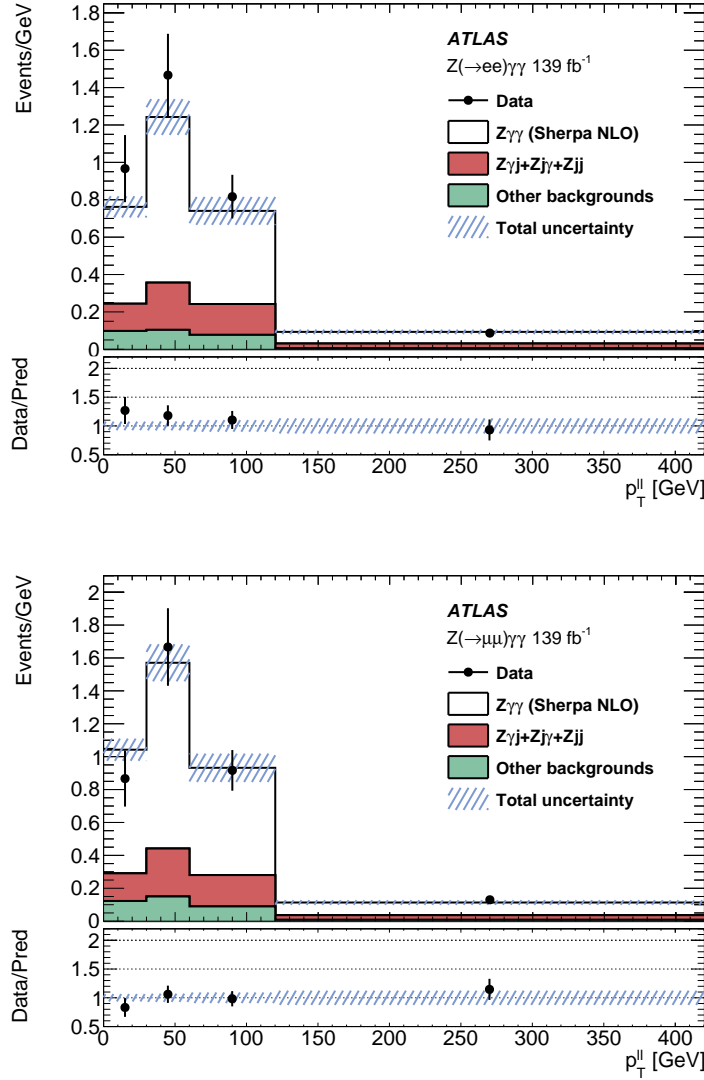
Figure E.1.: The observed $p_T^{\ell\ell}$ distribution is shown in (a) the electron channel and (b) the muon channel. It is compared to the sum of the total background contribution and the $Z\gamma\gamma$ prediction. The uncertainty band accounts for the statistical and systematic uncertainties on the number of background events, and for the CP uncertainties of the signal process. The figures are taken from [41].
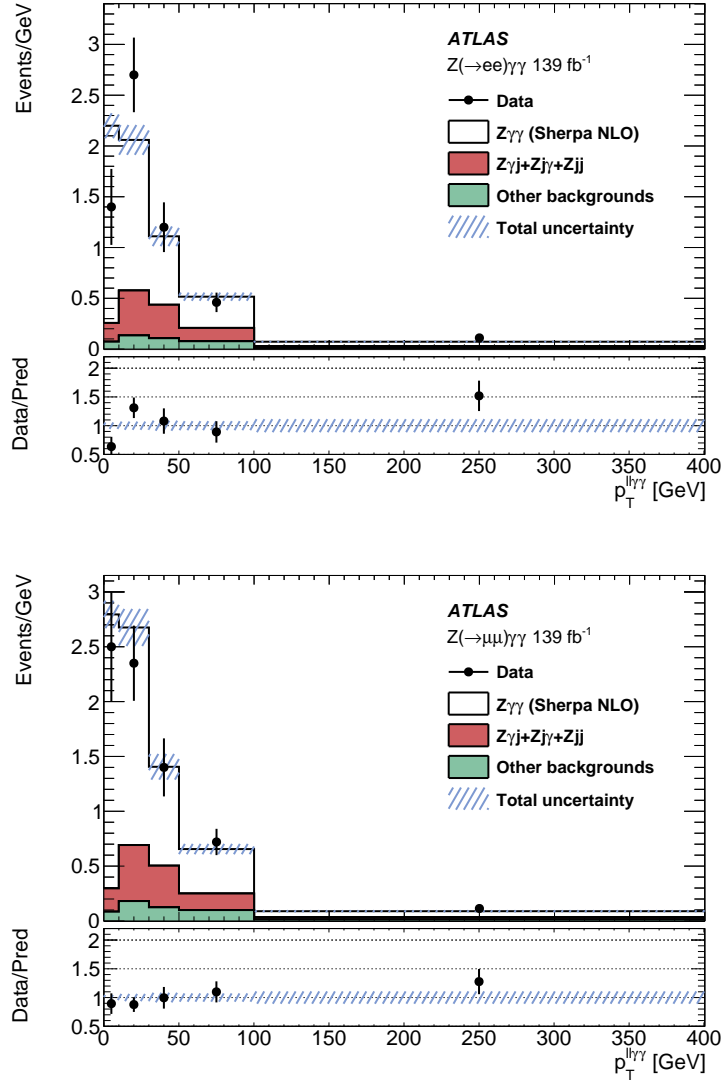
Figure E.2.: The observed $p_T^{\ell\ell\gamma\gamma}$ distribution is shown in (a) the electron channel and (b) the muon channel. It is compared to the sum of the total background contribution and the $Z\gamma\gamma$ prediction. The uncertainty band accounts for the statistical and systematic uncertainties on the number of background events, and for the CP uncertainties of the signal process. The figures are taken from [41].
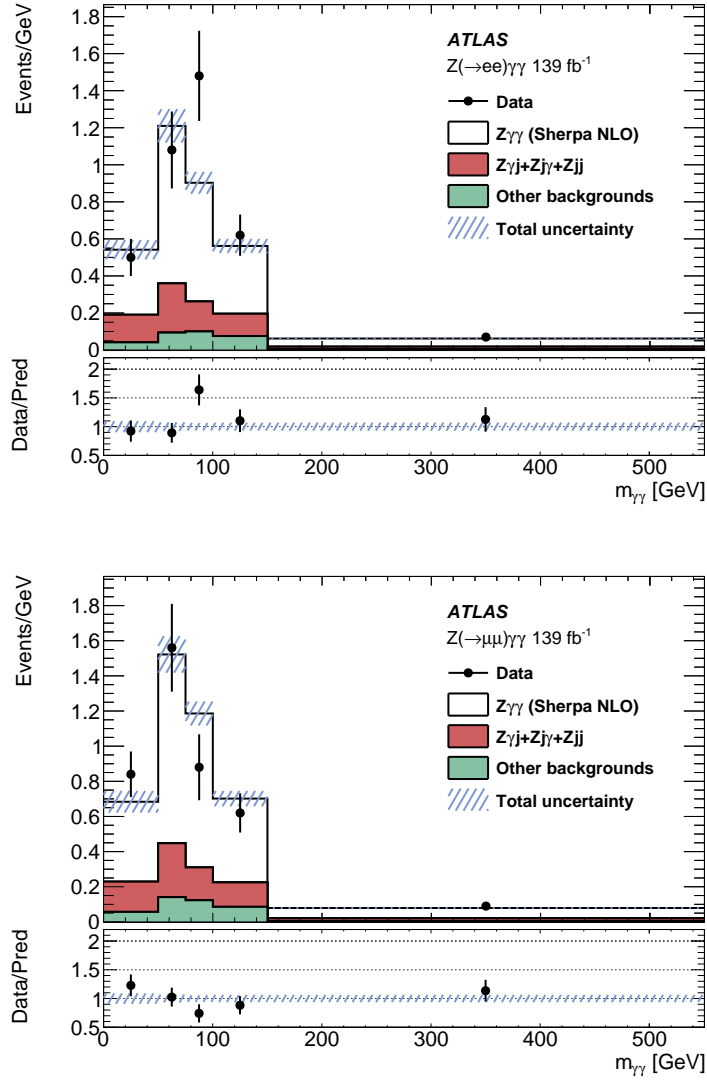
Figure E.3.: The observed $m_{\gamma\gamma}$ distribution is shown in (a) the electron channel and (b) the muon channel. It is compared to the sum of the total background contribution and the $Z\gamma\gamma$ prediction. The uncertainty band accounts for the statistical and systematic uncertainties on the number of background events, and for the CP uncertainties of the signal process. The figures are taken from [41].
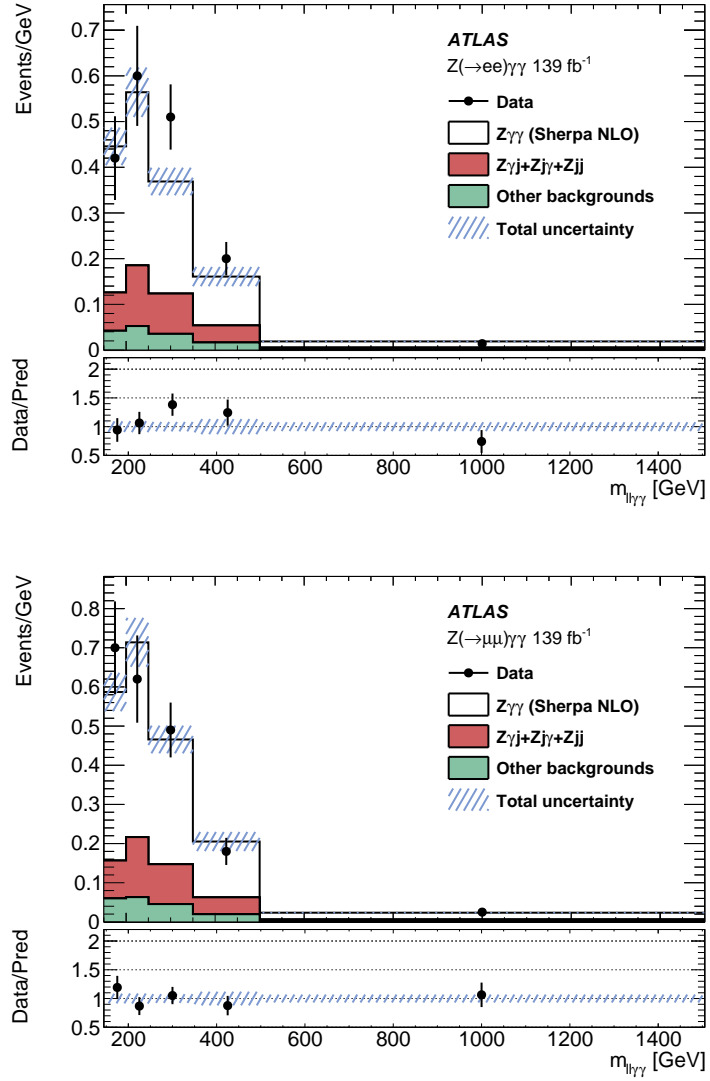
Figure E.4.: The observed $m_{\ell\ell\gamma\gamma}$ distribution is shown in (a) the electron channel and (b) the muon channel. It is compared to the sum of the total background contribution and the $Z\gamma\gamma$ prediction. The uncertainty band accounts for the statistical and systematic uncertainties on the number of background events, and for the CP uncertainties of the signal process. The figures are taken from [41].

F. Theory Uncertainties

The differential cross sections of $E_\mathrm{T}^{\gamma 1}$ and $p_\mathrm{T}^{\ell\ell\gamma\gamma}$ are shown in Figure F.1 for the particle-level predictions of the $Z\gamma\gamma$ MADGRAPH5_AMC@NLO NLO simulation. Theory uncertainties accounting for variations of μ_F and μ_R, and for combined PDF and α_s variations are displayed as well. The factorisation and renormalisation scale are shifted by a factor of two or one-half to obtain six variations (from which the envelop is formed). The PDF uncertainty incorporates, among others, experimental uncertainties from the fits to data. The α_s variation reflects roughly the uncertainty on the determination of the world-average of $\alpha_s(m_Z^2)$.
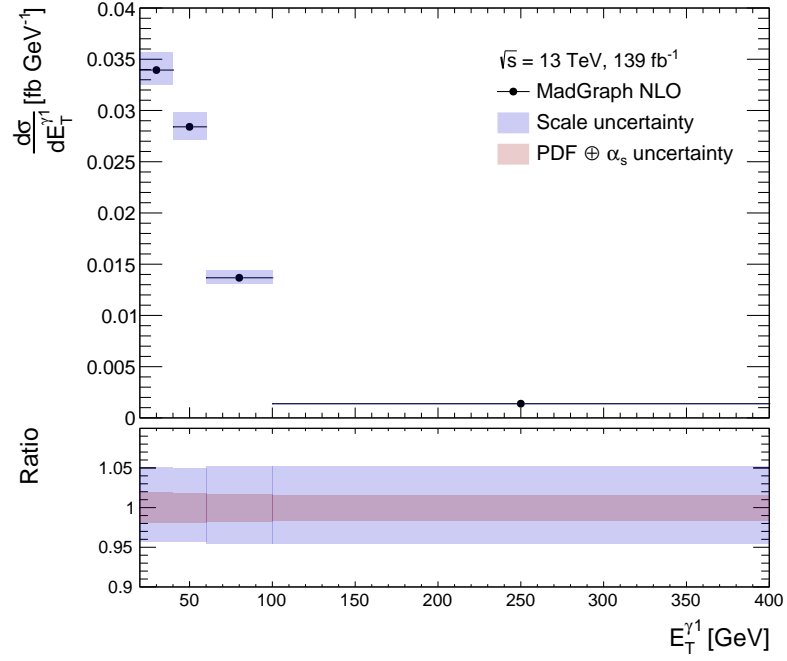
(a)
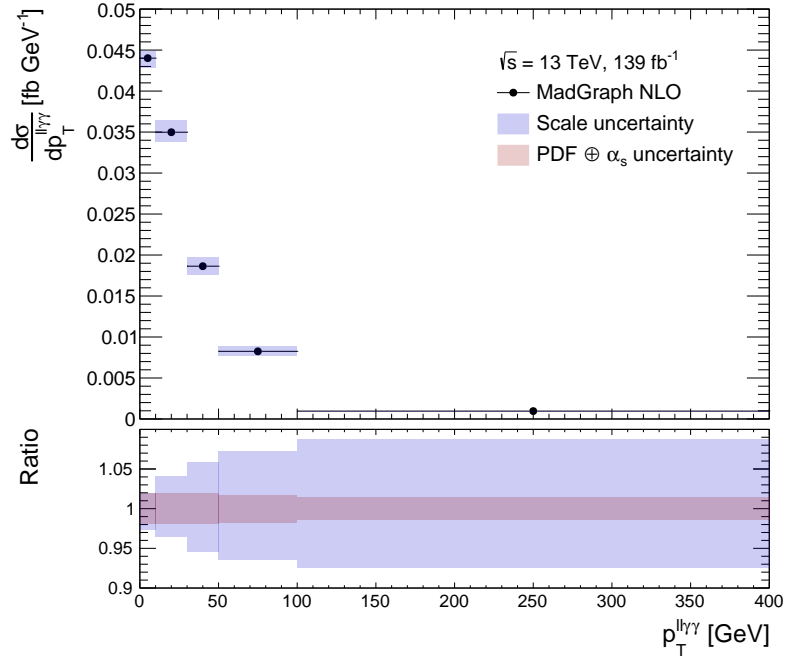
(b)

Figure F.1.: Predicted differential cross sections of $E_T^{\gamma 1}$ and $p_T^{\ell\ell\gamma\gamma}$ at particle-level for the $Z\gamma\gamma$ MAD-GRAPH5_AMC@NLO NLO simulation. Theory uncertainties consisting of μ_F and μ_R scale variations (blue band), and of the combined PDF and α_s uncertainty (red band) are shown as well. The lower panel displays the per-bin variation of each theory uncertainty with respect to the nominal prediction.

142

G. Unfolding

The efficiency correction C_{eff} and the fiducial correction C_{fid} are shown in Figure G.1 and Figure G.2, respectively, as functions of $p_{\text{T}}^{\ell\ell}$ in the electron and muon channel. The corrections are determined using the nominal SHERPA $Z\gamma\gamma$ signal simulation.
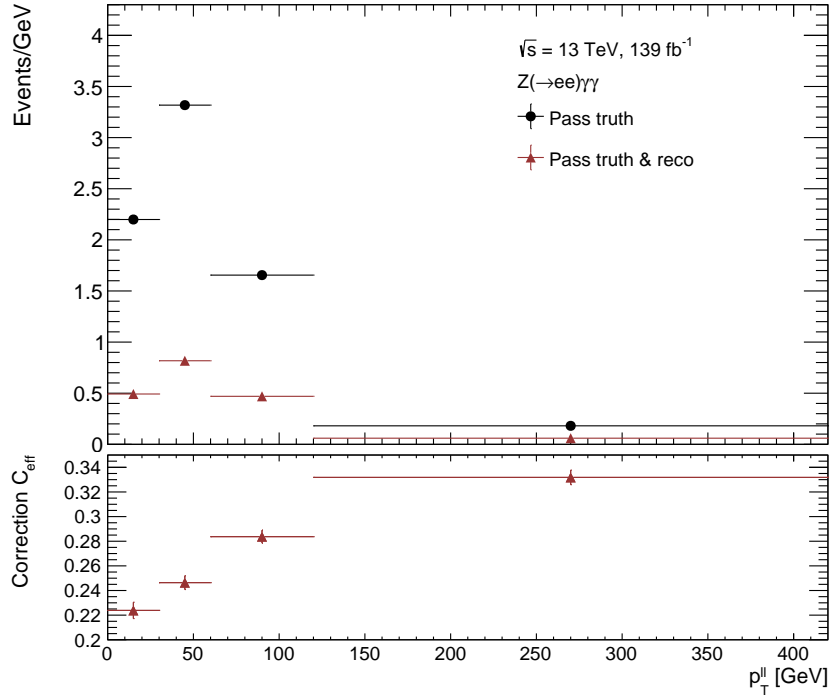
(a)
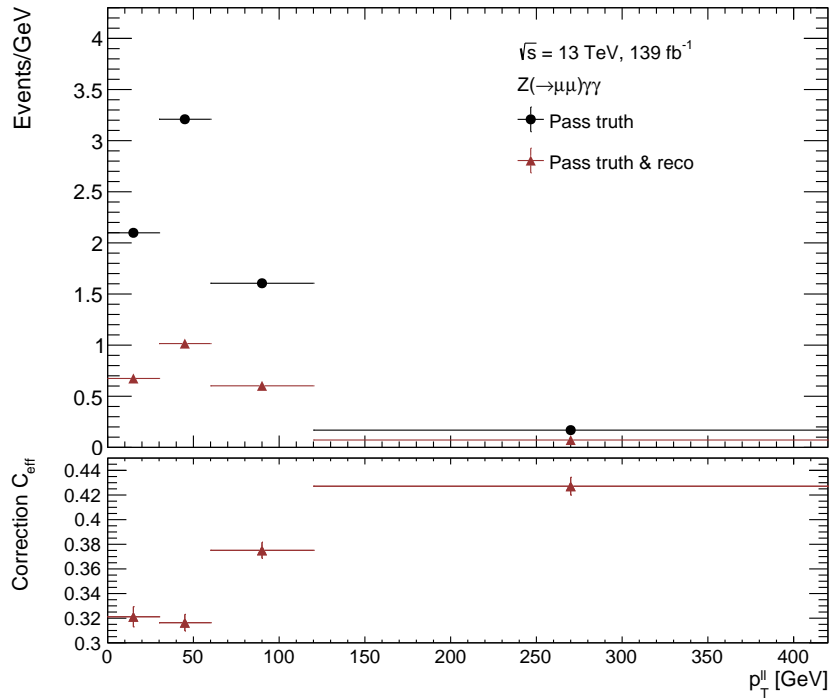
(b)

Figure G.1.: Dependency of the efficiency correction C_{eff} on $p_{\mathrm{T}}^{\ell\ell}$ in (a) the electron channel and (b) the muon channel. The nominal SHERPA $Z\gamma\gamma$ signal simulation is used to determine the correction.
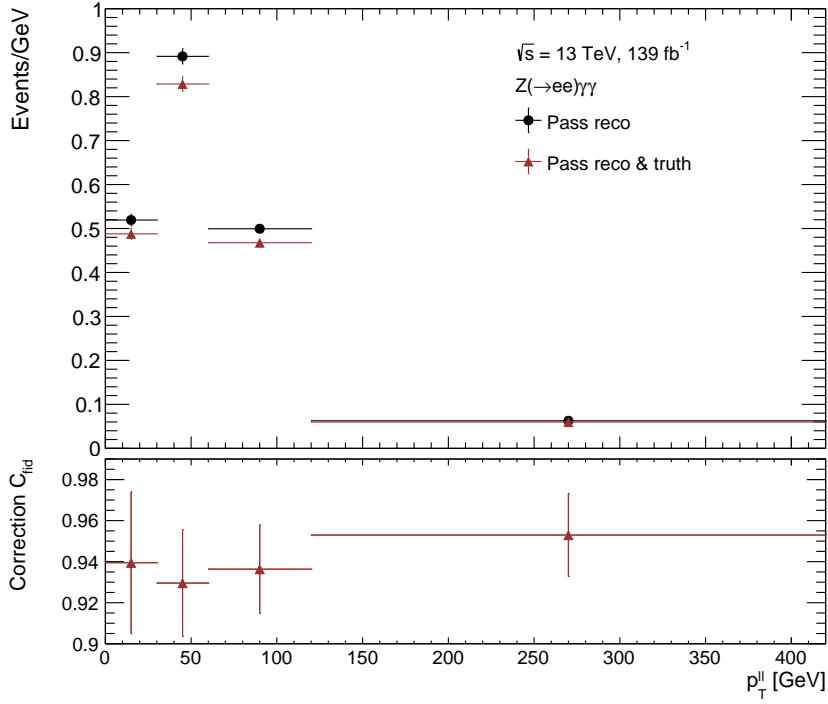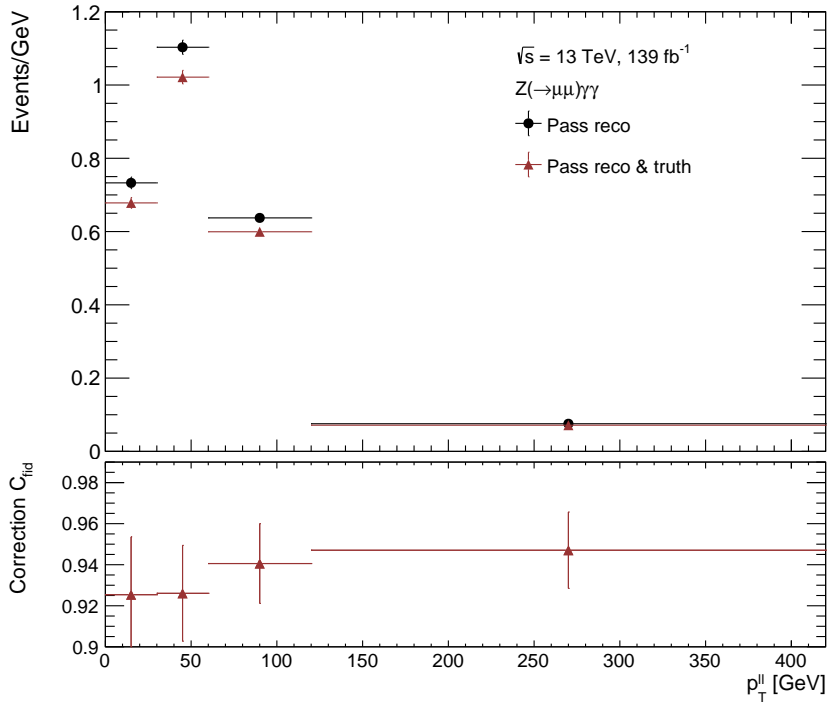
Figure G.2.: Dependency of the fiducial correction C_{fid} on $p_T^{\ell\ell}$ in (a) the electron channel and (b) the muon channel. The nominal SHERPA $Z\gamma\gamma$ signal simulation is used to determine the correction.

H. Effective Field Theory Interpretation

H.1. Validation of Decomposition Approach

The decomposition approach is validated using the cross sections predicted by $\mathcal{O}_{T,9}^8$ in the fiducial phase-space of the $Z\gamma\gamma$ analysis. The agreement between the sum of cross sections for individually generated samples – referring to an individual MC simulation of the SM, linear, and quadratic contribution – and one sample containing the full SM plus EFT expectation is verified. The result of this test is shown in Table H.1 for the integrated cross section predicted by $\mathcal{O}_{T,9}^8$. The deviation between the sum of contributions and the full simulation is smaller than 1%. Figure H.1 shows the same test for the differential $p_T^{\ell\ell}$ cross section. The cross section agrees reasonably well between the sum (orange distribution) and the full simulation (magenta distribution) in all bins. The same behaviour is observed for the remaining transverse operators.

Table H.1.: Validation of the decomposition approach for the integrated cross section predicted by $\mathcal{O}_{T,9}^8$ with $f_{T,9} = 1$ and $\Lambda = 1\,\mathrm{TeV}$ in the fiducial phase-space. The column 'Sum' contains the sum of the second to fourth column (SM + Lin + Quad). The column 'Full' contains the predicted cross section when generating the full SM plus EFT amplitude.

| Operator $\mathcal{O}_{T,9}^8$	SM	Lin	Quad	Sum	Full	$1 - \frac{\text{Full}}{\text{Sum}}$
cross section [fb]	2.540	0.004	0.140	2.684	2.666	0.7%
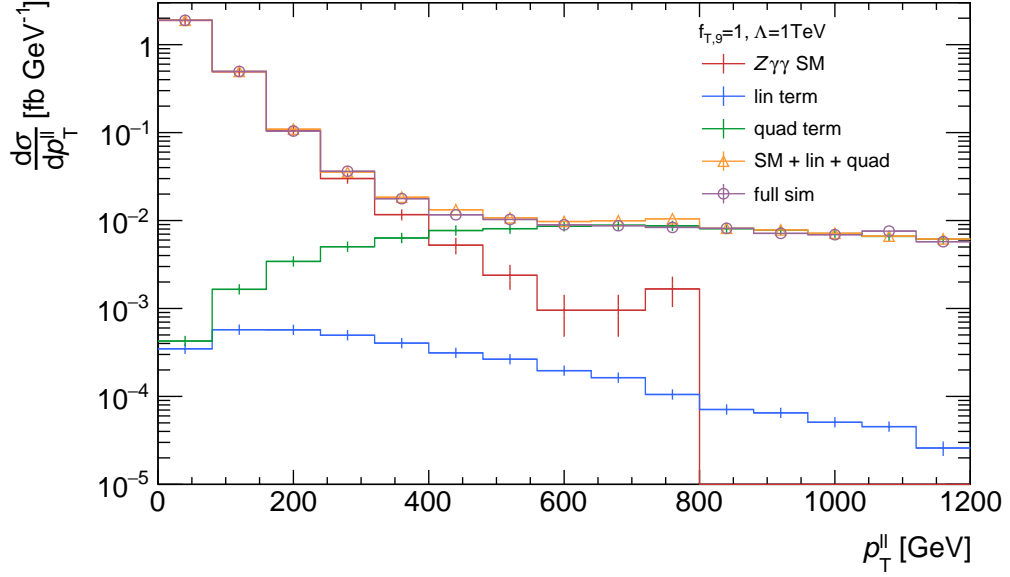
Figure H.1.: Validation of the decomposition approach for the differential $p_T^{\ell\ell}$ cross section predicted by $\mathcal{O}_{T,9}^8$ with $f_{T,9} = 1$ and $\Lambda = 1\,\text{TeV}$ in the fiducial phase-space. The orange distribution contains the sum of the SM (red), linear term (blue), and quadratic term (green). The full simulation (magenta) contains the predicted differential cross section when generating the full SM plus EFT amplitude.

H.2. Sensitivity Scan of Unfolded Observables

Out of the six differential cross sections measured in the fiducial phase-space at particle-level ($E_T^{\gamma 1,2}$, $p_T^{\ell\ell}$, $p_T^{\ell\ell\gamma}$, $m_{\gamma\gamma}$, $m_{\ell\ell\gamma\gamma}$), the one yielding the largest sensitivity for EFT contributions is chosen in the EFT interpretation. This scan is presented in Figures H.2 to H.4 for effects of $\mathcal{O}_{T,8}^8$. The SM $Z\gamma\gamma$ production is generated in MADGRAPH5_AMC@NLO at LO QCD precision. The predicted per-bin cross section of the quadratic term is much larger than that of the linear term and hence decisive for the sensitivity. The integrated cross section of the quadratic term is compared to the SM prediction and ranges from 0.6% ($E_T^{\gamma 1}$, $m_{\ell\ell\gamma\gamma}$) to 21% ($p_T^{\ell\ell\gamma}$). $p_T^{\ell\ell\gamma}$ shows by far the largest relative contribution. It measures the hadronic recoil in the fiducial volume, which is only simulated by the parton shower in PYTHIA as no jets are merged into the matrix element at LO in the event generation. The p_T modelling of high-energetic jets purely stemming from the parton shower is known to be imprecise – $p_T^{\ell\ell\gamma}$ is thus excluded in the sensitivity scan. The relative contribution of 3.1% of the $p_T^{\ell\ell}$ quadratic term (see Figure 8.1(b)) is the largest of any of the remaining observables. It is therefore expected that the differential cross section of $p_T^{\ell\ell}$ offers the dominant sensitivity for EFT contributions in the fiducial phase-space.
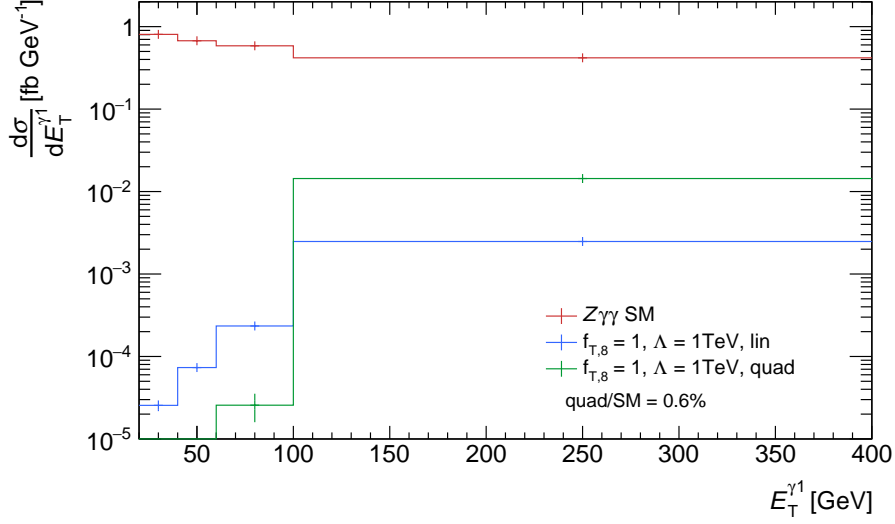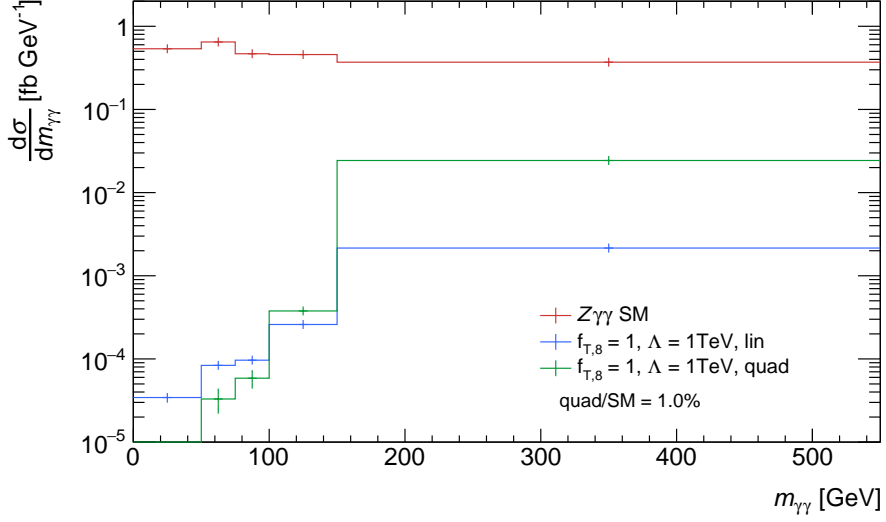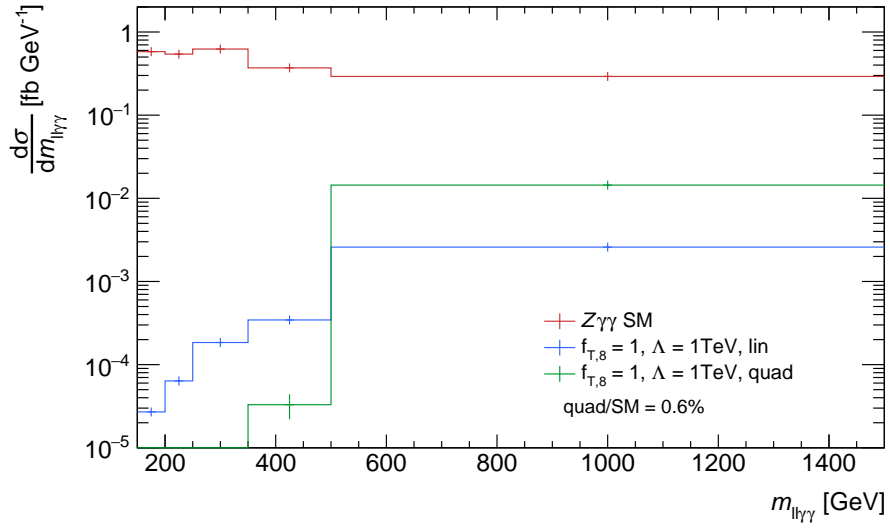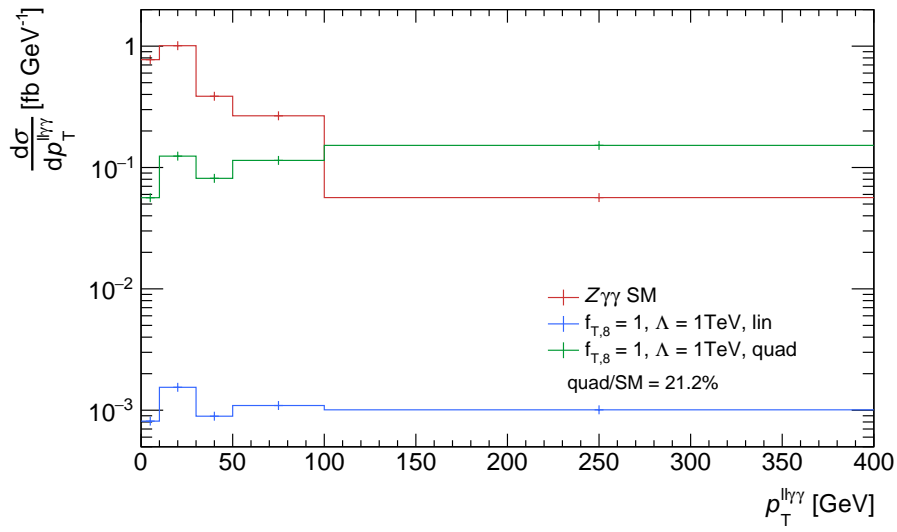
(a)
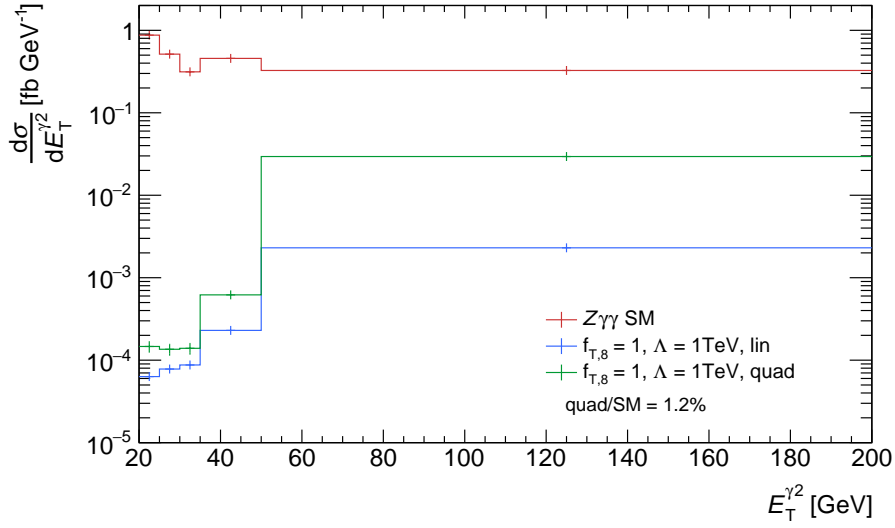
(b)

Figure H.2.: Differential cross section comparison between the $Z\gamma\gamma$ SM production and the linear and quadratic term of operator $\mathcal{O}_{T,8}^8$ generated with $\Lambda = 1\,\text{TeV}$ and $f_{T,8} = 1$. The comparison is shown for (a) $E_T^{\gamma 1}$ and (b) $E_T^{\gamma 2}$. The full fiducial phase-space selection is applied. The integrated cross section of the quadratic term divided by the $Z\gamma\gamma$ SM expectation represents a measure for the sensitivity to EFT effects (indicated by 'quad/SM').

(a)

(b)

Figure H.3.: Differential cross section comparison between the $Z\gamma\gamma$ SM production and the linear and quadratic term of operator $\mathcal{O}_{T,8}^8$ generated with $\Lambda = 1\,\text{TeV}$ and $f_{T,8} = 1$. The comparison is shown for (a) $m_{\gamma\gamma}$ and (b) $m_{\ell\ell\gamma\gamma}$. The full fiducial phase-space selection is applied. The integrated cross section of the quadratic term divided by the $Z\gamma\gamma$ SM expectation represents a measure for the sensitivity to EFT effects (indicated by 'quad/SM').

Figure H.4.: Differential cross section comparison between the $Z\gamma\gamma$ SM production and the linear and quadratic term of operator $\mathcal{O}_{T,8}^{8}$ generated with $\Lambda = 1\,\text{TeV}$ and $f_{T,8} = 1$. The comparison is shown for $p_T^{\ell\ell\gamma\gamma}$. The full fiducial phase-space selection is applied. The integrated cross section of the quadratic term divided by the $Z\gamma\gamma$ SM expectation represents a measure for the sensitivity to EFT effects (indicated by 'quad/SM').

H.3. Consistency Test of Fitting Procedure

The statistical model that was introduced in Section 8.2 is used to replicate the constraints placed on dimension-8 operator $\mathcal{O}_{T,8}^8$ published by the CMS experiment in the $13\,\mathrm{TeV}$ $W\gamma\gamma$ and $Z\gamma\gamma$ analysis [11]. The measured constraints on the coupling parameter $f_{T,8}^8$ are $[-1.06, 1.10] \times \Lambda^{-4}$. The phase-space of the CMS analysis is implemented in Rivet, which most notably differs from the analysis presented in this thesis by including events with FSR resulting in softer lepton and photon p_{T} spectra. MC simulations of the SM $Z\gamma\gamma$ production at LO QCD accuracy and the linear and quadratic term of $\mathcal{O}_{T,8}^8$ are propagated through the Rivet routine. The transverse momentum of the diphoton system $p_{\mathrm{T}}^{\gamma\gamma}$ is used in the CMS EFT interpretation. The same binning is chosen and the predicted $p_{\mathrm{T}}^{\gamma\gamma}$ differential cross section for all three MC simulations is determined in the FSR-enriched phase-space. The multivariate Gaussian and the Gaussian theory constraints are implemented using the published experimental and theoretical uncertainties. These uncertainties are assumed to be evenly distributed over all bins as no bin-by-bin dependence is published. This assumption is not true for the actual CMS analysis and the constraints measured in this validation are hence expected to slightly deviate from the published ones. The profile likelihood ratio is constructed and scanned to obtain $f_{T,8}^8$ constraints at 95% confidence level (see Figure H.5). The confidence intervals in the CMS phase-space are $[-1.12, 1.07] \times \Lambda^{-4}$, which deviates from the results of the CMS analysis by less than 6%. This is deemed as sufficient closure given the limited precision of the validation (most notably the LO $Z\gamma\gamma$ SM prediction and the assignment of flat experimental uncertainties).
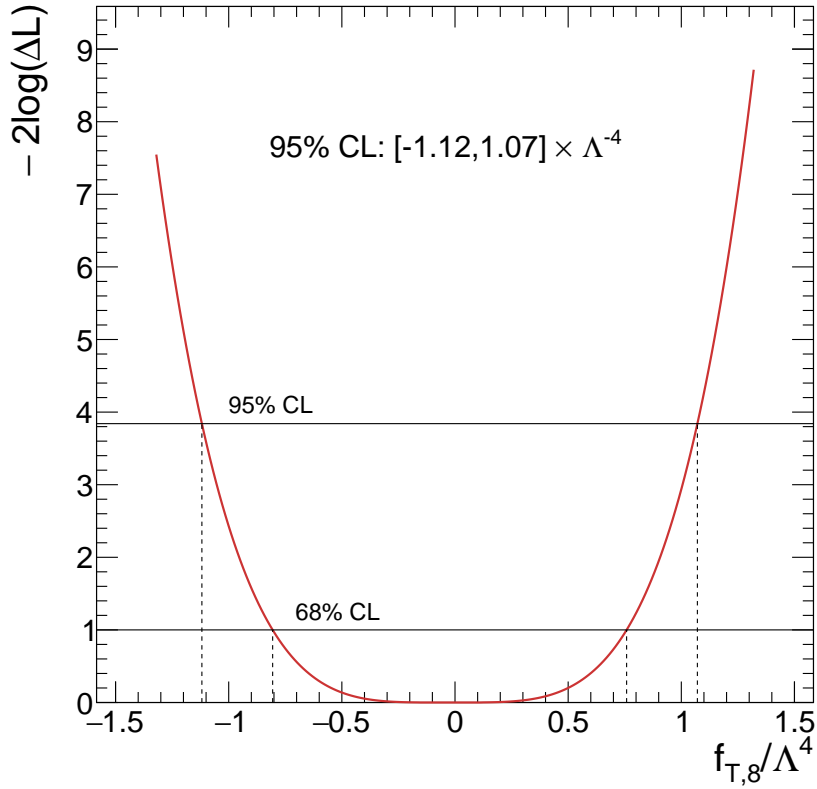
Figure H.5.: Distribution of the profile likelihood ratio λ_p in the CMS phase-space for NP contributions of $\mathcal{O}^8_{T,8}$. The vertical dashed lines indicate the confidence intervals at 95% and 68% CL. The horizontal solid lines represent the value of λ_p below which the area of a χ^2 distribution corresponds to the 95th and 68th percentile of the probability density.
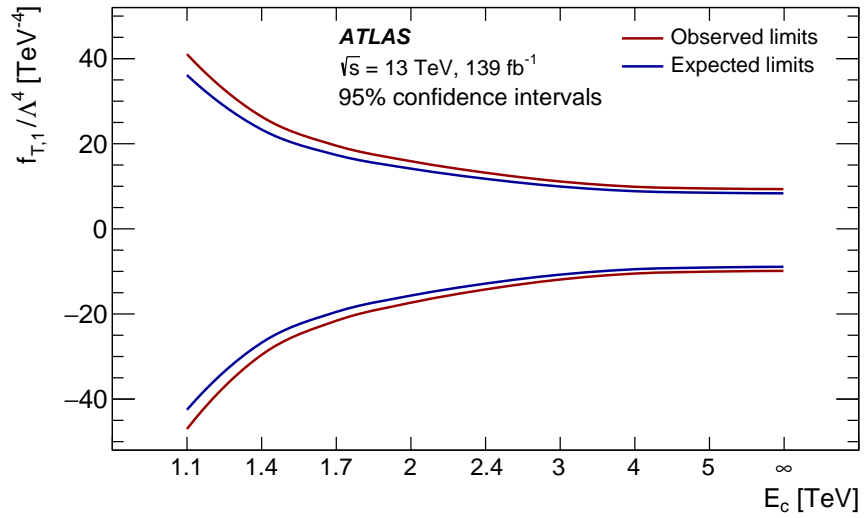
H.4. Unitarised Limits

The unitarised confidence intervals are presented for:

- the transverse operators $\mathcal{O}^8_{T,0}$ and $\mathcal{O}^8_{T,1}$ in Figure H.6

- the transverse operators $\mathcal{O}^8_{T,2}$ and $\mathcal{O}^8_{T,5}$ in Figure H.7

- the transverse operators $\mathcal{O}^8_{T,6}$ and $\mathcal{O}^8_{T,7}$ in Figure H.8

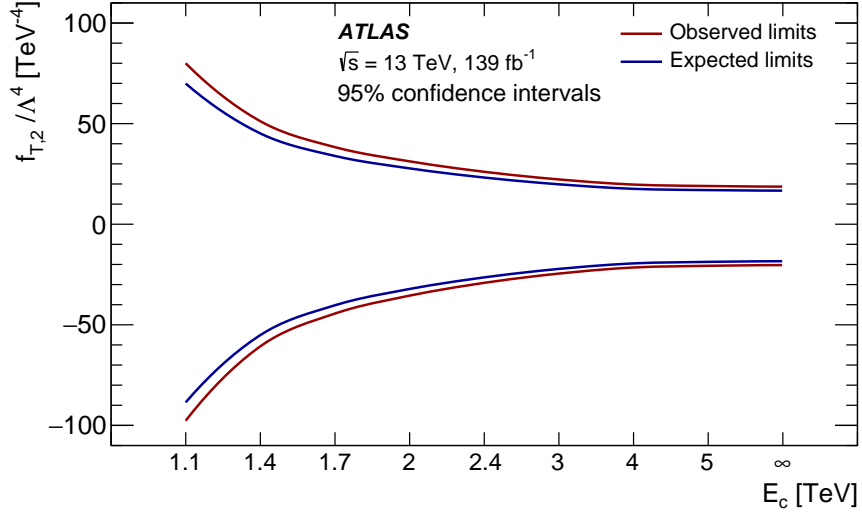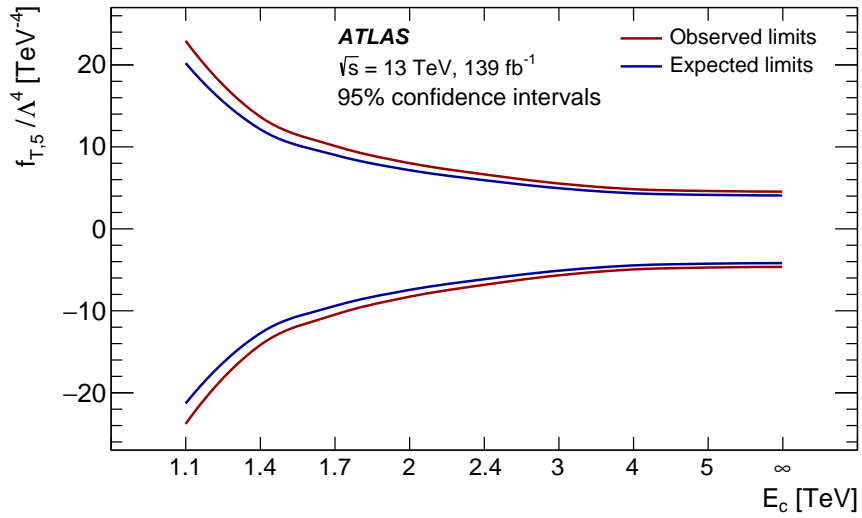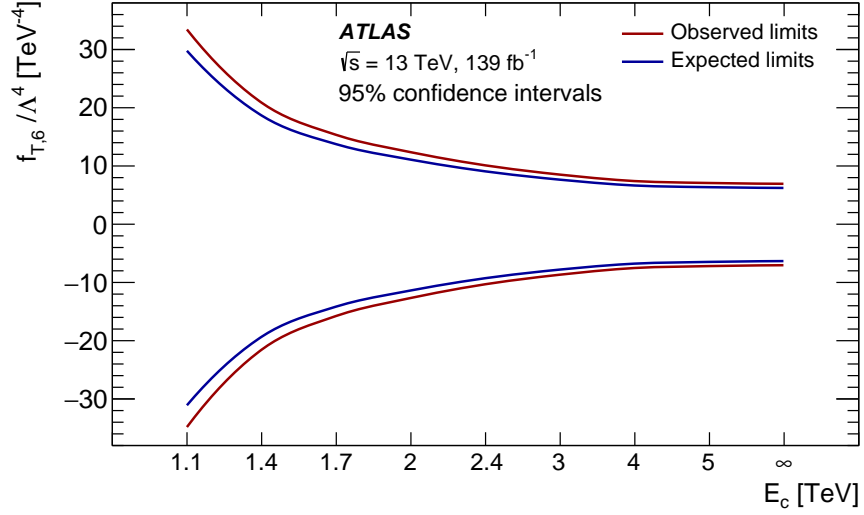- the transverse operator $\mathcal{O}^8_{T,9}$ in Figure H.9
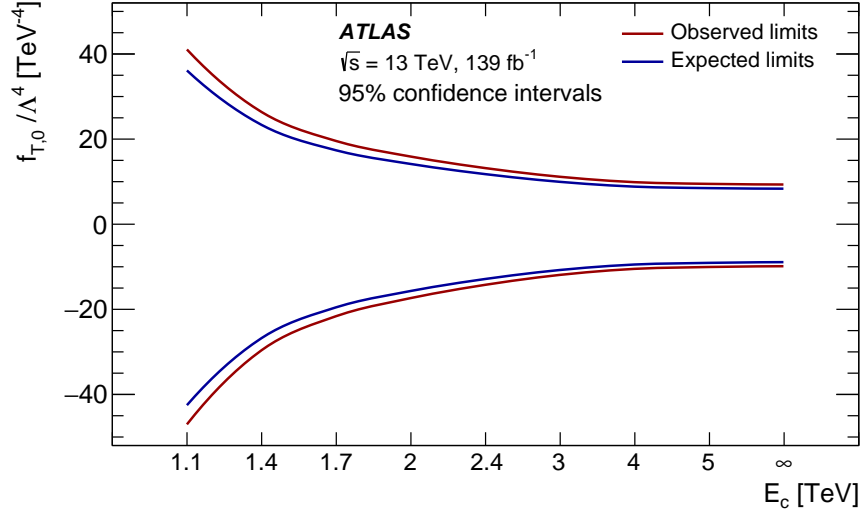
(a)

(b)

Figure H.6.: Evolution of the expected and observed limits as functions of the clipping energy between 1.1 TeV and 5 TeV for the coupling parameters (a) $f_{T,0}^8/\Lambda^4$ and (b) $f_{T,1}^8/\Lambda^4$. The non-unitarised limits correspond to $E_c = \infty$. The values of the coupling parameters above the upper or below the lower expected and observed limits are excluded at 95% confidence level. The figures are taken from [41].

(a)

(b)

Figure H.7.: Evolution of the expected and observed limits as functions of the clipping energy between $1.1 \, \text{TeV}$ and $5 \, \text{TeV}$ for the coupling parameters (a) $f_{T,2}^8/\Lambda^4$ and (b) $f_{T,5}^8/\Lambda^4$. The non-unitarised limits correspond to $E_c = \infty$. The values of the coupling parameters above the upper or below the lower expected and observed limits are excluded at 95% confidence level. The figures are taken from [41].
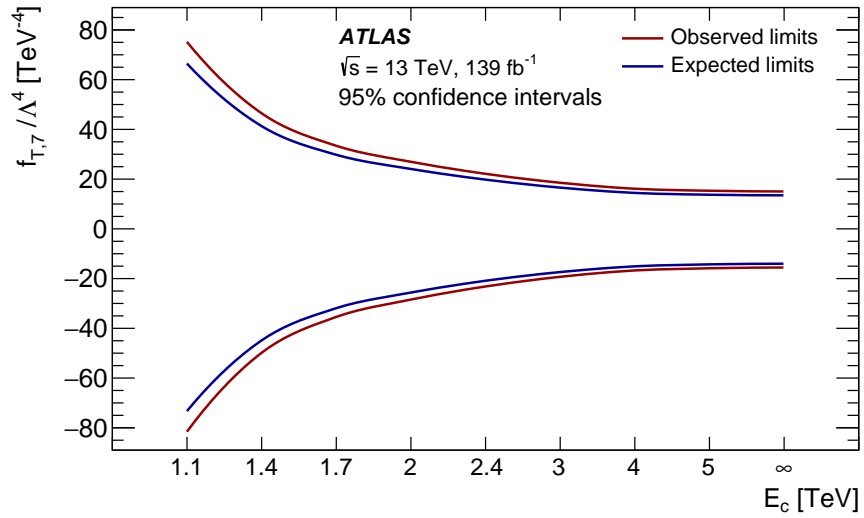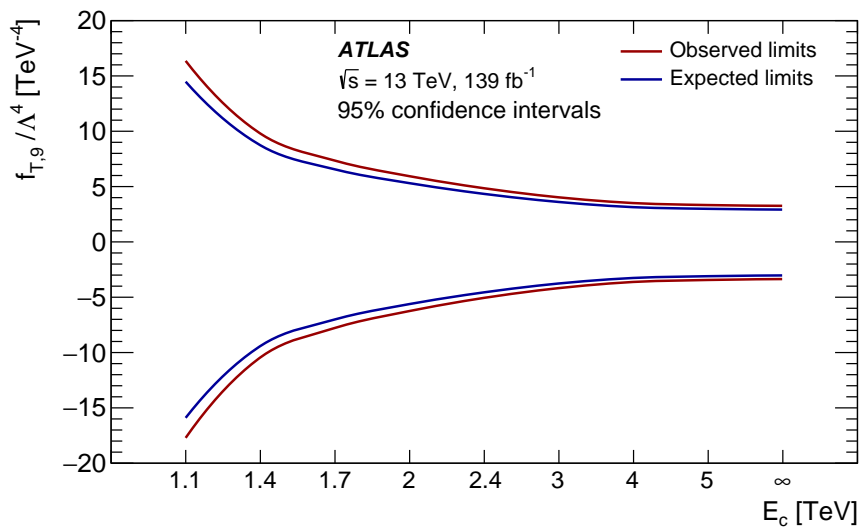
(a)

(b)

Figure H.8.: Evolution of the expected and observed limits as functions of the clipping energy between 1.1 TeV and 5 TeV for the coupling parameters (a) $f_{T,6}^8/\Lambda^4$ and (b) $f_{T,7}^8/\Lambda^4$. The non-unitarised limits correspond to $E_c = \infty$. The values of the coupling parameters above the upper or below the lower expected and observed limits are excluded at 95% confidence level. The figures are taken from [41].

Figure H.9.: Evolution of the expected and observed limits as functions of the clipping energy between $1.1\,\text{TeV}$ and $5\,\text{TeV}$ for the coupling parameter $f_{T,9}^8/\Lambda^4$. The non-unitarised limits correspond to $E_{\text{c}} = \infty$. The values of the coupling parameter above the upper or below the lower expected and observed limits are excluded at 95% confidence level. The figure is taken from [41].

Bibliography

[1] S. Bilenky. Neutrino oscillations: From a historical perspective to the present status. *Nuclear Physics B*, 908:2–13, 2016. ISSN 0550-3213. DOI: https://doi.org/10.1016/j.nuclphysb.2016.01.025. URL https://www.sciencedirect.com/science/article/pii/S0550321316000353.

[2] A. Arbey and F. Mahmoudi. Dark matter and the early Universe: a review. *Progress in Particle and Nuclear Physics*, 119:103865, 2021. DOI: 10.1016/j.ppnp.2021.103865. URL https://doi.org/10.1016%2Fj.ppnp.2021.103865.

[3] F. Kahlhoefer. Review of LHC dark matter searches. *International Journal of Modern Physics A*, 32(13):1730006, May 2017. DOI: 10.1142/s0217751x1730006x. URL https://doi.org/10.1142%2Fs0217751x1730006x.

[4] M. Aaboud et al. Constraints on mediator-based dark matter and scalar dark energy models using $\sqrt{s} = 13$ TeV pp collision data collected by the ATLAS detector. *Journal of High Energy Physics*, 05:142, 2019. DOI: 10.1007/JHEP05(2019)142. URL https://doi.org/10.1007%2Fjhep05%282019%29142.

[5] C. Degrande et al. Effective field theory: A modern approach to anomalous couplings. *Annals of Physics*, 335:21–32, Aug 2013. DOI: 10.1016/j.aop.2013.04.016. URL https://doi.org/10.1016%2Fj.aop.2013.04.016.

[6] D. R. Green, P. Meade, and M.-A. Pleier. Multiboson interactions at the LHC. *Reviews of Modern Physics*, 89(3):035008, 2017. DOI: 10.1103/RevModPhys.89.035008. URL https://doi.org/10.1103%2Frevmodphys.89.035008.

[7] A. Oh. Measurements of multi vector boson production processes at the LHC. *Progress in Particle and Nuclear Physics*, 108:103708, 2019. ISSN 0146-6410. DOI: https://doi.org/10.1016/j.ppnp.2019.06.002. URL https://www.sciencedirect.com/science/article/pii/S0146641019300432.

[8] M. Aaboud et al. Measurement of the production cross section of three isolated photons in pp collisions at $\sqrt{s} = 8$ TeV using the ATLAS detector. *Physics Letters B*, 781:55–76, 2018. ISSN 0370-2693. DOI: https://doi.org/10.1016/j.physletb.2018.03.057. URL https://www.sciencedirect.com/science/article/pii/S0370269318302533.

[9] A. M. Sirunyan et al. Measurements of the pp $\to W\gamma\gamma$ and pp $\to Z\gamma\gamma$ cross sections and limits on anomalous quartic gauge couplings at $\sqrt{s} = 8$ TeV. *Journal of High Energy Physics*, 10:072, 2017. DOI: 10.1007/JHEP10(2017)072.

[10] G. Aad et al. Measurements of $Z\gamma$ and $Z\gamma\gamma$ production in pp collisions at $\sqrt{s} = 8$ TeV with the ATLAS detector. *Physical Review D*, 93:112002, Jun 2016. DOI: 10.1103/PhysRevD.93.112002. URL https://link.aps.org/doi/10.1103/PhysRevD.93.112002.

[11] A. Tumasyan et al. Measurements of the pp $\to W^{\pm}\gamma\gamma$ and pp $\to Z\gamma\gamma$ cross sections at $\sqrt{s} = 13$ TeV and limits on anomalous quartic gauge couplings. *Journal of High Energy Physics*, 10:174, 2021. DOI: 10.1007/JHEP10(2021)174. URL https://doi.org/10.1007/JHEP10(2021)174.

[12] The ATLAS Collaboration. Letter of Intent for the Phase-II Upgrade of the ATLAS Experiment. Technical report, CERN, Geneva, 2012. URL https://cds.cern.ch/record/1502664.

[13] The ATLAS Collaboration. Technical Design Report for the Phase-II Upgrade of the ATLAS Tile Calorimeter. Technical report, CERN, Geneva, 2017. URL https://cds.cern.ch/record/2285583.

[14] B. Petersen et al. Expected performance of the ATLAS detector under different High-Luminosity LHC conditions. Technical report, CERN, Geneva, 2021. URL https://cds.cern.ch/record/2765851.

[15] A. Bednyakov. Quantum Field Theory and the Electroweak Standard Model. *CERN Yellow Reports: School Proceedings*, 6:1–41. 41 p, 2019. DOI: 10.23730/CYRSP-2019-006.1. URL https://cds.cern.ch/record/2702128.

[16] P. Langacker. *The Standard Model and Beyond; 1st ed.* Series in high energy physics, cosmology, and gravitation. 2010. URL https://cds.cern.ch/record/1226768.

[17] G. Ecker. *Particles, Fields, Quanta: From Quantum Mechanics to the Standard Model of Particle Physics*. Springer, Cham, 2019. ISBN 978-3-030-14478-4, 978-3-030-14479-1. DOI: 10.1007/978-3-030-14479-1. URL https://doi.org/10.1007/978-3-030-14479-1.

[18] J. M. Maldacena. Gravity, particle physics and their unification. *International Journal of Modern Physics A*, 15S1:840–852, 2000. DOI: 10.1142/

S0217751X00005449. URL https://doi.org/10.48550/arXiv.hep-ph/0002092.

[19] C. Pérez de los Heros. Status of direct and indirect dark matter searches. *Proceedings of Science,* EPS-HEP2019:694, 2020. DOI: 10.22323/1.364.0694. URL https://doi.org/10.48550/arXiv.2001.06193.

[20] M. Bauer and T. Plehn. *Yet Another Introduction to Dark Matter: The Particle Physics Approach*, volume 959 of *Lecture Notes in Physics*. Springer, 2019. DOI: 10.1007/978-3-030-16234-4. URL https://arxiv.org/abs/1705.01987.

[21] R. Jimenez et al. Neutrino masses and mass hierarchy: evidence for the normal hierarchy. *Journal of Cosmology and Astroparticle Physics*, 09:006, 2022. DOI: 10.1088/1475-7516/2022/09/006. URL https://doi.org/10.1088%2F1475-7516%2F2022%2F09%2F006.

[22] R. L. Workman et al. Review of Particle Physics. *Progress of Theoretical and Experimental Physics*, 2022:083C01, 2022. DOI: 10.1093/ptep/ptac097. URL https://doi.org/10.1093/ptep/ptac097.

[23] C. S. Wu et al. Experimental test of parity conservation in beta decay. *Physical Review*, 105:1413–1415, Feb 1957. DOI: 10.1103/PhysRev.105.1413. URL https://link.aps.org/doi/10.1103/PhysRev.105.1413.

[24] J. H. Christenson et al. Evidence for the 2π decay of the k_2^0 meson. *Physical Review Letters*, 13:138–140, Jul 1964. DOI: 10.1103/PhysRevLett.13.138. URL https://link.aps.org/doi/10.1103/PhysRevLett.13.138.

[25] R. Aaij et al. Observation of structure in the J/ψ-pair mass spectrum. *Science Bulletin*, 65:1983–1993. 11 p, Dec 2020. DOI: 10.1016/j.scib.2020.08.032. URL https://cds.cern.ch/record/2722544.

[26] R. Aaij et al. Observation of $J/\psi p$ Resonances Consistent with Pentaquark States in $\Lambda_b^0 \to J/\psi K^- p$ Decays. *Physical Review Letters*, 115:072001, 2015. DOI: 10.1103/PhysRevLett.115.072001. URL https://link.aps.org/doi/10.1103/PhysRevLett.115.072001.

[27] P. Abreu et al. Measurement of the triple-gluon vertex from 4-jet events at LEP. *Zeitschrift für Physik C Particles and Fields*, 59:357–368, 1993. DOI: 10.1007/BF01498617. URL https://cds.cern.ch/record/246874.

[28] A Geiser. Measurement of the triple-gluon vertex from jet and heavy flavour production at the CERN $p\overline{p}$ collider. Technical report, CERN, Geneva, 1994. URL https://cds.cern.ch/record/260276.

[29] F. Englert and R. Brout. Broken symmetry and the mass of gauge vector mesons. *Physical Review Letters*, 13:321–323, Aug 1964. DOI: 10.1103/PhysRevLett.13.321. URL https://link.aps.org/doi/10.1103/PhysRevLett.13.321.

[30] P. W. Higgs. Broken symmetries and the masses of gauge bosons. *Physical Review Letters*, 13:508–509, Oct 1964. DOI: 10.1103/PhysRevLett.13.508. URL https://link.aps.org/doi/10.1103/PhysRevLett.13.508.

[31] J. Goldstone. Field Theories with Superconductor Solutions. *Il Nuovo Cimento (1955-1965)*, 19:154–164, 1961. DOI: 10.1007/BF02812722. URL https://doi.org/10.1007/BF02812722.

[32] A. V. Manohar. Introduction to Effective Field Theories. Apr 2018. DOI: 10.1093/oso/9780198855743.003.0002. URL https://doi.org/10.1093/oso/9780198855743.003.0002.

[33] C. Degrande et al. Monte Carlo tools for studies of non-standard electroweak gauge boson interactions in multi-boson processes: A Snowmass White Paper. In *Community Summer Study 2013: Snowmass on the Mississippi*, Sep 2013. URL https://arxiv.org/abs/1309.7890.

[34] C. W. Murphy. Dimension-8 operators in the Standard Model Effective Field Theory. *Journal of High Energy Physics*, 10:174, 2020. DOI: 10.1007/JHEP10(2020)174. URL https://doi.org/10.1007%2Fjhep10%282020%29174.

[35] O. J. P. Éboli and M. C. Gonzalez-Garcia. Classifying the bosonic quartic couplings. *Physical Review D*, 93(9):093013, 2016. DOI: 10.1103/PhysRevD.93.093013. URL https://doi.org/10.1103%2Fphysrevd.93.093013.

[36] M. Aaboud et al. Measurement of the Inelastic Proton-Proton Cross Section at $\sqrt{s} = 13$ TeV with the ATLAS Detector at the LHC. *Physical Review Letters*, 117:182002, Oct 2016. DOI: 10.1103/PhysRevLett.117.182002. URL https://link.aps.org/doi/10.1103/PhysRevLett.117.182002.

[37] G. Aad et al. Evidence of $W\gamma\gamma$ Production in pp Collisions at $\sqrt{s} = 8$ TeV and Limits on Anomalous Quartic Gauge Couplings with the ATLAS Detector. *Physical Re-*

view Letters, 115:031802, Jul 2015. DOI: 10.1103/PhysRevLett.115.031802. URL https://link.aps.org/doi/10.1103/PhysRevLett.115.031802.

[38] M. Aaboud et al. Study of $WW\gamma$ and $WZ\gamma$ production in pp collisions at $\sqrt{s} = 8$ TeV and search for anomalous quartic gauge couplings with the ATLAS experiment. *European Physical Journal C*, 77(9):646, 2017. DOI: 10.1140/epjc/s10052-017-5180-3. URL https://doi.org/10.1140%2Fepjc%2Fs10052-017-5180-3.

[39] G. Aad et al. Observation of WWW production in pp collisions at $\sqrt{s} = 13$ TeV with the ATLAS detector. *Physical Review Letters*, 129(6):061803, 2022. DOI: 10.1103/PhysRevLett.129.061803. URL https://link.aps.org/doi/10.1103/PhysRevLett.129.061803.

[40] G. Aad et al. Evidence for the production of three massive vector bosons with the ATLAS detector. *Physics Letters B*, 798:134913, 2019. ISSN 0370-2693. DOI: https://doi.org/10.1016/j.physletb.2019.134913. URL https://www.sciencedirect.com/science/article/pii/S0370269319306355.

[41] The ATLAS Collaboration. Measurement of $Z\gamma\gamma$ production in pp collisions at $\sqrt{s} = 13$ TeV with the ATLAS detector. Nov 2022. URL https://arxiv.org/abs/2211.14171.

[42] The ATLAS Collaboration. Standard Model Summary Plots February 2022. Technical report, CERN, Geneva, 2022. URL http://cds.cern.ch/record/2804061.

[43] O. Brüning et al. *LHC Design Report*. CERN Yellow Reports: Monographs. CERN, Geneva, 2004. DOI: 10.5170/CERN-2004-003-V-1. URL https://cds.cern.ch/record/782076.

[44] M. Nicolet. CERN Quick Facts 2020 (English version). CERN Instantané 2020 (version anglaise). 2020. URL https://cds.cern.ch/record/2716422.

[45] E. Lopienska. The CERN accelerator complex, layout in 2022. Complexe des accélérateurs du CERN en janvier 2022. Feb 2022. URL https://cds.cern.ch/record/2800984.

[46] W. Herr and B. D. Muratori. Concept of luminosity. 2006. DOI: 10.5170/CERN-2006-002.361. URL https://cds.cern.ch/record/941318.

[47] C. Pralavorio. Record luminosity: well done LHC. Nov 2017. URL https://cds.cern.ch/record/2295027.

[48] G. Aad et al. *The ATLAS Experiment at the CERN Large Hadron Collider*, volume 3. 2008. DOI: 10.1088/1748-0221/3/08/S08003. URL https://cds.cern.ch/record/1129811.

[49] G. Aad et al. Observation of a new particle in the search for the Standard Model Higgs boson with the ATLAS detector at the LHC. *Physics Letters B*, 716(1):1–29, 2012. ISSN 0370-2693. DOI: https://doi.org/10.1016/j.physletb.2012.08.020. URL https://www.sciencedirect.com/science/article/pii/S037026931200857X.

[50] J. Pequenao. Computer generated image of the whole ATLAS detector. Mar 2008. URL https://cds.cern.ch/record/1095924.

[51] G. Aad et al. The ATLAS Inner Detector commissioning and calibration. *European Physical Journal C*, 70:787–821. 34 p, Jun 2010. DOI: 10.1140/epjc/s10052-010-1366-7. URL https://cds.cern.ch/record/1262789.

[52] A. Yamamoto et al. The ATLAS central solenoid. *Nuclear Instruments and Methods in Physics Research Section A: Accelerators, Spectrometers, Detectors and Associated Equipment*, 584(1):53–74, 2008. ISSN 0168-9002. DOI: https://doi.org/10.1016/j.nima.2007.09.047. URL https://www.sciencedirect.com/science/article/pii/S0168900207020414.

[53] G. Aad et al. ATLAS pixel detector electronics and sensors. *Journal of Instrumentation*, 3(07):P07007–P07007, Jul 2008. DOI: 10.1088/1748-0221/3/07/p07007. URL https://doi.org/10.1088/1748-0221/3/07/p07007.

[54] H. Pernegger. The Pixel Detector of the ATLAS Experiment for LHC Run-2. Technical report, CERN, Geneva, Feb 2015. URL https://cds.cern.ch/record/1985432.

[55] G. Aad et al. Operation and performance of the ATLAS semiconductor tracker in LHC Run 2. *Journal of Instrumentation*, 17:P01013. 55 p, Sep 2021. DOI: 10.1088/1748-0221/17/01/P01013. URL https://cds.cern.ch/record/2780336.

[56] A. Vogel. ATLAS Transition Radiation Tracker (TRT): Straw Tube Gaseous Detectors at High Rates. Technical report, CERN, Geneva, Apr 2013. URL https://cds.cern.ch/record/1537991.

[57] A. Andronic and J.P. Wessels. Transition radiation detectors. *Nuclear Instruments and Methods in Physics Research Section A: Accelerators, Spectrometers, Detectors and Associated Equipment*, 666:130–147, 2012. ISSN 0168-9002. DOI: https://doi.org/10.1016/j.nima.2011.09.041. URL https://www.sciencedirect.com/science/article/pii/S0168900211018134.

[58] C. W. Fabjan and F. Gianotti. Calorimetry for Particle Physics. *Reviews of Modern Physics*, 75:1243–1286. 96 p, Oct 2003. DOI: 10.1103/RevModPhys.75.1243. URL https://cds.cern.ch/record/692252.

[59] The ATLAS Collaboration. *ATLAS liquid-argon calorimeter: Technical Design Report*. Technical design report. ATLAS. CERN, Geneva, 1996. DOI: 10.17181/CERN. FWRW.FOOQ. URL https://cds.cern.ch/record/331061.

[60] T. Davidek. ATLAS Tile Calorimeter performance for single particles in beam tests. *Journal of Physics: Conference Series*, 160(1):012057, Apr 2009. DOI: 10.1088/1742-6596/160/1/012057. URL https://dx.doi.org/10.1088/1742-6596/160/1/012057.

[61] The ATLAS Collaboration. *ATLAS muon spectrometer: Technical Design Report*. Technical design report. ATLAS. CERN, Geneva, 1997. URL http://cds.cern.ch/record/331068.

[62] H. Herde. Muon reconstruction performance in ATLAS at Run-II. Technical report, CERN, Geneva, Oct 2015. URL https://cds.cern.ch/record/2059849.

[63] P. F. Åkesson and E. Moyse. Event Data Model in ATLAS. 2005. DOI: 10.5170/CERN-2005-002.255. URL https://cds.cern.ch/record/865580.

[64] The ATLAS collaboration. Operation of the ATLAS trigger system in Run 2. *Journal of Instrumentation*, 15(10):P10004–P10004, Oct 2020. DOI: 10.1088/1748-0221/15/10/p10004. URL https://doi.org/10.1088/1748-0221/15/10/p10004.

[65] G. Aad et al. Performance of the ATLAS muon triggers in Run 2. *Journal of Instrumentation*, 15(09):P09015, Sep 2020. DOI: 10.1088/1748-0221/15/09/p09015. URL https://doi.org/10.1088/1748-0221/15/09/p09015.

[66] M. Elsing et al. The ATLAS Tier-0: Overview and operational experience. *Journal of Physics: Conference Series*, 219(7):072011, Apr 2010. DOI: 10.1088/1742-6596/219/7/072011. URL https://doi.org/10.1088/1742-6596/219/7/072011.

[67] G. Aad et al. Electron and photon performance measurements with the ATLAS detector using the 2015-2017 LHC proton-proton collision data. *Journal of Instrumentation*, 14:P12006. 70 p, Dec 2019. DOI: 10.1088/1748-0221/14/12/P12006. URL https://cds.cern.ch/record/2684552.

[68] M. Aaboud et al. Electron and photon energy calibration with the ATLAS detector using 2015–2016 LHC proton-proton collision data. *Journal of Instrumentation*, 14(03):P03017, 2019. DOI: 10.1088/1748-0221/14/03/P03017. URL https://doi.org/10.1088%2F1748-0221%2F14%2F03%2Fp03017.

[69] M. Aaboud et al. Electron reconstruction and identification in the ATLAS experiment using the 2015 and 2016 LHC proton-proton collision data at $\sqrt{s} = 13$ TeV. *European Physical Journal C*, 79:639. 40 p, Aug 2019. DOI: 10.1140/epjc/s10052-019-7140-6. URL https://cds.cern.ch/record/2657964.

[70] G. Aad et al. Muon reconstruction and identification efficiency in ATLAS using the full Run 2 pp collision data set at $\sqrt{s} = 13$ TeV. *European Physical Journal C*, 81:578. 44 p, Jul 2021. DOI: 10.1140/epjc/s10052-021-09233-2. URL https://cds.cern.ch/record/2746302.

[71] G. Aad et al. Muon reconstruction performance of the ATLAS detector in proton–proton collision data at $\sqrt{s}$=13 TeV. Muon reconstruction performance of the ATLAS detector in proton–proton collision data at $\sqrt{s}$=13 TeV. *European Physical Journal C*, 76:292. 45 p, May 2016. DOI: 10.1140/epjc/s10052-016-4120-y. URL https://cds.cern.ch/record/2139897.

[72] M. Aaboud et al. Jet reconstruction and performance using particle flow with the ATLAS Detector. *European Physical Journal C*, 77(7):466, 2017. DOI: 10.1140/epjc/s10052-017-5031-2. URL https://doi.org/10.1140/epjc/s10052-017-5031-2.

[73] G. Aad et al. Muon reconstruction and identification efficiency in ATLAS using the full Run 2 pp collision data set at $\sqrt{s} = 13$ TeV. *European Physical Journal C*, 81(7):578, 2021. DOI: 10.1140/epjc/s10052-021-09233-2. URL https://doi.org/10.1140/epjc/s10052-021-09233-2.

[74] A. Buckley et al. General-purpose event generators for LHC physics. *Physics Reports*, 504:145–233, 2011. DOI: 10.1016/j.physrep.2011.03.005. URL https://www.sciencedirect.com/science/article/pii/S0370157311000846.

[75] T. Plehn. LHC Phenomenology for Physics Hunters. In *Theoretical Advanced Study Institute in Elementary Particle Physics: The Dawn of the LHC Era*, pages 125–180, 2010. DOI: 10.1142/9789812838360_0003. URL https://doi.org/10.1142/9789812838360_0003.

[76] H. Abramowicz et al. Combination of measurements of inclusive deep inelastic $e^{\pm}p$ scattering cross sections and QCD analysis of HERA data. *European Physical Journal C*, 75(12):580, 2015. DOI: 10.1140/epjc/s10052-015-3710-4. URL https://doi.org/10.1140/epjc/s10052-015-3710-4.

[77] G. Aad et al. Determination of the parton distribution functions of the proton using diverse ATLAS data from pp collisions at $\sqrt{s} = 7$, 8 and 13 TeV. *European Physical Journal C*, 82(5):438, 2022. DOI: 10.1140/epjc/s10052-022-10217-z. URL http://dx.doi.org/10.1140/epjc/s10052-022-10217-z.

[78] B. Andersson. Parton Fragmentation and String Dynamics. *Physics Reports*, 97:31–145, 1983. DOI: 10.1016/0370-1573(83)90080-7. URL https://www.sciencedirect.com/science/article/pii/0370157383900807.

[79] S. Agostinelli et al. GEANT4–a simulation toolkit. *Nuclear Instruments and Methods in Physics Research Section A: Accelerators, Spectrometers, Detectors and Associated Equipment*, 506:250–303, 2003. DOI: 10.1016/S0168-9002(03)01368-8. URL https://www.sciencedirect.com/science/article/pii/S0168900203013688.

[80] J. T. Boyd. LHC Run-2 and future prospects. *CERN Yellow Reports: School Proceedings*, 5:247, 2022. DOI: 10.23730/CYRSP-2021-005.247. URL https://arxiv.org/abs/2001.04370.

[81] G. Aad et al. ATLAS data quality operations and performance for 2015–2018 data-taking. *Journal of Instrumentation*, 15(04):P04003, 2020. DOI: 10.1088/1748-0221/15/04/P04003. URL https://doi.org/10.1088%2F1748-0221%2F15%2F04%2Fp04003.

[82] G. Aad et al. Performance of electron and photon triggers in ATLAS during LHC Run 2. *European Physical Journal C*, 80(1):47, 2020. DOI: 10.1140/epjc/s10052-019-7500-2. URL https://doi.org/10.1140/epjc/s10052-019-7500-2.

[83] G. Aad et al. Performance of the ATLAS muon triggers in Run 2. *Journal of Instrumentation*, 15(09):P09015, Sep 2020. DOI: 10.1088/1748-0221/15/09/P09015. URL https://dx.doi.org/10.1088/1748-0221/15/09/P09015.

[84] E. Bothmann et al. Event generation with Sherpa 2.2. *SciPost Physics*, 7(3):034, 2019. DOI: 10.21468/SciPostPhys.7.3.034. URL https://scipost.org/10.21468/SciPostPhys.7.3.034.

[85] R. D. Ball et al. Parton distributions for the LHC run II. *Journal of High Energy Physics*, 04:040, 2015. DOI: 10.1007/JHEP04(2015)040. URL https://doi.org/10.1007/JHEP04(2015)040.

[86] J. Alwall et al. The automated computation of tree-level and next-to-leading order differential cross sections, and their matching to parton shower simulations. *Journal of High Energy Physics*, 07:079, 2014. DOI: 10.1007/JHEP07(2014)079. URL https://doi.org/10.1007/JHEP07(2014)079.

[87] T. Sjöstrand, S. Mrenna, and P. Skands. A brief introduction to PYTHIA 8.1. *Computer Physics Communications*, 178:852–867, 2008. DOI: 10.1016/j.cpc.2008.01.036. URL https://www.sciencedirect.com/science/article/pii/S0010465508000441.

[88] P. Nason. A new method for combining NLO QCD with shower Monte Carlo algorithms. *Journal of High Energy Physics*, 11:040, 2004. DOI: 10.1088/1126-6708/2004/11/040. URL https://dx.doi.org/10.1088/1126-6708/2004/11/040.

[89] S. Alioli et al. NLO vector-boson production matched with shower in POWHEG. *Journal of High Energy Physics*, 07:060, 2008. DOI: 10.1088/1126-6708/2008/07/060. URL https://dx.doi.org/10.1088/1126-6708/2008/07/060.

[90] S. Frixione, P. Nason, and C. Oleari. Matching NLO QCD computations with parton shower simulations: the POWHEG method. *Journal of High Energy Physics*, 11:070, 2007. DOI: 10.1088/1126-6708/2007/11/070. URL https://dx.doi.org/10.1088/1126-6708/2007/11/070.

[91] S. Alioli et al. A general framework for implementing NLO calculations in shower Monte Carlo programs: the POWHEG BOX. *Journal of High Energy Physics*, 06:043, 2010. DOI: 10.1007/JHEP06(2010)043. URL https://doi.org/10.1007/JHEP06(2010)043.

[92] H.-L. Lai et al. New parton distributions for collider physics. *Physical Review D*, 82:074024, 2010. DOI: 10.1103/PhysRevD.82.074024. URL https://link.aps.org/doi/10.1103/PhysRevD.82.074024.

[93] J.-B. De Vivie De Regie et al. ATLAS electron, photon and muon isolation in Run 2. Technical report, CERN, Geneva, 2017. URL https://cds.cern.ch/record/2256658.

[94] G. Aad et al. Measurements of $Z\gamma$ and $Z\gamma\gamma$ production in pp collisions at $\sqrt{s} = 8$ TeV with the ATLAS detector. *Physical Review D*, 93(11):112002, 2016. DOI: 10.1103/PhysRevD.93.112002. URL https://doi.org/10.1103%2Fphysrevd.93.112002.

[95] G. Aad et al. Measurement of the isolated di-photon cross-section in pp collisions at $\sqrt{s} = 7$ TeV with the ATLAS detector. *Physical Review D*, 85:012003, 2012. DOI: 10.1103/PhysRevD.85.012003. URL https://doi.org/10.1103%2Fphysrevd.85.012003.

[96] G. Aad et al. Measurement of the $Z(\to \ell^+\ell^-)\gamma$ production cross-section in pp collisions at $\sqrt{s} = 13$ TeV with the ATLAS detector. *Journal of High Energy Physics*, 2003:054, 2020. DOI: 10.1007/JHEP03(2020)054. URL https://doi.org/10.1007/JHEP03(2020)054.

[97] S. Frixione. Isolated photons in perturbative QCD. *Physics Letters B*, 429(3-4):369–374, Jun 1998. DOI: 10.1016/s0370-2693(98)00454-7. URL https://doi.org/10.1016%2Fs0370-2693%2898%2900454-7.

[98] G. Aad et al. Measurement of the isolated diphoton cross section in pp collisions at $\sqrt{s} = 7$ TeV with the ATLAS detector. *Physical Review D*, 85:012003, Jan 2012. DOI: 10.1103/PhysRevD.85.012003. URL https://link.aps.org/doi/10.1103/PhysRevD.85.012003.

[99] G. Aad et al. Evidence of $W\gamma\gamma$ Production in pp Collisions at $\sqrt{s} = 8$ TeV and Limits on Anomalous Quartic Gauge Couplings with the ATLAS Detector. *Physical Review Letters*, 115:031802, Jul 2015. DOI: 10.1103/PhysRevLett.115.

031802. URL https://link.aps.org/doi/10.1103/PhysRevLett.115.031802.

[100] W. Verkerke and D. Kirkby. The RooFit toolkit for data modeling. 2003. DOI: 10.48550/ARXIV.PHYSICS/0306116. URL https://arxiv.org/abs/physics/0306116.

[101] J. J. Li, X. Tong, and P. J. Bickel. Generalized pearson correlation squares for capturing mixtures of bivariate linear dependences, 2020. URL https://doi.org/10.48550/arXiv.1811.09965.

[102] T. Skwarnicki. *A study of the radiative CASCADE transitions between the Upsilon-Prime and Upsilon resonances*. PhD thesis, Cracow, INP, Apr 1986. URL http://www-library.desy.de/cgi-bin/showprep.pl?DESY-F31-86-02.

[103] A. D. Bukin. Fitting function for asymmetric peaks, 2007. URL https://arxiv.org/abs/0711.4449.

[104] K. Cranmer. Kernel estimation in high-energy physics. *Computer Physics Communications*, 136(3):198–207, May 2001. DOI: 10.1016/s0010-4655(00)00243-5. URL https://doi.org/10.1016%2Fs0010-4655%2800%2900243-5.

[105] The ATLAS Collaboration. Evaluating statistical uncertainties and correlations using the bootstrap method. Technical report, CERN, Geneva, 2021. URL https://cds.cern.ch/record/2759945.

[106] G. Aad et al. Measurement of the inclusive isolated-photon cross section in pp collisions at $\sqrt{s} = 13$ TeV using 36 fb^{-1} of ATLAS data. *Journal of High Energy Physics*, 10:203, 2019. DOI: 10.1007/JHEP10(2019)203. URL https://doi.org/10.1007/JHEP10(2019)203.

[107] G. Aad et al. Measurement of the production cross section of pairs of isolated photons in pp collisions at 13 TeV with the ATLAS detector. *Journal of High Energy Physics*, 11:169, 2021. DOI: 10.1007/JHEP11(2021)169. URL https://doi.org/10.1007/JHEP11(2021)169.

[108] M. Aaboud et al. Measurement of the photon identification efficiencies with the ATLAS detector using LHC Run 2 data collected in 2015 and 2016. *European Physical Journal C*, 79:205. 55 p, Mar 2019. DOI: 10.1140/epjc/s10052-019-6650-6. URL https://cds.cern.ch/record/2643391.

170

[109] G. Aad et al. Measurements of WH and ZH production in the $H \rightarrow b\bar{b}$ decay channel in pp collisions at 13 TeV with the ATLAS detector. *European Physical Journal C*, 81(2):178, 2021. DOI: 10.1140/epjc/s10052-020-08677-2. URL https://doi.org/10.1140/epjc/s10052-020-08677-2.

[110] J. Butterworth et al. PDF4LHC recommendations for LHC Run II. *Journal of Physics G: Nuclear and Particle Physics*, 43:023001, 2016. DOI: 10.1088/0954-3899/43/2/023001. URL https://dx.doi.org/10.1088/0954-3899/43/2/023001.

[111] M. Aaboud et al. Electron and photon energy calibration with the ATLAS detector using 2015–2016 LHC proton-proton collision data. *Journal of Instrumentation*, 14(03):P03017, 2019. DOI: 10.1088/1748-0221/14/03/P03017. URL https://dx.doi.org/10.1088/1748-0221/14/03/P03017.

[112] G. Aad et al. Muon reconstruction performance of the ATLAS detector in proton–proton collision data at $\sqrt{s}$ =13 TeV. *European Physical Journal C*, 76(5):292, 2016. DOI: 10.1140/epjc/s10052-016-4120-y. URL https://doi.org/10.1140/epjc/s10052-016-4120-y.

[113] The ATLAS collaboration. Studies of the muon momentum calibration and performance of the ATLAS detector with pp collisions at $\sqrt{s}$=13 TeV. Dec 2022. URL https://arxiv.org/abs/2212.07338.

[114] W. Buttinger. Using Event Weights to account for differences in Instantaneous Luminosity and Trigger Prescale in Monte Carlo and Data. Technical report, CERN, Geneva, 2015. URL https://cds.cern.ch/record/2014726.

[115] The ATLAS Collaboration. Luminosity determination in pp collisions at $\sqrt{s} = 13$ TeV using the ATLAS detector at the LHC. Technical report, CERN, Geneva, 2019. URL https://cds.cern.ch/record/2677054.

[116] G. D'Agostini. A multidimensional unfolding method based on Bayes' theorem. *Nuclear Instruments and Methods in Physics Research Section A: Accelerators, Spectrometers, Detectors and Associated Equipment*, 362(2):487–498, 1995. ISSN 0168-9002. DOI: https://doi.org/10.1016/0168-9002(95)00274-X. URL https://www.sciencedirect.com/science/article/pii/016890029500274X.

[117] G. D'Agostini. Improved iterative Bayesian unfolding. In *Alliance Workshop on Unfolding and Data Correction*, Oct 2010. URL https://doi.org/10.48550/arXiv.1010.0632.

[118] F. D. Aaron et al. Measurement of the Inclusive ep Scattering Cross Section at Low Q^2 and x at HERA. *European Physical Journal C*, 63:625–678, 2009. DOI: 10.1140/epjc/s10052-009-1128-6. URL https://doi.org/10.1140/epjc/s10052-009-1128-6.

[119] F. D. Aaron et al. Combined Measurement and QCD Analysis of the Inclusive e+- p Scattering Cross Sections at HERA. *Journal of High Energy Physics*, 01:109, 2010. DOI: 10.1007/JHEP01(2010)109. URL https://doi.org/10.1007/JHEP01(2010)109.

[120] The ATLAS Collaboration. Measurement of $Z\gamma\gamma$ production in pp collisions at $\sqrt{s} = 13$ TeV with the ATLAS detector. HEPData (collection), 2023. URL https://doi.org/10.17182/hepdata.132903.

[121] B. E. Lindquist et al. Recommendations from the Anomalous Gauge Coupling Taskforce. Technical report, CERN, Geneva, 2017. URL https://cds.cern.ch/record/2261444.

[122] O. J. P. Eboli, M. C. Gonzalez-Garcia, and J. K. Mizukoshi. $pp \rightarrow jje^{\pm}\mu^{\pm}\nu\nu$ and $jje^{\pm}\mu^{\mp}\nu\nu$ at $\mathcal{O}(\alpha_{\mathrm{em}}^6)$ and $\mathcal{O}(\alpha_{\mathrm{em}}^4\alpha_s^2)$ for the study of the quartic electroweak gauge boson vertex at CERN LHC. *Physical Review D*, 74:073005, 2006. DOI: 10.1103/PhysRevD.74.073005. URL https://doi.org/10.1103%2Fphysrevd.74.073005.

[123] C. Bierlich et al. Robust Independent Validation of Experiment and Theory: Rivet version 3. *SciPost Physics*, 8:026, 2020. DOI: 10.21468/SciPostPhys.8.2.026. URL https://scipost.org/10.21468/SciPostPhys.8.2.026.

[124] ATLAS internal resource. URL https://gitlab.cern.ch/eft-tools/eft-fun.

[125] S. S. Wilks. The Large-Sample Distribution of the Likelihood Ratio for Testing Composite Hypotheses. *The Annals of Mathematical Statistics*, 9(1):60–62, 1938. DOI: 10.1214/aoms/1177732360. URL https://doi.org/10.1214/aoms/1177732360.

[126] The CMS Collaboration. Measurements of production cross sections of WZ and same-sign WW boson pairs in association with two jets in proton–proton collisions at $\sqrt{s} = 13$ TeV. *Physics Letters B*, 809:135710, 2020. DOI: 10.1016/

j.physletb.2020.135710. URL https://doi.org/10.1016/j.physletb.2020.135710.

[127] The ATLAS Collaboration. Measurement of electroweak $Z(\nu\bar{\nu})\gamma jj$ production and limits on anomalous quartic gauge couplings in pp collisions at $\sqrt{s} = 13$ TeV with the ATLAS detector. Aug 2022. DOI: 10.48550/ARXIV.2208.12741. URL https://arxiv.org/abs/2208.12741.

[128] The ATLAS Collaboration. Formulae for Estimating Significance. 2020. URL https://cds.cern.ch/record/2736148.

[129] M. Aaboud et al. Measurements of inclusive and differential fiducial cross-sections of $t\bar{t}\gamma$ production in leptonic final states at $\sqrt{s} = 13$ TeV in ATLAS. *European Physical Journal C*, 79(5), May 2019. DOI: 10.1140/epjc/s10052-019-6849-6. URL https://doi.org/10.1140%2Fepjc%2Fs10052-019-6849-6.

[130] G. Aad et al. Measurement of the transverse momentum distribution of Drell–Yan lepton pairs in proton–proton collisions at $\sqrt{s} = 13$ TeV with the ATLAS detector. *European Physical Journal C*, 80(7):616, 2020. DOI: 10.1140/epjc/s10052-020-8001-z. URL https://doi.org/10.1140/epjc/s10052-020-8001-z.

Acknowledgements

This work is the result of help and support I received during numerous stages of the PhD.

First and foremost, I would like to give a special thanks to Prof. Dr. Hans-Christian Schultz-Coulon, who gave me the opportunity to start the PhD in the ATLAS group at the Kirchhoff Institute for Physics. He was always very friendly and open minded, which was especially important to me in the beginning of my thesis where I did not know many people in Heidelberg. He also gave me enough freedom to gain confidence and grow as a physicist.

I would also like to thank my second referee Prof. Dr. Klaus Reygers, who kindly agreed to be part of the committee and review the thesis.

A special thanks goes to Rainer and Pavel, who both supervised me throughout my PhD and gave invaluable advice and support for the analysis. Rainer, I greatly appreciate that you proofread the whole thesis and always had an open ear and time for discussions. I am also thankful for the great integration into the KIP multiboson group.

To all the people of F8 and F11, thanks a lot for the seamlessly integration and the friendly atmosphere. I am especially grateful for the fun activities we had outside of physics, which made it feel like this was not just any other working group. These activities include cooking, wakeboarding, singing karaoke, bouldering, and more.

Thanks a lot to all the people proofreading various chapters of my thesis: Sebastian[38], Anke, Martin, Varsiha, Falk, Damir, Lisa, and Thomas.

To my family, I am forever grateful for the unconditional support and believe in me. I was always able to choose my own path and lifestyle without any doubts or criticism.

Lastly, I would like to thank my fiancée Mareike. I am immensely grateful for your unconditional support and the care I receive on a daily basis. You were always there for me, especially when I struggled during difficult times of the PhD. I am excited to start a new chapter of our life together.

---

[38]Thanks for the last minute advice and for reading a substantial amount of the thesis.